UNIVERSIDAD COMPLUTENSE DE MADRID

FACULTAD DE CIENCIAS FÍSICAS

Departamento de Física Atómica Molecular y Nuclear

TESIS DOCTORAL

Characterization of the very-high-energy emission from pulsars with the Magic telescopes

MEMORIA PARA OPTAR AL GRADO DE DOCTOR

PRESENTADA POR

Simon Bonnefoy

Directores

Marcos López
María Victoria Fonseca

Madrid, 2016

Characterization of the Very-High-Energy Emission from Pulsars with the MAGIC Telescopes

Caracterización de la emisión de muy alta energía de los púlsares con los telescopios MAGIC

A Thesis presented for the degree of
Doctor of Philosophy

Simon Bonnefoy
Departamento de Física Atómica Molecular y Nuclear
Universidad Complutense de Madrid

November 2015

Thesis Advisors:
Marcos López
María Victoria Fonseca

I hereby declare that I am the sole author of this thesis.
The data presented in this thesis are the property of the MAGIC collaboration when not otherwise stated.

Simon Bonnefoy

I authorize the Universidad Complutense de Madrid to lend this thesis to other institutions or individuals for the purpose of scholary research.

Simon Bonnefoy

Contents

Abstract

For several decades, since their discovery in 1967 by Jocelyn Bell Burnell, pulsars have been under intense investigation. Due to their huge magnetic and gravitational fields, pulsars are one of the best laboratories to study matter in extreme conditions. Recently, the detection of emission from the Crab pulsar at Very High Energies (VHE, > 100 GeV) was a breakthrough, as such emission was totally unexpected. Even though pulsars are being deeply studied, their emission location and mechanisms are still poorly understood. Several regions where the VHE gamma rays are expected to be emitted where proposed, each of them exhibiting different features in the pulsars emission, such as energy spectrum and light curve properties. The observation of pulsars at VHE is then fundamental in order to understand their emission properties and distinguish between the current models.

This thesis deals with the characterization of the VHE emission from pulsars. This study relies on the observations of pulsars with the MAGIC telescopes and the analytic calculation of the pulsar X-ray and gamma-ray emission efficiencies in the framework of the outer-gap model.

Two pulsars were selected for the observations with the MAGIC telescopes, namely, the Crab and Geminga pulsars. These pulsars are the two brightest gamma-ray pulsars observable from the Northern Hemisphere. The study of the Crab pulsar revealed the significant emission from the interpulse region, also called bridge, located between the two main peaks. This component, already observed at low energies and predicted at VHE, was not previously detected at VHE. Furthermore, the relative emission between the two main peaks and the bridge was computed, including the analysis of 6.5 years of *Fermi*-LAT data. The behaviors of P2/P1 and bridge/P1 revealed a similar trend, unveiling similar properties in the emission of these distinct components.

The second pulsar under study, the Geminga pulsar, turns out to be an interesting target as, besides discovering a new VHE pulsar which might exhibit the same features as observed for the Crab pulsar, the Geminga pulsar is much older than the Crab and could help us understand the evolution of pulsar physics with

the pulsar age. The observation of the Geminga pulsar and its surrounding nebula with MAGIC led to the computation of upper limits as not significant signal was detected. Besides, a deep study of Geminga was also carried out analyzing 5 years of *Fermi*-LAT data. We characterized the energy spectrum at HE with a power-law function with both exponential and sub-exponential cut-off. We could establish that the spectrum of Geminga is better characterized by a power-law function with a sub-exponential cut-off than an exponential cut-off at the 6, 11 and 24 σ level for P1, P2 and the phase-averaged emission, respectively.

Finally, we studied from a theoretical point of view the evolution of the X-ray and gamma-ray efficiency of pulsars with their age. Our calculations were done within the framework of an enhanced version of the outer-gap model, which is one of the favored model, including the development of cascades within the outer gap. Furthermore, we consider the minimal cooling scenario, assuming that the neutron star is made out of standard matter and its surface temperature depends only on the composition of the envelope, i.e., light or heavy element envelope. We computed the evolution of the gap trans-magnetic-field thickness for both cases, and the efficiencies for young and middle-aged pulsars. The results obtained considering light and heavy element envelope are in agreement with with the evolution of the efficiencies observed from pulsars, according to which, very young pulsars are efficient X-ray emitters and poor gamma-ray emitters, whereas it is the other way around for older pulsars.

Resumen

En 1967, la estudiante de doctorado Jocelyn Bell Burnell, observó por primera vez la señal procedente de un púlsar. Estos objetos estelares han sido desde entonces intensamente estudiados a todas las longitudes de onda. Debido a su intenso campo magnético y gravitatorio, los púlsares se han convertido en uno de los mejores laboratorios para el estudio de la materia en condiciones extremas.

Recientemente, la detección de emisión de muy alta energías (VHE $>$ 100 GeV) del púlsar del Cangrejo ha obligado a replantearnos nuestras ideas sobre el funcionamiento de estas estrellas, ya que tal emisión parecía descartada *a priori* por los modelos teóricos existentes. Estos modelos proponen distintos lugares en las magnetosferas de los púlsares, y en torno a éstas, como origen de la emisión de muy alta energía detectada, cada uno con características propias en la distribución espectrales de energía y en las curva de luz esperadas. Las observaciones de los púlsares a muy altas energías son por lo tanto fundamentales para entender la ubicación y los mecanismos de la emisión y distinguir entre los distintos modelos.

Esta tesis trata de la caracterización de la emisión de muy alta energía de los púlsares. Este estudio está basado en las observaciones de púlsares con los telescopios MAGIC y *Fermi*-LAT y en una estimación analítica de la eficiencia de emisión en rayos X y rayos gamma de los púlsares en el contexto del modelo del "outer gap" o de "zona externa".

Dos púlsares fueron seleccionados para las observaciones con los telescopios MAGIC: el púlsar del Cangrejo y Geminga. Estos dos púlsares son los más brillantes observables desde el hemisferio Norte. El estudio del púlsar del Cangrejo nos ha permitido detectar por primera vez señal de radiación pulsada en la zona denominada "puente", localizada entre los dos picos principales de emisión que presenta la curva de luz de este púlsar. La emisión en esta zona ya había sido detectada a energía inferiores, pero nunca en rayos gammas de muy alta energía hasta ahora. Además, hemos estudiado la evolución de la emisión relativa entre los picos y la "zona puente" a diferentes energías, incluyendo en nuestro análisis 6.5 años de datos del telescopio espacial *Fermi*-LAT, mostrando una evolución similar de los cocientes P2/P1 y "puente"/P1. Tal similaridad revela propiedades similares en la emisión de las distintas componentes.

El segundo púlsar estudiado, Geminga, es mucho más viejo que el Cangrejo, por lo que su detección con MAGIC ayudaría a entender la evolución de la física de los púlsares con su edad. El análisis de las observaciones de Geminga realizadas con los telescopios MAGIC no han dado lugar a la detección de ninguna señal procedente de este púlsar. Se han obtenido por tanto, limites superiores a la posible emisión de este púlsar en el rango de energías cubierto por MAGIC. Para el estudio de Geminga se han analizado así mismo 5 años de datos suministrados por el detector LAT, a bordo del satélite *Fermi*. Esto ha conducido a la caracterización de la distribución espectral en energía utilizando dos funciones, una ley de potencias con un corte exponencial y otra con un corte sub-exponential. Hemos podido establecer que la ley de potencias con corte sub-exponencial caracteriza mejor la emisión de Geminga a un nivel de 6, 11 y 24 σ para P1, P2, y la emisión total respectivamente.

Finalmente, hemos realizado un estudio teórico sobre la evolución de la eficiencia de emisión de los púlsares en rayos X y rayos gamma con la edad del púlsar. Nuestro cálculo está basado en una versión mejorada del modelo "outer gap", uno de los favoritos para la emisión de muy alta energía de los púlsares, incluyendo el desarrollo de cascadas electromagnéticas dentro del "gap". Además, hemos considerado el escenario de enfriamiento mínimo "minimal cooling scenario", suponiendo que la estrella de neutrones está hecha de materia estándar y que la temperatura de la superficie depende de la composición de la zona externa, es decir, de si está compuesta por elementos ligeros o pesados. Calculamos la evolución de la anchura de la zona externa en la dirección perpendicular a las líneas de campo magnético para ambos casos, y las eficiencias de emisión para púlsares jóvenes y de edad media. Los cálculos llevados a cabo, considerando tanto elementos ligeros y pesados, concuerdan con la evolución de la eficiencia observada de los púlsares, según la cual los púlsares muy jóvenes son buenos emisores de rayos X y débiles emisores en rayos gamma, mientras que para púlsares más viejos la tendencia es al revés.

Chapter 1

The gamma-ray sky

Standard astronomy and astrophysics used to rely on optical observations from thermal radiation emitted by hot objects. However, during the 20^{th} century, technological improvements widened the observation window from radio wavelengths up to very high energy (VHE, E > 100 GeV) gamma rays. In 1912, Victor Hess discovered Cosmic Rays (CRs) using balloon experiments (Hess, 1913a,b), and in 1938 Pierre Auger proved the existence of Extensive Air Showers (EAS) initiated by cosmic-ray particles with energies greater than 10^{15} eV (Auger et al., 1939). The study of CRs revealed that their spectrum extends up to 10^{20} eV and beyond. Thermal processes cannot explain particles at such high energies and other mechanisms have to be involved. Besides VHE photons and CRs, neutrinos and gravitational waves appeared to be useful messengers in order to understand the VHE phenomena occurring in the universe. Gamma-ray astrophysics is strongly linked to particle physics due to the nature of these messengers. The synergy of these two fields is called *astroparticle physics*.

The non-thermal radiation emitted by astrophysical objects can thus be studied by observing the CRs or the electromagnetic radiation. However, CRs due to their electric charge are deflected by Galactic magnetic fields and the information related to their incoming direction and acceleration is lost. Only information regarding their energy and chemical composition can be extracted. Thus, VHE astronomy has to rely on neutral particles such as gamma rays and neutrinos. Due to the magnetic deflection, an isotropic flux of CRs is expected on Earth. The emission of VHE gamma rays requires the acceleration of charged particles and their interaction with radiation and magnetic fields. Hence the study of the VHE gamma rays can shed light on the mechanisms of CR acceleration.

Within the field of astroparticle physics, the most extreme phenomena and conditions are studied, such as supernova remnants (SNRs), neutron stars (NS) and black holes (BH), the two latter being characterized by huge magnetic and gravitational fields. Besides physics in extreme conditions, the study of fundamental

physics such as the origin and characterization of the dark matter and Lorentz Invariance Violation (LIV) are under investigation.

1.1 Cosmic rays

Cosmic Rays are defined as the high energy (HE) charged particles originating from outer space colliding with the Earth's atmosphere. They are mostly comprised of protons and helium nuclei (98%) and a small amount of heavier nuclei, electrons and positrons. CRs were discovered in 1912 by Victor Hess by means of a balloon-borne experiment designed to study the ionization of the atmosphere with an electroscope (Hess, 1913a). Hess figured out that the the rate of discharges of the electroscope increased with altitude, and interpreted it as caused by an extraterrestrial penetrating radiation. Hess's results were confirmed a year later by Kolhörster (Kolhorster, 1913).

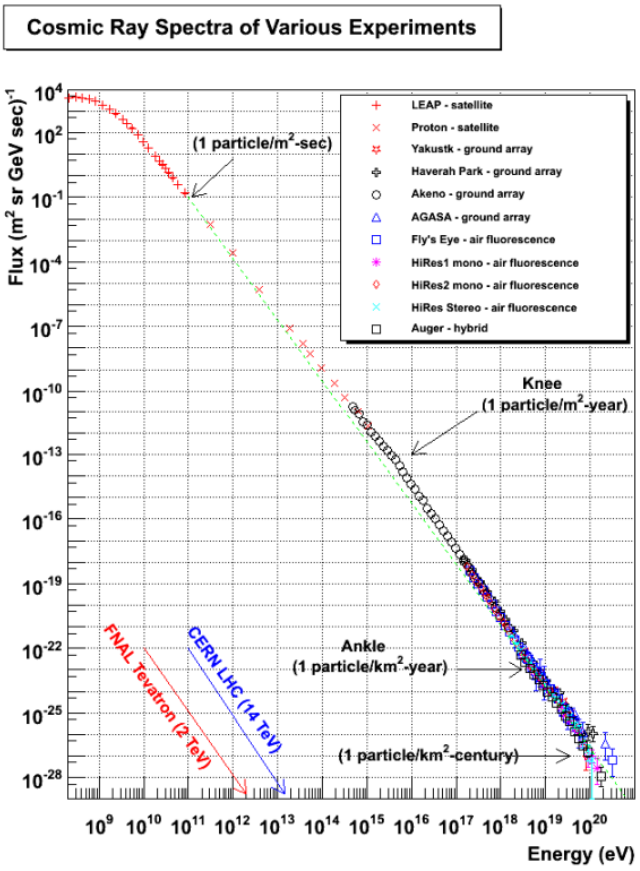

FIGURE 1.1: Full energy range of the Cosmic ray spectrum. Figure adopted from (Hanlon, 2015).

Figure 1.1 shows the CRs flux. It covers 11 orders of magnitude. The flux is characterized by two inflection points known as the *knee* at $\sim 3 \cdot 10^{15}$ eV and the *ankle* at $\sim 10^{18}$ eV. The CRs spectrum is characterized by a power-law function ($dN/dE \propto E^{\alpha}$). At the *knee* the spectral index changes from $\alpha = -2.65$ to $\alpha = -3.1$ and hardens back to $\alpha = -2.7$ at the *ankle*. The changes in the spectral slope are thought to be related to the origin of CRs: CRs below the *knee* are thought to be accelerated within the Galaxy, whereas CRs above the *ankle* are thought be of extragalactic origin. The latter assumption comes from the fact that protons with energy greater that 1 EeV would have a Larmor radius in the galactic magnetic field too big to be contained within the galaxy. The origin of CRs between the *ankle* and the *knee*, however, is still unknown. The cut-off observed at $4 - 6 \cdot 10^{19}$ eV results from the interaction of CRs with the Cosmic Microwave Background (CMB) photons, known as the Greisen-Zatsepin-Kuzmin (GZK) cut-off (Zatsepin and Kuz'min, 1966; Greisen, 1966). This effect limits the propagation of CRs with energy $E \sim 10^{20}$ eV to ~ 50 pc.

Galactic cosmic rays

Galactic CRs are believed to form the low energy part of the CR spectrum, i.e., up to the *knee*. However, they are not excluded from forming part of the intermediate region between the *knee* and the *ankle*. Low energy CRs, $E < 10^9$ eV, are expected to be mainly produced in the Sun. The calculated chemical abundance is in agreement with the one present in the stars. It was suggested in 1934 (Baade and Zwicky, 1934a) that SuperNovae (SNe) could be the source of galactic CRs. SNe are expected to accelerate CRs up to 10^{15} eV, which could explain the decrease of the flux above the *knee*. Other sources such as micro-quasars and pulsars are also thought accelerated CRs.

Extragalactic cosmic rays

As previously mentioned, the *ankle* is thought to be the point where extra-galactic CRs become dominant. However, there is, so far, no clear separation between the Galactic and extragalactic component of the CRs spectrum. The mechanisms responsible for the CRs acceleration up to 10^{18} eV is still unknown. One of the the most credited scenario suggests that such an acceleration arises in diffuse shocks in extragalactic sources such as gamma-ray bursts (GRBs), Galactic Active Nuclei (AGN), radio galaxy lobes and intergalactic magnetic fields (IGM). At such energies, particles are not significantly deflected by magnetic fields, thus, they may carry directional information.

1.2 Acceleration of cosmic rays

As previously mentioned, CRs are detected, and so accelerated, up to 10^{20} eV. Acceleration of charged particles can be a direct effect of very intense electric and magnetic fields, but it can also occur via diffuse shocks acceleration mechanisms. Acceleration shocks were formulated by Enrico Fermi (Fermi, 1949), who established two acceleration mechanisms.

- The **second order Fermi acceleration** lies on the interaction between a charged particle and a moving magnetic "cloud". On average, the energy gained by the charged particle during each interaction with the magnetic cloud is proportional to the cloud velocity:

$$\left\langle \frac{\Delta E}{E} \right\rangle \propto \beta^2 \equiv \alpha, \tag{1.1}$$

  where β is defined as $\beta = v_{cloud}/c$, where v_{cloud} is the cloud velocity and c is the speed of light. This acceleration is dubbed "second order" as it is proportional to β^2. For a typical molecular cloud velocity of $\beta = 10^{-5}$ the gain is $10^{-10}E_1$, with E_1 the energy of the charged particle before interaction, so, this is a slow and inefficient mechanism. After n collisions, the energy of the particle will be:

$$E(n) = E_1(1+\alpha)^n. \tag{1.2}$$

  Besides the fact that the energy spectrum of the accelerated charges is strongly dependent on the magnetic cloud properties, and so hardly predictable, this mechanism is unable to explain the VHE CRs observed.

- The **first order Fermi acceleration** was further introduced by Fermi in order to explain the observed CRs spectrum. In this mechanism CRs are supposed to be accelerated by plasma shock waves (Fermi, 1949, 1954). A shock identifies a blob of material with a velocity greater than the speed of sound in the medium. During the propagation of the shock, charged particles can cross the shock front several times due to magnetic scattering, see Figure 1.2. Every time the particle crosses the shock front it gains energy. The energy gain is proportional to $\beta : \beta = V_S/c$, where V_S is the speed of the shock. The greater the speed of the shock, the larger the energy gain each time a particle crosses the shock, and the larger the magnetic field strength, the higher the particle crossing frequency. This mechanism is referred to as the first order Fermi acceleration because the energy gained by the charged particle each time it crosses the shock depends linearly on β. Since typical β values are of the order of $10^{-2} - 10^{-3}$, this mechanism is much more efficient than the second order Fermi acceleration and is believed to be the major

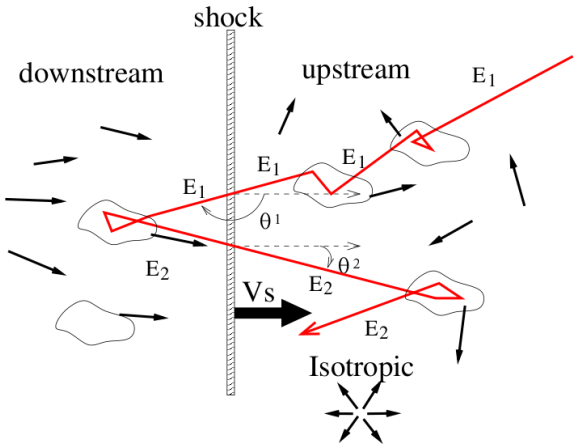

FIGURE 1.2: Scattering of charged particles at the shock front in the first order Fermi acceleration. Figure adopted from (Saito, 2010).

mechanism for CR acceleration at the TeV and PeV scale. Furthermore, it predicts a power-law spectrum, such as the one observed for CRs.

1.3 Gamma-ray production and absorption

In order to understand and characterize the gamma-ray sky and the non-thermal universe, an understanding of the processes leading to the production of gamma rays is necessary. The production and absorption of gamma rays are strongly influenced by the conditions and the elements present in the medium such as charged particles, electric and magnetic fields, etc. A brief overview of the gamma-ray emission mechanism is presented here. More details about radiative processes can be found in the literature, e.g., in (Rybicki and Lightman, 1991) and (Jackson, 1999).

Electron-positron annihilation

This process is independent of energy and occurs anytime a particle collides with its antiparticle resulting in the emission of two photons.

$$e^+ + e^- \rightarrow \gamma + \gamma \tag{1.3}$$

For an electron-positron pair at rest, each of the photons created will have an energy equal to $E_\gamma = m_e c^2 = 511$ keV. Other matter anti-matter annihilation processes can occur, such as proton anti-proton, however, this one is marginal in astrophysical environments compared to the electron-positron annihilation.

Bremsstrahlung

Bremsstrahlung stands for braking radiation in German. It describes the emission of electromagnetic radiation by a charged particle deflected by an electric field, typically the one of an atomic nucleus.

$$e + Z \rightarrow e + Z + \gamma \tag{1.4}$$

The Bremsstrahlung emission is referred to as a *free-free* process. The intensity of the emitted radiation is proportional to the charge of the nucleus. Electrons are more efficient than protons in producing Bremsstrahlung radiation due to the fact that the emission is an inverse square law of the mass of the emitting particle, $\propto m_e^{-2}$ (Longair, 2011). If the electron population has a power-law energy spectrum, the resulting gamma-ray spectrum will also be characterized by a power-law function with the same spectral index, as shown in (Saito, 2010). Bremsstrahlung process is the dominant gamma-ray emission mechanism up to 100 MeV. Synchrotron and inverse Compton (IC) processes are more likely to explain the VHE gamma-ray emission.

Synchrotron radiation

Synchrotron radiation results from the motion of a charged particle in a magnetic field. Due to the Lorentz force, the charged particle trajectory is bent and becomes helicoidal following the magnetic field lines, resulting in electromagnetic radiation emission.

$$e + B \rightarrow e + B + \gamma \tag{1.5}$$

In the case of a relativistic charged particle, the emitted radiation is beamed along a cone surface, centered on the particle trajectory and with an angular aperture of $\sim 1/\gamma$, with γ the Lorentz factor of the emitting particle. The synchrotron radiation from a mono-energetic electron population is a continuum that peaks at

$$E_\gamma \simeq 1.5 \cdot 10^{-5} \cdot \left(\frac{B}{\mathrm{G}}\right) \left(\frac{E_e}{\mathrm{TeV}}\right)^2, \tag{1.6}$$

where B is the magnetic field in Gauss and E_e the energy of the electron population. If electrons are not mono-energetic but are distributed according to a power-law energy spectrum with a spectral index $\alpha = -p$, the resulting synchrotron radiation spectrum will be characterized by a power-law function with a spectral $\alpha' = -(p+1)/2$. The observed VHE gamma rays require electron energies too large to be explained by synchrotron radiation. However, electrons are able to produce VHE gamma rays by means of other mechanisms such as IC scattering and curvature radiation. It may happen that the generated synchrotron photons act as target for IC scattering by the same charged particles that produced them in the first place. Due to this process, called synchrotron self-Compton (SSC), photons are able to reach greater energies than during a simple synchrotron process.

Curvature radiation

Curvature radiation is similar to synchrotron radiation. If the Larmor radius of the electron is much smaller than the magnetic field line curvature radius, then the electron will move along the magnetic field line. In this case, the gamma-ray photons are emitted parallel to the magnetic field line. The typical energy of an emitted gamma ray is proportional to the curvature radius of the magnetic field ρ_c and the Lorentz factor of the electron, γ:

$$E_\gamma = \frac{3}{2}\hbar c \frac{\gamma^3}{\rho_c} \tag{1.7}$$

Curvature radiation requires intense magnetic fields, such as the ones present in pulsar magnetospheres, and can be responsible of gamma-ray emission up to a few tens of GeV. However, in the case of pulsars, observation of TeV gamma rays requires a radius of curvature that is too large (Ahnen et al., 2015). If the curvature radiation is emitted by a population of electrons characterized by a power-law energy spectrum with a spectral index $\alpha = -p$, the resulting curvature radiation spectrum will be characterized by a power law with a spectral index $\alpha' = -(p+1)/3$.

Inverse Compton scattering

Inverse Compton scattering occurs when a HE electron interacts with a low-energy photon. Therefore, the electron will transfer a large amount of its energy to the photon.

$$e + \gamma_{low} \rightarrow e + \gamma_{high} \tag{1.8}$$

The energy transferred to the photon is given by:

$$\frac{E_2}{E_1} = \frac{1}{1 + \frac{E_1}{m_e c^2}(1 - \cos\theta)}, \tag{1.9}$$

where, E_1 and E_2 are the photon energy before and after interaction, respectively, and θ is the scattering angle in the electron rest frame. IC scattering can happen in two distinct regimes depending on the value of the parameter $b = 4Eh\nu_0/(m_e c^2)^2$, where E is the electron energy and $h\nu_0$ the initial photon energy.

- The non-relativistic or Thomson regime is defined as $b \ll 1$. In this regime the cross-section of the IC scattering is constant, and is referred to as the Thomson cross-section (Rybicki and Lightman, 1991), $\sigma_T = (8\pi/3)r_0^2 \approx 6.65 \times 10^{-29}$ m^2 . In case of a power-law electron spectrum with a spectral index $\alpha = p$, the resulting up-scattered photons will have a power-law spectrum with a spectral index $\alpha' = (p+1)/2$. The efficiency of the scattering

in this regime is directly proportional to the energy density of the target photons.

- The Klein-Nishina or relativistic regime is defined as $b \gg 1$. In this regime the cross section is not constant and takes into account the quantum dynamic effects. The Klein-Nishina cross section is defined as:

$$\sigma_{KT} = \frac{3}{8}\sigma_T x^{-1}(\ln 2x + \frac{1}{2}), \tag{1.10}$$

where x is the energy of the incident photon in units of $m_e c^2$. Scattering by nuclei can be neglected as they cause much less scattering than electrons, roughly by a factor $(m_e/m_N)^2$, where m_N is the mass of the nucleus. The efficiency of the IC process in the Klein-Nishina regime is proportional to the density of target photons, which implies that low energy photons can contribute to VHE gamma-ray emission. In case of a power-law electron spectrum with a spectral index $\alpha = p$, the resulting up-scattered photons will have a power-law spectrum with a spectral index $\alpha' = (p + 1)$

π^0 decay

π^0 decay is one of the most relevant hadron decay mechanisms in HE gamma-ray astrophysics. Neutral pions are formed during the collision between two CRs or via photo-pion pair production ($p + \gamma \rightarrow \Delta^+ \rightarrow p + \pi^0$). They have a rest mass of 135 MeV and a decay lifetime of 8×10^{-17} s. The most frequent channel (99%) of the π^0 decay is into two gamma rays:

$$\pi^0 \rightarrow \gamma + \gamma. \tag{1.11}$$

There is also a small chance (1%) that an $e^{\pm}$ pair is created instead:

$$\pi^0 \rightarrow e^+ + e^- + \gamma. \tag{1.12}$$

Both gamma rays produced in the decay carry half of the π^0 energy. Neutral, positive and negative charged pions are produced in the same quantities during most of hadronic processes. In the case of a power-law spectrum distribution of the π^0 parent hadrons, with a spectral index $\alpha = p$, the resulting gamma rays produced in π^0 decays are characterized by a power-law spectrum with the same spectral index $\alpha' = p$.

Pair production

It is the inverse process of the creation of gamma rays via e^+e^- annihilation. This process leads to the creation of an electron-positron pair by annihilation of a HE photon with a low-energy photon. This interaction can happen if the energy of

each photon is above a certain threshold given by:

$$E_1 E_2 \geq (m_e c^2)^2 \frac{1-\cos\theta}{2}, \tag{1.13}$$

where E_1 and E_2 are the energy of each interacting photon and θ the collision angle. The maximal efficiency of this process is obtained integrating the cross-section over the collision angle, and is given for photon energies satisfying $E_1 E_2/(m_e c^2)^2 \approx 3.7$. Thus, if one of the photons is a VHE gamma ray, the reaction will be maximized with a soft photon with energy from ultra-violet to infrared.

$$\gamma_{VHE} + \gamma_{soft} \rightarrow e^+ + e^- \tag{1.14}$$

Photons traveling through empty space do not undergo this process. However, photons traveling through intense magnetic fields can materialize as an electron-positron pair as one component of the momentum arises from the magnetic field. This process is of special importance for VHE gamma-ray astrophysics due to the large number of ambient soft photons in the universe. VHE gamma-ray emission from extragalactic sources, detected on Earth, can be attenuated due to the presence of low energy photons from the Extragalactic Background Light (EBL) (Mazin, 2009; Franceschini et al., 2008). This attenuation can be described as an optical depth, τ, depending on the energy of the gamma-ray photons E_γ and the red-shift, z, of the emitting source :

$$F(E) = F_0(E) e^{-\tau(E_\gamma, z)}, \tag{1.15}$$

where $F(E)$ is the observed flux of the source and F_0 is the intrinsic flux of the source.

1.4 Gamma-ray sources

The previously mentioned emission and absorption mechanisms, besides the GZK cut-off and the EBL attenuation, take place in astrophysical objects where the ambient conditions allow the corresponding mechanisms to occur. The sources of gamma-ray photons can be divided into two categories: Galactic and extragalactic.

1.4.1 Galactic sources

- **Pulsars** are rapidly rotating and highly magnetized neutron stars (NS) arising from supernova (SN) explosions. They typically have a radius of $\sim$ 10 km and a surface magnetic field of $\sim 10^{12}$ G. Due to the intense magnetic

fields, charged particles are torn off the stellar surface. HE radiation is emitted due to the motion of these charged particles in the magnetic fields. The electromagnetic radiation is beamed in the direction of the particles motion. As the magnetic and rotation axis are not aligned, an observer can see the pulsar emission when the beam crosses the observer's line of sight. Pulsars can emit gamma rays up to a few tens of GeV. Recently, emission from the Crab pulsar was detected up to the TeV scale (Ahnen et al., 2015). Mechanisms responsible of such emission are still poorly understood. More details about pulsar physics are given in Chapter 2.

- **Supernova remnants** (SNRs) are the leftovers of a supernova (SN) explosion. The material ejected during the SN explosion expands forming a shock wave against the interstellar medium (ISM). Particles are accelerated in these shocks trough the Fermi acceleration mechanisms. It has been theorized that SNRs are the accelerators of Galactic CRs. The ultra-relativistic particles produced in the shock emit radiation up to VHE by IC scattering. Several SNRs have been detected in the HE and VHE band, such as Cas A (Aharonian et al., 2001), IC443 (Albert et al., 2007a), RX J1713.7-3946 (Aharonian et al., 2006a), Vela X (Aharonian et al., 2006b).

- **Pulsar wind nebulae** (PWNe) are bubbles resulting from the interaction of ultra-relativistic particles, arising from the ultra-relativistic pulsar wind, with the ambient medium, ISM or SNR. PWNe are distinguished from SNRs as the latter are not fed by a central pulsar. The rotational energy of the pulsar is converted into a relativistic wind of particles which terminates in a shock as it collides with the ambient medium. The VHE emission is most likely leptonic, due to IC scattering of VHE electrons on ambient photons. The most famous PWN is the Crab Nebula which is the most steady and strong VHE emitter. The Crab Nebula is used as a standard reference for the HE and VHE regimes. However, recently, flaring states have been discovered (Mayer et al., 2013; Striani et al., 2013).

- **Gamma-ray binary systems** are composed by a massive O-A type star and a compact object, NS or black hole (BH). If the companion of the massive star is a pulsar, pulsar wind/stellar wind interaction can occur, forming a shock front wave where particles are accelerated. These accelerated particles can interact with the stellar photons emitting VHE radiation through IC process. On the other hand, if the companion is a BH, it will accrete matter from the companion star, forming an accretion disk. The accretion disk created will eject ultra-relativistic particles as jets. These particles can produce VHE radiation. Emission from binaries is dominant in the gamma-ray energy band. Gamma-ray binaries have been discovered at HE by the *Fermi*-LAT (Ackermann et al., 2012a) and at VHE by MAGIC (Albert et al.,

2006b, 2009) and HESS (Aharonian et al., 2005a,b). More detailed information about VHE gamma-ray binaries can be found in (Oramas, 2014).

- The **Galactic center** is a very crowded region hosting several gamma-ray emitters, among which, there is a super-massive black hole, *Sgr A**. Two scenarios are considered regarding the gamma-ray emission from *Sgr A**: gamma rays could originate in the base of the jets or it could be attributed to an accretion disk formed around the super-massive black hole. Emission from *Sgr A** has been detected at both HE and VHE (Abdo et al., 2009a; Aharonian et al., 2004; Albert et al., 2006a; Archer et al., 2014)).

1.4.2 Extragalactic sources

- **Active Galaxic Nuclei** (AGN) are the brightest intrinsic steady sources in the universe. Their emission is due to gas accretion by a massive black hole located at the center of the galaxy. An accretion disk is formed around the BH due to the huge gravitational field, attracting the galaxy's gas and star-like objects. The gravitational acceleration of the particles increases their energy up to relativistic regimes. AGN can be divided in two populations; *radio-loud* and *radio-quiet*. Emission from *radio-loud* AGN, higher in the gamma-ray regime, arises from the formation of two jets perpendicular to the accretion disk, see Figure 1.3. In the jets, particles are accelerated up to ultra-relativistic regime, producing electromagnetic radiation across the whole electromagnetic spectrum. The observed properties of AGN mainly

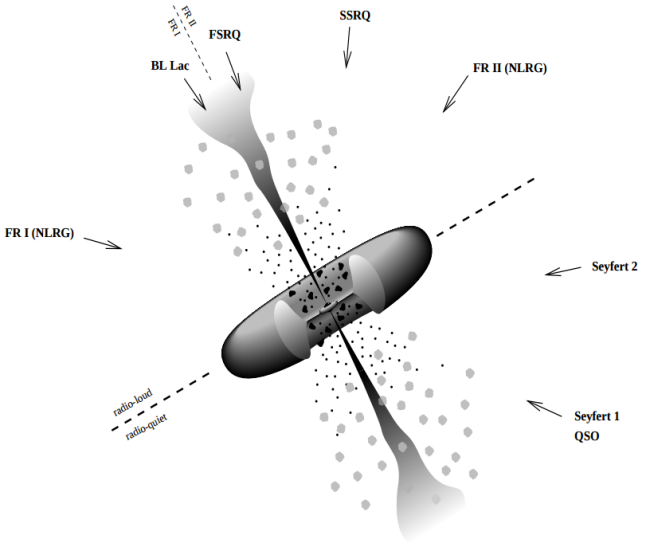

FIGURE 1.3: Sketch of the unified scheme of AGN representing the accretion disk and the relativistic jets. The classification of AGN depending of the viewing angle of the observer is represented in the picture. Figure adopted from (Torres and Anchordoqui, 2004).

depend on the viewing angle of the observer, the accretion rate and the mass of the central BH. AGN are classified depending on their observational properties in radio and optical wavelengths, see Figure 1.4

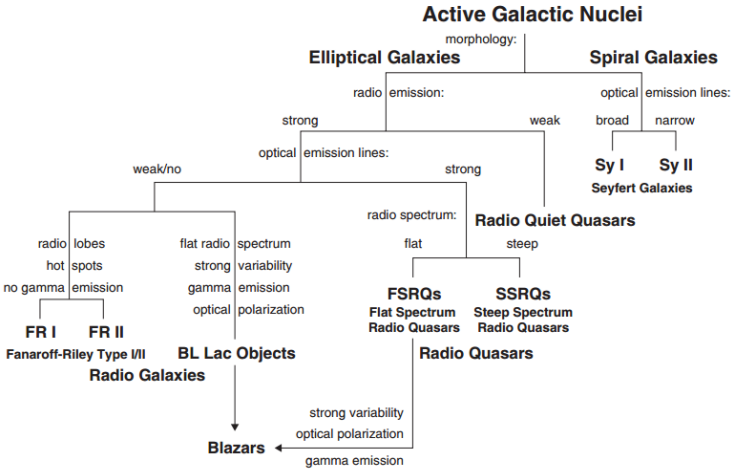

FIGURE 1.4: Classification of AGN. Figure adopted from (Mazin, 2007).

- **Starbust galaxies** are characterized by a high star-formation rate due to unusual concentration of gas, generally attributed to the effect of galaxy collisions. Consequently, these galaxies are also characterized by a high rate of SN explosions, $\sim$ 1 per year. This high rate guarantees both the mechanism for particle shock acceleration and a large production of gamma rays due to the presence of seed photons for IC scattering. The prototypes of starbust galaxies are M82 (Acciari et al., 2009) and NGC 253 (Acero et al., 2009).

- **Gamma-ray bursts** (GRBs) are the most energetic phenomena in the Universe. They are isotropically distributed in the sky, as can be seen in Figure 1.5, and, on average, occur at a redshift of $z = 2.3 - 2.7$. The energy released by a GRB, assuming an isotropic emission, lies between 5×10^{51} and 3×10^{54} erg, which is approximately the energy emitted by a galaxy similar to the Milky Way over a few years. They are characterized by a prompt emission during which mainly soft gamma-ray photons are emitted, and by an afterglow emission which is observed from radio up to X-rays. GRBs are classified in two categories; short-duration, which last between a few ms and 2 s and and long-duration, lasting from 2 s up to a few hundreds of seconds. Their origin is still not clear, however, short GRBs are thought to arise from binary mergers like NS, while long-duration are thought to arise from supernovae and hypernovae explosions. Although they have been detected at HE (Ackermann et al., 2013b), no GRB has been yet detected at VHE. However, detection of photons from *GRB 130427A* up to 95 GeV was repoted by the *Fermi* LAT (Ackermann et al., 2014).

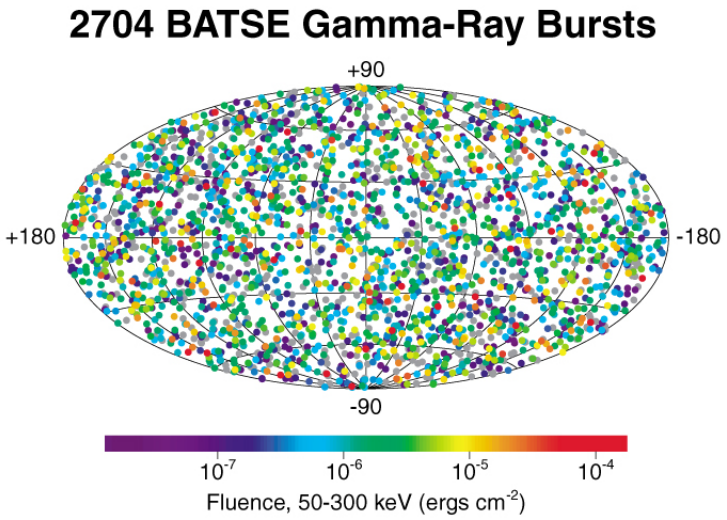

FIGURE 1.5: GRB sky as seen by the Burst and Transient Source Experiment (BATSE). From 1991 to 200, 2074 GRBs were detected by BATSE.

1.5 Gamma-ray observatories

Due to the opacity of the Earth's atmosphere to HE and VHE gamma rays (see Figure 1.6) they cannot be directly detected with ground-based detectors. Gamma rays can only be detected from the ground indirectly through the generation of the extensive air showers (EASs) developed in the atmosphere, see Section 3.1.1. Direct detection is only possible using spaceborne satellites.

1.5.1 Spaceborne telescopes

The detection of gamma rays started thanks to the boost in spacecraft technology after the Second World War, sending the first gamma-ray detector into orbit, carried by the Explorer 11 satellite in 1961, designed to detect gamma rays above 50 MeV. The two following experiments (*SAS-2* (1972) (Kniffen et al., 1973) and *COS-B* (1975)(Bignami et al., 1975)) were a success, with the detection of the first 25 point-like sources of gamma rays (Swanenburg et al., 1981) and a map of the Milky Way (see Figure 1.7). Later, in 1989, the detection of the Crab Nebula by Whipple (Weekes et al., 1989) opened the window of indirect detection of gamma rays using Imaging Atmospheric Cherenkov Telescopes (IACTs).

For several decades the continued technical developments have improved the sensitivity of the spaceborne telescopes. The launch of the *COMPTEL* (Ryan, 1989) and *EGRET* (Radecke and Kanbach, 1992) telescopes on board the Compton Gamma-Ray Observatory (CGRO) in 1991, led to the detection of gamma-ray

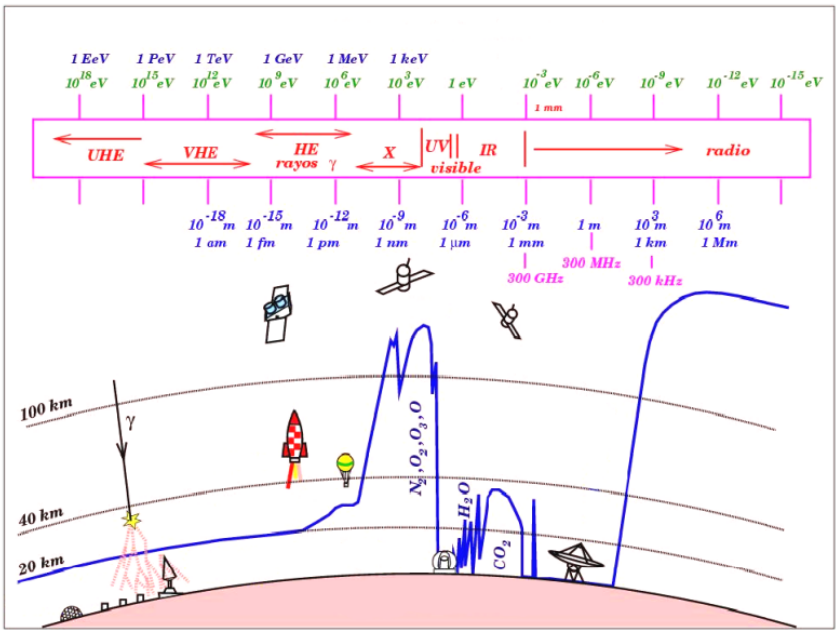

FIGURE 1.6: Electromagnetic spectrum together with the techniques used for radiation detection at the corresponding wavelength. The blue line represents the altitude where 50 % of the electromagnetic radiation is absorbed.

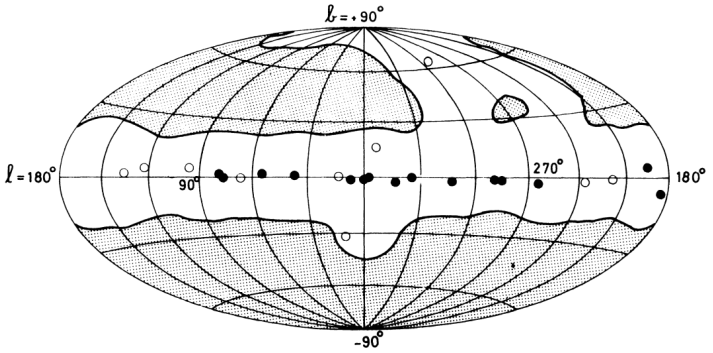

FIGURE 1.7: COS B sky map. The unshaded area was searched for gamma-ray sources. The filled circles denote the sources with a measured flux $\leq 1.3 \times 10^6$photons cm^{-2}s^{-1}. The open circles denote sources below this limit. Figure adopted from (Swanenburg et al., 1981).

pulsars. The lastest generation spaceborne telescopes is formed by the AGILE and *Fermi*-LAT space missions.

1.5.1.1 The AGILE space mission

AGILE (Tavani et al., 2008) (Astro-rivelatore Gamma a Immagini LEggero) is a HE astrophysics mission supported by the Italian Space Agency (ASI). The main goal of the AGILE program was to provide a powerful and cost effective mission

with excellent imaging simultaneously between 30 MeV - 50 GeV and 18-60 keV. The instrument was designed to achieve an optimal angular resolution ($\sim$ 15' for intense sources) and an unprecedented large field of view (FoV) (2.5 sr). A mini calorimeter operating in the burst mode was also included in the satellite. This third detector could detect transient sources in the 350keV-100MeV energy range.

1.5.1.2 The *Fermi* LAT

The *Fermi* Gamma-ray Space telescope is a space observatory designed to perform an all-sky survey of the observable universe in the HE range. It was launched on 2008 June 11^{th} and started scientific operations on 2008 August 04^{th}. It can sweep the whole sky every three hours corresponding to two complete orbits around Earth. Two complementary instruments are embedded on board of the *Fermi* satellite; the *Large Area Telescope* (LAT), observing gamma rays from 30 MeV to 300 GeV (Atwood et al., 2009), and the *Gamma-ray Burst Monitor* dedicated to the observation of transient sources from $\sim$ 8 keV to $\sim$ 40 MeV (Meegan et al., 2009).

The *Fermi* mission has produced many important scientific results. With over four years of data collected, the Third *Fermi* catalog (Acero et al., 2015) lists a total of 3033 point-like sources and 25 extended sources, showing a wide variety of source types, as can be seen in Figure 1.8. I addition, the second gamma-ray pulsar (Abdo et al., 2013) catalog reports 117 detected pulsar in the HE range. More details about the *Fermi* detector and its analysis tools are given in section 4.

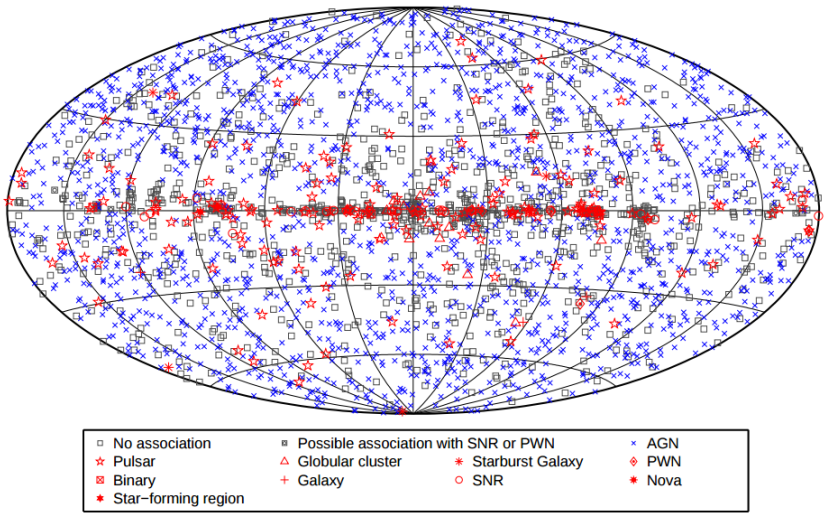

FIGURE 1.8: Full sky map showing the gamma-ray sources detected by the *Fermi* LAT space telescope after 4 years of observations. Figure adopted from (Acero et al., 2015).

1.5.2 Ground-based observatories

Since the discovery of gamma-ray emission from the Crab Nebula by the Whipple observatory, efforts have constantly been made in order to improve the indirect detection of gamma rays by means of imaging the Cherenkov light emitted by the EAS charged particles. Currently, three ground-based observatories are dedicated to the study of the gamma-ray sky, namely **MAGIC**, **HESS** and **VERITAS**, which are IACTs based on mirror reflections of the Cherenkov light.In addition, other observatories as HAWC works by detecting secondary shower particles hitting the detector.

1.5.2.1 MAGIC

FIGURE 1.9: The MAGIC telescopes. Credit: R. Wagner.

The MAGIC *Florian Goebel* telescopes are a set of two 17-meter IACTs located in El roque de los muchachos observatory, on la Palma Island (28° 45' N, 17° 54' W, 2225m above sea level), in the Canary Islands (Spain). MAGIC stands for Major Atmospheric Gamma ray Imaging Cherenkov telescopes. The first MAGIC telescope started operations in 2004 in stand-alone mode. MAGIC became a stereoscopic system in Autumn 2009. The MAGIC telescopes were the biggest IACTs until the construction of the HESS II telescope in 2013. The MAGIC telescopes have an energy threshold of 50 GeV making them ideal for the search for high red-shift AGN and gamma-ray pulsars. Thanks to its light structure made out of carbon fiber, the telescopes can point to any position in the sky in less than one minute, in order to catch GRBs.

1.5.2.2 HESS

The High Energy Stereoscopic System (HESS) is an array of five IACTs located at 1800 m a.s.l in the Khomas Highland, Namibia (23°16′18″S, 16°30′01″E). The

FIGURE 1.10: The HESS observatory

first phase of the HESS project consisted of an array of four telescopes with 13 m diameter reflectors placed in a square formation with a side length of 120 m. The HESS phase 1 went into operation in Summer 2002 with an energy threshold of 100 GeV. Each camera is equipped with 960 photo-multipliers tubes (PMTs) and the total FoV of the detector is 5° in diameter. In July 2012 a much larger fifth telescope, HESS-II, with a reflector of 27 m diameter started operation, becoming the largest IACT on Earth. The full system began operations in December 2013. With this fifth telescope, the energy threshold was lowered down to 30 GeV. The HESS observatory is the only one located in the Southern Hemisphere, opening a wide window on the Galactic plane and Galactic center observations, which is one of the most populated areas in the TeV sky.

1.5.2.3 VERITAS

FIGURE 1.11: The VERITAS observatory

The Very Energetic Radiation Imaging Telescope Array System (VERITAS) is a ground-based gamma-ray telescope array located at the Fred Lawrence Whipple Observatory, at the base of Mount Hopkins in southern Arizona. The array consists

of four IACTs with 12 m diameter reflectors. The VERITAS array is sensitive to gamma rays with energies between $\sim$ 80 GeV and 30 TeV. Each camera is equipped with 499 PMTs and has a FoV of 3.5°.

1.5.2.4 HAWC

The High altitude Air Water Cherenkov (HAWC) observatory is located in Sierra Negra, Mexico, at an altitude of 4100 m a.s.l. It consists of an array of 300 individual large water tanks and is sensitive to gamma-ray radiation between 100 GeV and 100 TeV with a wide FoV. Each detector has a diameter of 7.3 m and is 5 m high, containing a light-tight bladder holding about 188,000 liters of filtered water. Each tank contains three 8" PMTs and one high quantum efficiency 10" PMT to detect the Cherenkov light emitted in the water when EAS charged particles hit the tank. The sensitivity of HAWC is over an order of magnitude lower than its predecessor MILAGRO. Its design allows for the study of diffuse gamma-ray emission and TeV cosmic-ray anisotropy in our galaxy, which can shed light on the origin of CRs. Furthermore, it will explore for extragalactic sources, extending the *Fermi*-LAT detected AGN up to the TeV scale and its high duty cycle would allow for the detection of transient sources such as flares and GRBs. The sensitivity of the first stage of HAWC, HAWC-100, which contained 100 detectors is shown in Figure 1.12 together with the sensitivity of contemporaneous gamma-ray observatories. The completed observatory, made up of 300 detectors, was inaugurated in March of 2015.

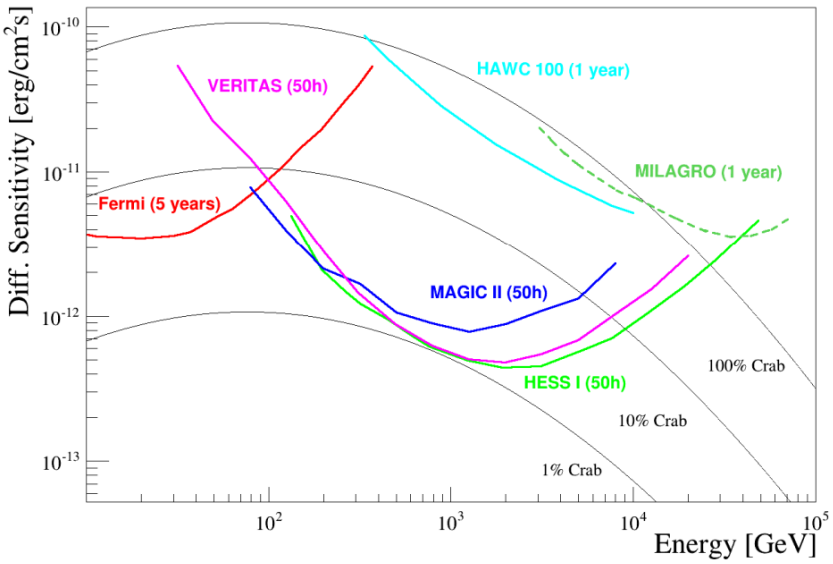

FIGURE 1.12: Sensitivity comparison between current and past IACTs and *Fermi*-LAT with the given integration time for a 5 σ detection. The sensitivity for the HAWC observatory is given for the first stage containing 100 detectors.

1.5.3 Future observatories

During the last decades technological progress has led to outstanding discoveries in gamma-ray astronomy. Currently, the next generation of telescope is development in order to further improve the sensitivity and the performance. The next generation of instruments includes two satellites, namely **Gamma 400** and **DAMPE** and an array of Cherenkov telescopes, **CTA**.

1.5.3.1 Gamma 400

Gamma 400 is one of the new generation of spaceborne telescopes and is part of the Russian Federal Space Program. It is designed to detect gamma rays from 20 MeV up to 1 TeV thanks to a thick detector ($\sim$ 25 radiation lengths for vertical incident gamma rays) and electrons, positrons and charged nuclei up to 10 TeV. Gamma 400 has a large FoV and can detect particles from vertical and lateral directions. The angular resolution is improved by a factor 2 at 100 MeV and a factor 10 above 100 GeV with respect to the *Fermi* LAT, as can be seen in Figure 1.13. Gamma 400 also embeds the KONUS-FG gamma-ray burst monitor and

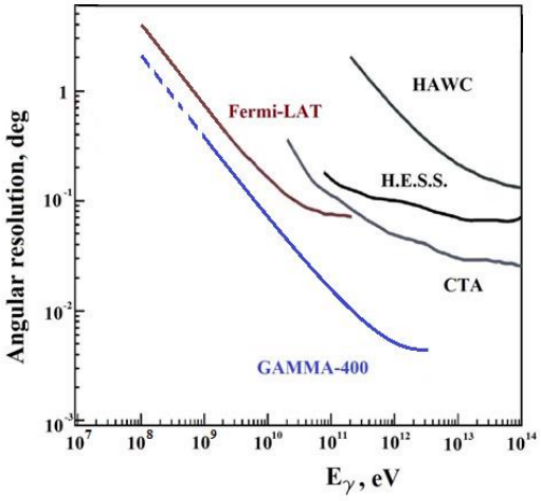

FIGURE 1.13: Comparison of angular resolution for Gamma 400, *Fermi*-LAT, HESS, HAWC and CTA. Figure adopted from (Topchiev, 2015).

two star sensors to determine the telescope axis with an accuracy of $\sim$ 5". It is designed to study the gamma-ray emission from the galactic center, the origin of dark matter and HE cosmic rays. Furthermore, it will also study emission from the Sun during periods of high activity and flares.

1.5.3.2 DAMPE

The DArk Matter Particle Explorer (DAMPE) is one of five satellite missions in the framework of the Strategic Pioneer Research Program In Space of the Chinese Academy of Sciences. Its launch date is planned for 2015-2016. DAMPE is designed for the detection of HE gamma rays, electrons and CRs. The calorimeter is about 31 radiation lengths thick (more than 3 time the thickness of the *Fermi*-LAT calorimeter) and the full instrument is about 33 radiation lengths thick, allowing to detect photons and electron up to 10 TeV and CRs up to 100 TeV. The main purpose of DAMPE is to investigate the origin of dark matter and the origin and propagation of HE CRs.

1.5.3.3 CTA

The Cherenkov Telescope Array (CTA) is the next step in the field of IACTs. CTA will be a ground-based array of IACTs sensitive to gamma rays from a few tens of GeV up to hundreds of TeV. The CTA sensitivity is improved by an order of magnitude with respect to current IACTs observatories (see Figure 1.14). The observatory will be divided into two sites, one in each hemisphere. Each site will be composed of small-size telescopes (SSTs) with a reflector of 4 m diameter, medium-size telescopes (MSTs) with a reflector of 12 m diameter and large-size telescopes (LSTs) with a reflector of 23 m diameter. The CTA consortium proposed key observing projects, gathering scientific targets. The distinct key observing projects will consist of a deep survey of the Galactic center in order to investigate the nature of the sources in this highly populated region, and where a detection of dark matter signature is expected. A Galactic and extragalatic survey will be carried out too, with the expected discovery of SNRs, PWNe and GRBs, together with an intense search for AGN in order to understand the physics in the vincinity of black holes. CTA is also expected to shed light on pulsar physics due to its low energy threshold with respect to current IACTs.

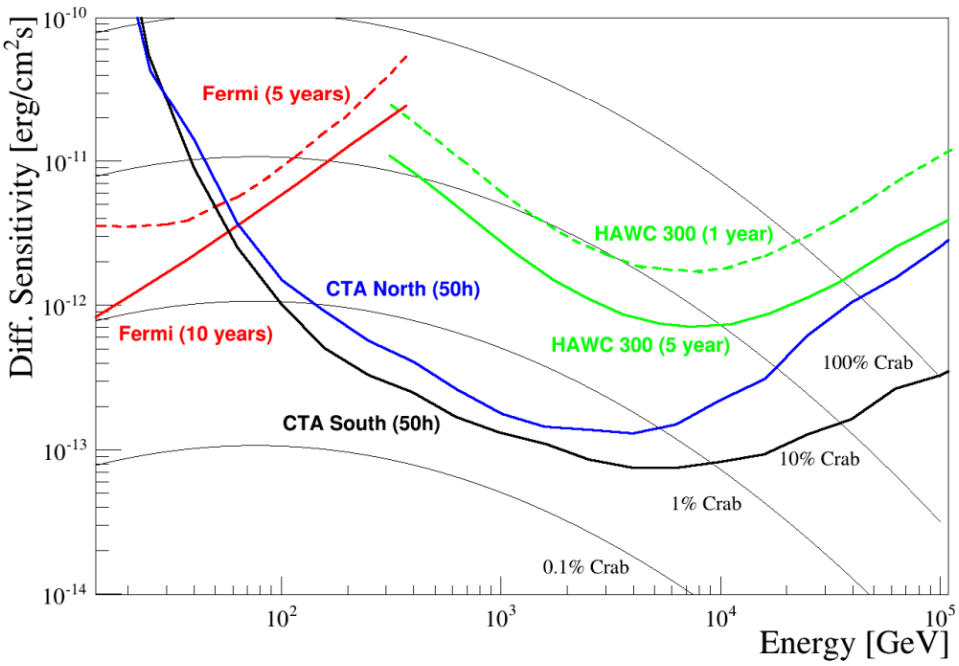

FIGURE 1.14: Comparison of the differential sensitivities of *Fermi*-LAT, HAWC (300) and CTA North and South for a given integration time. Figure adopted from (Collado, 2015).

Chapter 2

Pulsar physics

Pulsars are highly magnetized rotating neutron stars (NS) that emit periodic pulses of electromagnetic radiation. They were discovered in 1967 by Jocelyn Bell Burnell, with the detection of the radio pulsar PSR B1919+21 at 81.5 MHz (Hewish et al., 1968). Since their discovery, the number of observed pulsar has constantly grown, reaching currently over 2000 radio pulsars (Becker, 2009). Pulsar rotation periods lies between 1 ms up to 10 s. Pulsars with periods smaller than 10 ms are dubbed millisecond pulsars (MSPs), being the rest dubbed "normal" pulsars, including radio quiet and radio loud pulsars. Even though they have been under study for several decades, their emission mechanisms are not yet fully understood. Pulsars can emit radiation over the whole electromagnetic spectrum, from radio up to VHE gamma rays. At gamma-rays *Fermi* LAT has detected more than 160 pulsars (Laffon et al., 2015), with spectra well described by exponential cutoff with cutoff energies of few GeV.

2.1 Pulsars at all wavelengths

Emission from pulsars can cover the whole electromagnetic spectrum, from radio wavelengths up to gamma rays. Most pulsars emit radio waves. However, the radio emission, being beamed within a small cone, requires special geometrical conditions to be detected from Earth. Hence radio emission from certain pulsars cannot be observed from Earth. These pulsars are referred to as *radio-quiet* pulsars, whereas the pulsars detected at radio wavelengths are dubbed *radio-loud* pulsars. The radio emission from pulsars is believed to be due to coherent non-thermal processes. The optical emission is also, mainly, of non thermal nature and a small percentage appears to be due to thermal processes. In the case of the Crab, Vela and Geminga pulsars, the optical emission arising from thermal processes is

estimated to be $\sim 1\%$ of the total emission at optical wavelengths (Shearer and Golden, 2002).

In X-rays, pulsars are classified in three categories, namely, regular, anomalous and millisecond pulsars (Manchester et al., 2005).

- Anomalous pulsars are characterized by a slow rotation period, high magnetic field and irregular burst activities.
- Millisecond pulsars have a rotation period $P < 10$ ms. More than 75 % of the millisecond pulsars are in a binary system, usually with a low-mass white dwarf companion (Becker, 2009). The short period observed would result from angular momentum transfer due to mass accretion from the companion star, that would spin-up the neutron star (Bildsten, 1998).
- "Regular" pulsars exhibit a power-law component probably due to non-thermal radiation processes and a black-body component probably associated with the hot polar cap.

Radio-quiet pulsars are characterized by a fainter X-ray emission than radio-loud pulsars (Abdo et al., 2013).

Gamma-ray emission from pulsars extends up to a few tens of GeV. However, recently, the Vela pulsar has been detected above 50 GeV (Leung et al., 2014) and, the spectrum of the Crab pulsar has been extended up to the TeV scale (Aleksić et al., 2011). Gamma-ray pulsars are also classified in three categories, namely, *radio-loud*, *radio-quiet* and millisecond pulsars.

The *Fermi* LAT, launched in 2008, is playing a key role in our understanding of gamma-ray pulsar physics. It has increased the number of detected gamma-ray pulsars from 7 to 163 (Laffon et al., 2015), at the moment this thesis is being written. In figure 2.1 the SED and light curves of these gamma-ray pulsars discovered before the launch of the *Fermi*-LAT by EGRET and COMPTEL are shown from radio up to gamma-ray energies. None of these seven pulsars were detected above few GeV. Three other pulsars showed a hint of gamma-ray emission. In Figure 2.2 light curves of these pulsar are shown in optical, X-rays and gamma rays.

2.2 Pulsars and neutron stars

It was first suggested in 1939 by Baade and Zwicky (Baade and Zwicky, 1934b) that NS could arise from SNe explosions. SNe occur at the end of the life of stars with a mass $M \geq 8M_{\odot}$ (Longair, 2011). NS originate from SNe explosions

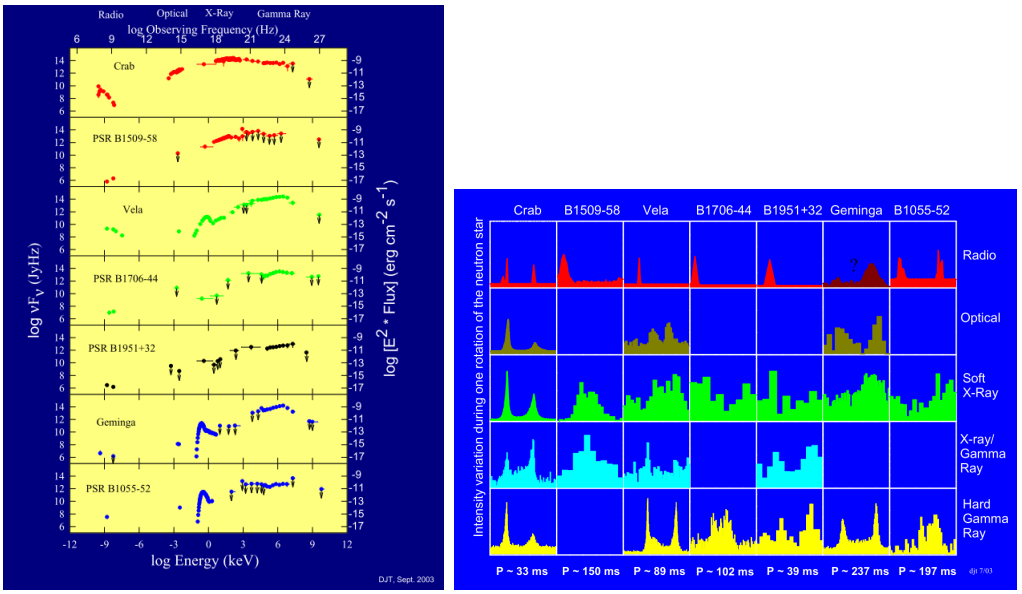

FIGURE 2.1: Spectral energy distributions (left) and light curves (right) of the detected gamma-ray pulsars by the telescopes on-board of the Compton Gamma-ray Observatory before the launch of the *Fermi*-LAT. Figures adopted from (Thompson, 2004).

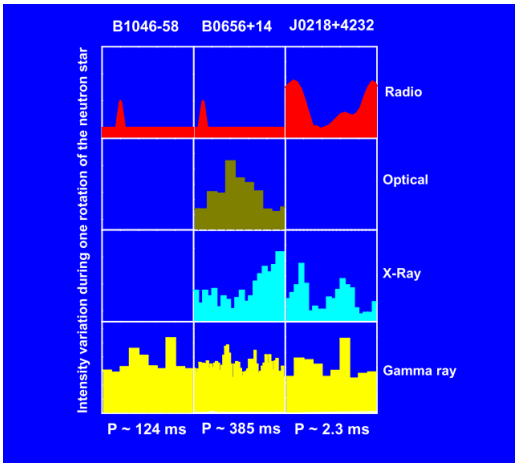

FIGURE 2.2: Light curves in optical, X-ray and gamma-ray of potential gamma-ray emitting pulsars observed by the EGRET telescope. Figure adopted from (Thompson, 2004).

resulting from the collapse of an iron core. Iron cores can be found in SNe of type II, Ib and Ic (Woosley and Janka, 2005).

If the mass of the remaining core after the SN explosion lies between the critical Chandrasekhar mass (Chandrasekhar, 1931) of $\simeq 1.44 M_{\odot}$ and $2.2 M_{\odot}$, the core will collapse until reaching nuclear densities, $\rho \simeq 10^{17}$ kg m^{-3}. As the density within the core increases, the degenerate electron gas becomes relativistic. When the total energy of the electrons exceeds the mass difference between the proton

and the electron, protons are converted into neutron via inverse β decay. This process is called *neutronization*. However, the upper limit on the mass of the NS has big uncertainties due to the fact that the equation of state of extremely high density matter is not well known.

The radius of the remaining NS after the supernova explosion is 5 orders of magnitude smaller than the one of the seed star. Thus, due to the conservation of the angular momentum and magnetic flux of the system, the angular velocity of the NS and the surface magnetic field are increased by about 10 orders of magnitude. Due to this high angular velocity increase, the pulsar rotation period lies between 1 ms up to 10 s and the surface magnetic field ranges from 10^8 to 10^{14} G.

Spin-down luminosity

The pulsar rotation period, P, increases with time due to energy losses. The first period derivative with respect to time is thus positive, $\dot{P} > 0$. The rotational energy of the pulsar is expressed as:

$$E = \frac{1}{2} I \Omega^2, \tag{2.1}$$

where I is the moment of inertia of the pulsar and Ω the angular velocity defined as $\Omega = 2\pi/P$. The pulsar energy loss rate is defined as the first time derivative of the pulsar rotation energy and is called the *spin-down luminosity*. It is defined as:

$$-\dot{E} = -I\Omega\dot{\Omega} = 4\pi^2 I \frac{\dot{P}}{P^3} > 0 \tag{2.2}$$

Taking for the moment of inertia a typical value of $I = 10^{45}$ g cm^2 together with the period and first period derivative of the Crab pulsar, $P = 3.37 \times 10^{-2}$ s and $\dot{P} = 4.2 \times 10^{-13}$, we obtain a spin down luminosity of $\dot{E} = 5.2 \times 10^{38}$ erg s^{-1}. A part of this energy is radiated as electromagnetic radiation and another part as high energy particles, both of them forming the pulsar wind which is particle-dominated at large distances from the pulsar.

Generally, the evolution of the angular velocity is described by the following differential equation:

$$\dot{\Omega} = -k\Omega^n \tag{2.3}$$

with n the so-called braking index. The braking index value can be computed by means of the angular velocity second derivative given the relation $n = \Omega\ddot{\Omega}/\dot{\Omega}^2$, and lies between 1 and 3. An index of 3 corresponds to a spin-down completely caused by losses of magnetic dipole radiation. The integration of Equation 2.3 leads to the characteristic age of the pulsar τ:

$$\tau_c = \frac{\Omega^{-(n-1)}}{k(n-1)} = -\frac{\Omega}{(n-1)\dot{\Omega}} = \frac{P}{(n-1)\dot{P}}. \tag{2.4}$$

It is conventional to set $n = 3$ to derive the pulsar characteristic age. This expression tends to overestimate the pulsar age, for example, the computed characteristic age of the Crab pulsar is $\tau_c = 1240$ years, whereas the SN explosion giving birth to the Crab pulsar was reported by Chinese astronomers in 1054 (Duyvendak, 1942), i.e., $\tau_{obs} = 961$ years.

The evolution of the previously derived quantities and their correlation can be summarized in the so-called $P - \dot{P}$ diagram, see Figure 2.3. The $P - \dot{P}$ diagram sorts the pulsars according to their rotation period and first period derivative. This plot also shows the correlation between the pulsar characteristic age, spin down luminosity and surface magnetic field, with its rotation period and first period derivative. From this plot, two populations can easily be distinguished with the millisecond pulsar with low rotation period and first period derivative, and the "normal" pulsar with higher rotation period and first period derivative.

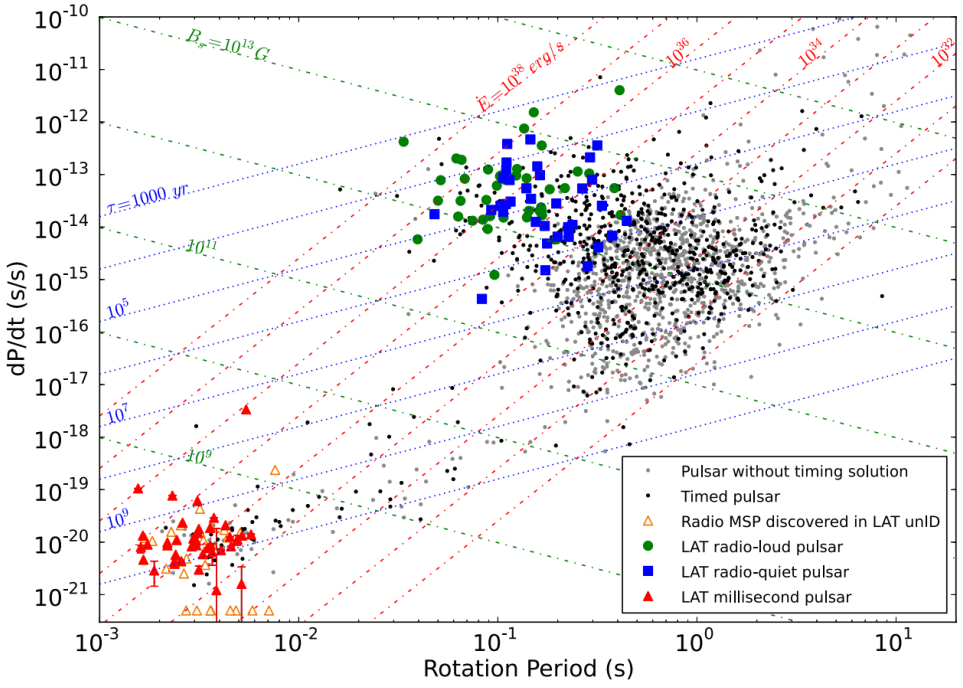

FIGURE 2.3: $P - \dot{P}$ diagram, showing the pulsar rotation period and first period derivative. Pulsar characteristic age, spin down luminosity and surface magnetic field are given according to the pulsar rotation period and first period derivative. Figure extracted from (Abdo et al., 2013).

2.3 Pulsar magnetosphere and accelerating regions

Pulsars can be approximated by a rotating magnetic dipole surrounded by a magnetosphere. The magnetosphere is defined as the region between the NS surface and the light cylinder (LC). The LC is a surface on which particles co-rotating with the pulsar would reach the speed of light. The distance from the pulsar to the LC cylinder is given by:

$$R_{LC} = \frac{c}{\Omega}, \tag{2.5}$$

with c the speed of light. Beyond the LC, particles are not co-rotating with the pulsar anymore. The pulsar magnetosphere can be divided into two regions; the closed magnetosphere, a region defined by the magnetic field lines closing within the LC and the open magnetosphere, defined by the magnetic field lines crossing the LC. The null surface defines a fictitious surface on which the magnetic field lines are perpendicular to the rotation axis, $\mathbf{\Omega} \cdot \mathbf{B} = 0$, see Figure 2.4. The SN outburst gives rise to an expanding shell, sweeping the interstellar material over a distance D. The region beyond the LC extending up to $\simeq D/10$ is called the pulsar wind. The wind is formed by highly relativistic particles flowing out of the LC along the open magnetic field lines. Within the magnetosphere, the energy flux is Poynting flux dominated. However, beyond the LC and before the termination shock, the energy flux becomes kinetically dominated. The energy transfer from Poynting flux to kinetically dominated is still under debate (referred to as the σ problem, σ being the ratio between the Poynting flux and the kinetic energy flux (Kennel and Coroniti, 1984)).

First attempts of the description of the pulsar environment assumed a quasi-vacuum surrounding the pulsar (Pacini, 1968). An analytical description of the magnetosphere of a pulsar was proposed in 1969 by Goldreich and Julian (Goldreich and Julian, 1969) and still remains a reference work to describe pulsars magnetosphere. They found out that due to intense magnetic field of the NS together with its rotation, NS cannot be surrounded by vacuum. Indeed, the strong electric field generated by the rotation of NS is intense enough to overcome the gravitational forces, resulting in an outflow of charged particles from the star surface to the magnetosphere. As the magnetic field lines are very nearly electric equipotential in the magnetosphere and wind zone, charged particles slide along the magnetic field lines which co-rotate rigidly with the star. The charged particles attached to the closed field lines will, thus, co-rotate and form the co-rotating magnetosphere, whereas the charged particles attached to the open magnetic field lines will escape through the LC and form the pulsar wind. In this model, the electric potential of the stellar surface is highest at the equator and decreases toward the poles. The negative charges stream out along the higher altitude lines and positive along the lower altitude lines, as depicted in Figure 2.4. The magnetic

fields are mainly poloidal within the magnetosphere region. However, toward the LC and beyond, the currents due to escaping charges are the main source for the magnetic fields. A toroidal magnetic field component is present as a minor component near the NS surface and becomes the major component in the wind region. Goldreich and Julian computed the charged particles density within the magnetosphere, assuming that the particles surrounding the pulsar can be described by the quasi-steady-state solution of the Maxwell equations and that the forces working on the particles is 0, i.e, $\mathbf{E} + \boldsymbol{\beta} \times \mathbf{B} = 0$, with $\boldsymbol{\beta} = \mathbf{v}/c$ with v the particles velocity. The charge density is referred to as the Goldreich-Julian charge density and is defined as:

$$\rho_{GJ} = \frac{-\boldsymbol{\Omega} \cdot \mathbf{B}}{2\pi c} \frac{1}{[1 - (\Omega r/c)^2 \sin^2 \theta]} \tag{2.6}$$

where r is the distance from the pulsar, θ is the inclination angle with respect to the magnetic dipole axis, $\mathbf{E}$ and $\mathbf{B}$ the electric and magnetic field vectors, respectively, and $\boldsymbol{\Omega}$ the angular velocity. This expression of the density applies only to the co-rotating portion of the magnetosphere. Note that ρ_{GJ} changes sign at the null surface.

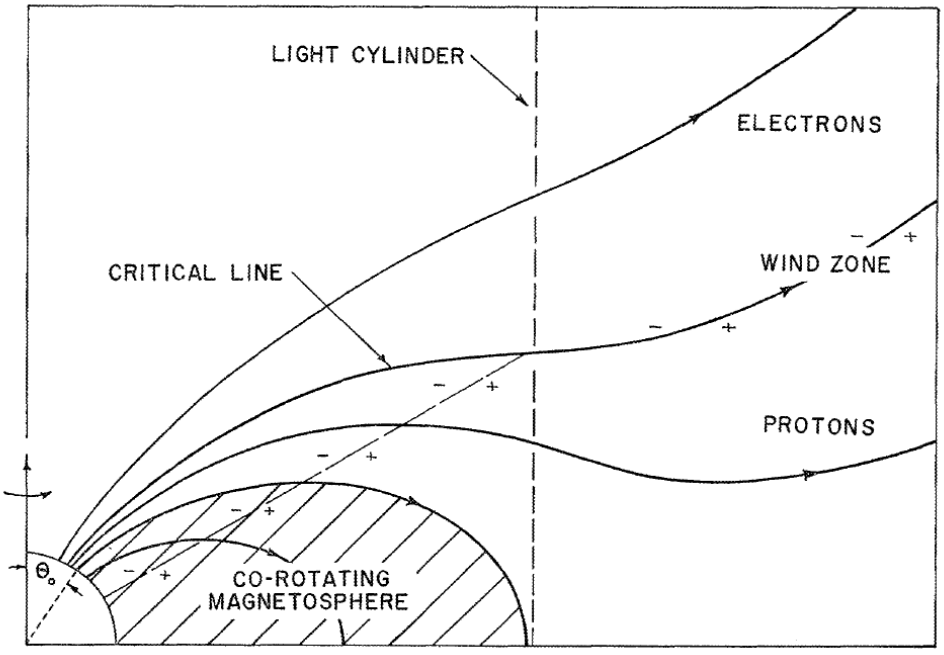

FIGURE 2.4: Sketch of the magnetosphere from the Goldreich-Julian model. The light cylinder sets the limit between the magnetosphere and the wind region. The charge density changes sign at the null surface. Figure adopted from (Goldreich and Julian, 1969)

This description of the pulsar magnetosphere is based on the assumption that the magnetic field lines along which the charged particles are flowing are very nearly to the electric equipotential implying $\mathbf{E} \cdot \mathbf{B} = 0$. Thus, the electric component parallel

to the magnetic field is null, $E_{||} = 0$, and charged particles cannot be accelerated within the LC. However, in order to explain the gamma-ray emission observed from pulsars (Abdo et al., 2013), charged particles must be accelerated and radiate HE photons due to their motion in the intense magnetic fields. The models describing the HE emission from pulsars suppose regions, in the open magnetosphere, where the charge density differs from the Goldreich Julian charge density, $\rho \neq \rho_{GJ}$. The Poisson equation can then be expressed as:

$$E_{||} = -\Delta\phi = 4\pi(\rho - \rho_{GJ}) \tag{2.7}$$

Thus, in the region where the charge density differs from the Goldreich Julian charge density, the magnetic-aligned electric field component is not null, $E_{||} \neq 0$, allowing acceleration of charged particles.

Three locations were proposed where such a difference between the charge density and the Goldreich Julian charge density can occur. The **polar cap** located close to the NS surface at the magnetic pole, that was then extended to the **slot gap** at higher altitudes. The third region, the **outer gap**, is located below the null charge surface and extends up to the LC.

2.4 Polar cap and slot gap accelerators

The polar cap model (Sturrock, 1971; Fawley et al., 1977; Arons and Scharlemann, 1979) predicts that $\rho \neq \rho_{GJ}$ in the open magnetosphere above the magnetic poles, see Figure 2.5. The region where such density appears extends up to ~ 30 km from the NS surface. The edges of the polar cap on the NS surface are defined by the last closed field lines. The charged particles, torn off the polar cap surface, accelerated by the magnetic-field-aligned electric field will acquire negligible energy transverse to the magnetic field line, thus, the synchrotron emission will be negligible. However, due to their motion in a curved magnetic field, the charged particles will emit curvature radiation. The emitted curvature photons will propagate through the gap until they reach sufficient angle θ_{kB} between their momentum and the curved magnetic field to create pairs via magnetic pair creation process, $\gamma + B \rightarrow e^+e^-$. This process takes place when the energy of the photons is above the magnetic pair creation threshold, $E_\gamma \geq 2m_e c^2/\theta_{kB}$. Due to the absorption of curvature photons by the magnetic field, a super-exponential cut-off is expected in the spectral energy distribution of the photons arising from the polar cap. The maximum energy of photons escaping from magnetic absorption is given by (Baring, 2004):

$$\epsilon_{max} = 0.4\sqrt{P}\left(\frac{r}{R_0}\right)^{1/2} \max\left\{1, \frac{0.1B_{cr}}{B_0}\left(\frac{r}{R_0}\right)^3\right\} \text{GeV}, \tag{2.8}$$

where B_0 is the surface magnetic field, B_{cr} the critical magnetic field and R_0 the NS radius. The creation of pairs will induce the formation of a so-called *pair formation front* (PFF) above the polar cap. Above the PFF, the magnetic-field-aligned electric field is screened by the created pairs, and charged particles cannot be accelerated. Some of the produced e^+ will be inwardly accelerated toward the NS. It was argued (Ruderman and Sutherland, 1975) that except for the Crab

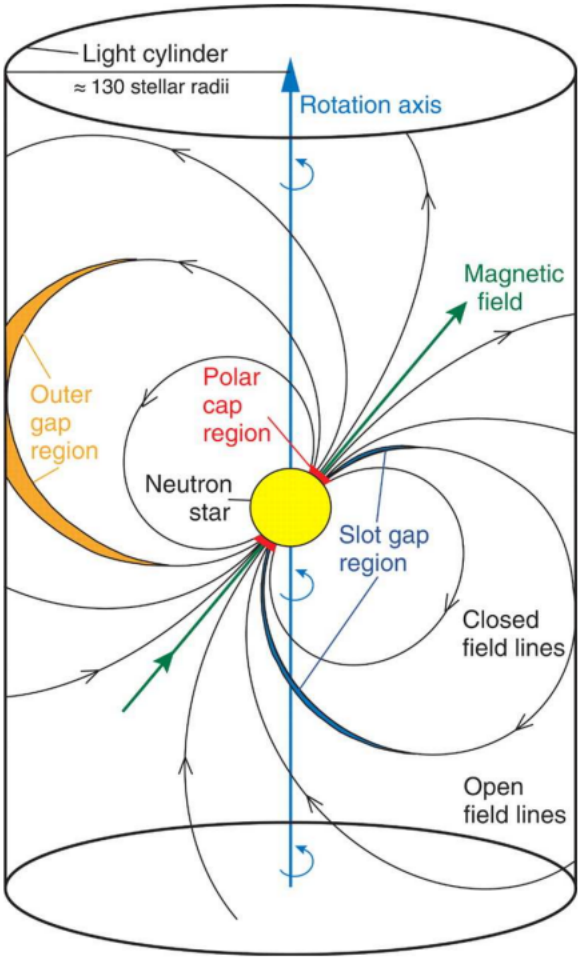

FIGURE 2.5: Pulsar magnetosphere. The closed magnetic field lines are within the light cylinder, whereas the open lines cross the light cylinder. The polar cap, slot gap and outer gap, where the charged particles are accelerated, are represented. Figure adopted from (Aliu et al., 2008)

pulsar, no positive charge can be ripped out the NS surface, resulting in a vacuum gap due to the charge separation, above the polar cap. Due to some instabilities against perturbations, the vacuum gap will grow until reaching a potential drop of $\sim 10^{12}$ volts, which would correspond to an altitude of $\sim 10^4$ m. The sparking, resulting from the instability, will cause the electrons to flow back to the surface, keeping the gap from growing.

In fact, if the NS surface temperature is high enough, positive charges will be emitted from the NS and a space charge limited flow (SCLF) will form between the NS surface and the PFF. This phenomenon is similar to a flow of electrons accelerated by an electric field from an anode to a cathode, see for example (Langmuir, 1913). However, in this case, the electric field intensity in the SCLF does not grow linearly but quadratically.

Emission from the polar cap can reproduce all types of light curves, with a distance between both peaks up to 0.5 in phase. However, small values of α and ζ are required, see Figure 2.6, where ζ is defined as the angle between the observer's line of sight and the rotation axis, and α is the inclination angle, defined as the angle between the magnetic field and rotation axis. This assumption is inconsistent with the observations, where higher values of the inclination angle are observed, $45° \leq \alpha \leq 75°$, and the Crab pulsar viewing angle, $\zeta \sim 63°$ (Ng and Romani, 2008). The detection of gamma-ray emission at several tens of GeV from the Crab

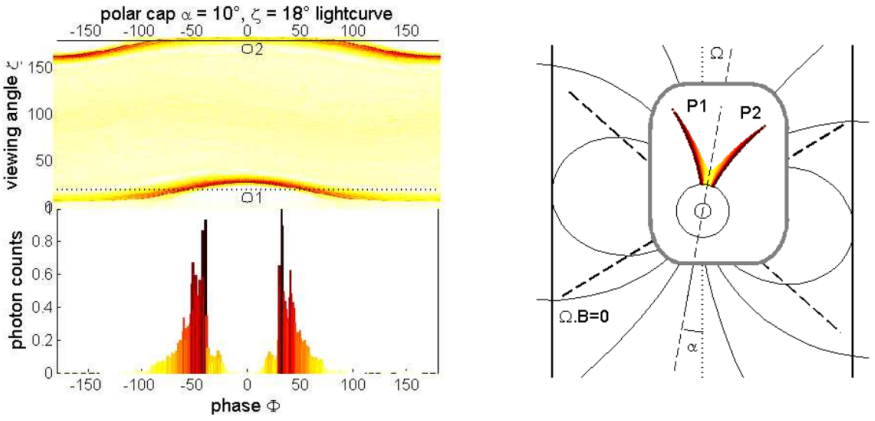

FIGURE 2.6: Emission from the polar cap for a typical inclination angle of 10° between the magnetic and rotation axis. Sky map of the polar cap emission from pulsar (top left) and the computed light curve for a given viewing angle (bottom left). On the right is shown the extension of the polar cap according to the distance from the center of the gap. Figure adopted from (Grenier and Harding, 2006)

pulsar (Abdo et al., 2010a; Aliu et al., 2008; Aliu et al., 2011) tends to rule out the polar cap scenario, in which a super-exponential cut-off is expected. Thus, charged particles must be accelerated at higher altitudes in order to prevent the magnetic absorption of the emitted HE photons.

Near the magnetic poles and at the center of the polar cap region, $E_{||}$ is relatively strong and the PFF is close to the NS surface. However, toward the edges of the polar cap region, $E_{||}$ decreases, requiring the particles to be accelerated over larger distances in order to reach energies high enough to radiate photons able

to materialize as pairs, forming a so-called slot gap along the last closed field line (Arons and Scharlemann, 1979). The PFF is then farther from the NS. This effect is shown in Figure 2.7. The emitted photons, due to their higher emission altitude, do not undergo magnetic absorption. In the original description of the slot gap model, some discrepancies appeared in the estimation of the HE emission from pulsars due to some inconsistencies in the calculation of the acceleration of the electrons and pair formation. A revised version was proposed (Muslimov and

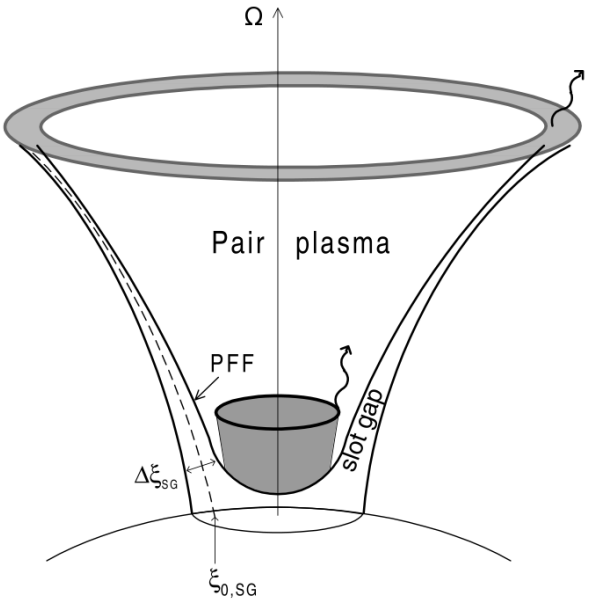

FIGURE 2.7: Geometry of the open field lines at the polar cap. The slog gap region is located between the closed magnetosphere and the pair plasma column. The ring-like structure on top indicates the elevated PFF. Figure adopted from (Muslimov and Harding, 2003)

Harding, 2003) including relativistic effects of the frame dragging (Muslimov and Tsygan, 1992) and the effect of the gap boundary on the accelerating electric field. They defined the slot gap location as the region bounded by the last open field line and the magnetic line with a co-latitude $(1 - \Delta\zeta_{SG})$ times smaller than the colatitude of the last open field line (Muslimov and Harding, 2003), where $\Delta\zeta_{SG}$ is the colatitunal gap thickness in unit of ζ ($\zeta = \theta/\theta_0$ with θ the colatitude of a PC magnetic field line and θ_0 the foot point of the last open field line). They estimated that the HE radiation forms a cone, due to the flaring of the magnetic field lines. However, the study was restricted to altitudes below 5 stellar radii.

Numerical simulations (Muslimov and Harding, 2004) predict hard curvature radiation (with a photon index $\alpha = 2/3$), which is much harder than the observed gamma-ray pulsar. In this scenario, only the emission from the primary electrons, uniformly accelerated from low altitude (few stellar radii above the PC), is taken into account. Secondary electrons are not expected to be accelerated as they are created above the PFF where $E_{||}$ is screened. Inverse Compton scattering of low

energy photons was not taken into account either. However, a double peaked light curve, arising of emission from caustics (Dyks and Rudak, 2003) from both poles is expected, also predicted by Dyks et al. (2004). Caustics are regions of high photon intensity, arising from the pile-up of photons in the trailing side, emitted at different altitudes, due to aberration and time of flight delay, see Figure 2.8. The characteristic funnel beam emission from the slot gap is represented on Figure

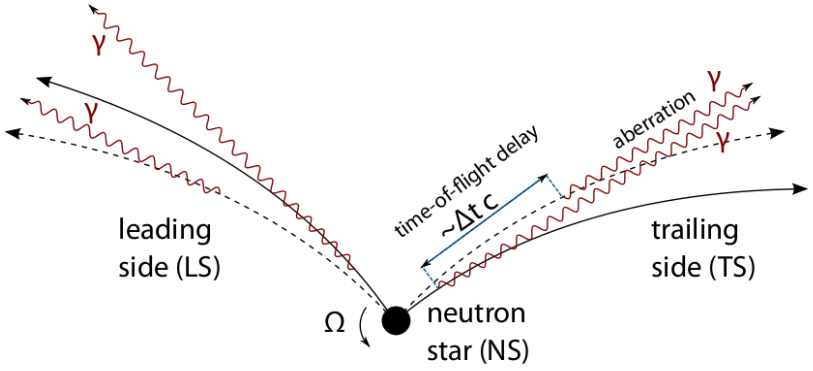

FIGURE 2.8: Sketch of caustics formation. The black filled and dashed lines represent the magnetic field lines at time t and $t + \Delta t$, respectively. Gamma-ray photons emitted at low altitude at time t, will pile-up with those emitted at time $t+\Delta$ at higher altitudes, due to aberration and time delay. Figure adopted from (Giavitto, 2013).

2.9 together with the expected light curve for a viewing angle of 100°. In the case of the Crab pulsar, the slot-gap emission underestimates the HE emission and can only explain 20% of the Crab pulsar luminosity (Hirotani, 2008).

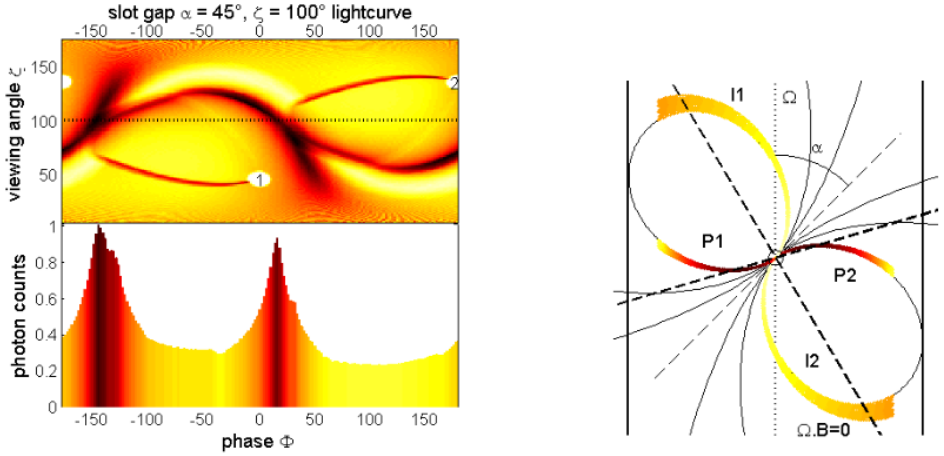

FIGURE 2.9: Same figure as 2.6 for the emission from the slog gap. Figure adopted from (Grenier and Harding, 2006)

The polar cap and slot gap models have difficulties to reproducing the observed spectrum of gamma-ray pulsars. The outer gap, extending from the null surface to the vincinity of the LC appears to be more suitable to explain pulsars HE emission.

2.5 Emission from the outer gap

The outer gap model (Cheng et al., 1986a; Romani, 1996; Hirotani, 2008) appears to be one of the best candidates in order to reproduce HE emission from pulsars. The outer gap model is based on the assumption of an oblique rotator, with $\mathbf{\Omega} \cdot \mathbf{B} < 0$, surrounded by a magnetosphere filled with a co-rotating plasma. The plasma density in the magnetosphere follows the Goldreich Julian charge density, ρ_{GJ}, except for some slab like regions where $\rho \neq \rho_{GJ}$ and $\rho \simeq 0$. Thus, in these vacuum gaps, the magnetic-field-aligned electric field is not screened, $\mathbf{E} \cdot \mathbf{B} \neq 0$ and charged particles can be accelerated. The electrostatic acceleration of charged particles is expected to exist far from the NS surface, where the co-rotating speed reaches a significant fraction of c. The gap is bounded on one side by a surface layer on the boundary of the last closed field line and on the other side by a charge layer on the surface of an open magnetic field line, (see Figure 2.13). In the classical

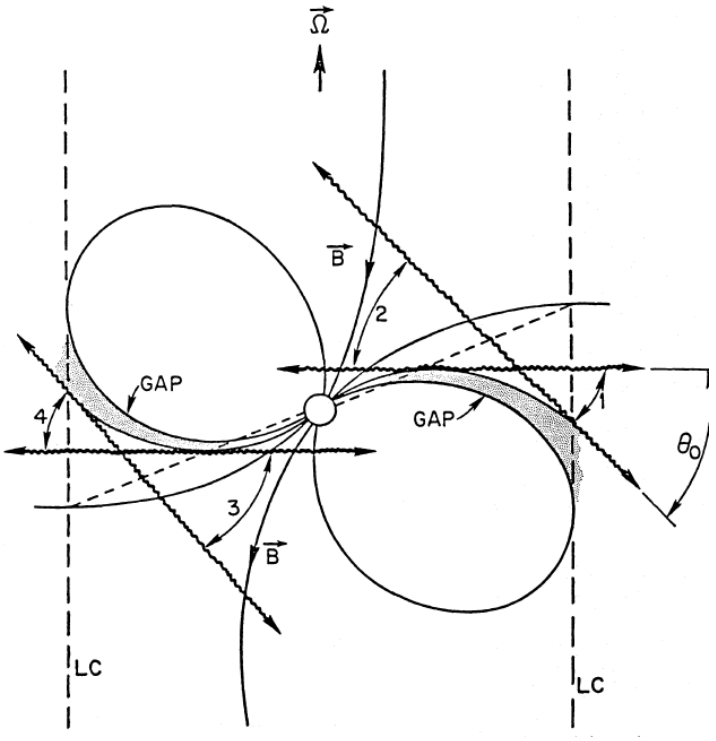

FIGURE 2.10: Sketch of the pulsar magnetosphere. Two of the four outer gap regions are represented. Gamma rays stream out in the regions 1, 2, 3 and 4 in fan beams. Figure adopted from (Cheng et al., 1986a)

outer gap model, the formation of the gap arises from a charged separated plasma,

assuming a current flow. The negative charged particles located between the null charge surface and the last closed field line flow out of the LC, leaving behind a negative charge-depleted region, that will act electrostatically as a positively charged region with respect to the plasma filled magnetosphere, where $\rho \simeq \rho_{GJ}$. This positively charged region pushes the positively charged-separated plasma on the starward side of the null-charge surface, allowing a growing gap. Hence, $\mathbf{E} \cdot \mathbf{B} \neq 0$ everywhere but in the gap. Positive charges entering the gap through the LC are accelerated toward the star, and the negatively charged particles are outwardly accelerated on the same magnetic field lines. The growth of the gap is limited by the pair creations process within the gap. An $e^{\pm}$ plasma will be created within the gap in the regions where the accelerating electric field is intense enough to support gamma ray creation with energy high enough to produce pairs. The two main mechanisms of pair creation within the gap are by collision of gamma-ray and X-ray photons arising from synchroton emission of secondary $e^{\pm}$ generation, or by collision of gamma rays with soft optical or IR photons. Within the gap the HE photons arise from curvature radiation from accelerated $e^{\pm}$ and from IC scattering of $e^{\pm}$ on soft photons. The curvature photons within the gap are emitted into a narrow cone whose axis is parallel to the local magnetic field. A self-sustained and self-regulated pair production cascade therefore forms, preventing the charge depletion, the screening of $E_{||}$ and the extension of the gap. It was shown that in order for an outer gap to be self-sustained, each $e^{\pm}$ should cascade and materialize into one $e^{\pm}$ pair (Hirotani, 2013). In this scenario, a direct relation between the gap thickness and the luminosity can be made (Zhang and Cheng, 1997):

$$L_{\gamma} = 3.6 \times 10^{31} f^3 P^{-4} B_{12}^2 \quad \text{erg s}^{-1} \tag{2.9}$$

where f is the ratio between the gap thickness and the LC radius and $B_{12} = B/10^{12}$. Young pulsars, due to their hotter polar caps and larger vacuum electric fields tend to have narrow gaps streching from near the null surface to near the LC (Cheng and Ding, 1994). As a pulsar ages, the gap tends to grow due to a decrease of the magnetic-field-aligned electric field (Zhang and Cheng, 1997).

As previously mentioned, a self-sustained gap is regulated by the pair creation process which limits the growth of the gap and the quenching of the accelerating electric field. However, there is a limit in the $P - \dot{P}$ diagram, the so-called death line (Chen and Ruderman, 1993; Zhang et al., 2004), below which the outer gap is not self-sustained anymore, hence the outer gap is no longer active. In recent calculations (Wang and Hirotani, 2011) the death line was derived, taking into account the pair multiplicity and pair creation within the gap. The strongest contraint arises from the pair creation process, where, due to the increase of the pulsar rotation period, curvature photons within the gap are not energetic enough to create pairs by colliding with ambient X-rays. The death line and the so-called death valley are shown on Figure 2.11.

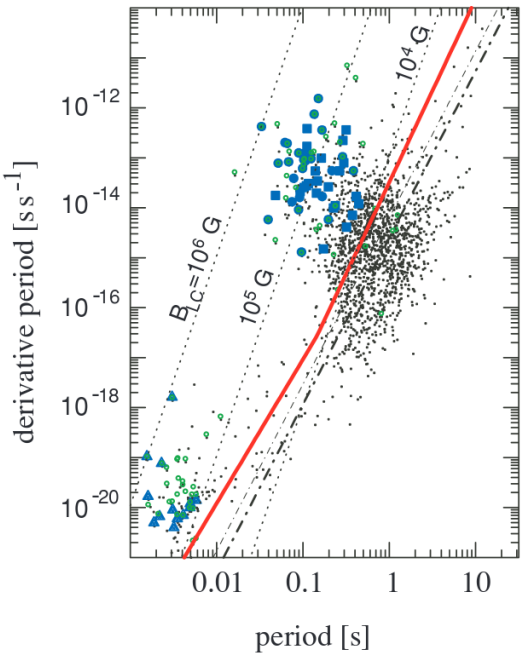

FIGURE 2.11: Outer gap death line according to the pulsar period and first time period derivative. The red line represents the death line computed by (Wang and Hirotani, 2011) which is more constraining compared to previous computation by (Zhang et al., 2004) (point dashed line). Below the death line, in the death valley, gamma-ray emission from pulsars is not efficient anymore. Figure adopted from (Wang and Hirotani, 2011).

In the original outer gap scenario a vacuum gap is assumed. However, recent calculations (Hirotani, 2015a) made simultaneously solving the Poisson equation for the electro-static potential, the Boltzmann equations for relativistic electrons and positrons, and the radiative transfer equation showed that for a non-vacuum outer gap the magnetic-field-aligned electric field is screened at low altitudes (below 0.7 R_{LC}), as can be seen on Figure 2.12. Due to this screening, the positively charged particles created at low altitudes are not effectively accelerated toward the NS. Consequently, the inward gamma-ray flux becomes negligible in comparison to the outward gamma-ray flux. A non-negligible inward gamma-ray flux would lead to a light curve exhibiting more that two peaks. In the framework of the outer-gap model, a light curve exhibiting two peaks is expected, as can be seen in Figure 2.13. However, the separation between the peaks would depend on the inclination and viewing angle.

A enhanced version of the outer gap considering magnetospheric cascades is further dicussed in order to explain the VHE emission from the Crab pulsar in Section 5.3.1

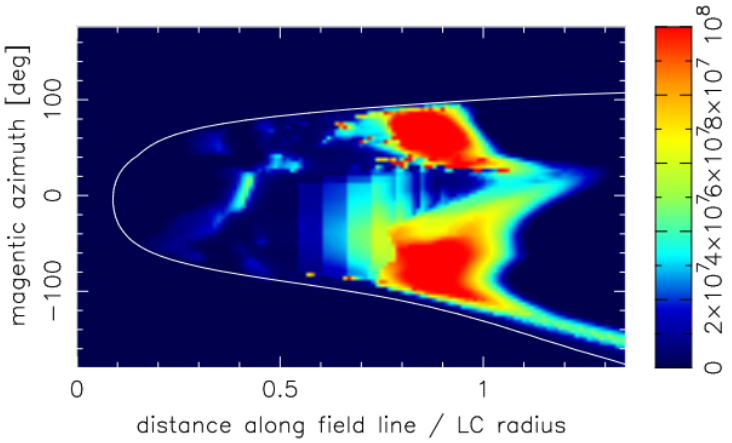

FIGURE 2.12: Accelerating electric field (z-axis) for a non vacuum outer gap. Figure adopted from (Hirotani, 2015a)

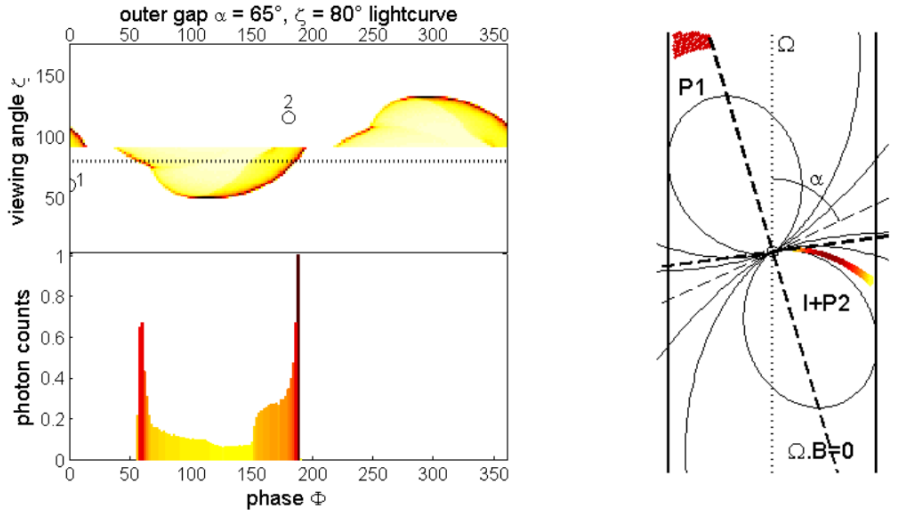

FIGURE 2.13: Same figure as 2.6 for the emission from the outer gap. Figure adopted from (Grenier and Harding, 2006)

2.6 Wind emission

The three previous models described above suppose the formation of gaps in the open magnetosphere, within the LC, where the charged particles density differs from the Goldreich-Julian charge density. Hence the charged particles are accelerated resulting in the emission of HE radiation. On the other hand, two scenarios were proposed in order to explain the origin of HE emission in the wind zone, beyond the LC (Bogovalov and Aharonian, 2000; Lyubarsky and Kirk, 2001):

- the unshocked relativistic pulsar wind model supposes that HE emission arises from IC scattering of soft photons on the accelerated pulsar wind.

- the striped wind model supposes that HE emission arises from synchrotron radiation from the accelerated pulsar wind due to reconnection of the magnetic field.

Unshocked wind acceleration model

The unshocked wind acceleration model (Bogovalov and Aharonian, 2000) assumes the acceleration of the pulsar unshocked wind at a distance R_W from the NS, much larger than the LC radius, $R_{LC} << R_W$. The wind, being radially ejected by the NS, is assumed to be electromagneticaly dominated $\sigma > 1$ (σ being the ratio between the Poynting flux and the kinetic energy flux, see Section 2.3). After the acceleration, the wind becomes kinematically dominated, $\sigma < 1$. At distances greater than R_W, due to the acceleration, the particles forming the wind move along straight lines (see Figure 2.14). The lines of flow of the kinetic energy dominated wind after acceleration are not exactly radial. In this model, the HE emission arises from the IC scattering of relativistic wind on the soft pulsed photons, emitted as a fan-like beam from the inner magnetosphere. This assumption implies that only particles moving toward the Earth can produce observable emission. Optical to X-ray pulsed photons play the most important role in the emission of IC gamma rays. The optical depth characterizing the Compton scattering of the wind electrons, and thus, the spectra of IC photons, strongly depends on R_W. In case of small values of R_W, the collision angle is large and the IC process takes place in the Klein-Nishina regime, see Section 1.3. In the case of a cold wind, the cooling of the electrons via synchroton is totally supressed, thus, the electrons forming the wind lose their energy only by IC scattering.

The estimates of the HE emission from this description should be taken as a lower limit due to the fact that only soft pulsed photons emitted toward the Earth are considered. However, the existence of an additional component from soft photons illuminating the wind, not propagating in the observer's direction, should be taken into account. An enhanced version of the unshocked wind acceleration model is further dicussed in order to explain the VHE emission from the Crab pulsar in Section 5.3.2

Wind striped model

The wind striped scenario (Lyubarsky and Kirk, 2001) is based on the assumption that for an oblique rotator surrounded by plasma, the energy lost is shared between an axisymmetric component of the Poynting flux and a component due to magneto-hydro-dynamic waves. The relative intensity between both depends on the inclination angle. The waves can be seen as current sheets separating magnetized stripes of plasma from the two hemispheres with opposite polarities beyond the LC, see Figure 2.15. The waves propagate with a phase speed less than that of light. Hence a field line at a given radius alternates in direction, being connected

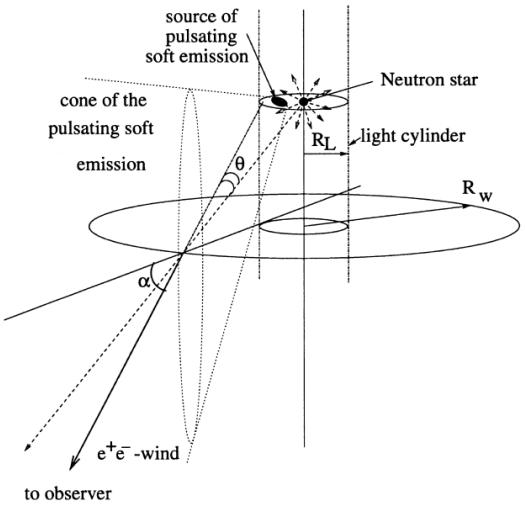

FIGURE 2.14: Sketch of the trajectory of the plasma after acceleration. Figure adopted from (Bogovalov and Aharonian, 2000)

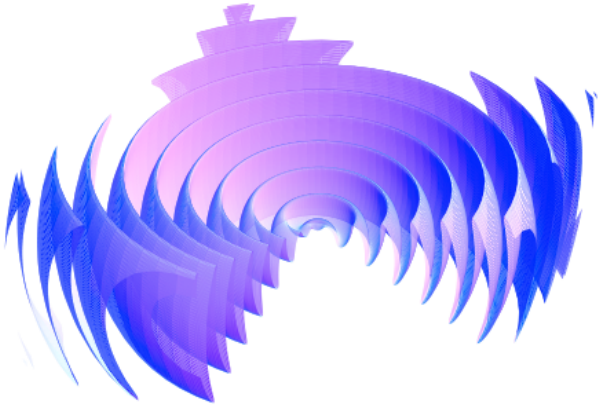

FIGURE 2.15: Current sheet around an oblique rotator. The neutron star is located at the center. Figure adopted from (Pétri and Lyubarsky, 2007)

to a different magnetic pole every half period. In this case, most of the energy is transported by the striped wind in the equatorial belt of the pulsar wind, whose thickness is controlled by the inclination angle. At high latitudes, the magnetic field does not change sign, and there are no current sheet embeded in the flow. It was shown (Usov, 1975; Michel, 1982)) that these waves must decay at large distances, as the current required to maintain them evolves as r^{-1} and the available number of charge carriers as r^{-2} (Michel, 1982). The dissipation of the wave can be considered as a reconnection and annihilation of the oppositely directed magnetic field. The distance at which the wave decays is proportionnal to the Lorentz factor of the flow of particles maintaining the waves. The flow is accelerated during the dissipation process due to some work from the hot plasma in the current sheet on the wind. The HE radiation arises from the synchrotron and SSC emission from the accelerated wind. Furthermore, provided that $R/R_{LC} \lesssim \Gamma^2$,

where R denotes the radius of the radiating source and Γ the Lorentz factor of the wind, the radiation will be pulsed at the NS rotation period. This mechanism appears to be consistent with the emission from the Vela pulsar above 50 GeV and from the Crab pulsar up to 400 GeV. However, in the case of the Crab pulsar, a new SSC component at tens of GeV is expected (Mochol and Pétri, 2015).

Chapter 3

The IACT technique and the MAGIC telescopes

Due to the opacity of the Earth's atmosphere to HE radiation, gamma-ray photons cannot be directly detected from the ground. However, direct detection is possible with spaceborne telescopes such as *AGILE* (Tavani et al., 2008) and *Fermi*-LAT (Atwood et al., 2009). Such space detectors, with small effective areas about $\sim 1\text{m}^2$, lack sensitivity above 10 GeV, where the photon flux is very low. On the other hand, gamma rays with energy greater than 10 GeV can be detected by ground-based Imaging Atmospheric Cherenkov Telescopes (IACTs), which have a larger effective area, exceeding 10^5 m^2. However, the main problem of the IACT technique is the discrimination between CRs and gamma-ray initiated showers. The IACT technique uses the atmosphere as a huge calorimeter in which a shower of secondary particles develops when a gamma-ray photon hits the upper atmosphere. Along the development of the shower, ultra-relativistic charged particles, with a velocity greater than the speed of light in the air, emit so-called Cherenkov radiation. The collection of these Cherenkov photons with IACTs and the analysis of the image left in the telescope cameras allow the reconstruction of the parameters of the primary particles.

3.1 Extensive air showers

An air shower is initiated by the interaction between a HE cosmic particle and a nucleus in the Earth's atmosphere, and results in the creation and propagation of secondary particles and photons, forming a cascade. Secondary particles are collimated along the direction of the incoming particle. Particles interact on average after one interaction length, which depends on the density of the target medium. Hence it is more convenient to express the interaction length in term of distance

and density, called atmospheric depth, X, which is given in units of g cm^{-2}. For vertical showers, the atmospheric depth is defined as the integral of the density along the height h:

$$X(h) = \int_h^\infty \rho(h')dh'. \tag{3.1}$$

In this case, the atmospheric depth at sea level (h=0) is $X_{air} \sim 1013$ g cm^{-2}.

3.1.1 Electromagnetic Showers

Electromagnetic showers result from the interaction between a HE photon or electron with the nuclei present in the Earth's upper atmosphere. When a gamma-ray photon enters the atmosphere, it will create, by interaction with the nuclei present in the atmosphere, an $e^{\pm}$ pair. The electron and the positron created will both carry half the energy of the incident photon, and so, they will be in turn very energetic. The created pair will then interact with the electric field of atmospheric nuclei and emit HE photons via bremssthralhung, see Section 1.3. The HE photons will create a second generation of $e^{\pm}$ pairs. A view of the electromagnetic shower development is shown on Figure 3.1. This process will keep going as long as

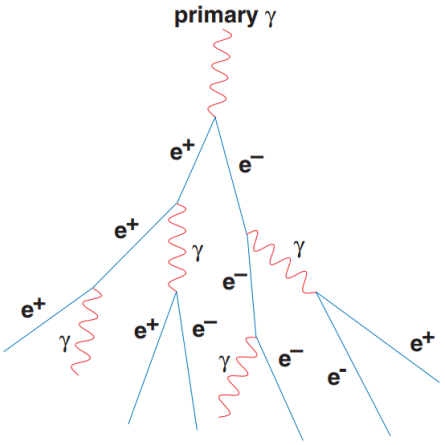

FIGURE 3.1: Characterization of the development of an electromagnetic shower in the air. Figure adopted from (Wagner, 2006).

the energy of the electrons and positrons is high enough to be lost via bremsstralhung. The critical energy is defined as the energy at which the loss rates via bremsstralhung and ionization are equal. In the air, with a pressure of 1 atm, the critical energy is 87.9 MeV[1]. Thus, when secondary electrons and positrons reach an energy lower than 87.9 MeV, they mainly lose energy via ionization and the development of the shower is stopped. The development of secondary particles from an incident gamma-ray photon or electron over a large area is referred to as

[1]http://pdg.lbl.gov/2014/AtomicNuclearProperties/HTML/air_dry_1_atm.html

an electromagnetic extensive air shower (EAS). Figure 3.5 shows the size of the electromagnetic shower, given as the number of secondary electrons, depending on the energy of the incoming particle and the altitude above sea level.

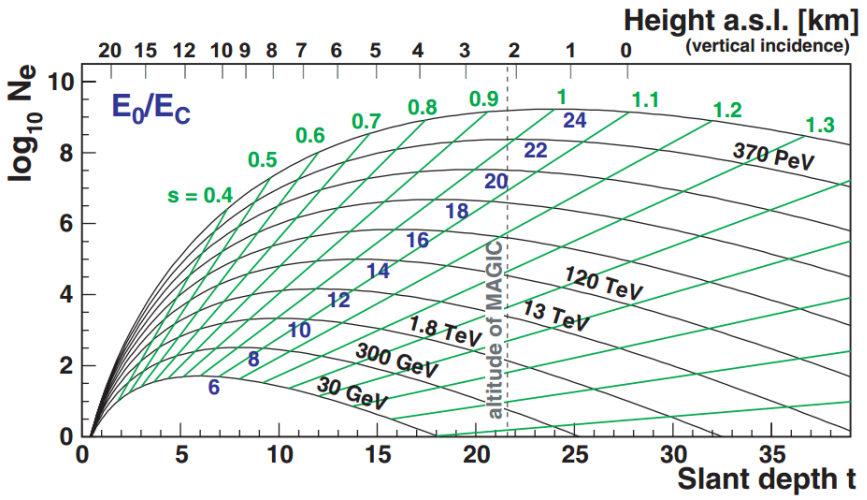

FIGURE 3.2: Longitudinal development of electromagnetic showers. The shower size, characterized by the number of secondary electrons, is plotted versus the radiation length in the air. The green lines characterize the shower age. The MAGIC altitude is indicated (2200 m a.s.l). Figure adopted from (Wagner, 2006).

The Heitler model

The basic features of the electromagnetic showers can be understood using a simple scaling model, referred to as the Heitler model (Heitler, 1954). In this model, we consider one particle of energy E which after any interaction produces two new particles of energy E/2. Each interaction takes place after the particle has traveled a distance $\lambda_e = X_B \ln 2$, see Figure 3.3, where X_B is the bremssthralhung interaction length (Giavitto, 2013). It is assumed that a photon will materialize as an $e^{\pm}$ pair after traveling a similar distance, which is actually a good approximation since the interaction length for pair production is longer than X_b by a factor $\frac{7}{9}$. Following this assumption, and denoting n as the number of generations, the number of particles at a given depth $X = n\lambda_e$ follows $N(X) = 2^n = 2^{X/\lambda_e}$. The energy of a particle at the n^{th} generation is therefore $E(X) = E_0/2^{X/\lambda_e}$, where E_0 is the energy of the primary particle. The number of particles reaches the maximum at $E = E_c$ which leads to:

$$N_{max} = \frac{E_0}{E_c} \qquad \text{and} \qquad X_{max}(E_0) \sim \lambda_e \ln\left(\frac{E_0}{E_c}\right) \tag{3.2}$$

The numerical simulations of EASs development in the atmosphere confirm the predictions of the Heitler model: The number of expected particles at the shower

maximum depends on the energy of the particle initiating the cascade, and the depth of the shower maximum logarithmically depends on the energy of the initiating particle.

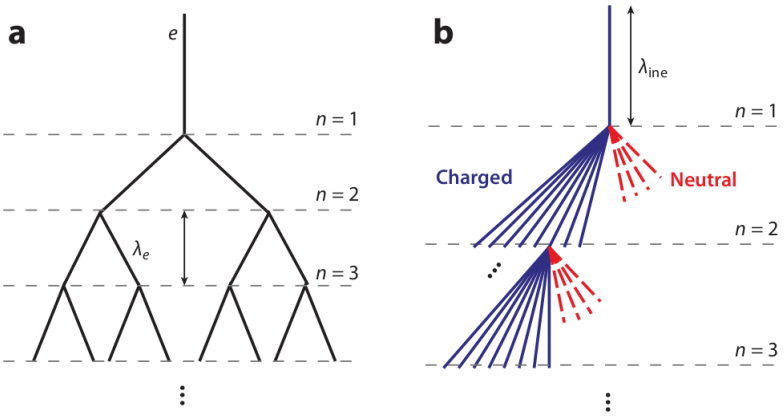

FIGURE 3.3: Development of an electromagnetic shower according to the Heitler model (left) and hadronic shower (Heitler-Matthew model) (right). Figure adopted from (Engel et al., 2011).

3.1.2 Hadronic showers

CRs can also produce air showers when interacting with the Earth's atmosphere, described by the Heitler-Matthew model (Engel et al., 2011). When hitting the atmosphere, CRs cause hadronic interactions with the nuclei in the atmosphere. The inelastic interactions between hadrons result in the production of several types of secondary particles, mainly pions, and in smaller abundance kaons and light baryons ($p, \bar{p}, n, \bar{n}$). The hadrons produced form part of the so-called hadronic core of the shower. The secondary particles continue to undergo hadronic interactions until the energy per nucleon is smaller than the pion production threshold ($E_{pr} \simeq 1$ GeV). Charged pions will interact with air nuclei if their energy is greater than some typical decay energy E_{dec}. Once the energy of the charged pions falls below E_{dec}, the particles decay producing muons and neutrinos;

$$\pi^{\pm} \rightarrow \mu^{\pm} + \nu_{\mu}(\bar{\nu}_{\mu}). \tag{3.3}$$

The created muons can decay into

$$\mu^{\pm} \rightarrow e^{\pm} + \nu_e^{\pm} + \nu_{\mu}^{\pm}. \tag{3.4}$$

However, muons with energy greater than 3 GeV can reach the ground before decaying, interacting almost exclusively by ionization. These muons are useful for

the calibration of IACTs. The neutral pions generated immediately decay into two photons,

$$\pi^0 \rightarrow \gamma\gamma. \tag{3.5}$$

Thus an electromagnetic sub-shower develops within the hadronic shower. The probabilities of production of π^+, π^- and π^0 being equal, about one third of the energy in inelastic interaction is transferred to electromagnetic showers. As the generation of electromagnetic sub-showers within the hadronic shower is not reversible, i.e., no hadronic sub-shower can arise from electromagnetic showers, hadronic showers end up in their electromagnetic components. A view of the hadronic shower development is shown on Figure 3.4.

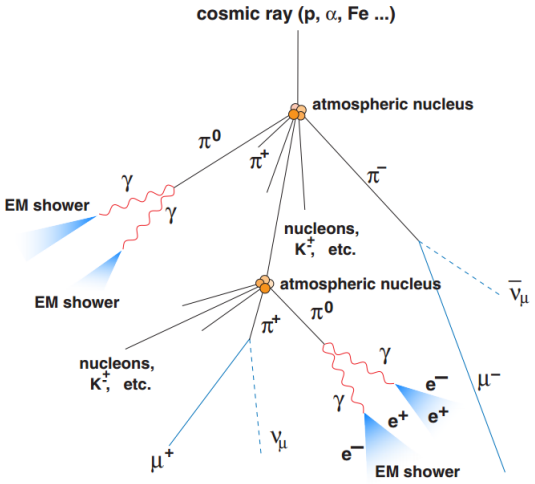

FIGURE 3.4: Characterization of the development of a hadronic shower in air. Figure adopted from (Wagner, 2006).

The cross section of the inelastic proton-proton collision has been measured experimentally[2] being almost constant between 3 GeV and 1 TeV, $\sigma_{pp} \sim 40$ mb. The cross section becomes $\sigma_{pA}^{inel} \sim 45 A_2^{0.691}$ for a nucleus target with a mass number A_2. When the colliding particle is a nucleus with a mass number A_1 the cross-section becomes $\sigma_{AA} \sim 65(A_1^{1/3} + A_2^{1/3} + 1.12)^2$ mb. Therefore, in the air ($A_2 \sim 14.5$), the proton-proton interaction has a cross section of 280 mb in this energy range, corresponding to a mean free path of 85 g cm^{-2}. So the first interaction for a proton is around 18 km a.s.l which is a bit lower than for a gamma ray (47 g cm^{-2}, 20 km).

Electromagnetic and hadronic EAS present major differences in their geometry and in the secondary particles created during their development. Hadronic showers present a wider lateral development than electromagnetic ones, as can be seen on Figure 3.5. The hadrons are produced with an energy dependent transverse momentum, leading to a larger angle for low energy hadrons with respect to the

[2] http://pdg.lbl.gov/2014/hadronic-xsections/rpp2014-pp_pbarp_plots.pdf

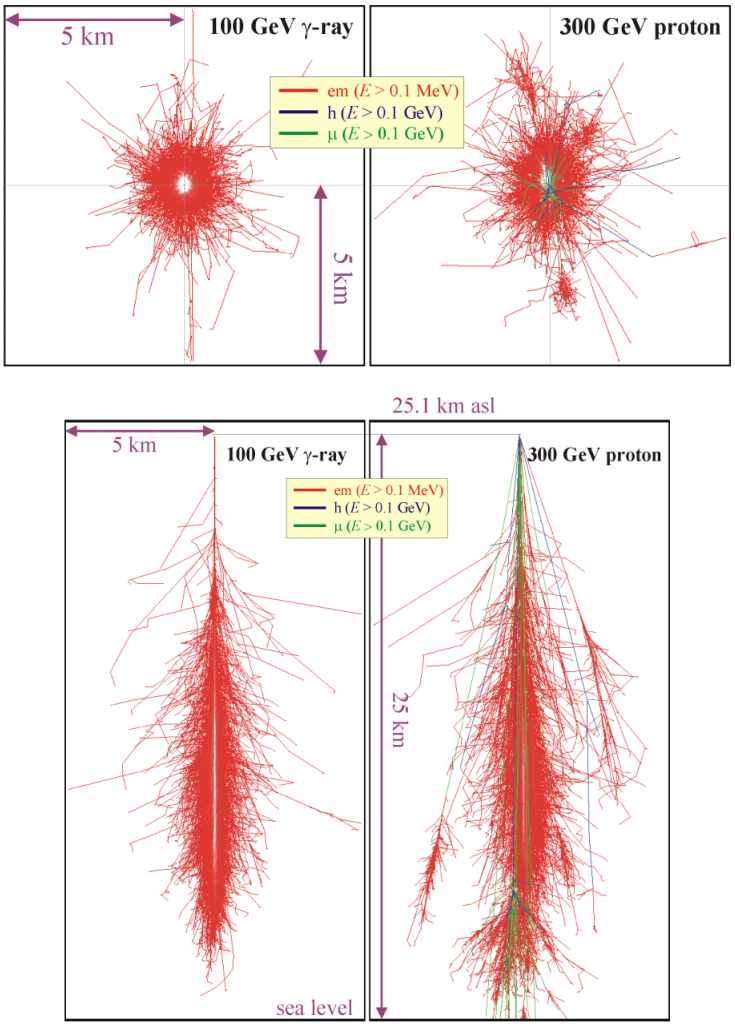

FIGURE 3.5: Shower lateral (top) and longitudinal (bottom) development initiated by a 100 GeV gamma ray (left) and a 300 GeV proton (right). Figure adopted from (Hrupec, 2008).

shower axis. The lateral distribution of secondary muons is also larger than the one of electromagnetic showers due to the fact that muons are mainly produced by charged pions decay (Meurer et al., 2006).

3.2 Atmospheric Cherenkov radiation

Cherenkov radiation appears when a charged particle travels in a dielectric medium with a speed greater than the speed of light in the medium, defined as $c_{med} = c/n$ with c the speed of light in the vacuum and n the optical index of the medium. When the charged particle travels through the medium, the molecules surrounding the particle path will temporarily be polarized. The molecules go back to their

normal state after the passage of the charged particle. If the particle has a speed smaller than the speed of light, the arrangement of the dipoles will be symmetrical around the particle, as can be seen on Figure 3.6 (a). Owing to the complete symmetry of the polarization field, there will be no resultant field at large distances. On the other hand, if the speed of the particle is greater than the speed of light in the medium, the symmetry along the particle path with respect to the particle disappears, however, the azimuth symmetry is preserved. The resulting dipole emission is constructive. As the charged particle is traveling faster than the light in the medium, it is possible for the emitted waves along of the track of the charged particle to be in phase with one another, generating the Cherenkov radiation, see Figure 3.6 (b). According to Huygens' Principle, a coherent radia-

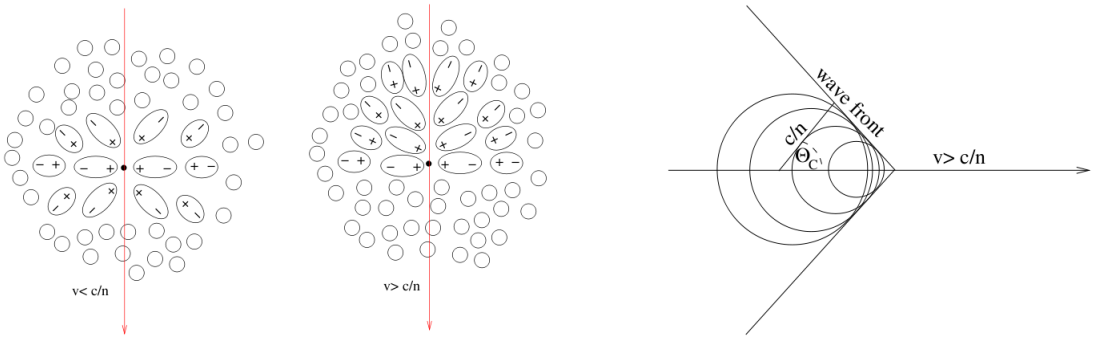

(a) Medium polarization **(b)** Cherenkov shock wave front

FIGURE 3.6: Medium polarization due to the passage of a charged particle (left) and emission of a Cherenkov wave from (right). Figure adopted from (Nieto, 2012).

tion will be emitted as a cone characterized by a given angle θ referred to as the Cherenkov angle. The value of the θ angle can be expressed as:

$$\cos\theta = \frac{1}{\beta n} \tag{3.6}$$

where β is defined as $\beta = v/c$ with v the speed of the charged particle. Thus, the minimal speed a charged particle needs to reach in a given medium in order to emit Cherenkov radiation is $\beta_{min} \geq 1/n$, and would carry an minimum energy of

$$E_c = \frac{m_0 c^2}{\sqrt{1-\beta_{min}^2}} = \frac{m_0 c^2}{\sqrt{1-n^{-2}}}. \tag{3.7}$$

The maximum Cherenkov angle, obtained for a particle at speed $\beta = 1$, is $\theta_{max} = \cos^{-1}(1/n)$. It can be seen from Eq. 3.7 that, due to their masses, electrons need less energy than muons and protons to emit Cherenkov photons. The threshold energy of Cherenkov emission, computed at sea level ($n \simeq 1.00029$) is of 21 MeV, 4.4 GeV and 39 GeV for electrons, muons and protons, respectively.

Due to the high energy of the particles hitting the Earth's atmosphere, charged secondary particles traveling at $\beta \geq \beta_{min}$ are created in the development of an EAS. The emitted Cherenkov photons during the EAS development are referred to as atmospheric Cherenkov radiation. The number of Cherenkov photons produced per unit of path length of a particle with charge ze per unit of wavelength, λ, is given by (Olive and Particle Data Group, 2014).

$$\frac{dN^2}{dxd\lambda} = \frac{2\pi\alpha z^2}{\lambda^2}\left(1 - \frac{1}{\beta^2 n^2(\lambda)}\right), \tag{3.8}$$

where α denotes the fine structure constant. As the spectral index of the atmosphere does not depend strongly on λ for the characteristic wavelengths range to which of Cherenkov telescopes are sensitive, Eq 3.8 can simply become $\frac{dN^2}{dxd\lambda} \propto \lambda^{-2}$. However, n depends on the altitude. The number of photons created per unit of wavelength per meter of path is ~ 100 at sea level versus ~ 8 at 10 km. A single particle traversing the atmosphere produces a total of $\sim 10^5$ photons (Polikarov, 1954). Cherenkov photons in the atmosphere suffer absorption due to the elements present in the atmosphere (Bernlöhr, 2000). The absorption below 300 nm is mainly due to O_2, O_3 and N_2. The molecules in the atmosphere cause Rayleigh scattering, which has a λ^{-4} dependency, thus, mainly short wavelength are affected. Aerosols such as dust and water droplets cause Mie scattering which has a $\lambda^{-(1;1-5)}$ dependency, that affects all the wavelengths.

The observed spectrum at the altitude of the MAGIC telescopes peaks at ~ 330 nm, as can be seen in Figure 3.7, where the Cherenkov photons spectrum after absorption and without absorption are plotted for different energies of primary gamma rays.

As previously mentioned, the Cherenkov angle, θ, depends on the particle speed, β, and the refraction index, n. The Cherenkov angle is getting greater as the altitude decreases, due to the impact of the atmosphere density on the refraction index. The emitted Cherenkov photons are thus spread on the ground over a ring called the **light pool**. The light pool, has a radius of ~ 120 m for a vertical incident photon, independent of the energy of the primary particle.

Shower development lasts for ~ 100 μs and Cherenkov photons are produced at several heights. The particles of the shower and the Cherenkov photons have a spread in time of ~ 2 ns. The time spread of the Cherenkov photons and the EAS particles starts to increase at more than 120 m away from the shower core.

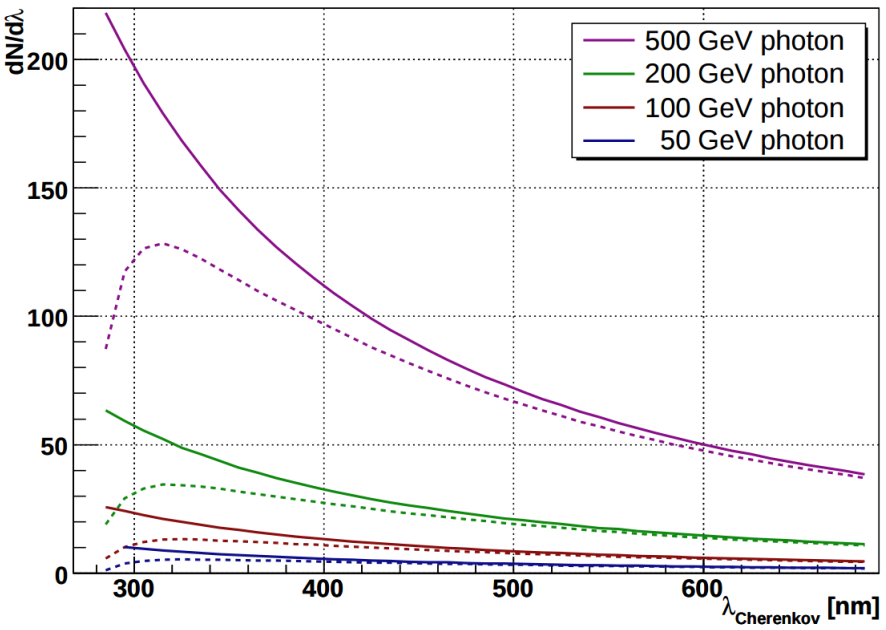

FIGURE 3.7: Cherenkov radiation spectrum from air showers with different initiating particle energy. Full curve are the non absorbed spectrum, while dashed lines represent the light arriving at the MAGIC site (2200 m a.s.l) after atmospheric absorption. Figure adopted from (Wagner, 2006).

3.3 Imaging Atmospheric Cherenkov Telescopes

The concept of Imaging Atmospheric Cherenkov Telescopes (IACTs) is based on the previously mentioned emission of Cherenkov photons in the EAS. In 1948, it was pointed out that Cherenkov radiation produced by EAS could be detected on the ground (M. S. Blackett, 1948). In 1972, a detection of the Crab Nebula was reported by the Smithsonian group (Fazio et al., 1972) at the 3σ level. In 1989 this detection was confirmed by the Whipple observatory (Weekes et al., 1989) after the development of new analysis methods.

In order characterize the primary particles initiating the EAS, the atmospheric Cherenkov photons emitted during the EAS development are reflected on the telescope mirrors and focused on the camera made of hundreds of photo-detectors (PMTs or Silicon photo detectors). The image of the focused Cherenkov photons is ellipse-shaped, representing the development of the shower, with the main axis of the ellipse representing the shower axis. As the Cherenkov angle, θ, is smaller for photons emitted at high altitudes compared to photons emitted closer to the observation level, photons emitted at high altitude will be reflected closer to the shower axis. A schematic view of the focusing of EAS photons is shown in Figure 3.8. The images recorded in the camera are then parametrized by means of the so-called Hillas parameters (Hillas, 1985). The distribution of the Hillas parameters is different for electromagnetic and hadronic showers, providing an efficient way to

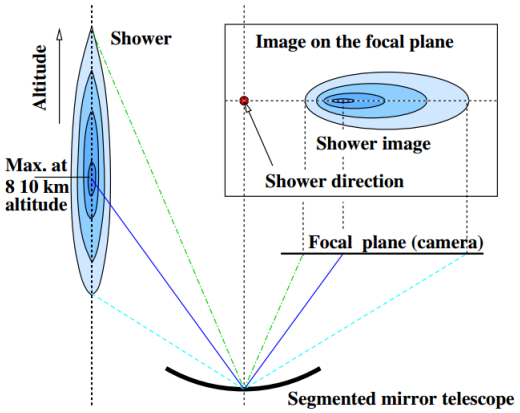

FIGURE 3.8: Reflection and focusing of the Cherenkov photons in the telescope reflector. Figure adopted from (Völk and Bernlöhr, 2009).

reject part of the CR background. As the major axis of the ellipse represents the axis of the shower, we can estimate the incoming direction of the shower initiating particle. However, stereoscopic observations allow a more precise reconstruction of the incoming direction of the particle, by crossing the main axis of several ellipses, as can be seen on Figure 3.9. Besides a gain in accuracy of the reconstructed position, the stereoscopic mode rejects more background due to the coincidence of detected photons required between both telescopes.

3.4 The MAGIC telescopes

The MAGIC *Florian Goebel* telescopes are a set of two 17 m diameter IACTs located in El roque de los muchachos observatory, on la Palma Islands (28° 45' N, 17° 54' W, 2225 m above sea level), in the Canary Islands (Spain). MAGIC stands for Major Atmospheric Gamma ray Imaging Cherenkov telescopes. The first MAGIC telescope started operation in 2004 in stand-alone mode. MAGIC became a stereoscopic system in Autumn 2009. The MAGIC telescopes are designed to detect photons from 50 GeV up to 50 TeV. Due to the differences between both telescopes, MAGIC underwent several upgrades in order to homogenize the system. A first upgrade was done in summer 2011 in order to upgrade the readout system of both telescopes to a new one based on the Domino Ring Sample v4 chip (DRS4) (Ritt, 2008). The second upgrade was performed in summer 2012 in order to upgrade the MAGIC-1 camera and trigger to new ones similar to the one at work in MAGIC-2.

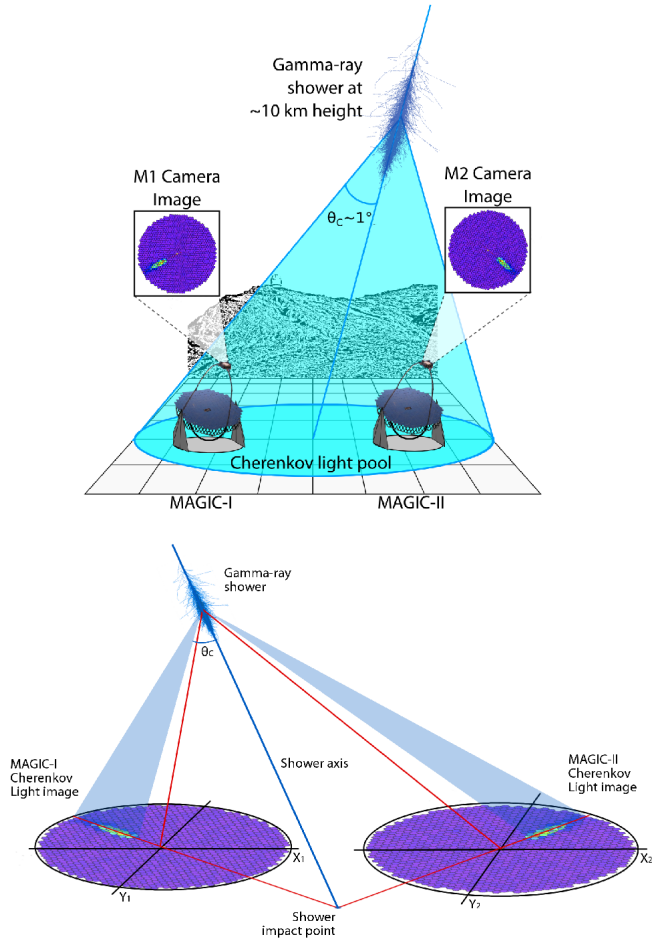

FIGURE 3.9: Sketch of the stereo observation (top) and stereoscopic reconstruction principle (bottom). Figure adopted from (Giavitto, 2013).

3.4.1 Structure and drive

The structure of the MAGIC telescopes is made out of carbon fiber reinforced plastic (CFRP) tubes, weighing only ~ 5 tons without mirrors and has negligible thermal expansion. It is one third as heavy as the standard steel structures. The camera is held by a metallic arch and stabilized by 10 pairs of steel cables tied to the main frame. The total weight of the telescope (camera, frame and mirrors) is about 60 tons. The light structure of the MAGIC telescopes, together with the fast and accurate reaction of the drive, allows a fast repositioning, reaching any position in the sky in less than 1 minute.
The drive system of the telescopes consists of an alt-azimuth mount, which means that in order to point to a source, the telescopes have to be moved around two axes. Each telescope structure is equipped with three servo-motors (two in azimuth and one in altitude). The Altitude range spans from $-10°$ to $160°$ and the Azimuth spans from $-90°$ to $318°$. During normal operations, the telescopes can track a source with a precision of $0.02°$ thanks to the monitoring of the position of the

telescopes with two absolute shaft encoders. The calibration of the shaft encoder is made by dedicated models. The models are computed by comparing positions of the stars in the sky and the reflected position of the star in the camera center, (See section A.0.1).

3.4.2 Mirrors and active mirror control

The diameter, D, of the parabolic reflector is 17 m, as well as its focal distance, leading to a ratio focal length over diameter $f/D = 1$. The area of the reflector is ~ 236 m^2. The MAGIC-1 reflector is tessellated and each of the facets has an area of 1 m^2. The 247 facets are made up of four thin single 0.5×0.5 m^2 all-aluminum mirrors attached to a honeycomb structure. The MAGIC-2 reflector, on the other hand, is made up of 143 facets consisting of a single 1×1 m^2 all-aluminum mirror and 104 facets made up of a single 1×1 m^2 glass-aluminum mirror. Each of the facets in both telescopes is spherical in shape with a curvature radius varying from 34 m to 36.7 m. The reflectors have approximately a paraboloid shape. The advantage of such a shape is that it is isochronous, reducing the required integration time to extract the signal by reducing the time window of the Level-1 trigger, see Section 3.4.4, and, consequently, the integrated noise. It also allows to use the time evolution of the shower as a discrimination criteria between electromagnetic and hadronic showers.

The typical overall point spread function (PSF) is ~ 10 mm wide, so most of the reflected light is contained inside a single camera pixel (3cm). However, the structure of the telescope is not rigid and can suffer from bending. This bending of the structure would result in a smearing of the reflected image, and, consequently, in a worsening of the PSF. In order to keep this bending under control and to limit such aberrations, the Active Mirror Control (AMC) system is in charge of readjusting the position of each facet during data taking. Each facet is fixed on three pistons; one is immobile and the two other can adjust the mirror position with a precision of 10 μm. A set of Look-Up Tables (LUTs) are built in order to adjust the position of the pistons according to the pointing Altitude.

3.4.3 Camera

The camera of the telescopes has to be sensitive to short and faint Cherenkov flashes. After the upgrade of 2012, the cameras of both telescopes are almost identical. The former MAGIC-1 camera was made up of 577 hemispherical PMTs and was ~ 200 kg lighter than the current MAGIC-1 camera. Now, both cameras are equipped with 1039 30 mm (0.01° FoV) PMTs, having a total FoV of 3.5°. A small pixel size is required in order to have a better sampling of the shower.

Each PMT provides a response on the order of a few ns and has a peak quantum efficiency (QE) of 32% in the blue band. They are composed of six dynodes and have a gain of around 3×10^4. This gain allows observations with moonlight (moon phase up to 75%). As the PMTs response is strongly dependent on temperature, a cooling system is mounted in both cameras to regulate the temperature. A plexiglas window and movable lids protect the PMTs from dust and light. Winston cones are located between the PMTs and the Plexiglas window in order to focus the light on the PMTs to reduce the dead area between pixels. The Winston cones have a circular shape on one side, to match the shape of the PMTs, and hexagonal on the other side to ensure a geometrical filling close to 1. The behavior of the cameras can be tested in daylight thanks to pulse generator boards that can inject pulses similar to those of the Cherenkov light into the pre-amplifier of the PMTs. The trigger area of both cameras comprises the inner 2.5° region. The central pixel of each camera was modified in order to be sensitive to small variations of the optical flux of pulsars. It has a target bandwidth of 1 Hz - 1 kHz. Dedicated electronics were installed in the MAGIC-2 camera in order to use the central pixel for both optical and standard gamma-ray observations.

In order to have an accurate calibration of the pixels, a calibration box is located in the center of the reflectors. The calibration box periodically pulses light at 355 nm to illuminate the camera. The pulse intensity is regulated by two rotating filter wheels. The calibration allows for an on-line calibration in order to take into account the uneven response of the PMTs.

3.4.4 Receivers and triggers

Due to the short Cherenkov flashes illuminating the camera, fast readout electronics are required. The Cherenkov flashes hitting the photocatode of the pixels are then converted into analog (electrical) signals at the base of the PMTs. The analog signals are amplified by the pre-amplifiers. The amplified signal is converted into optical signal via a VCSEL (Vertical Cavity Surface Emitting Laser) and sent to the counting house via optical fibers. After arriving at the counting house, the optical signals are converted back to electrical signals and are split into two branches. This step is done by means of a MONSTER (MAGIC Optical NanoSecond Trigger and Event Receiver) board able to process 24 channels simultaneously. One signal branch goes to the *level 0* trigger, consisting of a discriminator with an adjustable threshold. If the signal surpasses a given threshold, it is digitized and sent to the trigger system. The second signal branch is routed to an analog readout where the signal is digitized. The signal is digitized by a Domino Ring Sample chip (DRS4) working at a speed of 1.7 GSamples s^{-1} using an array of 1024 capacitors acting as a ring buffer. Until November 2014 the signal was digitized at a frequency of 2 Gsamples/s. However, this frequency was reduced to 1.7 Gsamples s^{-1} in order

to get rid of so-called "dead sky zone", see Section 3.4.4. The capacitors, which are synchronized to a clock, are charged by the analogue signal during a given amount of time controlled with a special clock, that controls the switching, called Domino wave. The sequence loops until a trigger occurs and stops the Domino wave. The charge stored in the capacitors is then read out sequentially at 33 MHz and the voltage is digitized using an ADC. Each receiver is connected to a PULSAR (PULSer And Recorded) board. A PULSAR board handles a total of 96 channels.

Triggers

The trigger system evaluates incoming events and decides, according to predefined criteria, whether to keep an event or not. The main purpose of the triggers is to reject the NSB. Currently, two trigger systems are at work in the standard MAGIC data taking: the standard digital trigger, and the analog sum-trigger.

The standard digital trigger system is organized in several layers:

- Level 0 (L0): The L0 trigger is the one implemented in the MONSTER boards. It checks whether the charge of individual pixels exceeds a given threshold. The threshold is controlled according to the IPRC (Individual Pixel Rate Control). The IPRC sets the L0 rates between 300 KHz and 1.1 MHz. This way, it can also regulate the Level 1 trigger with a target rate of 10 - 20 KHz.

- Level 1 (L1): The L1 trigger combines spatial and temporal information from the pixels. It checks whether a pixel triggered by the L0 has a sufficient number of significant neighbors in a given time window. The number of neighbors required, going from 2 to 5, is set depending on the kind of observation (mono, stereo, etc).

- Level 3 (L3): The L3 trigger is the stereoscopic trigger. The purpose of this trigger is to keep only events that were detected by both telescopes in a given time window. In order to take into account the delay in the arrival time of the Cherenkov photons between the two telescopes, a time delay, depending on the pointing position, has to be added to the L1 trigger. Depending on the pointing position (strongly azimuth dependent), the time delay to be set between both telescopes can be too big as to keep the event in the time, so the event would be lost. These sky positions are referred to as "dead zone", as no event coming from those areas in the sky can trigger the L3.

3.4.5 Sum-Trigger

The standard MAGIC trigger has a threshold of around 50 GeV. However, in order to lower this threshold and have a better overlap between the ground-based and spaceborne telescopes, a new trigger was developed, the so-called Sum-Trigger. As previously mentioned, the standard trigger relies on a first threshold set at the pixel level. After this step, the topology and arrival time of the signal in each pixel are taken into account. The sum-trigger is based on a different algorithm. It considers several neighboring pixels and clips the signal of each pixel to a given clipping value. The clipped values are then summed. If the resulting sum exceeds a given threshold, the event is kept. The aim of the clipping is to reject large signals due after-pulses, that may appear due to charged particles in the PMTs that can hit the photocathode and generate a signal at the PMT output. Summing the charge of several pixels enables the detection of fainter signals with respect to the standard trigger. Figure 3.12 showed a simplified version of the algorithm at work in the sum-trigger.

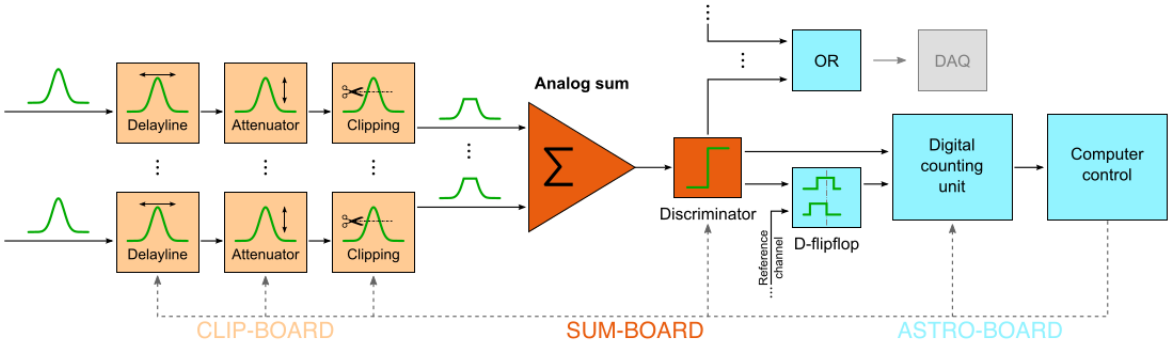

FIGURE 3.10: Sketch depicting the principles of the sum-trigger algorithm. The clipped signals are summed in the sum-board and then sent to the astroboard for digitalization. Figure adopted from (Völk and Bernlöhr, 2009).

3.4.6 Starguider

The starguider is a high-sensitivity CCD camera with a 4.6° FoV located in the center of the reflector of each telescope. Its purpose is to provide a real time estimate of the mispointing of the telescopes. The starguider continuously monitors the background stars and compares their observed positions with those from a catalog.The mispointing information is stored in the data files to be corrected later in the *offline* data analysis. However, in order to estimate the mispointing of the telescope, the starguider first has to be calibrated. This is done by means of dedicated models for MAGIC-1 and MAGIC-2. As the author of this thesis was

involved in the check and update of the starguider models, more information can be found in the technical documentation in the appendix A.0.1.

3.4.7 DAQ

The MAGIC Data AcQuisition program (DAQ), in charge of the data storage at the raw level, is a multi-thread C++ program (Tescaro et al., 2013). The main threads of each DAQ are:

- Reading: The data coming from the readout boards are collected. This thread continuously checks if there are new data. If a new event is detected, it is treated and a header containing the information of the different sub-systems is built. A first integrity check is done in this step.
- Analysis: A first pre-processing is done here. A time correction is applied in order to take into account the time the event has spent in the several sub-systems. The pulse intensity and the event arrival time is computed. A second-level integrity check is done.
- Writing: the event is removed from the read buffer and stored on disk.

3.4.8 Telescope Observation

Two observation strategies are used in MAGIC; the ON/OFF and the *wobble* mode. During ON observations, the telescopes are pointed directly at the source, consequently, the source is located at the center of the camera. The effective collection area is higher in this mode than with the *wobble* one. In order to estimate the signal strength, dedicated OFF observations are required. The OFF observations are made pointing the telescopes toward a region of the sky where no VHE sources are expected. For consistency, the OFF observations have to be made close to the source of interest, with similar zenith angle. During observations made in the so-called *wobble* mode (Fomin et al., 1994) or *false-source tracking*, the source is offset from the camera center. A typical offset of 0.4° is used. In order to reduce possible biases, the source position in the camera is changed every 20 minutes. Typicall, four wobble positions are used in MAGIC. The advantage of this observation mode is that it allows us to gather at the same time data from the target source and from the background region. The background region is defined as the source position rotated by 180° around the camera center, and is call the *anti-source*. The amount of background data can be increased by up to a factor three by taking into account the region corresponding to the target position rotated by 90° and 270° around the camera center, see Figure 3.11. This

method has a lower sensitivity than the ON mode one but has the advantage of not requiring additional time for dedicated OFF observations and suffers from less systematic uncertainties.

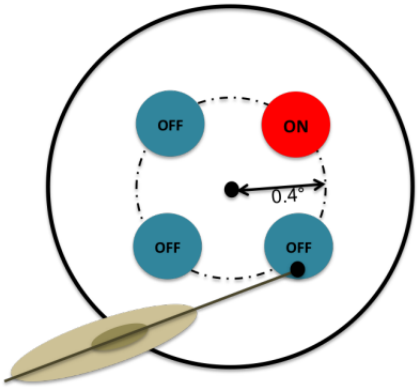

FIGURE 3.11: Representation of the *on* and *off* regions in *wobble* observation. Figure adopted from (Zanin, 2011).

3.5 MAGIC Data Analysis

The aim of the observation is to extract physical parameters such as the flux, spectral shape and morphology of a given source. In order to proceed to the reduction and analysis of the MAGIC data, a dedicated software was built, based on *ROOT* (Brun, 1997) and C++, called *MARS* (MAGIC Analysis Reconstruction Software) (Zanin et al., 2013). The *MARS* package is under constant development in order to take into account hardware modifications and to optimize the analysis chain, improving the performance of the system (Aleksić et al., 2016a). The MAGIC analysis pipeline goes through the following major steps:

- Signal extraction: Calibration and determination of the charge and arrival time, in each pixel, of the signal left in the camera by the EAS Cherenkov photons.
- Image cleaning and parametrization: During the image cleaning, pixels containing signal due solely to the NSB are removed. This estimation is made using the charge of each pixel and timing information. The parameters that describe the image shape are computed after cleaning.
- Stereo reconstruction: The previously characterized events for each telescope are matched, and the stereoscopic parameters are computed.

- Energy reconstruction and event characterization: Reconstruction of the energy and nature of the primary particle originating the detected image (gamma ray or cosmic ray).
- Signal determination: The gamma-ray excess coming from the source under study is computed. High level plots such as spectral energy distributions and sky maps are produced.

3.5.1 Calibration

The calibration consists of extracting the arrival time and signal intensity in each pixel and converting them into physical quantities. The RAW data files consist of digitized samples of the signal from each pixel. In particular, 60 samples of 0.5 ns each are saved to disk for each pixel. The dedicated program for data calibration of MAGIC data is called *Sorcerer* (Simple, Outright Raw Calibration; Easy, Reliable Extraction Routines). First the pedestal has to be subtracted from the received signal, and corrections for non-linearities in the amplitude and the timing of individual pixels have to be applied. These corrections often depend on the position of the event in the domino ring. In order to correct these non-uniformities, calibration, pedestal runs and interleaved events are obtained regularly during data taking. Calibration and pedestal runs are taken each time a new source is observed, whereas interleaved events are taken at a frequency of 25 Hz in order to monitor the evolution of the signal transmission and readout performance during the observation. The pulse produced by a pixel due to the Cherenkov light hitting the camera is extracted after the pedestal has been removed. The arrival time of an event is defined as the position of the rising edge of the pulse at half maximum height. The signal amplitude from ADC count has to be converted to a number of *ph.e*. As the PMTs have no single-*ph.e* resolution, the conversion is computed using the F-factor method. The F-factor uses the calibration pulses, assuming that the number of *ph.e* follows a Poisson distribution, with mean N and standard deviation $\sqrt{N}$. If the mean measured charge of the FADC for a calibration event is $< Q >$, and σ_Q the standard deviation, then the F-factor for each PMT is defined as:

$$F = \frac{\sqrt{N}\sigma_Q}{< Q >}. \tag{3.9}$$

The conversion factor from FADC counts to *ph.e* is defined as:

$$C = \frac{N}{< Q >} = \frac{F^2 < Q >}{\sigma_Q^2}. \tag{3.10}$$

During data taking, the conversion factor might vary due to some response variability of the VCSELs. The interleaved calibration events are used to update

the conversion factor during the observations and interleaved pedestal events to estimate the evolution of the pedestal.

3.5.2 Image cleaning and parameter reconstruction

At this step of the analysis, the calibration has been done, i.e., the charge of each pixel and the arrival time of the Cherenkov photons have been estimated. However, due to the NSB, some pixels do not contain information of the shower, but only noise. In order to be able to extract the image left in the camera by the EAS, these pixels containing only noise have to be removed. This is done during the *cleaning*. Once the pixel containing only noise have been identified and discarded, the parameters of the image that characterize the shower development can be computed. The image cleaning and parameters reconstruction are done by the *star* (STandard Analysis and Reconstruction) program.

Image cleaning

In order to proceed to the cleaning of the images, three categories of pixel are defined. The core and boundary pixels containing information about the shower development and characterizing the image left in the camera by the EAS, and the rest of the pixels containing only noise. In order to classify these pixels, different thresholds on the signal of the pixels are set taking into account the arrival time of the signal in each pixel. A pixel is accepted as a core if its charge is above a certain threshold (6 *ph.e* for M1 and 9 *ph.e* for M2) and its arrival time is within a certain time window, set to 4.5 ns from the mean arrival time of its boundary pixels. This sets the first cleaning level. Once the core of the image has been identified, the boundary pixels have to be determined. In order for a pixel to be a boundary pixel, it has to be adjacent to at least one core pixel, needs to have a charge above a certain threshold (3 *ph.e* for M1 and 4.5 *ph.e* for M2) and its arrival time has to be within a time window, set to 1.5 ns, from the mean arrival time of the core pixels.

This cleaning algorithm was the official one at work for the MAGIC telescopes until 2011 (Zanin, 2011). A second cleaning, more efficient at low energies (E $<$ 100 GeV) was developed, the so-called *sum-cleaning* (Lombardi, 2011). In the *sum-cleaning* algorithm, the core pixels are selected if the clipped sum of x (x=2, 3, 4) pixels is above a certain threshold and if their arrival time is within a given window from the mean of the corresponding pixels in the same group. The time window depends on the number of pixels summed. The sum and clipping prevent to accept pixel signals dominated by after-pulses. A pixel is accepted as boundary pixel if it is contiguous to at least one core pixel, its charge is above a certain threshold (3 for M1 and 4.5 for M2) and its arrival time is within a time window of of 1.5 ns from the mean arrival time of the core pixels.

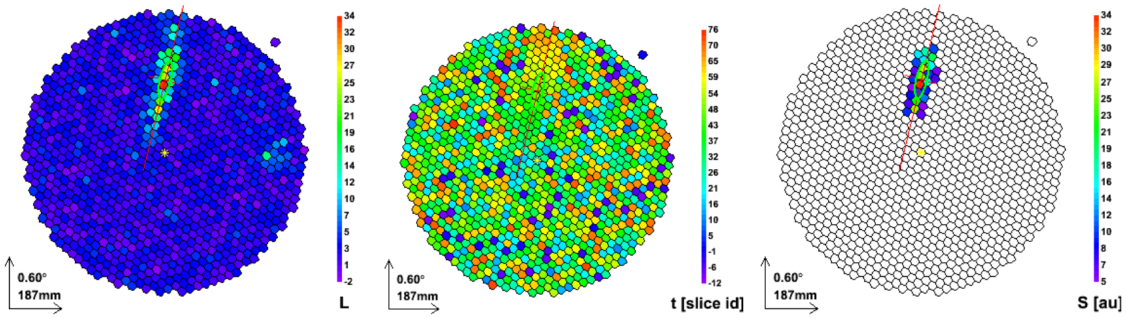

FIGURE 3.12: Image cleaning process. Each raw event (left) has to be cleaned according to the photons arrival time in each pixel (middle). In the resulting image only the pixels containing shower information are kept (right). Figure adopted from (Giavitto, 2013).

Image parametrization

The images left by gammas in the camera are characterized by an elliptical shape while the hadronic ones are more diffuse. This leads to a natural description of the showers as ellipses, or more specifically, in term of their second order momentum. This was introduced by Hillas (Hillas, 1985) in 1985. The parameters can be sorted into two categories; source-dependent and source-independent parameters. The source-dependent parameters are computed according to the position of the source in the camera plane. The source-independent parameters are:

- Size: This parameter corresponds to the sum of the charge from each pixel. The size is strongly correlated to the energy of the incoming particle.
- Length: Represents the spread of the light along the major axis of the ellipse.
- Width: Represents the spread of the light along the minor axis of the ellipse.
- Conc: Represents the "compactness" of the image, i.e., the fraction of the total charge contained in the two brightest pixels.
- Time RMS: This parameter represents the spread of the distribution of the arrival times of the signal in each pixel.
- Time gradient: Represents the arrival time profile of the Cherenkov photons at the camera. It is defined as the slope of the fit of the arrival time along the major axis of the ellipse.

The source-dependent parameters are:

- Dist: Is the angular distance between the center of gravity of the image (CoG) and the source position in the camera plane.

- Alpha: Is the absolute value of the angle between the major axis of the ellipse and the axis made by the image CoG and the source position in the camera plane.
- Asymmetry: This parameter is defined as the distance between the brightest pixel to the CoG of the ellipse. It is positive if directed toward the camera center and negative in the opposite case.
- M3Long: The third moment of the image along the major axis. This parameter is used to distinguish between the head and the tail of the image. The sign convention is the same as for the Asymmetry parameter.
- LeakageN: This parameter is defined as the fraction of the signal in the N-outermost ring of the camera to the total signal (usually N=1). Events with a large leakage value are likely to suffer from bad reconstruction.
- Number of islands: This parameter represents the number of pixel groups that survived the cleaning.

Stereoscopic parameters

The stereoscopic parameters are estimated combining the images of both telescopes. The *SuperStar* program combines both images using the stereo event number assigned by the DAQ to match an event from both telescopes. The stereoscopic parameters allow for a 3-dimensional reconstruction of the events (Kohnle, 1996).

- Shower direction: The shower direction is obtained crossing the main axes of the two ellipses, surimposed on a single camera plane.
- Impact point: The impact point on the ground is obtained crossing the main axes of the two ellipses taking into account the telescopes position.
- Impact parameter: This parameter represents the angular distance between the shower axis and the pointing axis of the telescopes. This value is different for each telescope.
- Shower maximum height: This parameter represents the altitude at which the maximum development of the shower took place. It is good CRs background discriminator.
- Cherenkov radius: radius of the light pool at ground
- Cherenkov photon density: density of Cherenkov photons at ground. Both the Cherenkov radius and photon density are computed from the Shower maximum height.

- θ^2: After the reconstruction of the 3-D development of the shower, the θ parameter can be reconstructed. This parameter is the angular distance between the reconstructed shower direction and the expected position of the source. In order to work with positive values, one uses the squared value of this angular distance, θ^2.

The disp method

In the case of monoscopic observations, the 3-D development of the shower is more complicated to compute. Only the projection of the shower direction on the camera plane (main axis of the ellipse) is known. The distance of the impact from the CoG can be estimated using the so-called *disp* method (Fomin et al., 1994). The *disp* parameter is estimated as follows:

$$disp = A(size) + B(size) \times \frac{width}{length + \eta(size) \times leakage2} \tag{3.11}$$

The A and B parameters are estimated from Monte Carlo simulations. However, at VHE, the leakage is getting important and this parametrization is not very efficient. To improve the parametrization, the *disp* is computed in MAGIC by methods based on the *Random Forest* algorithm, see 3.5.4. The *disp* method returns a degenerate reconstructed source position, see Figure 3.15. The head/tail ambiguity can be solved taking into account the shape of the image and the time gradient information.

For stereo analysis, the position of the crossing point of the two ellipses axes is taken into account too. Thus, in order to get rid of the head/tail ambiguity, the 4 distances between the 2 reconstructed positions for each image are computed, and the two points estimated with the highest values discarded. The reconstructed source position is set to the average of the two remaining points. The θ parameter is set to be the angular distance between this reconstructed source position and the expected source position in the camera plane. However, at low energies this method may fail if the axes of the ellipses are almost parallel.

3.5.3 Monte Carlo simulations

The remaining part of the analysis relies on Monte Carlo (MC) simulations of the development of the atmospheric shower initiated by gamma rays and the later detection of the emitted Cherenkov light by the telescopes. The development of the gamma-ray-initiated EASs in the atmosphere are simulated with the CORSIKA (Heck et al., 1998) program. The simulation of the reflection of the Cherenkov photons in the telescopes mirrors and the response of the camera and readout are simulated by two distinct programs; *Reflector* simulates the absorption in the atmosphere of the Cherenkov photons as well as their reflection in the telescopes

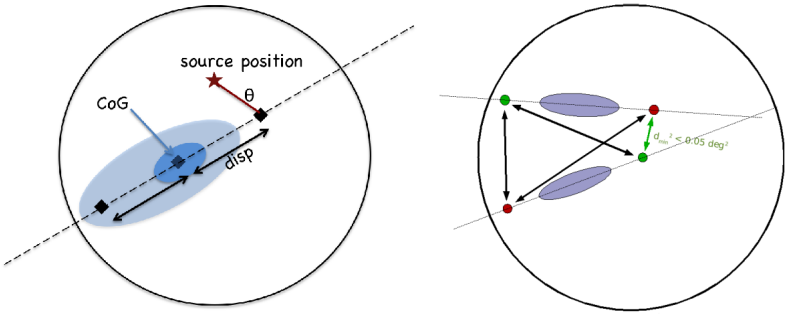

FIGURE 3.13: Reconstruction of the *disp* parameter for monoscopic observation where the source position is degenerate (left; credit: R. Zanin)) and stereoscopic observation removing the ambiguity (right; credit: S. Klepser).

mirrors, and *Camera* simulates the camera electronics, the readout and the trigger response. A new program is under development, *MaTelSim*, in order to provide MC simulation for the new sum-trigger system (López et al., 2013). Several zenith angle ranges are considered for the MC simulations; 0° to 35° for low-zenith, 35° to 50° for med-zenith, 50° to 62° for high-zenith and 62° to 70° for very-high zenith. Different sets of MC are produced for different PSFs. Every upgrade of the system requires a new MC production in order to match the data.

3.5.4 γ/hadron separation and energy estimation

The recorded data are dominated by background coming from CRs and NSB light fluctuations. In order to reject the cosmic background, a discrimination between gamma rays and hadrons is made, known as γ/hadron separation. The γ/hadron separation in MAGIC relies on an algorithm called Random Forest (RF) (Albert et al., 2008a). The RF is an algorithm based on decision trees. It will classify each image left in the cameras, using several image parameters, according to whether it is more likely to have been initiated by a gamma ray or a hadron. In order to be able to classify an event, the RF first has to be trained with events of known nature, i.e., gamma rays from MC simulations and hadrons from real data. The gamma ray and hadron sample must have a similar *size* and zenith distribution as the final data sample, in order to avoid artifacts. The RF uses a set of N parameters to compute a large number of decision trees (typically 100 trees are computed). In order to grow the decision trees, a cut is applied on a randomly-chosen parameter to split the data sample into two sub-samples called branches. The value of the cut is set in order to minimize the Gini index (Gini, 1921), defined as:

$$Q_{Gini} = 4 \cdot \frac{N_\gamma}{N} \cdot \frac{N_{bg}}{N} \tag{3.12}$$

The two resulting branches are then split according to the same algorithm. The process is iterated until a sub-sample is composed only of one of the two initial categories, and the end leaf is labeled as 0 or 1 depending whether it contains gamma ray or hadron events.

The RF is then applied on the data. Each event will go through all the decision trees, and a value will be assigned to the event according to the leaf reached at the end of each tree. The *hadronness*, defined as the average of the obtained values over the N trees is then computed. Values of *hadronness* close to 0 correspond to a gamma-ray-like events whereas values close to 1 correspond to hadron-like events.

The energy reconstruction for stereoscopic observations in MAGIC is made from look up tables (LUTs), relating the event energy to its size and the ratio between the impact parameter and the Cherenkov radius, (Aleksić et al., 2012, 2016a), and are binned according to these two parameters. The LUTs are built by means of MC simulations. The values in the LUTs are the mean and RMS of the the true energy distribution (E_{true}) of simulated gamma-ray events in each bin. The estimated energy (E_{est}) of an event is the weighted average of both telescopes average E_{true}. The average true energy of each telescope is extracted from the LUTs bin to which the event corresponds. In order to correct for a zenith-angle-dependent bias, corrections are applied on the atmospheric absorption. Corrections are also applied to take into account the azimuth dependence due to the geo-magnetic field and improve the reconstruction for large images that are partially contained in the camera. The energy resolution of MAGIC, defined as (E_{est}-E_{true})/E_{true}, is estimated to be 16% above 220 GeV (Aleksić et al., 2016a).

3.5.5 Sensitivity

The integral sensitivity of the MAGIC telescopes is defined as the integrated flux of a source above a given energy for which $N_{ex}/\sqrt{N_{bckg}} = 5$ after 50 hours of effective observation time, where N_{ex} denotes the number of excess events from the source under study and N_{bckg} is the number of background events. Furthermore, in order to gather enough statistics, it is required that $N_{ex} > 10$. The differential sensitivity is defined in the same way, integrating the signal in a given energy bin. The sensitivity is strongly determined by the hardware (mirrors, triggers, readout, etc) and software (image cleaning, parametrization, γ/hadron separation, etc) configurations, and by the type of observations carried out (wobble, ON, zenith angle, moon, etc). The sensitivity of the MAGIC telescopes has been continuously improved by upgrading the different systems. An evolution of the MAGIC integral sensitivity, according to the different upgrades, is shown on Figure 3.14.

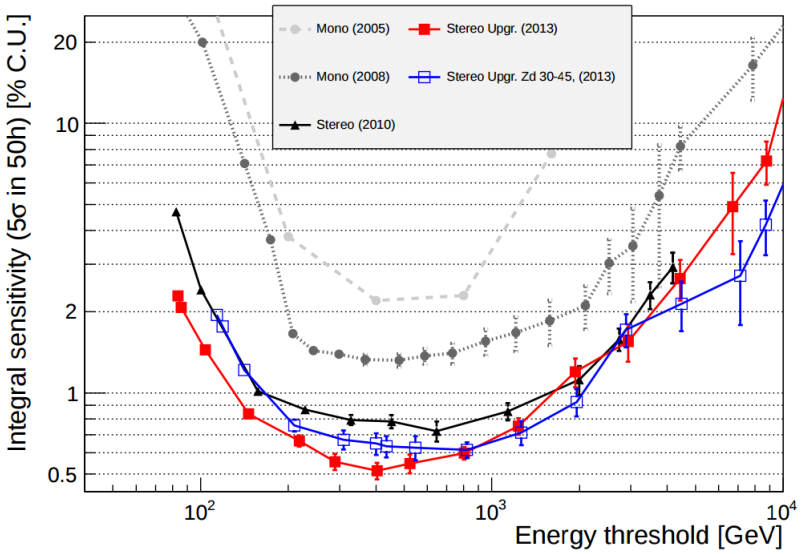

FIGURE 3.14: Evolution of the integral sensitivity of the MAGIC telescopes for different configurations of the system. Dashed-light-circle: MAGIC-1 with Siegen readout. Dashed-dark-circle: MAGIC-1 MUX readout. Black triangles: stereo before upgrade. Squares: stereo after upgrade: zenith angle below 30° (red, filled), 30 - 45 ° (blue, empty). Figure adopted from (Aleksić et al., 2016a).

3.5.6 Source detection and characterization

Once the energy and the nature of the events have been estimated, gamma-ray or hadronic events, the signal from the target source can be sought. In order to claim a detection, several methods are used in MAGIC:

θ^2-plot

The signal strength of the source under study can be estimated by means of the θ^2 distribution. Gamma rays coming from the observed source exhibit a peaked distribution around the value $\theta^2 = 0$, implying that the reconstructed and assumed position of the source in the camera are compatible. The signal region is set by an upper cut in the θ^2 distribution. The number of excess events coming from the source is estimated as $N_{ex} = N_{on} - \alpha N_{off}$, where N_{on} is the number of events coming from the source direction, N_{off} the number of background events estimated from the *wobble partners* (anti-sources) in the camera and α the normalization factor between the ON and OFF observation times. Since MAGIC background events are taken from three *wobble partners*, the ratio is set to 1/3. The signal significance is computed using the Li & Ma method (Li and Ma, 1983), using the number of ON and OFF events that survived the θ^2 cut. The Li & Ma significance is based on the likelihood ratio method, (see Section 4.2.1) and has to be computed with the number of ON and OFF events and the time ratio between the ON and

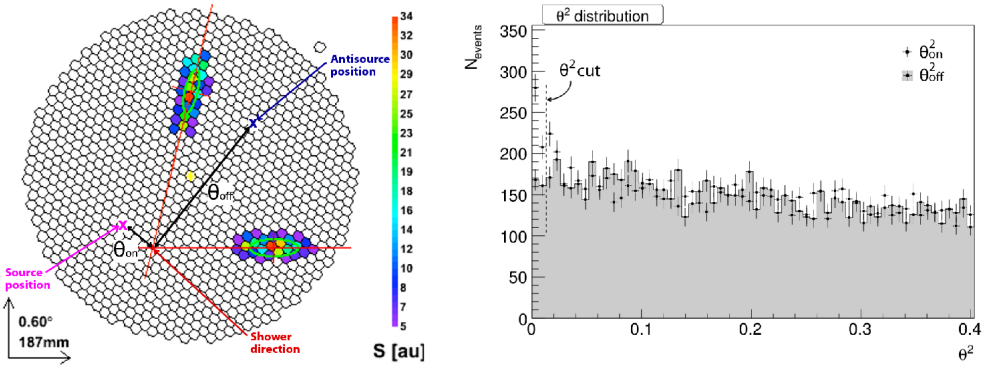

FIGURE 3.15: Signal detection using from the θ^2 distribution. The reconstruction of θ^2 is made for *on* and *off* events (left). The θ^2 distribution is then computed and the significance of the signal obtained (right). Credit: G. Giavitto.)

OFF observations time. The Li & Ma significance is defined as:

$$\sigma = \sqrt{2\left(N_{on}\ln\left[\frac{1+\alpha}{\alpha}\left(\frac{N_{on}}{N_{on}+N_{off}}\right)\right] + N_{off}\ln\left[\alpha\left(\frac{N_{off}}{N_{on}+N_{off}}\right)\right]\right)}, \quad (3.13)$$

The θ^2 method is efficient in order to search for signal. However, no information regarding the shape of the source can be extracted. This information can be obtained by means of the sky map.

Sky maps

The calculation of the incoming direction of the gamma rays allows us to obtain the sky map around the source. The sky map represents the distribution of the gamma-ray excess according to the sky position and is built transforming the reconstructed arrival directions into sky coordinates. In order to compute the excess in every bin of the sky map, the background has to be modeled and corrections of the camera inhomogeneities have to be applied. An example of a Crab Nebula sky map is shown in Figure 3.16.

Spectra

The differential energy spectrum is defined as:

$$E^2\frac{dF}{dE} = E^2\frac{dN_\gamma(E)}{t_{eff}\cdot A_{eff}(E)\cdot dE}, \quad (3.14)$$

where N_γ is the number of detected gamma rays, t_{eff} the observation effective time and A_{eff} the effective are of the instrument. The effective area characterizes the area around the telescopes on which Cherenkov photons light pool can be

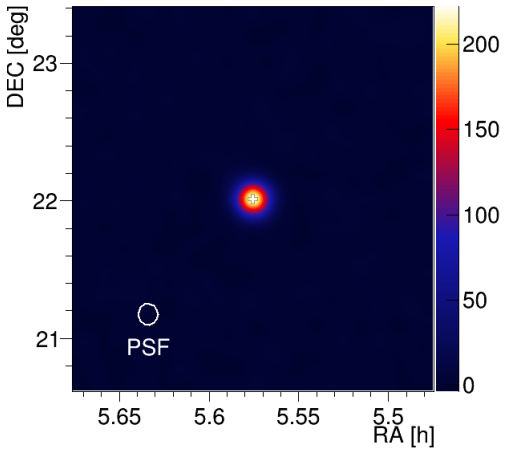

FIGURE 3.16: Sky map of the Crab Nebula.

detected, and is computed from MC simulations. It is defined as

$$A_{eff} = A_{sim} \frac{N_{\gamma,sel}}{N_{\gamma,tot}}, \tag{3.15}$$

where A_{sim} is the total area considered for MC simulations, $N_{\gamma,tot}$ the total number of simulated events and N_{γ} the number of detected γ-rays after all the reconstruction steps (cleaning, stereo reconstruction, γ/hadron separation, etc.).

The spectra of a source is computed using loose cuts for background rejection in order to obtain a better matching between MC and data. The estimation of the effective time, effective area and differential spectrum is computed using *Flute* (FLUx vs. Time and Energy).

3.5.7 Mola

The MAGIC OnLine Analysis is a multi-thread C++ program used to estimate in real time the gamma-ray flux of the source being observed. MOLA runs simultaneously with the DAQ software. Two *reading* threads receive the data stream from the DAQs and start processing the analysis at non-stereo level (calibration, image cleaning, image parametrization, etc). Another analysis thread will match the individual telescopes events and proceed with the stereoscopic analysis. The analysis thread will compute the *hadronness* and θ^2 parameters for each stereo event, and reconstruct its incoming direction. A set of θ^2 plots and sky maps are produced for low and high energies. A real time estimation of the flux is given, in order to detect a source in flaring state and alert other observatories. The estimated sensitivity of MOLA at high energy is $\sim 1.4\%$ of the Crab Nebula in 50 hours observation time.

Unfolding

The obtained spectrum is binned according to the estimated energy of the events. Due to the imperfect estimation of the energy of each event, the reconstructed spectrum may be biased with respect to the true spectrum of the source. In order to recover the original spectrum we use the *unfolding* method (Albert et al., 2007b). The distribution of the estimated energy is affected by the resolution of the telescopes, what can be mathematically expressed as:

$$Y(y) = \int M(x,y)S(x)dx + n(x)dx, \tag{3.16}$$

where Y and S are the measured and true energy distribution, respectively, M the migration matrix, representing the probability of an event with true energy E_{true} to having reconstructed energy E_{est}, and n the noise. The aim of the unfolding is to retrieve the true energy from the measured estimated energy distribution. As the migration matrix is not invertible, a least square minimization, (χ_0^2), is applied. However, this minimization leads to unstable results. The solution to this problem is to add a regularization parameter in the least square regression,

$$\chi^2 = \chi_0^2 + \frac{\tau}{2} Reg, \tag{3.17}$$

where large values of τ correspond to no regularization. Several regularization methods are used in MAGIC: Tikhonov (Tikhonov and Arsenin, 1977), Schmelling (Schmelling, 1994) and Bertero (Bertero, 1989).

Pulsar detection

The search for signals using the θ^2 distributions and sky maps is not really suitable for pulsars due to their faint emission at very high energies. In order to detect VHE gamma-ray emission from pulsars, additional information on the arrival time of each event is required. The photon arrival times are folded using the pulsar ephemeris to characterize their emission with respect to the pulsar period. In order to take into account the Earth's motion during the observations, and correct the shifts in the arrival time of the photons due to this effect, barycenter corrections must first be applied (notice that for the central pixel data one does not need barycenter correction). These corrections consist of transforming the photon arrival times to those which would have been measured at the solar system barycenter, assumed to be an inertial frame with respect to the pulsar. In order to convert the arrival time of the photon on Earth into its arrival time in the solar system barycenter, the following relation is applied,

$$t_b = t_{UTC} + \Delta_{prop} + \Delta_{rel} + \Delta_{UTC}, \tag{3.18}$$

where t_b is the arrival time that would have been measured at the solar system barycenter, t_{UTC} is the measured time on Earth in UTC, Δ_{prop} is the difference

between the time the photon would have needed to travel from the pulsar to the barycenter with respect to the time needed to travel from the pulsar to the observatory, Δ_{rel} represents some general relativistic corrections due to time delay and space time distortion around the sun. The last parameter, Δ_{UTC} represents a change in the time scale. After applying the correction, the event phase at time t is obtained using a Taylor development:

$$\phi = \phi_0 + f_0 \cdot (t - T_0) + \frac{1}{2} f_1 \cdot (t - T_0)^2 + \frac{1}{6} f_2 \cdot (t - T_0)^3, \tag{3.19}$$

where f_0 is the pulsar rotation frequency and f_1 and f_2 are the first and second frequency derivatives, respectively. This approximation is only valid in a small time interval around T_0 due to the timing noise of the pulsar. In the case of the Crab pulsar, the timing noise is handled using monthly updated ephemeris.

Several statistical tests are used to detect the pulsation; the well-known χ^2, which is strongly dependent on the light curve binning, and the Z^2_m (Buccheri et al., 1983) and the H-test (de Jager et al., 1989) which are based on a Fourier decomposition of the signal. In order to compute the signal, signal and background regions are assigned to the pulsar rotation. The signal regions correspond to the peak phase region and the background is estimated from the off-region, where no signal is expected from the pulsar. At VHE, due to the strong background, the Li & Ma method (Li and Ma, 1983) is also used.

Chapter 4

The Fermi Large Area Telescope

The *Fermi Gamma-ray Space Telescope*, hereafter referred to as *Fermi*, was launched on 2008, June 11^{th} and started scientific operations on 2008, August 04^{th}. *Fermi* followed the launch of AGILE by the Italian space agency (Tavani et al., 2008) in April 2007. It embeds two complementary instruments, the *Large Area Telescope* (LAT), observing HE gamma rays from 20 MeV up to 300 GeV (Atwood et al., 2009), and the *Gamma-ray Burst Monitor* (GBM) dedicated to the observation of transient sources from $\sim$ 8 keV up to $\sim$ 40 MeV (Meegan et al., 2009). The purpose of the *Fermi* mission was to understand the mechanism of particles acceleration, in particular in AGN, pulsars and SNR. Furthermore, deep studies are carried out in order to understand the behavior of GRBs and transient sources and to probe dark matter. Among the *Fermi* highlights, one which stands out is the discovery of gamma-ray emission from more than 160 pulsars (Laffon et al., 2015), among which, most was not known before.

4.1 The Large Area Telescope (LAT)

High energy gamma rays cannot be reflected or refracted, so they cannot be simply focused by conventional telescopes. Instead, they are indirectly detected being converted into a $e^{\pm}$ pair. The LAT is therefore a pair conversion telescope. From the electromagnetic shower initiated by the $e^{\pm}$ pair, the LAT can reconstruct the incoming direction of the initiating particle and its energy. To do so, a precision converter-tracker (TKR), in which the shower develops, traces the positions of the charged particles created in the medium, and a calorimeter measures the energy, see Figure 4.9. The LAT is made up of 16 columns, each of them combining a TKR and calorimeter system. The tracker array is covered by an anti-coincidence detector (ACD) sensitive to the charged particles, helping to reject the background of charged CRs. The principal characteristics and performance of the Fermi LAT

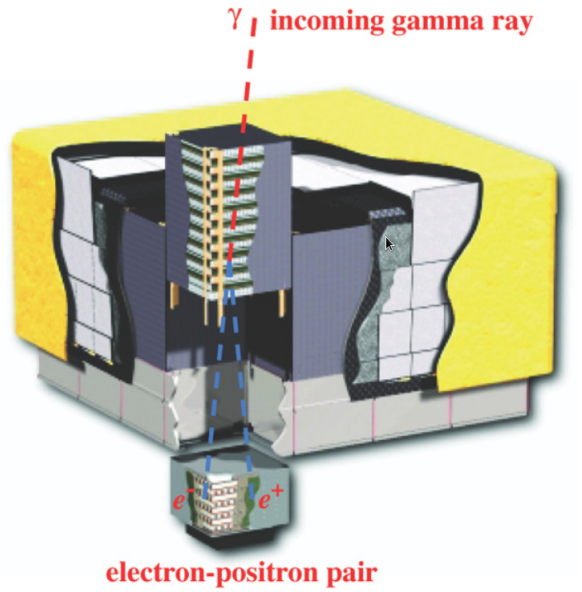

FIGURE 4.1: Lateral view of the TKR and calorimeter of the LAT.

are listed in table 4.1. The *Fermi* satellite orbits the Earth at an altitude of ~ 565 km and an inclination of 25°. In the main observation mode, the so-called "survey mode", after two orbits of three hours, the sky exposure is almost uniform and each part of the sky has been observed for ~ 30 minutes.

Parameter	Value or Range
Energy range	20 MeV - 300 GeV
Effective Area at normal incidence	9,500 cm^2
Energy resolution (equivalent Gaussian 1 σ)	
100 MeV - 1 GeV (on-axis)	9%-15%
1 GeV-10GeV (on-axis)	8%-9%
10 GeV-300GeV (on-axis)	8.5%-18%
>10GeV (>60° incidence)	$\leq$ 6%
Single Photon Angular Resolution	
on-axis, 68% containment radius $\theta_{68\%}$:	
>10GeV	$\leq 0.15°$
1 GeV	0.6°
100MeV	3.5°
on-axis, 95% containment radius:	$3 \times \theta_{68\%}$
off-axis, containment radius at 55°	1.7× on-axis value
Field of View (FoV)	2.4 sr
Timing accuracy	<10 μs
Event read-out time (dead time)	26.5μs

TABLE 4.1: Summary of LAT Instrument Parameters and Estimated Performance.

After the development of the shower within the TKR, the calorimeter is used to reconstruct the energy of the incoming particles. The subsystems, together with the ACD which helps to reject the background due to charged CRs, are coupled to the data acquisition system (DAQ) before the down-link of the data to Earth. Each of these subsystems will be described in the following sections. More detailed information can be found in (W. B. Atwood, et al , 2009).

4.1.1 The Converter-tracker

The TKR constitutes the highest part of each of the 16 towers, being the main detector part. It contains 16 planes of high-Z material (Tungsten) to favor the conversion of gamma rays into $e^{\pm}$ pairs. The converter planes are interleaved with position sensitive detectors that record the passage of the charged particles, measuring their trajectory. This information is used to reconstruct the direction of the incident gamma rays. Each tracker module has 18 (x, y) tracking planes, consisting of two layers (x and y) of single-side silicon detectors (see figure 4.2). The last two tracking planes are not coupled to converter material as an event has to deposit energy in at least three of the planes to be triggered.

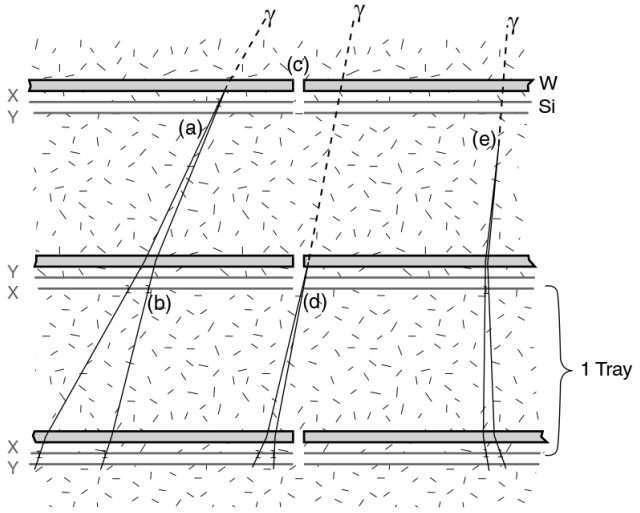

FIGURE 4.2: Side view of the converter-tracker.

Due to multiple scattering inside the tracker, the angular resolution of the telescope is limited. To get an optimal resolution, the electrons and positrons have to be measured directly after the conversion. At 100 MeV the penalty for missing one of the hits results in a worsening of the angular resolution by a factor 2. One trade-off that had to be considered in the LAT design was the balance between a good PSF at low energy, requiring thin converter material, and high effective area, important at high energies, requiring thick converter material. Therefore, the TKR was divided in two parts; front and back. The front part (first 12 planes)

consists of thin converter layers, each of 0.03 radiation lengths to optimize the PSF at low energies, while the back part (4 layers after the front tracker section) has converter layers ∼6 times thicker than the front part, in order to maximize the effective area, resulting in a worsening of the angular resolution by a factor ∼2.

4.1.2 The Calorimeter

The purpose of the calorimeter (CAL) is twofold: it measures the deposition of energy from the electrons and positrons created by the incident photon and it images the shower development, resulting in a powerful tool for background rejection. The calorimeter modules are located at the bottom of each tower of the LAT. Each module is made up of 96 CsI crystals which are optically isolated from each other and arranged horizontally in 8 layers of 12 crystals, as can be seen in Figure 4.3. The total vertical depth of the calorimeter is 8.6 radiation lengths, and the total instrument is 10.1 radiation lengths. Each module layer of the calorimeter is oriented 90° with respect to its neighbors. Photo-diodes are located at both ends of each crystal to measure the scintillation light that is transmitted to each end. The difference in light between both ends provide a determination of the energy deposition in the crystal. Two photo-diodes are mounted at each end; a big one that measures low energy (2 MeV - 1.6 GeV) and a small one that measures high energy (100 MeV - 70 GeV). The position resolution scales with the deposited energy and ranges from a few millimeters for low energy depositions (∼ 10 MeV) to a fraction of a millimeter for large energy depositions (≥ 1 GeV)

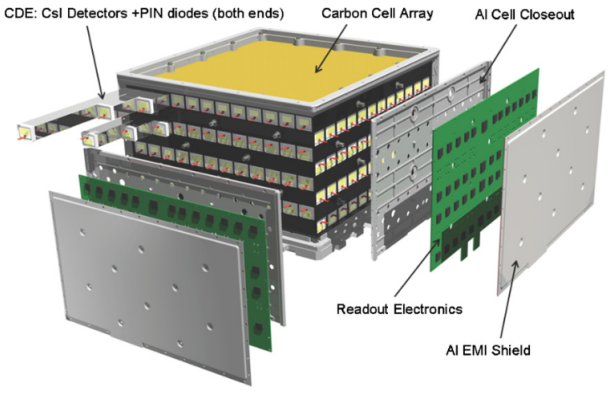

FIGURE 4.3: Exploded view of the calorimeter with the 8 layers of 12 crystals. Figure adopted from (W. B. Atwood, et al , 2009).

4.1.3 The Anticoincidence detector

The purpose of the anticoincidence detector (ACD) is to provide a charged-particle background rejection. The ACD was designed to reject 99.97 % of charged particles. It is made up of 89 plastic scintillator tiles 1 cm thick, scintillating at the passage of charged particles. If there is no signal from the ACD associated with a reconstructed direction of a shower, the event is interpreted as a photon. If there is a signal from the ACD associated with the reconstructed direction of the shower, it means that the shower was initiated by a charged particle and the event is rejected. Finally, if there is a time coincidence between a shower and the ACD, but the signal is not consistent with the reconstructed direction of the shower, it corresponds to a back-splash. Back-splashes happen when secondary particles are up-scattered by Compton process and then create false signal. In order to reduce the back-splash effect, the ACD is segmented and only the segments in the direction of the incident candidate photon are considered. This effect was a main problem in EGRET, reducing its sensitivity at high energies.

4.1.4 The Data Acquisition System (DAQ)

The Data Acquisition system (DAQ) collects data from the subsystems described in the previous section, triggers the events according to certain given rules, and provides an on-board event processing to reduce the event rate from 2-4 KHz down to $\sim$ 400 Hz, to down-link them to Earth. Furthermore, an on-board analysis is processed in order to rapidly search for transients. The events are processed as follows:

- At the lowest level, each of the 16 Towers Electronics Modules (TEMs) provides the interface to the tracker and calorimeter pair in one of the towers.
- A primitive trigger is generated based on the combination of the tower subsystems (tracker and calorimeter).
- The TEMs then communicate with the Event Builder Module (EBM) which is a part of the Global-trigger/ACD-module/Signal distribution Unit (GASU).
- The GASU consists of:
  - a Command Response Unit (CRU) that distributes the DAQ clock signal;
  - the ACD Electronics Module (AEM), which has a role similar to the TEMs for the ACD;
  - the Global-Trigger Electronics Module (GEM) that generates readout decision based on the TEMs and ACD;

  - and the EBM that builds response events out of the information from the TEMs and AEM;

- The events built by the EMB are sent to the Events Processor Units (EPU). There are two EPUs to support on-board processing, filtering the events to reduce the event rate from 2-4 kHz down to $\sim$ 400 Hz, before down-linking them to be processed on the ground.

- The control interface of the spacecraft is contained in the Spacecraft Interface Unit, that also controls the LAT.

A general view of the DAQ subsystems can be seen on figure 4.4.

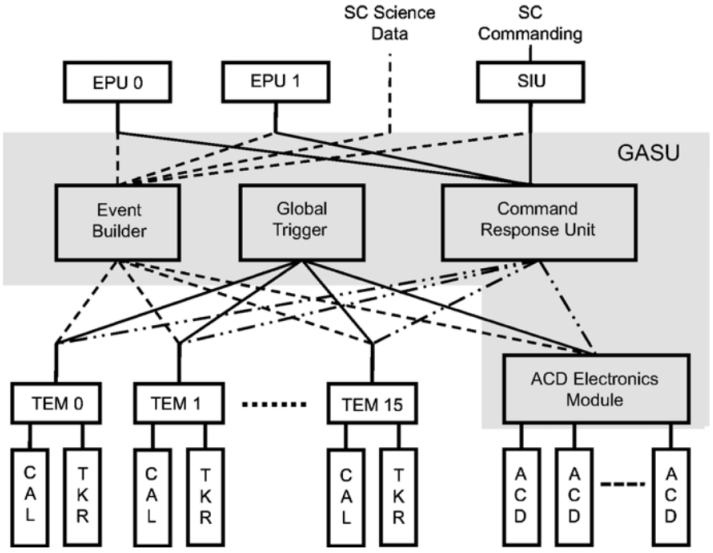

FIGURE 4.4: LAT Data Acquisition System. The GASU consists of the TEMs, the EBM the ACD and the CRU. The TEMs support the readout and the trigger of the 16 towers made from the tracker and calorimeter. There are two EPUs and one primary SIU. Figure adopted from (W. B. Atwood, et al , 2009).

4.1.5 The Instrument Response Functions

The performance of the LAT is determined by its technical characteristics along with the algorithms used for the selection and reconstruction of the events. The Instrument Response Functions (IRFs), that depend on the class of events studied, characterize the performance of the LAT in term of:

- The effective area, characterizing the "useful" area of the detector, which is smaller than the physical detector area.

- The PSF or angular resolution, which characterizes the precision of the incident photon direction reconstruction.
- The energy resolution, which defines the accuracy of the reconstructed energy of an event.

The IRFs depend on two parameters; the energy of the incident photon and the incident angle. A set of IRFs is developed for the front and back parts of the detector and for the whole detector.

Prior to launch, the LAT team relied on beam tests and Monte Carlo simulations of gamma rays interactions with the LAT to characterize the performance and calculate the IRFs. After launch of the telescope, the real flight revealed unexpected features that had to be corrected. Several updates to the IRFs have been made since the start of the mission which led to two majors releases; `Pass 6` and `Pass 7`. At the moment of writing this thesis, the `Pass 8` IRFs have just been released, however, the data analysis presented in this thesis relies on the `Pass 7` IRFs. For a given set of IRFs, several classes of event selection can be chosen depending on the kind of source analyzed. Four classes are available for the Pass 7 IRFs (Ackermann et al., 2012b):

- `Pass7TRANSIENT` with loose cuts and a remaining background rate of few Hz, designed for the analysis of transient sources with small time observation windows.
- `Pass7SOURCE` designed for the analysis of point-like sources. This class has a lower background rate than the `Pass7TRANSIENT` in order to conserve a high enough signal-to-background ratio.
- `Pass7CLEAN` and `Pass7ULTRACLEAN` are designed for the study of Galactic diffuse sources and extragalactic diffuse sources, respectively. The `Pass7CLEAN` reduces the background to ~ 0.1 Hz. The `Pass7ULTRACLEAN` class provides a residual contamination 40% lower than the `Pass7CLEAN` class around 100 MeV. The residuals become similar for both class as the energy increase and become the same at 10 GeV.

Figure 4.5, shows the evolution of the IRFs of the LAT for front, back and the whole detector for the `P7SOURCE` class.

4.1.6 LAT sensitivity

The sensitivity of an instrument can be defined as the minimal flux that can be detected at 5 σ level. It depends on the observation time, the energy and

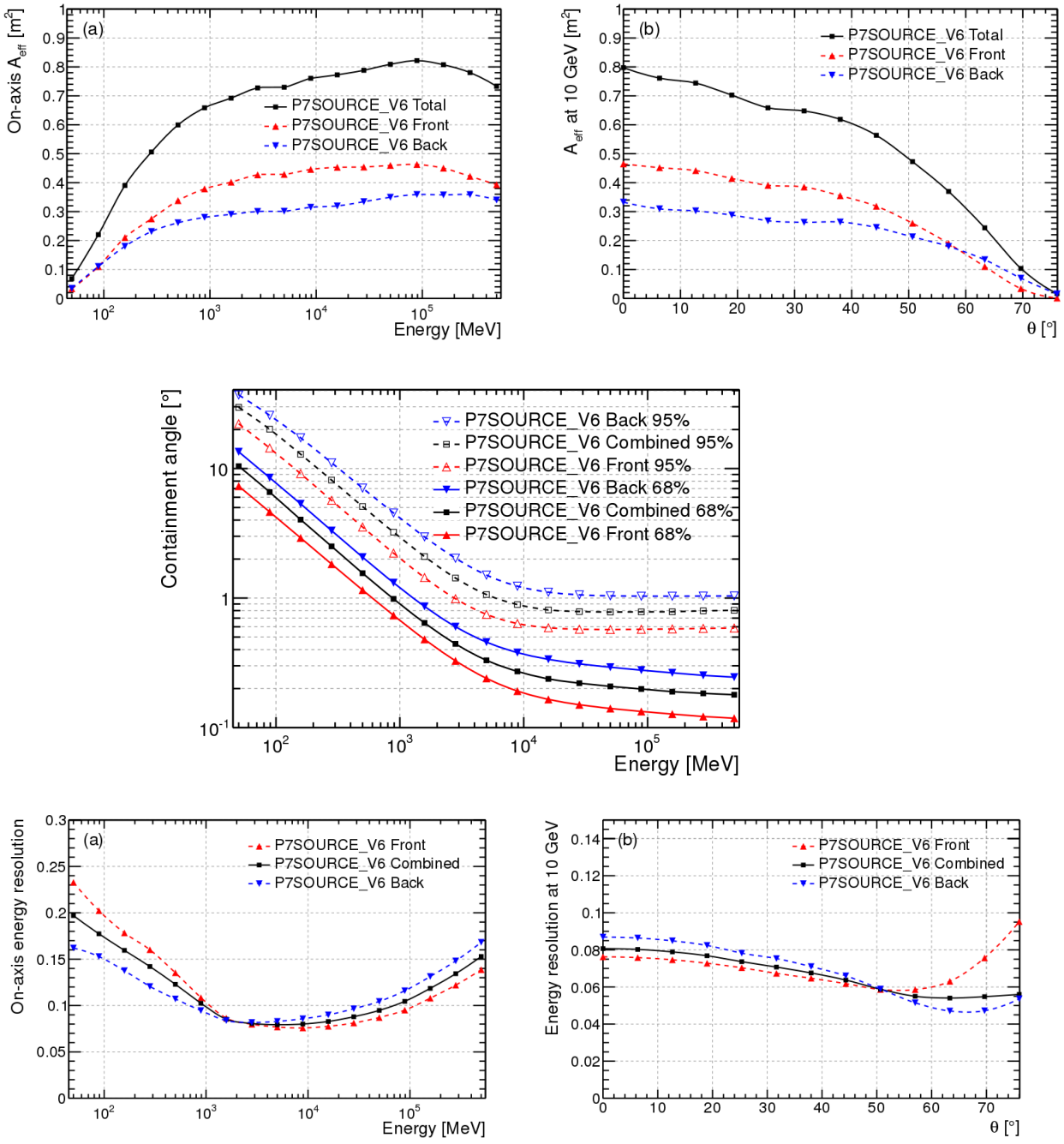

FIGURE 4.5: IRFs of the LAT using the Pass 7 classification for *FRONT* events (red), *BACK* (blue) and the combination of both (black). *Top:* evolution of the effective area depending on the energy (left) and the angle of incidence θ (right). *Middle:* variation of the PSF for a 68% confidence level (full line) and 95% confidence level (dashed). *Bottom:* evolution of the energy resolution with the energy (left) and incidence angle θ (right). Figure adopted from (W. B. Atwood, et al , 2009).

the spectral shape of the source. The sensitivity depends also strongly on the position in the sky as the background is not homogeneous. A faint source will

be more difficult and will require more time to be detected if it is located in the Galactic plane, than if it is located at higher latitude. These inhomogeneities of the sensitivity depending on the sky position are shown in Figure 4.6. The integral sensitivity was calculated for a point-like source, using the `PASS7` IRFs and assuming a power-law spectrum with a spectral index $\alpha = -2$, integrated over a period of 3 years in the scanning mode. The Figure 4.7 shows the differential sensitivity for several positions in the sky.

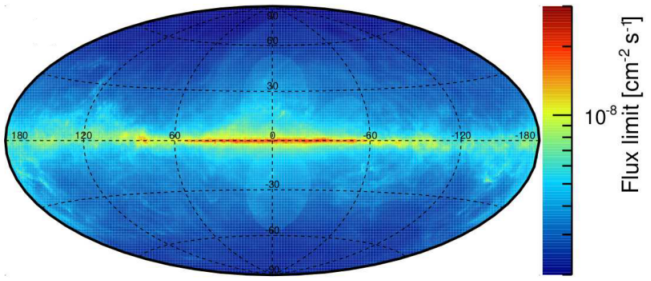

FIGURE 4.6: Sensitivity above 100 MeV for the P7SOURCE_V6 event class for a point source with a power-law spectrum with index $\alpha = -2$.

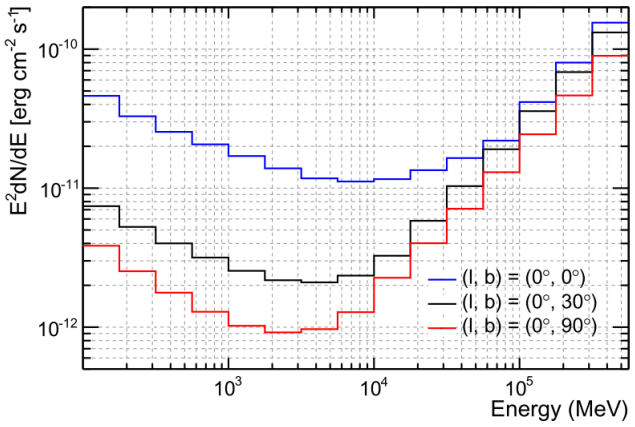

FIGURE 4.7: Differential sensitivity computed for a 3-years exposure. The sensitivity is calculated for several pointing direction; toward the galactic pole(red), intermediate latitude (black) and galactic place (blue). Figure adopted from (W. B. Atwood, et al , 2009).

4.2 Fermi analysis chain and the Fermi Science Tools

The Fermi Science Support Center (FSSC) in collaboration with the LAT collaboration, developed a complete set of analysis chain tools [1] in order to analyze *Fermi* data. The tools package, known as the Fermi Science Tools, gathers programs and macros based on Python, C++ and ROOT. Besides these programs, the IRFs that characterize the telescope performance and features are directly embedded in the package.

In this part, I briefly introduce the maximum likelihood method, which forms the basis for most *Fermi* LAT analysis, and also describe the different programs used in this thesis.

4.2.1 The Maximum Likelihood

One of the principles of the LAT analysis chain relies on the maximum Likelihood ratio method. This method aims to adjust a model describing the spectral and spatial properties of the source of interest and the surrounding sources to the observations, as described in Section 4.2.5 . The likelihood characterizes the paramter value most likely to have yielded the observed data, and is estimated comparing the number of observed events with the number of expected events from the model. In the maximum Likelihood approach, the likelihood is maximized in order to obtain the most reliable model possible.

Suppose a random vector $\vec{N}$ with random variables admitting a probability density function (PDF) which is parametrized by a vector $\vec{\lambda}$. We can express the PDF, $f_{\vec{N}}(\vec{n}, \vec{\lambda})$, which gives the probability to measure $\vec{n}$. Seen in this way, the parametrization $\vec{\lambda}$ is set and the PDF is a function of $\vec{n}$. On the other hand, if we have performed the experiment and obtained a given $\vec{n}$, we can interpret $f_{\vec{N}}(\vec{n}, \vec{\lambda})$ as a function of $\vec{\lambda}$. Thus, the PDF characterizes the parameter values most likely to have yielded the observed $\vec{n}$. When seen this way, as a function of the parameters, the PDF is called Likelihood and it is noted $\mathcal{L}(\vec{\lambda}, \vec{n})$.

As previously seen, the events rate depends on the IRFs used. Thus, in order to compute the number of expected events from the model, we first have to fold the model using the LAT IRFs. We can estimate the rate of detected events for a

[1] The Fermi Science Tools can be downloaded at http://fermi.gsfc.nasa.gov/ssc/data/analysis/software/

given source from the model by:

$$r(E', \vec{\Omega}', t'; \vec{\lambda}) = \int d\Omega \mathcal{F}(E', \vec{\Omega}', t'; \vec{\lambda}) A[E', \cos\theta(t')] e(E', t') f_{psf}[\vec{\Omega}'; \vec{\Omega}, \cos\theta(t'), E'] \tag{4.1}$$

for a diffuse source, and

$$r(E', \vec{\Omega}', t'; \vec{\lambda}, \vec{\Omega}_0) = \mathcal{F}(E', t'; \vec{\lambda}) A[E', \cos\theta(t)] e(E', t') f_{psf}[\vec{\Omega}'; \vec{\Omega}_0, \cos\theta(t), E'] \tag{4.2}$$

for a point-like source. The $\mathcal{F}$ parameter represents the flux of the source, $\vec{\Omega}$ the direction of the source in the sky, $A[E', \cos\theta(t')]$ characterizes the energy dispersion, $e(E', t')$ the effective area and $f_{psf}[\vec{\Omega}'; \vec{\Omega}_0, \cos\theta(t), E']$ the PSF. The angle $\theta(t)$ is defined as the angle between the photon momentum vector and the z-axis in the spacecraft frame.

The observed photons are binned according to the observed quantities, particularly energy and sky directions. At this step of the analysis, two likelihood methods can be chosen: the unbinned and binned analysis. The unbinned analysis requires a binning for each parameter such that the bins are small enough contain either 1 or 0 events. This way, there is no loss of information from the photons during the data processing. However, it requires big computing resources and time and is only used for the analysis of data collected over a small amout of time such as GRBs analysis. The other method, the binned analysis, makes use of larger bins and averages the values of the photons characteristics inside the bin. With this method the computing resources required are less demanding, but some information is loss due to the average of photons within a bin. The binned analysis is the one used in this thesis.

The number of observed counts, N_i, in a given bin i will be an element of $\vec{N}$. Each element of $\vec{N}$ is distributed according to a Poisson distribution with a mean value, r_i, determined from the model. The Poisson distribution is defined as:

$$p(N; r) = \frac{r^N}{N!} \exp(-r) \tag{4.3}$$

The mean will be modeled integrating either Eq. 4.1 (diffuse sources) or Eq. 4.2 (point-like sources) over the bin. As the components of $\vec{N}$, N_i, are statistically independent (Kerr, 2010), the likelihood function can be expressed as the product of the Poisson distributions in each bin, and can thus be written as:

$$\mathcal{L} = \prod_{i=1}^{Nbins} \frac{r_i^{N_i}}{N_i!} \exp(-r_i) \tag{4.4}$$

Due to the broad PSF of the LAT and the strong diffuse background, the number of counts in a given bin involves contribution from several sources. Furthermore, in

order to maximize the likelihood we take the logarithm that will simplify the equation turning products into sums. As the logarithm is a continuous and monotonous function, the function $\log(\mathcal{L})$ maximizes for the same values as the function $\mathcal{L}$. We can thus rewrite the likelihood, taking the logarithm and summing over all the bins and sources, as:

$$\log \mathcal{L}(\vec{\lambda}, \vec{N}) = \sum_{i=1}^{N_{bins}} \left[- \iiint_{bin_i} \sum_{j=1}^{Ns} r_j(E', \vec{\Omega}', t'; \vec{\lambda}_j) + N_i \log \sum_{j=1}^{Ns} \iiint_{bin} r_j(E', \vec{\Omega}', t'; \vec{\lambda}_j) \right] \quad (4.5)$$

$$= \sum_{i=1}^{N_{bins}} \left[- \sum_{j=1}^{Ns} R_{ij} + N_i \log \sum_{j=1}^{Ns} R_{ij} \right], \quad (4.6)$$

where the triple integral is over the energy, position and time and N_s is the number of sources in the ROI. The term $N!$ is discarded from the equation since it is independent of the parameters of the model. In the second line, the term R_{ij} is the number of expected counts in the i^{th} bin for the j^{th} source. We can see that the likelihood only depends on the number of observed events, N_i, and the number of events expected from the model, R_{ij}.

The bins considered for the analysis are continuous, and the ROI around the source of interest containing the whole data is selected. The likelihood can then be written:

$$\log \mathcal{L}(\vec{\lambda}, \vec{N}) = - \iiint_{ROI} \sum_{j=1}^{N_s} r_j(E', \vec{\Omega}', t'; \vec{\lambda}_j) + \sum_{i}^{N_{bins}} N_i \log \sum_{j=1}^{Ns} R_{ij} \quad (4.7)$$

As previously said, for the unbinned likelihood the number of events in each bin is either 0 or 1, thus, $N_i = 0; 1$ The unbinned likelihood is thus given by:

$$\log \mathcal{L}(\vec{\lambda}, \vec{N}) = - \iiint_{ROI} \sum_{j=1}^{N_s} r_j(E', \vec{\Omega}', t'; \vec{\lambda}_j) + \sum_{i=1}^{N_{events}} \log \sum_{j=1}^{Ns} r_j(E'_i, \vec{\Omega}', t'_i, \vec{\lambda}_j). \quad (4.8)$$

The obtained value of the log-likelihood is then maximized to obtain the most consistent model parameters according to the data.

4.2.2 The likelihood ratio and the source significance

Once the model is established, after the likelihood maximization, the likelihood ratio is computed by comparing the likelihood value of the null hypothesis (there is no source) to the likelihood of an alternative hypothesis (there is a source with some position/spectrum). The likelihood ratio is a test statistic (TS), rejecting the

null hypothesis if the TS exceeds some threshold. The likelihood ratio is defined as:

$$\lambda = \frac{\mathcal{L}_{max,0}(\vec{N}; \tilde{\theta}_1, \tilde{\theta}_2, ..., \tilde{\theta}_p)}{\mathcal{L}_{max,1}(\vec{N}; \tilde{\theta}'_1, \tilde{\theta}'_2, ..., \tilde{\theta}'_n)}, \tag{4.9}$$

where $\mathcal{L}_{max,0}$ and $\mathcal{L}_{max,1}$ are the maximized likelihood for the null hypothesis and alternative hypothesis, respectively. The TS value is defined as

$$TS = -2(\ln \mathcal{L}_{max,0} - \ln \mathcal{L}_{max,1}) = -2 \ln \lambda \tag{4.10}$$

The significance can be obtained from the TS value using the Wilks' theorem (Wilks, 1938). The Wilks' theorem says that if a population of variables $\vec{N}$ is distributed according to a probability distribution function $f(\vec{N}; \theta_1, \theta_2, ..., \theta_p)$ with a set of $\tilde{\theta}_i$ that maximizes the PDF and considering a large sample, then, the likelihood ratio, λ, asymptotically behaves as a χ^2 distribution, with $p-n$ degrees of freedom (where p is the number of degrees of freedom of the alternative hypothesis and n is the number of degrees of freedom of the null hypothesis). However, the Wilks' theorem is not applicable to our study as it says that the parameters cannot reach their limits, which is the case when computing the likelihood for the null hypothesis. As both hypotheses have to be nested to compute the likelihood ratio, the null hypothesis is computed setting the normalization factor of the source of interest to 0. The normalization factor is a positive parameter, setting it to 0 reaches the limit of the parameter. Fortunately, an extension of the Wilks' theorem proposed by Chernoff (Chernoff, 1954) allows us to set the parameter at its limit. Thus, the significance can be computed thanks to the fact that the TS value behaves as a χ^2 distribution with $p - n$ degrees of freedom.

4.2.3 The LAT data

The *Fermi* LAT data analysis is processed from files, provided by the LAT collaboration, in FITS format. In order to send a request to download the file for the analysis, the user has to provide several pieces of informations regarding the data required:

- The name of the source;
- The region of interest (ROI), which is the angular extension wanted around the source, set in degrees. Due to the large LAT PSF at low energies, the ROI has to be chosen sufficiently large to take into account photons emitted by the source that could come from a large angular distance from the source, as well as neighboring sources that would emit photons appearing to come from the direction of the source.

- The time interval, specified in Gregorian calendar, modified Julian date, or the so-called Mission Elapsed Time (MET). The latter is the number of seconds since the reference time of January 1, 2001, at 00h:00m:00s in the Coordinated Universal Time (UTC) system;
- The energy range;

Two kinds of files are downloaded. The first kind contains a list of the events triggered by the different subsystems of the DAQ. It is called photon file or "FT1 file" and contains the energy, incoming direction, time of arrival and the kind of event associated. The FT1 file is often split into several files depending on the observation time requested. The second kind of file is the spacecraft file or "FT2 file". It contains information relative to the spacecraft position, orientation and operating mode when the spacecraft is active. The the quantities are given in 30-s intervals. An overview of the Fermi tools [2] programs is shown on Figure 4.8.

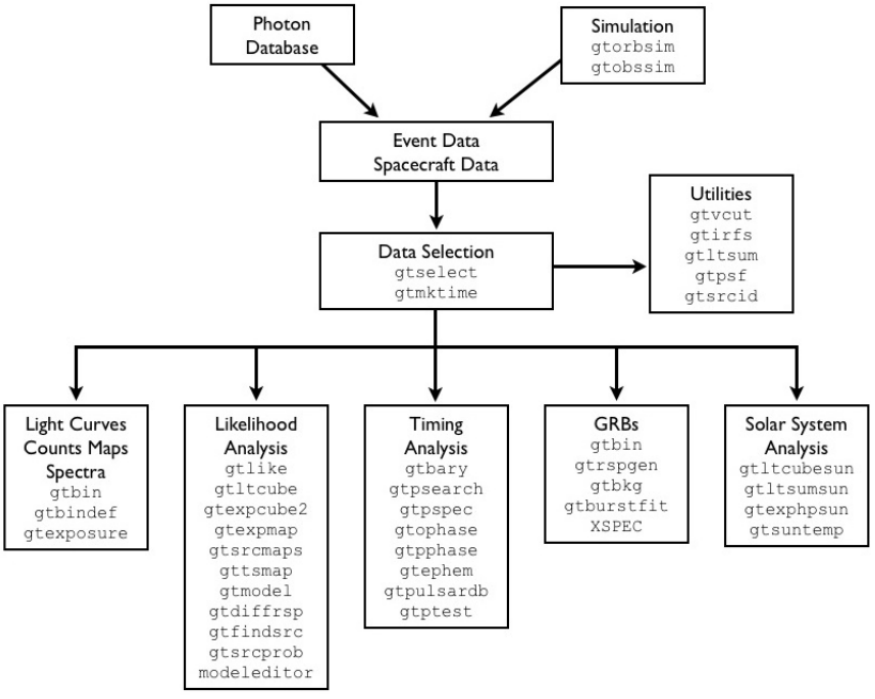

FIGURE 4.8: Overview of the LAT analysis chain using the *Fermi* Sciences Tools[2].

4.2.4 Data selection

The first step of the analysis consists of the event selection. The tool used for this task is *gtselect*. It allows us to have a more precise selection of the events

[2]http://fermi.gsfc.nasa.gov/ssc/data/analysis/scitools/overview.html

we want. As suggested by the Fermi Science Support Center (FSSC), we will select events having a zenith angle below 100° to avoid photons arising from the interaction between cosmic rays and the Earth's limb. Also, events that are not recorded when the LAT was not in nominal science operation or the spacecraft rocking angle exceeded 52° were discarded. We can here redefine the cuts in energy and reset the ROI with a smaller extension than the one set for the download of the data. Cuts on other parameters can be applied such as on the arrival time of photons which is done for pulsar analysis. After the selection step, a filter is applied on the good time intervals (GTI), according to some set parameters. A GTI is a time interval in which the data can be considered valid. The *gtmktime* tool filters the GTIs and excludes time periods when some spacecraft events have affected the quality of the data, or the satellite was not working in data taking mode.

4.2.5 Source model

The study of a region of the sky requires a model that describes all the sources in that region. The model includes the source of interest, the surrounding sources, the Galactic diffuse emission and the isotropic extragalactic diffuse emission. Each source in the model is characterized by its spectral emission and its position in the sky. The parameters of the source of interest are left free to fit them to the data. For the analysis processed in this thesis, the surrounding sources located at less than 10° from the source of interest and with a TS value greater than 25, are set with only the normalization factor free. We only set the normalization factor free, since the fit struggles converging if too many parameters are left free. The Galactic and extragalactic background are also left with the normalization factor free. The sources with a TS value < 2 are discarded. For all the remaining sources, their parameters are fixed to their 3FGL catalog values.

The models used in this thesis are based on the *Fermi* LAT Third Sources Catalog (3FGL) catalog (Acero et al., 2015). This catalog includes 3033 sources above 4σ with 25 extended sources. The model is built using a macro in python, namely, *make3FGLxml.py*, provided by the FSSC, and returns an XML file containing the different sources with their positions and spectral shape. Two spectral shapes are used in this thesis:

Power law

$$\frac{dN}{dE} = N_0 \left(\frac{E}{E_0}\right)^{-\alpha} \tag{4.11}$$

with N_0 the normalization factor, E_0 the energy scale and α the index.

Power-law with exponential cut-off

$$\frac{dN}{dE} = N_0 \left(\frac{E}{E_0}\right)^{-\alpha} \exp(-(E/E_c)^b) \tag{4.12}$$

with E_c the energy cut-off. The b parameter represents the hardness of the cut-off. If $b = 1$ the cut-off is said to be exponential, if $b < 1$ then the cut-off is smoother and it is dubbed sub-exponential. On the other hand, if $b > 1$, then the cut-off is harder and the function represents a power-law with a super-exponential cut-off.

4.2.6 Livetime and exposure calculation

The data input for the binned likelihood method is a three dimensional counts map with one energy axis and two spatial axes, called a counts cube or *CCUBE*. The cube is computed using the *gtbin* tool. The binning of the cube has to be chosen in order to take into account quick variations of the effective area. If the bins are too wide the analysis will not be sensitive to such variations. A sampling of the sky with 0.2° per bin together with ten logarithmically spaced bins per decade in energy is a recommended choice. The binning applied for the cube computation determines the one that must be used for the exposure calculation. The maps resulting in the computed cube are squared, whereas the photons, in the files from the LAT, are distributed over a circular area centered on the source of interest with a radius equal to the ROI. In order to optimize the size of the square used to compute the cube without losing information, we have to take a square that fits on the edge of the circle, see Figure 4.9. If the square is too big, some dark corners will appear and the exposition map will be badly computed. Thus, to take advantage of the largest surface, one takes a square with edge $s = r\sqrt{2}$, with s the edge of the square and r the radius of ROI.

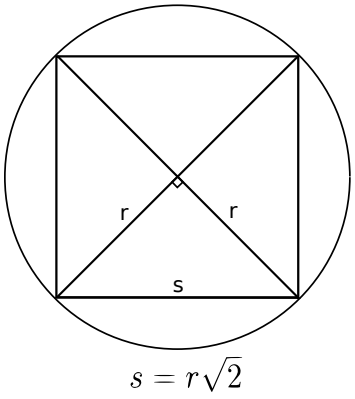

FIGURE 4.9: Fit of the cube used to bin the data into the ROI

The next step in the data preparation is to compute the exposure time using the *gtltcube* tool. The effective area of the telescope and the number of events detected for a source depend on the inclination angle (the angle between the source direction and the instrument z-axis). Thus, the number of photons collected from a source depends on the position of the source in the field of view of the telescope and on how much time the source spends at different inclination angles over the course of an observation. The *gtltcube* tool computes the livetime as a function of the inclination angle and the sky position for a given observation period.

The livetime previously calculated has now to be applied to the data in the ROI. This step is done using *gtexpcube2*. This tool will generate a binned exposure map from the *CCUBE* and the livetime cube. As the PSF of the LAT is large at low energies, sources outside the region analyzed can affect sources inside that region. To take into account these sources, we include all the sources up to 10° outside of the ROI. As the same effect can happen on these sources, we expanded another 10° the region for the calculation of the exposure map. This step is the first that takes into account the IRFs. Finally, the last step before the likelihood computation is to convolve the model describing the sources inside the ROI with the IRFs. This step is done with *gtsrcmaps*. The program takes as input the XML source model, the livetime cube, the *CCUBE* and the exposure map. It will create a cube model containing the expected number of counts for each energy range.

Finally, the fit of the parameters left free in the model is made using *gtlike*. This tool is based on the maximum likelihood method, see Section 4.2.1, and has to be provided with the livetime, the exposure map, the source maps generated with *gtsrcmaps*, the XML model and the set of IRFs required. The program produces, after minimization, an XML file with the estimated parameters for all the sources. Several results regarding the source of interest such as the TS value, the integrated flux, the expected number of photons, etc, can be obtained.

The *gtlike* tool only computes the flux and returns the analytic functions describing the flux of the sources. In order to obtain the Spectral Energy Distribution (SED), we first compute the parameters of the model using the *gtlike* tool for the full energy range. A second fit will then be computed in each energy bin. The energy bins are the same as defined for the *CCUBE* calculation. In each bin, the flux will be assumed to be a power law. The normalization factor of the source of interest is extracted from the function previously computed over the whole energy range, and only the normalization factor and the power-law index of the source of interest are left free. All the other parameters are fixed to the values previously computed. The resulting normalization factor is taken as the flux level in the given energy bin.

4.3 Pulsar studies with Fermi

Before the launch of the Large Area Telescope (LAT) on board the *Fermi* satellite, only 7 gamma-ray pulsars were detected with a high confidence by the telescopes on board the Compton Gamma-Ray Observatory (CGRO), namely, *COMPTEL* (Ryan, 1989) and *EGRET* (Radecke and Kanbach, 1992). After more than six years of observations of the gamma-ray sky with the *Fermi* satellite, the number of detected gamma-ray pulsars, at the moment this thesis is being written, has increased up to 163 (Laffon et al., 2015). The LAT uses different methods in order to search for pulsars (Abdo et al., 2013). The first one, which is the same as done in VHE searches, is to observe pulsars discovered in radio and X-ray. All the known radio pulsars are in principle able to emit gamma rays, though, young pulsars with a high spin down luminosity, $\dot{E} > 1 \times 10^{34}$erg s^{-1}, are the most likely to emit gamma-ray photons (Thompson, 2008). Phase folding with a radio or X-ray ephemeris is the most sensitive way to detect pulsars as there are not penalties due to the number of trials in position, P, $\dot{P}$ or other parameters.

The second method is the so-called *Blind Periodicity Search*, that relies on periodicity searches on selected targets. Some targets are sources known at other wavelengths, that are suspected to harbor a pulsar. These sources are SNR, PWNe, central compact objects (CCOs), unidentified TeV sources and other HE sources mostly located along the Galactic plane. On top of that, an increasing number of gamma-ray sources are discovered and characterized but are not associated to previously known objects. These sources are ranked according to their probabilities of being a pulsar, such as variability and presence of an exponential cut-off in the few GeV band. The sensitivity of this method depends on the rotation frequency, the energy, the pulsed fraction level, the level of background, the events extraction parameters and the position used to barycenter the data. The blind searches, due to the wide pulsar parameter space that must be searched and, due to the sparseness of the photons, are very challenging. They require long integration times (months, years) making the computation of the Fast Fourier Transfrom prohibitively expensive. New semi-coherent techniques have been successful at discovering gamma-ray pulsars with modest computational requirement (Atwood et al., 2006; Abdo et al., 2009b).

The third method is based on the search of radio pulsations in the unassociated *Fermi*-LAT objects. When a pulsation is found in radio, the gamma-ray data can be folded using the corresponding radio, as done in the first method described. Radio pulsar searches are sensitive to binary systems, with the application of techniques to correct the orbital acceleration in data sets much shorter than a binary period (Ransom et al., 2002). This allows for the discovery of MilliSecond Pulsars (MSPs), which are almost inaccessible to gamma-ray blind searches. The

second *Fermi* LAT catalog of gamma-ray pulsars reported the detection of 43 MSPs, using this technique.

Chapter 5

Study of the Crab pulsar at very high energies

The Crab pulsar, PSR B0531+21 or NP 0532, and its surrounding nebula (also know as M1) are the remnant of the supernova of 1054 AD reported by Chinese astronomers (Lundmark, 1921; Duyvendak, 1942). Its age is therefore 961 years. The Crab Nebula was the first VHE gamma-ray source ever detected by an IACT, by Whipple (Weekes et al., 1989), and has been the subject of detailed studies by all subsequent Cherenkov observatories (Krennrich et al., 1993; Smith et al., 2000; Aharonian et al., 2006c; Albert et al., 2008b; Celik, 2008). The non-thermal emission of the Crab Nebula is due to high energy electrons and positrons which emit via synchrotron process and IC scattering (Aharonian, 2004; Abdo et al., 2010). The nebula is fed by the wind of ultra relativistic electrons and positrons injected by the pulsar placed at nebula center.

The Crab pulsar has a spin-down luminosity of $\dot{E} = 4.6 \times 10^{38}$ erg s^{-1} and is located at a distance of (2.0 ± 0.2) kpc. It has a rotation period of 33 ms and a first period derivative $\dot{P} \sim 4.2 \times 10^{-13}$ s/s, which gives a spin-down age of ~ 1270 years, close to the true age. From our viewing angle with respect to the rotation axis, $\sim 60°$ (Ng and Romani, 2004), the Crab pulsar light curve exhibits two peaks with the interpulse, hereafter P2, coming at 0.4 in phase after the main pulse, hereafter P1. One of the remarkable features is that it is observable at all wavelengths with an extreme stability in the phase position of the peaks across the whole electromagnetic spectrum, see Figure 5.1. To this date, it is the only pulsar detected above 100 GeV.

The Crab pulsar was first discovered as a radio pulsar (Staelin and Reifenstein, 1968; Comella et al., 1969) and was the first pulsar to be discovered in optical (Cocke et al., 1969), with a reported optical flux more than twice as large as the radio flux. At the same time, a "light bridge" or interpeak component appeared faintly in the optical range (Wampler et al., 1969). The Crab pulsar was then

detected in X-rays (Fritz et al., 1969; Bradt et al., 1969), by an Aerobee rocket, sensitive to photons from 0.25 keV up to 13 keV. The emission from the bridge was also detected at these energies (Kurfess, 1971). The measured frequency and position of the peaks were compatible with the previous observations made in optical and radio. Also, at these energies, P2 appears to be fainter than P1 with a pulse width twice as big, mimicking the optical pulse.

In 1972, gamma-ray emission from the Crab pulsar was detected from 10 up to 100 MeV (Albats et al., 1972) and in 1977 pulsed emission was detected by *COS-B* from 2 up to 12 KeV and from 50 MeV up to 1 GeV (Bennett et al., 1977). In 2004 *XMM-Newton* reported a harder spectrum for the interpulse and the intermediate pulse region than the main pulse, between 0.6 and 15 keV. The intermediate pulse region is harder in index than the main pulse by 0.3 (Kirsch et al., 2004).

The *EGRET* and *COMPTEL* telescopes, on board CGRO confirmed the emission up to 100 MeV and an extension of the pulsed emission up to 5 GeV was observed by *EGRET* (Kuiper et al., 2001; Nolan et al., 1993). The pulsation up to 5 GeV was later confirmed by the *AGILE* and *Fermi* satellites (Pellizzoni et al., 2009; Abdo et al., 2010a). In 2008, the observation of the Crab pulsar by the MAGIC collaboration led to a detection of pulsed emission above 25 GeV (Aleksić et al., 2011), challenging the models describing HE emission from pulsars. Such a discovery ruled out the HE emission from the polar cap, where a super-exponential cut-off is expected due to the magnetic pair creation. Later, the VERITAS and MAGIC collaborations detected pulsed emission above 100 GeV with an extension up to 400 GeV (Aliu et al., 2011; Aleksić et al., 2012). Recently, observations by MAGIC showed an extension of the pulsed emission up to 1 TeV for P2 (Ahnen et al., 2015). The obtained SED for the interpulse is well characterized by a power-law function from 50 GeV up to 1.7 TeV. Such a parametrization of the emission with a single function suggests that the entire emission from 50 GeV to 2 TeV arises from the same mechanism. Hence it seems unlikely that the VHE emission arises from curvature radiation due to the big curvature radius required for the emitting particle.

The Crab pulsar is also known to emit giant radio pulses (Staelin, 1970; Heiles and Campbell, 1970). This property has been observed in a few pulsars (Knight et al., 2006). A search for gamma-ray giant pulses correlated with those observed in radio has been carried out for several years (Nepomuk Otte et al., 2009; Schroedter et al., 2010; Aliu et al., 2012)). Most recent calculations set the upper limits of 5 to 10 times the average Crab pulsar flux for the interpulse and combined interpulse and main pulse.

The observations of the Crab pulsar and the data analysis presented in this thesis deal with the detection of the interpulse with the MAGIC telescopes. This

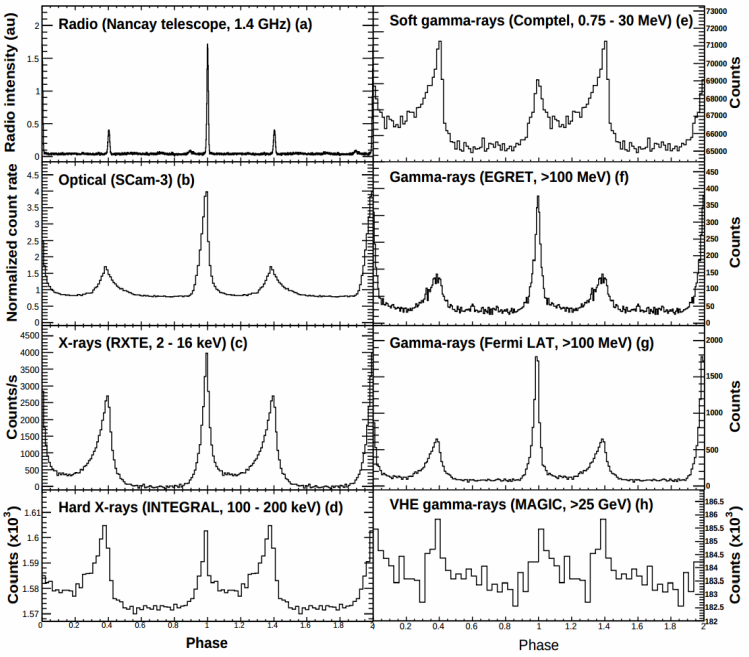

FIGURE 5.1: Light curves of the Crab pulsar for different energy ranges. From (Abdo et al., 2010).

component, already observed at low energies and predicted at VHE, was not previously detected at VHE. In order to discuss the Crab spectra at energies lower than those accessible to MAGIC, 6.5 years of *Fermi* LAT data have been analyzed for this thesis.

5.1 Observations with Fermi-LAT

A deep study of the Crab pulsar and its surrounding nebula was published by the *Fermi* LAT collaboration using 8 months of data (Abdo et al., 2010). They characterized the spectral shape of the Crab Nebula in the transition regime, where the decreasing synchrotron emission starts to be dominated by the IC process above $\sim$ 200 GeV. Regarding the Crab pulsar, the SED was characterized by a power-law function with an exponential cut-off at $E_c = (5.8 \pm 0.5 \pm 1.2)$. They reported a hint of a third peak emission at phase ~ 0.75 with significance of 2.3σ above 10 GeV.

5.1.1 Data sample

We analyzed 6.5 years of *Fermi*-LAT data (from 2008-09-01 to 2015-03-01). The data were downloaded from the *Fermi Science Support Center* web site[1], selecting

[1] http://fermi.gsfc.nasa.gov/cgi-bin/ssc/LAT/LATDataQuery.cgi

events within a Region Of Interest (ROI) of 15° around the Crab pulsar, and with energies between 100 MeV and 300 GeV. The analysis was done using the P7REP_SOURCE_V15 IRFs and the Fermi Science tools version v9r31p1. For the analysis, only events recorded when the telescope was in nominal science mode were selected. A cut was applied in order to select events taken with a rocking angle below 52°. In order to reject the gamma rays coming from the interaction between the CRs and the Earth's atmosphere, only events with a zenith angle below 100° are used. The phase of the events and the barycenter corrections were computed using the *gtpphase* tool. As the Crab is a young pulsar and suffers glitches and instabilities in its emission, we use monthly updated ephemeris, provided by the Jodrell Bank Centre for Astrophysics[2] (Lyne et al., 1993) (see Appendix B.0.4).

In order to make the ephemeris readable by *gtpphase*, they have to be transformed into a FITS files using the *gtpulsardb* program. The computed light curve above 100 MeV is shown in Figure 5.2. The light curve was obtained using an energy-dependent angular selection, R, around the source of interest, according to the formula $R = \max(6.68 - 1.76 \times \log(E/MeV), 1.3)$. The model used to describe

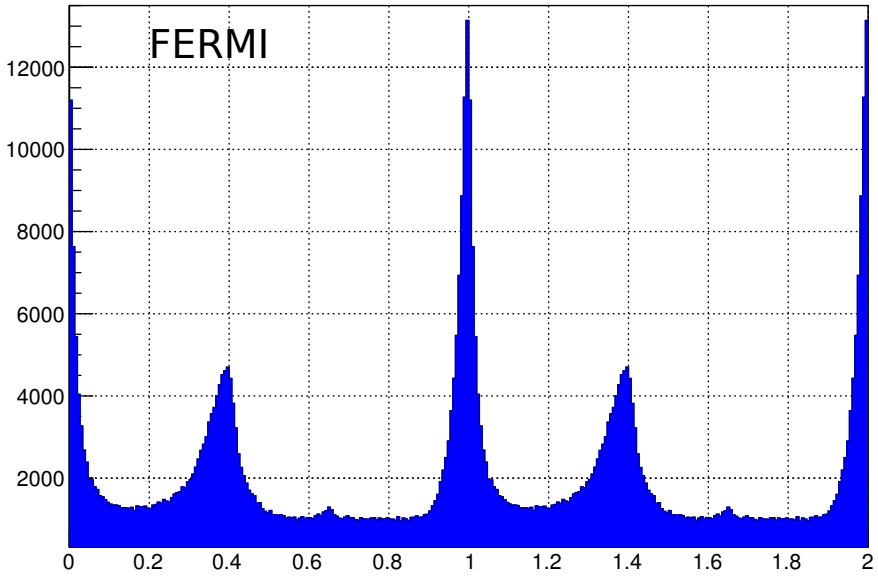

FIGURE 5.2: Light curve obtained from the analysis of 6.5 years of *Fermi*-LAT data above 100 MeV. For better visibility the phase is plotted twice.

the Crab pulsar and the surrounding sources includes two extended sources. The model parametrization used for this analysis is similar to the one described in Section 4.2.5

[2]http://www.jb.man.ac.uk/ pulsar/crab.html.

5.1.2 Spectral energy distribution

The SED of the source of interest is computed by means of the maximum likelihood method, see section 4.2.1. It was computed from 100 MeV up to 300 GeV using 15 bins logarithmically spaced in energy. Only points with a significance greater that 2σ are plotted. At ~ 1 GeV, the flux level of the pulsar and the surrounding nebula are of the same order of magnitude (Abdo et al., 2010). Thus, one has to take into account the emission from the nebula to compute the pulsar spectrum. As the Crab Nebula cannot be spatially resolved, its emission has to be computed from the off pulse of the Crab pulsar. The emission from the nebula is then added into the source model as a background source for the pulsar analysis.

5.1.2.1 Crab Nebula characterization

The emission from the Crab Nebula is made of two components (Abdo et al., 2010), namely, synchrotron and IC. The synchrotron emission arises from the HE electrons in the nebular magnetic fields. This emission is responsible of the observed spectrum from radio to MeV scale. The IC emission is due to the scattering of the synchrotron photons, far infrared and CMB photons on the nebular electrons. The IC emission is dominant above $E \sim 200$ MeV. Both components are characterized by a power-law function. To compute the emission from the nebula, we only take photons coming from the off-pulse, i.e, outside the peaks region. This region is taken as [0.52-0.87] in phase and is the same as for the analysis of MAGIC data (Aleksić et al., 2012). As the flux obtained is the one of the nebula in the off-pulse region, and the nebula emits over the whole pulsar rotation, the obtained flux has to be corrected by a factor 1/0.35, in order to take into account the emission over the full pulsar rotation period. The Crab Nebula differential flux is then defined as:

$$\frac{dN}{dE} = N_{sync}\left(\frac{E}{GeV}\right)^{-\alpha_{sync}} + N_{IC}\left(\frac{E}{GeV}\right)^{-\alpha_{IC}} \tag{5.1}$$

where, N_{sync} and N_{IC} are the normalization factors of the power-law functions describing the synchrotron and IC emission, respectively, computed at 1 GeV, and α_{sync} and α_{IC} their spectral indices.

The resulting SED computed for the Crab Nebula is shown in Figure 5.3. The green line represents the synchrotron emission and the blue one characterizes the IC component. The red line represents the sum of both components. The fit parameters for both components to a power-law function are shown in Table 5.1. The systematic errors are dominated by the uncertainties of the Galactic background model, resulting in errors of 14% on the spectral index (Abdo et al., 2013).

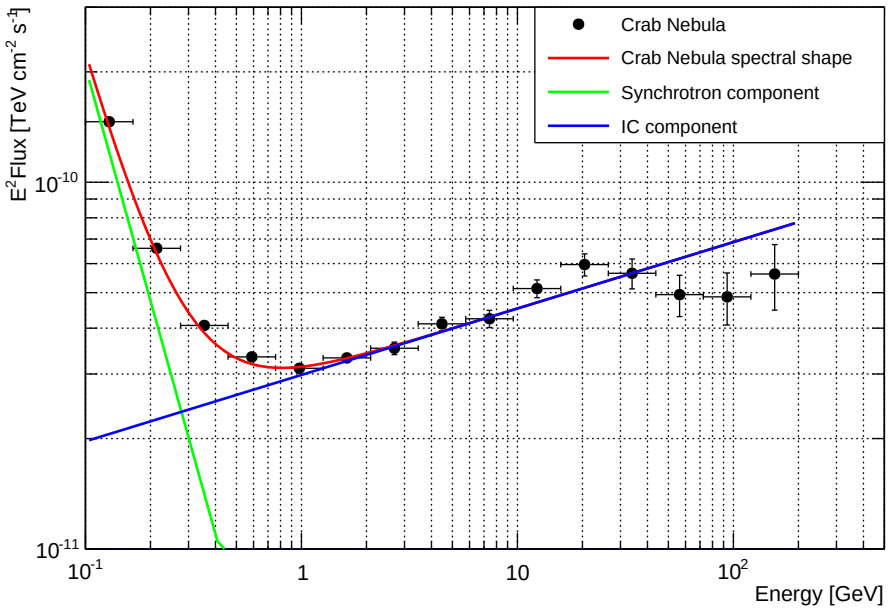

FIGURE 5.3: Crab Nebula SED obtained from the *Fermi*-LAT data. The green and blue lines characterize the synchrotron and IC components, respectively. The red line is the sum of both emission.

Emission	N_0	α
Synchrotron	$(5.5 \pm 1.2) \times 10^{-13}$	$4.12 \pm 0.1 \pm 0.58$
Inverse Compton	$(1.04 \pm 0.03) \times 10^{-11}$	$1.82 \pm 0.02 \pm 0.25$

TABLE 5.1: Crab Nebula synchrotron and inverse Compton spectral parameters. The normalization factors, computed at 1 GeV, are given in units of $[\mathrm{MeV}^{-1}\mathrm{s}^{-1}\mathrm{cm}^{-2}]$.

5.1.2.2 Pulsar emission

For the pulsar spectra calculation, the previously computed synchrotron and IC Crab Nebula components are taken into account in the model to describe the Crab pulsar background sources. The model contains then two components arising from the Crab Nebula, namely, synchrotron and IC components, and one component arising from the Crab pulsar. The parameters coming from the nebula, in the model, are fixed to the previously obtained values. The phase region for the computation of P1 and P2 are set to [-0.017 - 0.026] and [0.377 - 0.422], respectively, as done in (Aleksić et al., 2012). The emission from the bridge is computed in the whole region between P1 and P2 set as [0.026-0.377] in phase. The normalization factor of all the sources in the catalog is scaled down according to the considered pulsar phase. We characterized the pulsar emission using a power-law function

with an exponential cut-off, defined as:

$$\frac{dF}{dE} = N_0 \left(\frac{E}{E_0}\right)^{-\alpha} \exp(-(E/E_c)), \tag{5.2}$$

with N_0 the normalization factor, E_0 the energy scale, α the spectral index and E_c the energy cut-off. The power-law with exponential cut-off function was chosen in order to better estimate the systematic error of the spectral index and energy cut-off.

The obtained SEDs for P1, P2 and the bridge emission are shown in Figure 5.4. The spectral points are plotted together with the spectral fits. The red, blue and green points represent the P1, P2 and Bridge SEDs, respectively. The pulsed emission from P2 The spectral parameters for each region are shown in Table 5.2. The systematic errors are dominated by the uncertainties of the Galactic diffuse background, resulting in an error of 14% on the spectral index and of 4% on the energy cut-off ((Abdo et al., 2013)).

	N_0	α	E_{cut} [GeV]
P1	$(8.77 \pm 0.1) \times 10^{-11}$	1.86 ± 0.01	3.3 ± 0.1
P2	$(3.0 \pm 0.1) \times 10^{-11}$	1.96 ± 0.01	7.5 ± 0.6
Bridge	$(7.4 \pm 0.1) \times 10^{-11}$	1.70 ± 0.01	6.6 ± 0.3

TABLE 5.2: Characterization of the different Crab pulsar components. The systematic errors are of 14% on the spectral index and 4 % on the energy cut-off. The normalization factors are given in units of [$\mathrm{MeV}^{-1}\mathrm{s}^{-1}\mathrm{cm}^{-2}$].

5.2 Observations with the MAGIC telescopes

The Crab pulsar and its surrounding nebula have been studied by MAGIC for almost a decade. The deep observations carried out led to the detection of the Crab pulsar emission above 25 GeV in 2008, which was then extended up to 400 GeV in 2012. The analysis presented here led to discovery of the VHE energy emission from the bridge. The bridge emission was already known at lower energies (Abdo et al., 2010a; Wampler et al., 1969; Kurfess, 1971). The detection of the VHE energy bridge emission is challenging from a theoretical point.Indeed, even though the emission from the bridge region is expected from several models, (Aleksić et al., 2012; Aharonian et al., 2012) the spectral features and light curves exhibited by the Crab pulsars are hard to reproduce. The Crab pulsar and its surrounding nebula are observable from the location of the MAGIC telescopes from November to May. The data used for the analysis presented here were collected over several years and with several telescope configurations (camera, readout, PSFs, etc) in stereoscopic

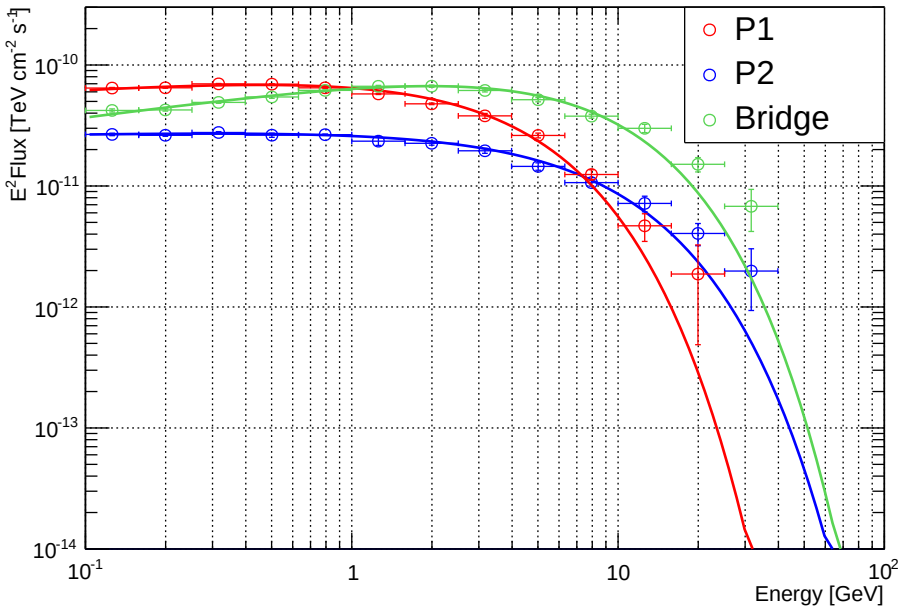

FIGURE 5.4: Crab pulsar SED obtained using 6.5 years of *Fermi*-LAT data. The red, blue and green lines represents the emission from P1, P2 and the bridge, respectively. A power-law with exponential cut-off spectral shape was assumed for the calculation.

mode. The sample consists of data taken before and after the major upgrade of the MAGIC telescopes (Aleksić et al., 2016b), during which the MAGIC-1 camera was replaced by a camera similar to the one at work in MAGIC-2.

5.2.1 Data set

The present analysis was processed collecting data from cycle-5 (2009-2010), cycle-6 (2010-2011) and cycle-8 (2012-2013). Only data taken in stereo mode and during dark conditions were used. Moon and twilight data were discarded due to the higher background collected during these observations. The telescope configurations for the cycle-5 and cycle-6 were the same, thus, only one single Monte Carlo sample can be used to analyze these two samples together. Both wobble and ON observations were carried out during this period. After cycle 6, the MAGIC-1 camera was upgraded, and new sets of Monte Carlo were required. During cycle-8, data were taken only in the wobble mode. This period had to be split into two sub-samples due to an upgrade of the LUTs in January 2013. Each sub-sample was analyzed with a dedicated Monte Carlo sample. Among all the data collected from these three observation periods, only data taken in wobble mode with an offset angle of 0.4° and ON data were selected. Furthermore, in order to preserve the low energy threshold, only data taken at zenith angles below 35° were used.

As the nebula surrounding the Crab pulsar is strong and can be detected in a few minutes, the reconstructed nebula signal in each sample was used as a data quality check. The samples with an integral sensitivity better 0.9% of the Crab Nebula are selected for the analysis. Bad quality ON samples from cycle 5 and 6 were discarded based on their rates. We selected only runs with a rate comprised between 1σ around the mean value $\sim$ 350 Hz. In total, 142 hours of good data quality were selected. The effective times, after data selection, according to the observation periods are shown in Table 5.3. The corresponding dead time after an event has been recorded of 5×10^{-4} s for cycle-5 and cycle-6 and 26×10^{-6} s for cycle-8 are taken into account.

Cycle 5	37 hours
Cycle 6	60 hours
Cycle 8	45 hours
Total	142 hours

TABLE 5.3: Effective time of good data quality for each observation period.

5.2.2 Cuts computation

The observation of VHE gamma rays cannot be done without accumulating a lot of noise coming from the CR background. To improve the signal-to-noise ratio, we apply cuts in order to reject as many events that are not photon-like as possible. In order to compute the cuts, we use a background sample, taken from the anti-source position in the camera and a gamma-ray Monte Carlo sample to avoid overtrainning. The cuts are energy dependent, therefore, the samples used for the computation are divided in logarithmic energy bins with 10 bins per decade. The cuts applied in pulsar analysis to search for pulsed emission rely on the hadronness and θ^2 distributions. In each energy bin a scan is made over these parameters in order to optimize the so-called *Q-factor* defined as:

$$Q = \frac{\epsilon_\gamma}{\sqrt{\epsilon_{off}}} \tag{5.3}$$

where ϵ_γ and ϵ_{off} are the efficiency cuts on the gamma and off samples, respectively. We require $\epsilon_\gamma > 0.5$ to insure enough statistics for the calculation. The evolution of the Q-factor depending on the energy, hadronness and θ^2 parameters is shown in Figure 5.5. The star represents the values that maximize the Q-factor. The cuts used for the cycle-8 are shown in Table 5.4.

For each Monte Carlo sample used, new cuts have to be computed. The computed cuts do not allow us get rid of the background coming from the surrounding

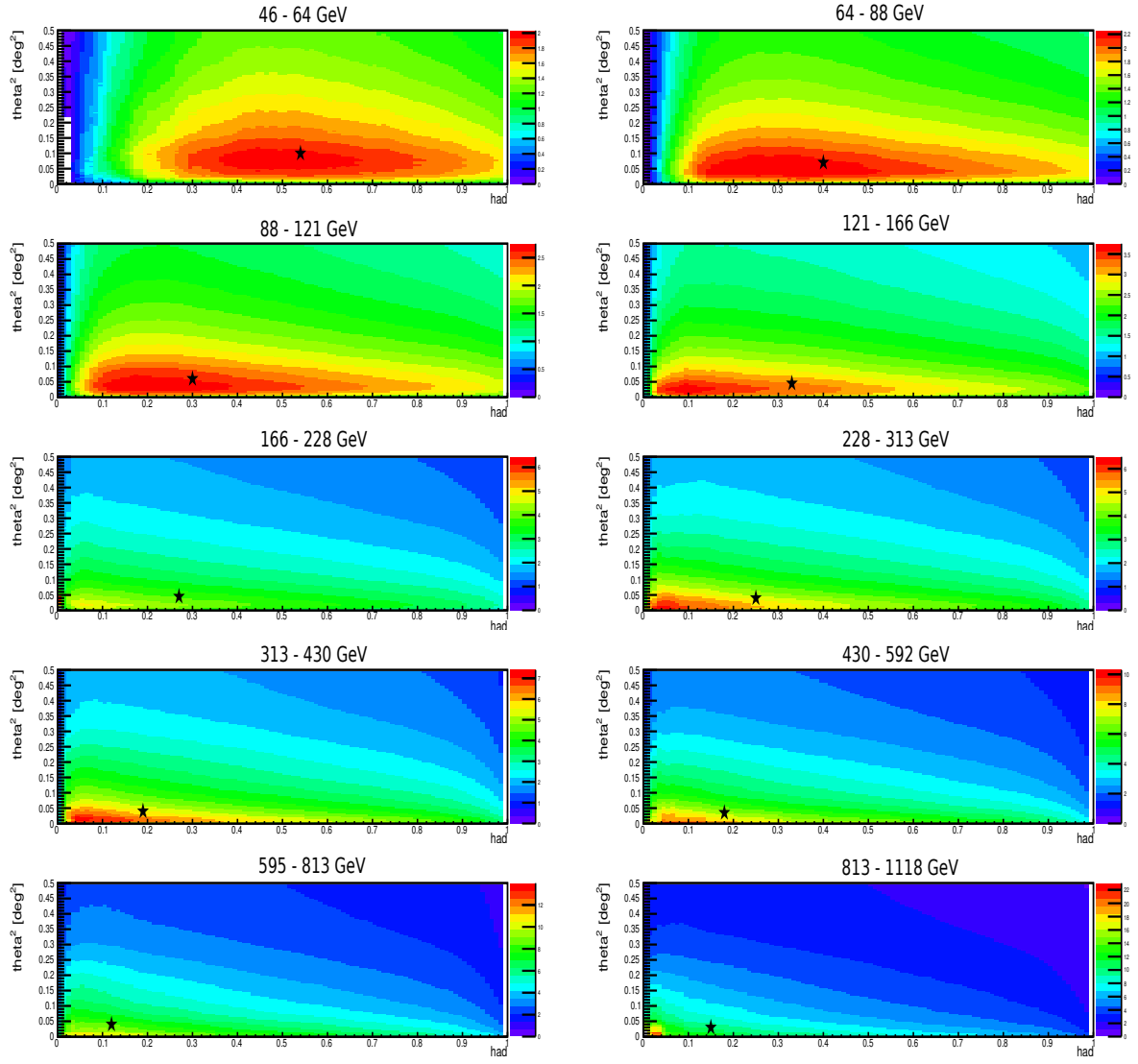

FIGURE 5.5: Q factor evolution as a function of the hadronness (x-axis) and θ^2 (y-axis) for several energy bins. The star represents the cuts in hadronness and θ^2 that maximize the Q-factor and preserve the condition $\epsilon_\gamma > 50\%$.

nebula as the cuts are only sensitive to the nature of the incoming particles. The number of events coming from the pulsar has to be estimated from the folded light curve.

5.2.3 Folded light curve and detection of the pulsation

The detection of pulsed emission relies on the time of arrival (TOA) of the photons coming from the observed pulsar. Each event detected by the telescopes is recorded together with its TOA using a high precision GPS clock coupled with a rubidium clock. This information is used to fold the events time with the ephemeris of

E_{min} [GeV]	E_{max} [GeV]	Had.	θ^2 [deg^2]
46	64	0.54	0.10
64	88	0.40	0.07
88	121	0.30	0.06
121	166	0.33	0.05
166	228	0.27	0.05
228	313	0.25	0.04
313	430	0.19	0.04
430	592	0.18	0.04
592	813	0.12	0.04
813	1118	0.15	0.03

TABLE 5.4: Energy-dependent cuts computed for the cycle-8 data sample

the pulsar under study. During this step, corrections of the Earth's motion with respect to the pulsar are applied, as described in Section 3.5.7. The phase of the events and the timing corrections are computed and applied using *psearch* (Lopez, 2006), a dedicated software for pulsar analysis within the *MARS* package. After this step, the events are characterized by their phases according to the pulsar rotation period. In order to check the timing analysis chain, we used a dedicated PMT at the center of the MAGIC cameras, the so-called *central pixel*, that was modified to detect the optical pulsations of the Crab pulsar. The optical pulsation of the Crab can detected at high significance in a few minutes with the central pixel. Figure 5.6 shows the normalized light curve computed after 10 minutes of observation with the central pixel, where the pulsed signal was detected at more than 20 σ using the χ^2 statistical test.

We used for the analysis of the MAGIC data the same ephemeris as for the analysis of the *Fermi*-LAT data. In order to characterize the emission from the different components, ie, P1, P2 and the bridge, the light curve was computed for several energy ranges: above 50 GeV, 50-400 GeV and 100-400 GeV. The lower energy limits was set according to the lowest energy that can be reconstructed in the Crab Nebula spectral analysis (Zanin, 2011), while the upper limit on the energy was set to the highest reported emission from the Crab pulsar (Aleksić et al., 2012). As described in Section 5.2.2, we used logarithmically-spaced energy bins, resulting in 8 bins between 50 and 400 GeV. The significance of the signal was computed using several statistical tests; the χ^2, the Z_{10}-test and the H-test (de Jager et al., 1989). None of these tests takes advantage of the a priori knowledge of the expected position of the peak (signal regions) in the folded light curve, and the proper significance of the two peaks or the bridge cannot be disentangled. However, the Li & Ma significance (Li and Ma, 1983) (Eq. 17) based on the likelihood ratio method uses this information. The Li & Ma method takes the number of events in the signal and background region and the ratio of the effective

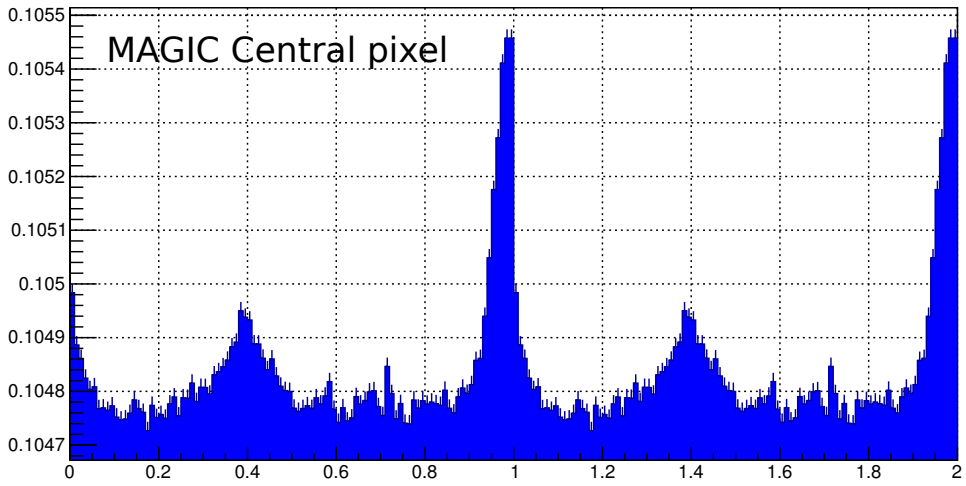

FIGURE 5.6: Normalized folded light curve computed using optical data from the central pixel, over 10 minutes of observation.

observation times between them. The computed light curves are shown in Figure 5.7. The grey areas represent the signal region for P1 and P2 and the dashed area the background region. The red lines represent the average number of events extrapolated from the background region. The Li & Ma significances and the computed excess are displayed in Table 5.5. The results of the statistical tests for the above mentioned methods are displayed in Table 5.6.

Energy [GeV]	P1	P1 Excess	Bridge	Bridge Excess	P2	P2 Excess
50-100	5.0 σ	332 ± 86	5.7 σ	1428 ± 357	9.9 σ	683 ± 91
50-400	7.6 σ	642 ± 110	6.0 σ	1910 ± 452	12.3 σ	1077 ± 115
100-400	5.9 σ	311 ± 69	2.4 σ	483 ± 279	7.9 σ	394 ± 71

TABLE 5.5: Significance and excess computed for the three signal regions for different energy range.

Energy [GeV]	χ^2	Z_{10}-test	H-test
50-100	6.8	8.6	8.8
50-400	6.4	7.5	7.8
100-400	10.1	12.3	12.6

TABLE 5.6: Results of the standard statistical tests applied to the folded light curves, for several energy ranges.

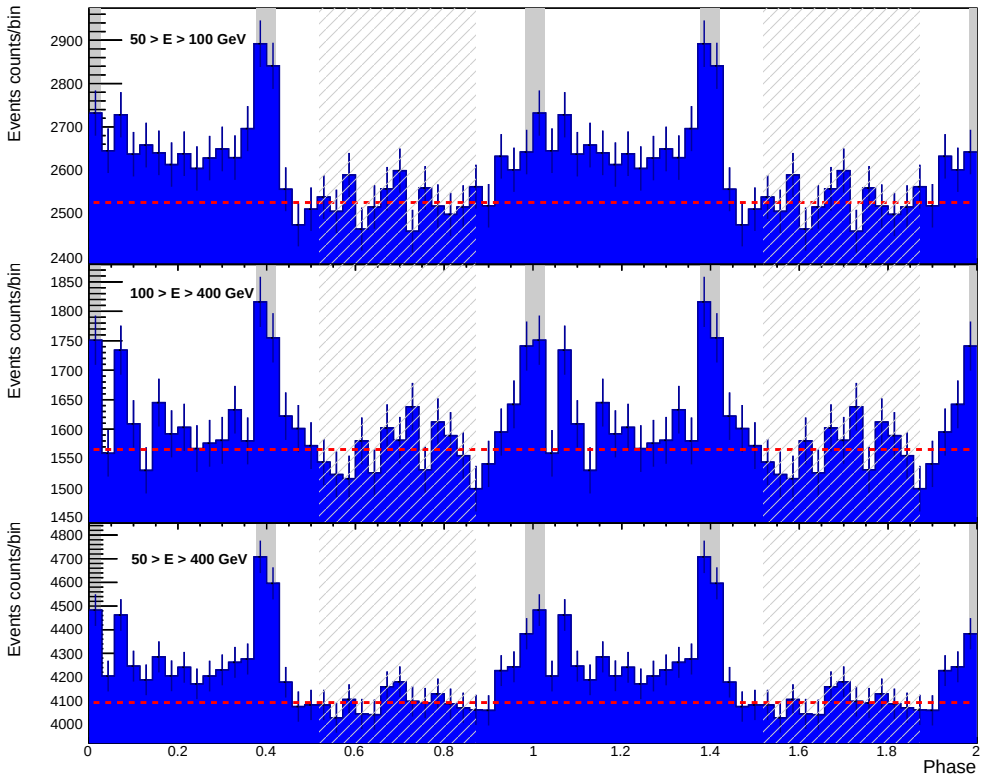

FIGURE 5.7: Folded light curve of the Crab pulsar over three energy ranges: between 50-100 GeV, 100-400 GeV and 50-400 GeV. The grey areas show the signal region for P1 and P2. The dashed area is the region used to estimate the background (cosmic rays and unpulsed gamma rays from the Crab Nebula). The red lines represents the average number of events in the background region.

5.2.4 Peaks ratio

The Crab peaks position is remarkably stable over the electromagnetic spectrum. However, the relative intensity between the peaks and the bridge exhibits a strong energy dependence, as well as the bridge emission, as can be seen in Figures 5.1 and 5.8. At optical wavelengths, P1 is dominant with respect to P2, whereas at very high energies P2 gets brighter. A first study of the evolution of the ratio between the peaks and the bridge was done in 2001 (Kuiper et al., 2001), using data from optical up to hard gamma rays, see Table 5.7.

Energy range	Instrument
Optical	UCL MIC detector , NUV/FUV HST STIS
X-rays	ROSAT HRI , BSAX LECS , BSAX MECS
X-rays and soft gamma rays	BSAX PDS, CGRO BATSE
Medium/hard gamma rays	CGRO COMPTEL, CGRO EGRET

TABLE 5.7: Data used for the computation of P2/P1 and bridge/P1 ratio from optical to hard gamma-rays by (Kuiper et al., 2001).

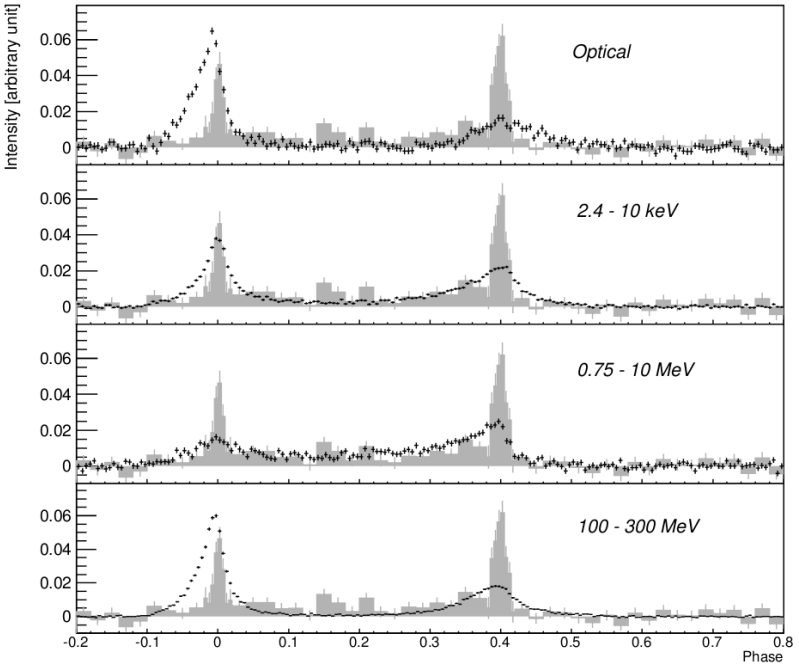

FIGURE 5.8: Light curve of the Crab pulsar at different energies; optical, 2.4-10 keV, 0.75-10 MeV, 100-300 MeV. The grey area represents the light curve computed with MAGIC data between 50-400 GeV. On MAGIC data the background is subtracted. The optical light curve was obtained with the MAGIC telescope using the central pixel. Figure taken from (Aleksić et al., 2014).

Energy range [GeV]	P2/P1	Bridge/P1
0.1- 0.5	0.59 ± 0.01	0.077 ± 0.002
0.5 - 1	0.56 ± 0.02	0.12 ± 0.01
1 - 5	0.59 ± 0.02	0.25 ± 0.01
5 - 10	0.76 ± 0.08	0.52 ± 0.06
10 - 50	1.1 ± 0.2	0.77 ± 0.2
50 - 400	1.7 ± 0.1	0.8 ± 0.2

TABLE 5.8: Values of the ratios P2/P1 and bridge/P1 between 100 MeV and 400 GeV using *Fermi*-LAT and MAGIC data.

Similar trends were found in the behavior of the P2/P1 and bridge/P1 ratios with both ratios reaching maximum at ~ 1 MeV. However, the emission from the bridge never exceeds the one coming from P1, whereas P2 can get more intense than P1. We computed these ratios above 100 MeV using the *Fermi*-LAT and MAGIC data. The signal region used here for the ratio P2/P1 is the one previously reported in Section 5.1.2.2. However, the ratio Bridge/P1 is computed using the *EGRET* bridge definition (phase - 0.14 to 0.25) (Fierro et al., 1998a). This bridge definition was chosen due to the fact that the peaks get wider as the energy

decreases. Thus, defining the bridge region as the whole region between P1 and P2 would gather events from the peaks when computing the bridge excess from the *Fermi*-LAT data sample. The background coming from the nebula was computed and subtracted in each signal region according to the signal region width. The resulting computation for the P2/P1 and bridge/P1 ratio is shown in Figure 5.9 together with the previously-computed values by (Kuiper et al., 2001). The ratios computed using the *Fermi*-LAT data span from 100 MeV to 50 GeV and the MAGIC data from 50 to 400 GeV. To compute the ratio using the *Fermi*-LAT data, an energy-dependent ROI was used. The value of the ROI was set as $R = \max(6.68 - 1.76 \times \log(E), 1.3)°$. The values of the excess used for the *Fermi*-LAT and MAGIC data are directly extracted from the folded light curves. The computed ratios for several energy ranges are shown in Table 5.8.

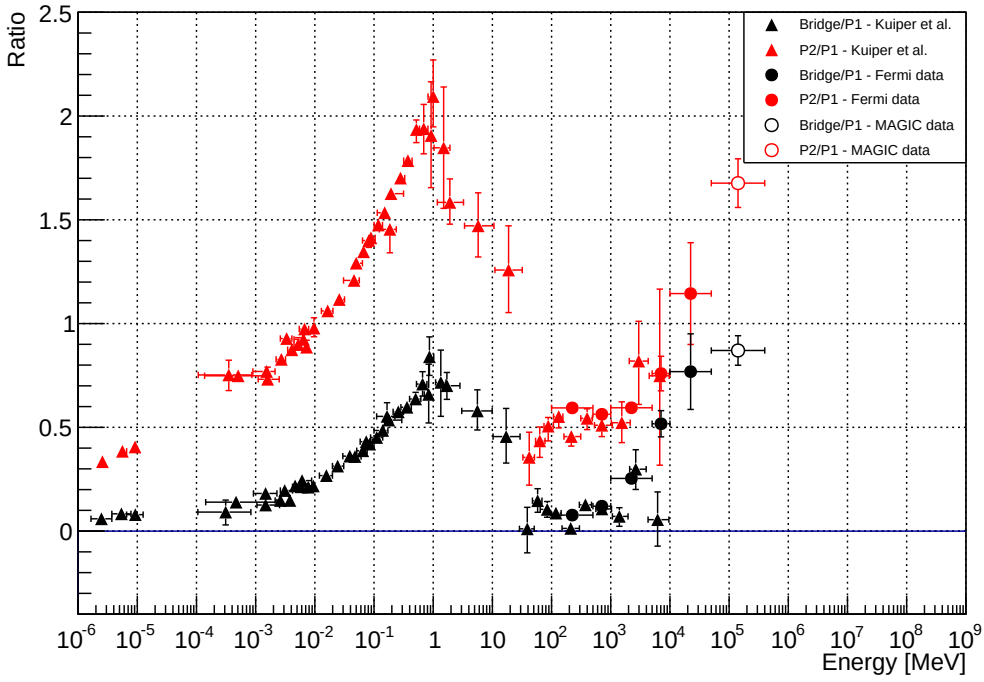

FIGURE 5.9: P2/P1 ratio (red markers) and Bridge/P1 ratio (black markers) as a function of the energy. Values computed by (Kuiper et al., 2001) between 1 eV and 100 MeV are represented by the full triangles. The computations from *Fermi*-LAT data are represented by the full circles, and the empty circles represent the calculation using MAGIC data.

5.2.5 Spectral energy distribution

The SEDs were independently computed for data from cycle-5 and cycle-6 and the two samples of cycle-8. The data were then combined further, during the

unfolding procedure. The calculation of the SEDs requires looser cuts than those applied for the search of a pulsed signal, in order for Monte Carlo to better match the data. For the calculation of the SED of the pulsed emission of the Crab, we required an efficiency of 80% in the hadronness cuts and 90% in the θ^2 cuts. The background considered in order to compute the number of excess events from P1, P2 and the bridge is taken from the off region between P2 and P1. The effective time was computed taking into account the dead time of the readout system after each event recorded of 5×10^{-4} s for cycle 5 and 6 and 26×10^{-6} s for cycle 8. Each data set was split into 30 logarithmic spaced bins between 5 GeV and 50 TeV. The effective area used for the flux estimation was computed using the reconstructed energy of the Monte Carlo events, averaged over the zenith range covered. The SEDs for P1, P2 and the bridge were fit, after unfolding, with a power-law function defined as:

$$\frac{dN}{dE} = F_{100} \times \left(\frac{E}{100GeV} \right)^{-\alpha}, \tag{5.4}$$

where F_{100} is the normalization factor at 100 GeV, E the energy and α the spectral index. The unfolding method (Albert et al., 2007b) is used to correct for the bias and energy migration expected of the reconstructed event energies, see Section 3.5.7. During the unfolding, events are re-weighted each time with the appropriate spectrum derived in the previous iteration. The results of the fits are shown together with the resulting χ^2 in Table 5.9. The first error is statistical and the second is systematic. The systematic errors on the normalization factor were computed according to (Aleksić et al., 2016a), where the systematics error on the normalization factor were estimated to be 18% ($E \lesssim$100 GeV). However, the systematic errors on the spectral index are dominated by the unfolding. The data were, thus, unfolded using several regularization methods in order to estimate the error due to this process. The results were checked using different regularization methods for the unfolding algorithm, with all of them compatible within the statistical errors. The computation of the nebula spectrum, as a sanity check, was computed for the whole sample, using only wobble data, with the same cuts and energy binning as for the pulsar. Figure 5.10 shows the SEDs of the Crab Nebula, P1, P2 and the bridge computed with MAGIC and 6.5 years of *Fermi*-LAT data (see Section 5.1). The MAGIC data are represented after unfolding using the Tikhonov regularization (Tikhonov and Arsenin, 1977).

The computed ratio between the normalization factors for P1 and P2 at 100 GeV is 1.7 ± 0.4, which is in agreement with the previous value computed using the folded light curve, see Table 5.8.

	$F_{100}[10^{-11}\mathrm{TeV}^{-1}\mathrm{cm}^{-2}\mathrm{s}^{-1}]$	α	χ^2/d.o.f
P1	$4.2 \pm 0.5 \pm 0.76$	$3.6 \pm 0.5 \pm 0.7$	1.95/3
P2	$7.0 \pm 0.7 \pm 1.26$	$3.1 \pm 0.3 \pm 0.4$	1.93/3
Bridge	$8.2 \pm 2.4 \pm 1.48$	$3.8 \pm 0.7 \pm 0.3$	1.02/2

TABLE 5.9: Results of the Crab pulsar spectral energy distribution calculation fitted to a power-law function for P1, P2 and the bridge.

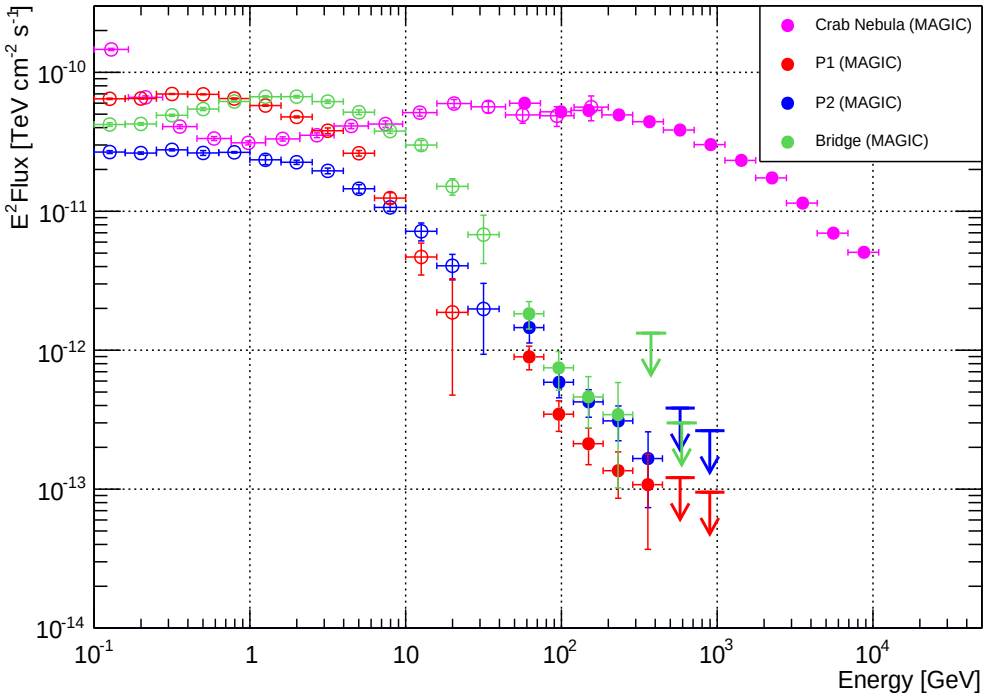

FIGURE 5.10: Spectral energy distribution of the Crab nebula (pink), P1 (red), P2 (blue) and the brdige (green) combining *Fermi* (empty markers) and MAGIC (full markers) data.

5.3 Results and Discussion

The observation of the Crab pulsar and its surrounding nebula with the MAGIC telescopes resulted in the analysis of 142 hours of good data quality taken at zenith angles below 35°. In order to discuss the Crab pulsar at lower energies than those accessible to MAGIC, 6.5 years of *Fermi*-LAT data were also analyzed. The results of the *Fermi*-LAT data analysis is in good agreement with the previously presented results by the *Fermi* collaboration (Abdo et al., 2010). The spectrum from P2 and the bridge could be extended up to 32 GeV using the *Fermi* LAT data. In order to study the pulsed emission with the MAGIC data, we computed the folded light curve for several energy ranges, using an ephemeris from the Jodrell Bank that

is updated monthly, and the SED for both peaks, together with the interpeak emission. In order to check the validity of the analysis, the Crab Nebula SED was also computed using the same data sample. The computed nebula SED using the *Fermi*-LAT and MAGIC data connect smoothly around 50 GeV.

The study of the light curve at MAGIC energies revealed the presence of an emission above 50 GeV coming from the interpeak region. The computed SED of the interpeak emission, together with the emission from both peaks is well characterized by a power-law function above 50 GeV. However, the interpeak emission tends to be softer than the peaks emission. The interpeak was significantly detected up to 200 GeV, above this value, the limited statistics and the MAGIC sensitivity preclude the detection of a cut-off.

In order to characterize the relative emission of the different components, we computed the ratio P2/P1 and bridge/P1. The P1/P2 and bridge/P1 ratios were computed using the *Fermi*-LAT data between 100 MeV and 50 GeV. The computed values are in good agreement with those previously computed by (Kuiper et al., 2001) using *COMPTEL* and *EGRET* data up to 1 GeV. The behavior of both ratios appears to be identical with a local maximum in both distributions around 1 MeV, and an increase at high and very high energies with the bridge/P1 ratio being always smaller than P2/P1.

Several attempts were made in order to describe the Crab pulsar VHE emission from a theoretical point of view. From the variety of models proposed, we can distinguish between two kinds: emission taking place inside and outside the LC.

5.3.1 Emission within the light cylinder

In order to explain the emission within the LC, radiating charged particles have to be accelerated in a vacuum gap to emit HE photons. Three locations, in which such gaps appear were proposed; the polar-cap, the slot gap and the outer gap. In the polar-cap, being it located close to the NS surface, one expects a super-exponential cut-off at a few GeV due to magnetic pair creation in the very strong magnetic field. This model has recently been ruled out in the Crab pulsar thanks to the discovery of pulsed emission up to hundreds of GeV, as well as by the spectral shape of the Fermi pulsars.

In order compute the luminosity of the pulsed and phase-averaged emission, the Poisson together with the Boltzmann equations have to be solved. This work was done by (Hirotani, 2006a; Aleksić et al., 2011; Aleksić et al., 2012; Hirotani, 2015a) in the framework of the outer gap. They combined it with the transfer equation between 0.005 eV up to 10 TeV. However, in their approach they considered a new non-vacuum outer-gap (i.e., $\rho \neq 0$), solving the distribution of ρ from the pair

created at each point. In this scenario, the emission arises from several generations of pairs creation within the gap. Since the outer gap is located in the outer magnetosphere, the magnetic field is not intense enough to produce pair creation by the magnetic absorption of the gamma-ray photons. A first generation of $e^{\pm}$ is created by pair production mechanism from $\gamma\gamma$ interaction in the gap. The particles created are accelerated by magnetic-field-aligned electric field, $E_{||}$, up to Lorentz factors $\sim 10^{7.5}$. Cascades will develop within the gap, due to collision of gamma rays with thermal X-rays from the NS surface. The charged density within the gap is sustained by the created pairs. Within the gap, the accelerated charged particles will radiate via curvature radiation and up-scatter soft photons via IC. The resulting high and very high energy photons emitted arise from synchrotron emission below 10 GeV and SSC between 10 GeV and 1 TeV along with the scattering of magnetospheric of magnetospheric UV-IR photons between 1 and 300 GeV.

From this interpretation, the emission above 10 GeV arises from the secondary and tertiary pairs IC scattering on magnetospheric IR-UV photons and exhibits a power-law tail. This scenario naturally includes the emission from the bridge due to the bending of the magnetic field lines near the LC. The standard outer gap interpretation suggests a thin gap, $h_m << 1$ that should suppress the interpeak emission. However, the resolution of the Maxwell-Boltzmann equation shows that $h_m \sim 0.12$ (Hirotani, 2015a), allowing the interpeak emission.

Other emission locations within the light cylinder were proposed. The so-called annular-gap model (Du et al., 2012) was made up to explain the Crab pulsar emission from radio up to TeV scale. In this scenario, the emission from the peaks from the annular gap, which is the region located between the last closed field line and the critical line. They argue that the radio emission would arise from the same region, which explains the stability of the position of the peaks over the entire electromagnetic spectrum. In this framework, the bridge emission would arise from the core gap, the region located in the open magnetosphere above the critical line. Based on this assumption, not all gamma-ray pulsars can be detected in radio band, and not all radio pulsars can have a gamma-ray flux high enough to be detected. The TeV emission would arise from IC scattering on created pairs with Lorentz factor spanning from 10^2 to 10^5. The curvature radiation process would be dominant until ~ 20 GeV.

Due to the small ratios computed between the Bridge and P1 in optical and gamma rays with respect to the P2/P1 ratio, it has been suggested (Kuiper et al., 2001) that the emission from the bridge and the two pulses would be of different nature, which is the case in the annular gap model. However, the similarities of the emission above 50 GeV would suggest that the VHE emission from the three pulsar components have the same origin.

5.3.2 Emission beyond the light cylinder

The vast majority of theoretical models try to explain the gamma-ray emission from pulsars within the light cylinder. However, a region located out of the light cylinder was proposed in order to explain the VHE emission from the Crab pulsar (Bogovalov and Aharonian, 2000; Aharonian et al., 2012; Mochol and Pétri, 2015). It is assumed that the pulsar wind, which is electromagnetically dominated, goes under abrupt acceleration in a region located at 20-50 LC radii away from the pulsar. Due to the abrupt acceleration, the wind becomes kinetically dominated. The pulsed X-rays are then up-scattered by the wind. In this framework, emission from the bridge is expected, as it is observed in X-rays (Wampler et al., 1969), but a special density profile is required in order to explain the narrow peak emission at the same time. However, the estimated ratio P1/P2 is not in agreement with the one reported in the gamma-ray data, which appears to be smaller. This suggests the presence of a non-negligible wind anisotropy, noticeable in the correction of the shape of the gamma-ray light curve. In this scenario a cut-off is expected around 500 GeV. However, the recent observations of the Crab pulsar by MAGIC showed an extension of the pulsed emission up to the TeV scale, suggesting that the acceleration region should extend up to 70 LC radii in order for the charged particles to reach high enough Lorentz factor.

Chapter 6

Study of the Geminga pulsar at very high energies

Geminga is the first-known radio-quiet pulsar, the second brightest persistent source in the GeV sky.It is located at a distance $d \sim 250$ pc (Halpern and Ruderman, 1993) from the Earth. Its light curve exhibits two peaks, hereafter P1 and P2, separated by 0.5 in phase. Also, emission from an interpulse region, located between P1 and P2 was reported (Fierro et al., 1998b). The period of Geminga ($P \sim 237$ ms) (Halpern and Holt, 1992) and its derivative ($\dot{P} \sim 1.1 \times 10^{-14}$ s/s) correspond to a spin-down age of $\tau \sim 340$ kyr, a spin-down luminosity $\dot{E}_{\rm rot} = 3.3 \times 10^{34}$ erg s^{-1} and a surface magnetic field $B_{\rm surf} \sim 1.6 \times 10^{12}$ G. Although its spin-down luminosity is not as high as that of the Crab and Vela, the short distance to this source makes the spin-down flux very large, which results in a high gamma-ray flux.

Geminga was first detected as an unidentified gamma-ray source by the *SAS-2* satellite (Fichtel et al., 1975). In 1977, the *COS B* satellite (Hermsen et al., 1977) confirmed a gamma-ray emission from the same region. Timing variations in the emission were observed (Masnou et al., 1977). In 1983 an X-ray counterpart of the *COS B* source was observed (Bignami et al., 1983) and given the name *Geminga*, and in 1987 the optical counterpart (Bignami et al., 1987). The X-ray pulsation was discovered by the ROSAT experiment (Halpern and Holt, 1992), and was further observed in gamma ray in by *EGRET* (Bertsch et al., 1992) and *COS B* (Bignami and Caraveo, 1992). The first Geminga spectrum was computed using the *EGRET* telescope, on-board of the *Compton Gamma-Ray Observatory* (Mayer-Hasselwander et al., 1994). No information regarding the emission model could be extracted from such a spectrum due to the lack of statistics above 2 GeV. A review on the historical observations of Geminga can be found in (Bignami and Caraveo, 1996). A deeper observation with the *Fermi* LAT telescope using one year of data reported a power-law with an exponential cut-off at (2.5 ± 0.2) GeV

(Abdo et al., 2010b). The study of the phase-resolved emission in fine phase bins shows a strong dependency of the cut-off energy with the phase region considered. Nevertheless, it is interesting to note that a deviation from the exponential cut-off is seen above 20 GeV in the Geminga phase-averaged spectrum (see Fig. 6 in (Abdo et al., 2010b)). The pulsation is still clearly seen above 10 GeV with a reported significance greater than 6 σ (Ackermann et al., 2013a).

The combination of an exponential cut-off spectral shape and the presence of the pulsed emission above 25 GeV from the Geminga pulsar rules out the polar-cap model, in which a super-exponential cut-off is expected at few GeV. The *Fermi*-LAT collaboration also reported that the relative peak intensity between P1 and P2 is changing with energy, with P2 becoming stronger than P1 at $\sim$ 200 MeV (Abdo et al., 2010b). Recently, the VERITAS collaboration reported on the search of VHE emission from the Geminga pulsar with no signal detected above 100 GeV (Aliu et al., 2015).

Several investigations were carried out to look for radio emission from the Geminga pulsar. A first detection of radio pulsed signal at 102.5 MHz was claimed in 1997 (Malofeev and Malov, 1997), with a flux varying between 5 and 500 mJy. Strong variations in the emission and pulses width were reported too. A soft spectrum would explain the absence of detection of pulsed emission above 102 MHz. Recent detections of pulsed emission from the Geminga pulsar was reported at 42, 62 and 111 MHz (Malov et al., 2015). They interpreted the radio silence from the Geminga pulsar as a long-term variability of the radio emission with a period of several years.
However, no further dectection of the radio pulsation from Geminga has been made by other experiments, so far.

The Geminga pulsar, being one of the pulsars with the highest gamma-ray flux (Acero et al., 2015), is a perfect candidate for gamma-ray detectors. Its timing and spectral measurements can shed light on the location and emission mechanism at work in such an aged pulsar. The comparison of a possible VHE emission in the Geminga pulsar with that found in the Crab could provide insights into the pulsar evolution, the impact of the magnetic field and the spin-down luminosity.

Besides the emission from the pulsar, an X-ray nebula was discovered around the Geminga pulsar by the *XMM*-Newton and *Chandra* satellites (de Luca et al., 2006; Pavlov et al., 2010). Both detections showed the presence of an extended structure behind the pulsar, aligned with its proper motion direction. The *Chandra* satellite reported the detection of three tail-like structures behind the pulsar; one 25" tail aligned to the pulsar proper motion, and two 2' outer tails. Another 50" emitting region ahead of the pulsar was reported.

At gamma-ray energies, LAT team reported a continuous emission over the whole pulsar rotation, but no detection of a surrounding nebula (Abdo et al.,

2010b). The Whipple collaboration obtained an integral flux upper limit for continuous emission of 8.8×10^{-12} cm^{-2} s^{-1} above 0.5 TeV (Akerlof et al., 1993), while HEGRA obtained an upper limit of 13% of the Crab flux between 0.8 and 1.5 TeV (Aharonian et al., 1999). At higher energies, the Milagro collaboration reported the detection of steady extended TeV emission from Geminga at a significance level of 6.3σ. They observed an emission region that is extended by 2-3 degrees, with a flux at 35 TeV of $(38 \pm 11) \times 10^{-17}$ TeV^{-1} cm^{-2} s^{-1} (Abdo et al., 2009c). This detection has recently been confirmed by HAWC (Baughman et al., 2015). At radio frequencies, many observers have attempted to detect a continuous emission from Geminga. Only the deepest VLA interferometric observation of Geminga performed in 2004 (Giacani et al., 2005), resulted in the detection of continuous radio emission. Overall, the Geminga radio tail is compatible with the scenario of a synchrotron-emitting PWN.

6.1 Observations and data analysis with the *Fermi*-LAT

A deep study of the Geminga pulsar and its surrounding nebula was made by the LAT collaboration (Abdo et al., 2010c) using one year of data. They characterized the pulsed emission and searched for a surrounding nebula. The resulting phase-averaged pulsar spectrum deviates from a power-law with an exponential cut-off function. A study of the phase-resolved spectra was made by computing the SED in phase bins of variable width, such that each bins contained 2000 photons. The spectra in each phase bin was well described assuming a power law plus an exponential cut-off.

An investigation of the surrounding nebula was carried out too. Even though an emission was detected from the Geminga pulsar over the whole pulsar rotation, the presence of a nebula was rejected (Acero et al., 2013). The study of the energy cut-off of the SED over the pulsar period showed a continuity in the distribution of the energy cut-off. A discontinuity in the energy cut-off distribution is expected in case the pulsar were surrounded by a nebula.

In this thesis, the aim of the analysis of *Fermi*-LAT data is to help to search for pulsed VHE gamma-ray emission with MAGIC at energies above those detected by *Fermi*-LAT. First, we derived the light curve from LAT data above 100 MeV, to characterize the position of the peaks and their widths. Then, the HE spectrum was fit to a power-law function above 10 GeV in order to evaluate the possible extrapolation of the HE emission in the VHE range. Furthermore, a study of the phased energy-resolved spectra was carried out in order to investigate the mechanisms responsible for the HE emission of the Geminga pulsar.

6.1.1 Data analysis

A data sample of 5 years (from 2008-09-01 up to 2013-10-01) of *Fermi*-LAT data was analyzed. This data set was analyzed using the P7REP_SOURCE_V15 IRFs and the *Fermi* Scient Tools version v9r31p1. We selected events that were recorded when the telescope was in nominal science mode and when the rocking angle was lower than 52°. To reject the background coming from the Earth limb, we selected photons with a zenith angle $\leq 100°$. A region of interest (ROI) of 15° around the Geminga pulsar was considered. The phasing and barycenter corrections of the events were computed using *tempo2* (Hobbs et al., 2006) with the *Fermi* plugin. The ephemeris, provided by the *Fermi*-LAT collaboration[1] (see Appendix B.0.5), is the same used later for the analysis of MAGIC data, see Section 6.2.2. The model used to describe the source of interest and the background sources is similar to the one described in Section 4.2.5. As the Crab and Geminga pulsar are close in the sky, the same extended sources are found in the Geminga and Crab source model, namely, IC 443 and S 147.

6.1.2 Characterization of the light curve at high energies

In order to enhance the sensitivity in the search of pulsed emission with the MAGIC telescopes we will make use of the a priori knowledge of the position and extension of the emission peaks of the light curve, which will constitute the signal region of the folded phase distribution. The pulsar light curve was computed using an energy-dependent ROI with a radius defined as $R = \max(6.68 - 1.76 \times \log(E), 1.3)°$ as done in (Abdo et al., 2010a). Both peaks were fit using an asymmetric Gaussian function. The signal regions were set to the peak center $\pm 1\sigma$. Figure 6.1 shows the light curve computed above 100 MeV. The shapes of the peaks strongly depend on energy and get narrower as the energy increases (Abdo et al., 2010c). Only photons with energy greater than 5 GeV and 10 GeV were used to fit P1 and P2, respectively. Such energy ranges were motivated by the aim to significantly detect each peak, and, at the same time, obtain the parameters for the peaks close to those we would expect at MAGIC energies. The light curve obtained above 100 MeV and the signal and background regions are shown in Figure 6.1 together with a close-up view of the fits of P1 and P2 at the corresponding energies. The background region is taken in the OFF region between P2 and P1. The resulting χ^2/d.o.f computed for the fits are 61/26 and 31.8/29 for P1 and P2, respectively. The computed values for the signal region are shown in Table 6.1

[1] http://www.slac.stanford.edu/~kerrm/fermi_pulsar_timing/J0633+1746/html/J0633+1746_54683_56587_chol.par

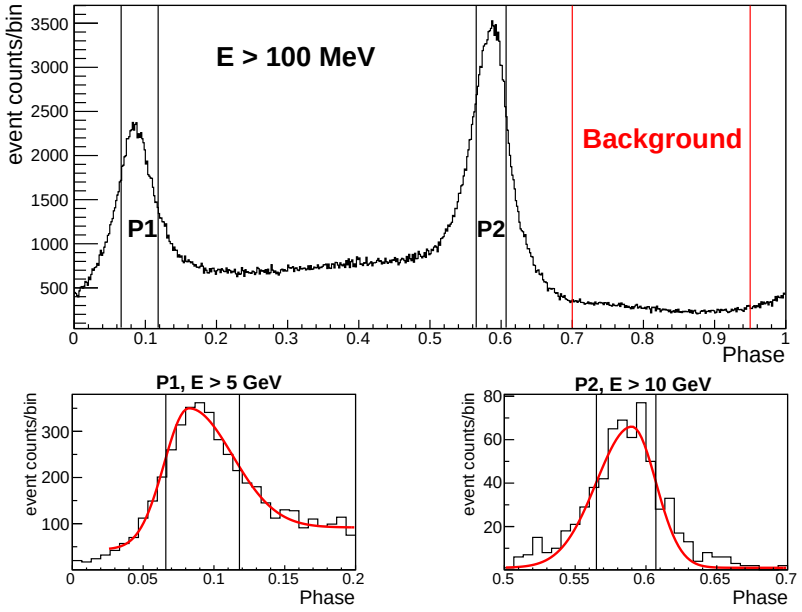

FIGURE 6.1: Light curve computed with the *Fermi*-LAT data above 100 MeV (top). A close-up is made on both P1 above 5 GeV and P2 above 10 GeV and their corresponding fits (bottom), the black lines represent the selected signal regions. The resulting χ^2/d.o.f values computed for the fits are 61/26 and 31.8/29 for P1 and P2, respectively.

P1	P2	Off-region
0.066 - 0.118	0.565 - 0.607	0.7 - 0.95

TABLE 6.1: Definition of the signal and off regions derived from the fit of the Geminga pulsar light curve obtained with the LAT data.

6.1.3 Spectral energy distribution

The SED was computed for P1 and P2 and the phase-averaged emission, using the binned likelihood method. The ROI was set to 15° as done in (Abdo et al., 2013). For the three components, i.e, P1, P2 and the phase-averaged emission, a power-law function with an exponential cut-off was used to characterize the SED, defined as:

$$F(E) = N_0 \left(\frac{E}{E_0}\right)^{-\alpha} \exp(-(E/E_c)^b), \tag{6.1}$$

where E_0 is the energy scale set to 927.9 MeV as computed in the 3FGL (Acero et al., 2015), α the spectral index, and E_c the energy cut-off. The b parameter defines the difference between an exponential (b=1), sub-exponential (b <1) and super-exponential (b >1) cut-off.

For the calculation of the spectral points the procedure was repeated in each energy bin assuming that the emission can be characterized by a single power-law function in this energy range. The SED was computed from 100 MeV up to 100 GeV using 30 bins logarithmically spaced in energy. Only the normalization factor and the spectral index of the source of interest were left free int this case. All the others parameters describing the source model were fixed to the values obtained for the overall spectral shape calculation. Only spectral points with a significance greater than 2 σ are shown on the plots, see Figure 6.3. For P1 and P2 the spectral energy distribution was computed according to the signal regions computed in Section 6.1.2. The background sources in the source model were scaled down to the phase region considered for the SED calculation. The results of the fits to a power-law function with an exponential and sub-exponential (b < 1) cut-off above 100 MeV are shown in Table 6.3 and 6.2, respectively.

	N_0	α	E_c [GeV]
P1	$2.12 \pm 0.03 \pm 0.04$	$1.27 \pm 0.01 \pm 0.01$	$1.87 \pm 0.03 \pm 0.03$
P2	$2.43 \pm 0.02 \pm 0.04$	$1.03 \pm 0.01 \pm 0.01$	$2.79 \pm 0.03 \pm 0.05$
PA	$13.8 \pm 0.06 \pm 0.3$	$1.23 \pm 0.03 \pm 0.01$	$2.31 \pm 0.01 \pm 0.05$

TABLE 6.2: Parameters obtained with the likelihood method using a power-law function with an exponential cut-off to characterize the P1, P2 and phase averaged emission of the Geminga pulsar between 100 MeV and 100 Gev. The normalization factor, N_0, is given in unit of 10^{-10}MeV s^{-1} cm^{-2}. The first error is statistical whereas the second is systematic arising from the uncertainties in the Galactic diffuse model, see Section 6.1.5.

	N_0	α	E_c [GeV]	b
P1	$3.0 \pm 0.3 \pm 0.3$	$1.12 \pm 0.04 \pm 0.04$	$1.2 \pm 0.1 \pm 0.2$	$0.81 \pm 0.04 \pm 0.2$
P2	$4.3 \pm 0.4 \pm 0.4$	$0.78 \pm 0.03 \pm 0.03$	$1.1 \pm 0.1 \pm 0.2$	$0.70 \pm 0.03 \pm 0.2$
PA	$28.3 \pm 1.8 \pm 3$	$0.94 \pm 0.02 \pm 0.04$	$0.8 \pm 0.1 \pm 0.1$	$0.67 \pm 0.02 \pm 0.2$

TABLE 6.3: Parameters obtained with the likelihood method using a power-law function with a sub-exponential cut-off to characterize the P1, P2 and phase averaged emission of the Geminga pulsar between 100 MeV and 100 Gev. The normalization factor, N_0, is given in unit of 10^{-10}MeV s^{-1} cm^{-2}. The first error is statistical whereas the second is systematic arising from the uncertainties in the Galactic diffuse model, see Section 6.1.5.

The log-likelihood values, see Chapter 4.2.1, computed for each phase region are given in Table 6.4 for both exponential and sub-exponential cut-off. The deviation between the exponential and sub-exponential cut-off is also given, assuming the exponential cut-off to be the null hypothesis. The significance of the deviation between both spectral shapes is computed as following:

$$S = \sqrt{-2(\mathcal{L}_{exp} - \mathcal{L}_{sub})}, \tag{6.2}$$

where $\mathcal{L}_{exp}$ and $\mathcal{L}_{sub}$ denote the log-likelihood values computed for the exponential and sub-exponential cut-off, respectively.

	$\mathcal{L}_{exp}$	$\mathcal{L}_{sub}$	Significance
P1	-26053	-26031	7 σ
P2	40598	40661	11 σ
PA	2458681	2458969	24 σ

TABLE 6.4: Log-likelihood values computed for each phase region assuming a power-law with exponential and sub-exponential cut-off spectral function with the significance of the deviation of the sub-exponential cut-off from the exponential cut-off.

Besides the fact the the b parameter is significantly smaller than 1, the sub-exponential cut-off appears to be in better agreement with the data than the exponential cut-off, by comparing the likelihood values. The sub-exponential cut-off results in a deviation of 6 σ, 11 σ and 22 σ with respect to the exponential cut-off for P1, P2 and the phase-averaged, respectively.

Characterization of the pulsed emission above 10 GeV

In order to characterize the pulsed emission at VHE, the emission from P1 and P2 was fit above 10 GeV to a simple power-law defined as:

$$F(E) = N_0 \left(\frac{E}{E_0}\right)^{-\alpha} \tag{6.3}$$

The results of the fits are shown in Table 6.5.

	N_0	α
P1	$(5.9 \pm 1.4) \times 10^{-5}$	5.3 ± 0.7
P2	$(7.2 \pm 0.1) \times 10^{-4}$	5.2 ± 0.3

TABLE 6.5: Results of the likelihood fit of P1 and P2 spectral energy distribution with a power law above 10 GeV. The normalization factor, N_0, is given in unit of 10^{-10}MeV s^{-1} cm^{-2}.

The statitical error contour was also computed above 10 GeV as done in (Abdo et al., 2010d). In order to compute the error contour, we first have to estimate the error on the flux calculation, $\Delta F(E)$, defined as:

$$\Delta F(E) = F(E)\sqrt{\frac{N_{err}^2}{N_0^2} + \log^2\left(\frac{E}{E_0}\sigma_\alpha^2\right)}, \tag{6.4}$$

where N_{err} and σ_α are the statistical errors on the normalization factor and the spectral index, respectively. The computed SEDs for P1, P2 and the phase averaged emission of the Geminga pulsar are shown in Figure 6.2 and 6.3.

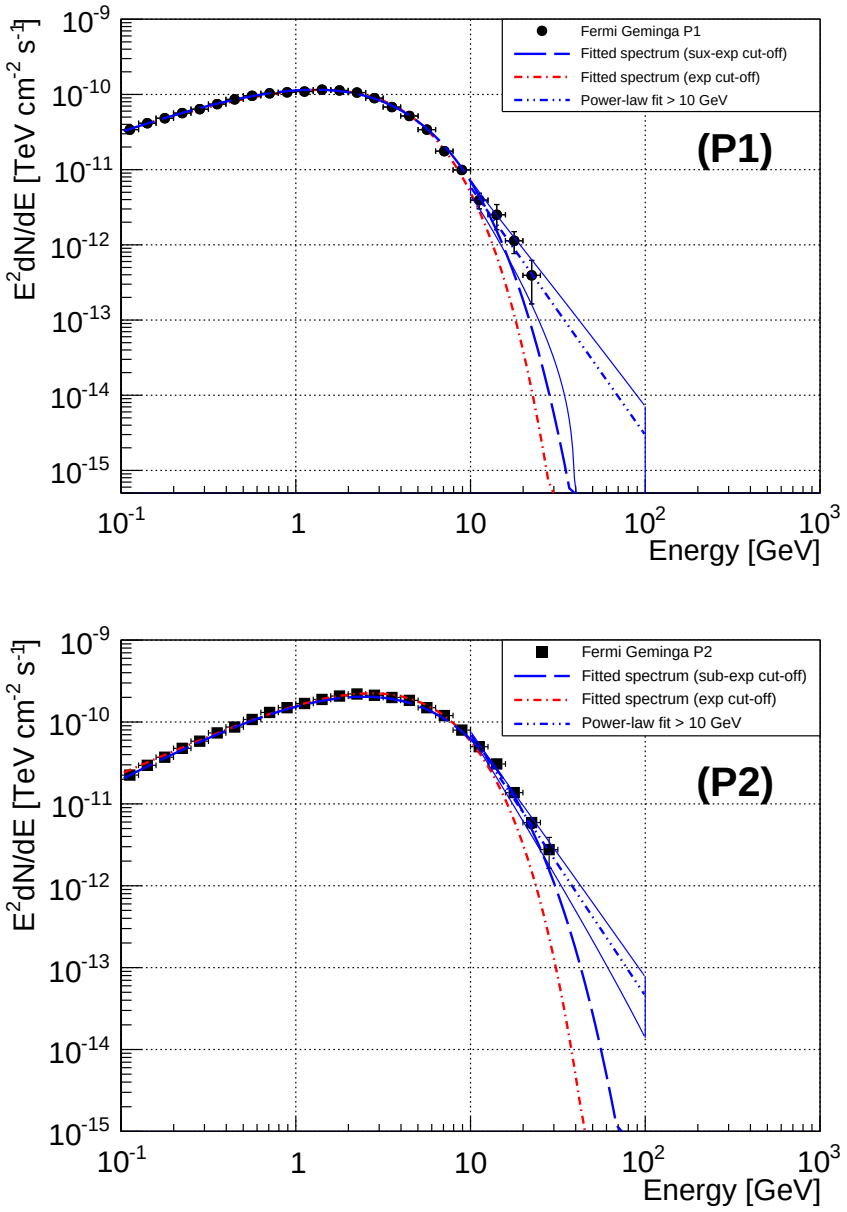

FIGURE 6.2: SED computed using the likelihood method for P1 (top) and P2 (bottom). The red dot-dashed line represents the SED fit to a power-law with an exponential cut-off and the blue dashed line the fit to a power-law with a sub-exponential cut-off.

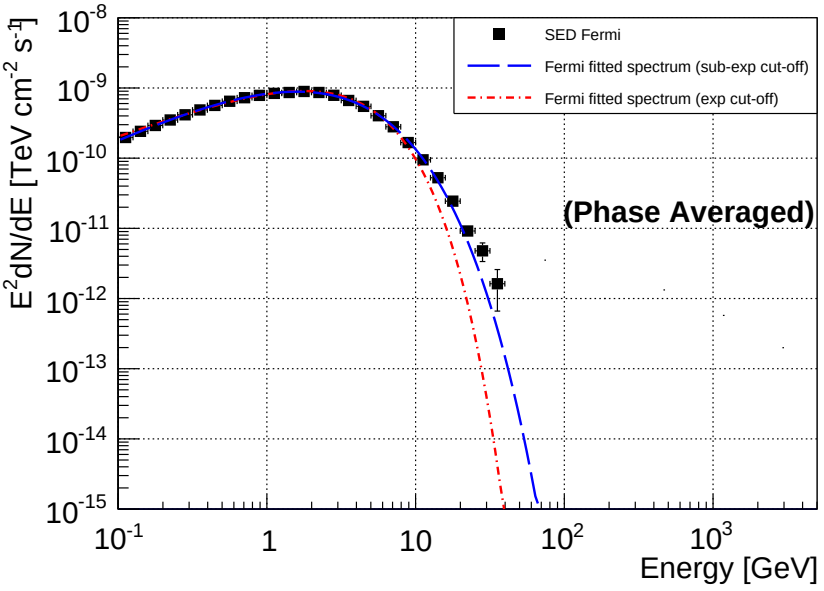

FIGURE 6.3: SED computed using the likelihood method for phase-averaged emission from the Geminga pulsar. The red dot-dashed lines represent the SED fit to a power-law with an exponential cut-off and the blue dashed lines the fit to a power-law with a sub-exponential cut-off. The blue dot-dot-dashed line is the extrapolation above 10 GeV using a simple power-law function.

6.1.4 Finer Phase-resolved SED

The analysis made by the LAT collaboration using one year of data showed that the SED was well characterized by a power-law with an exponential cut-off (b=1 in Eq 6.1) using fine binning in phase. For this analysis they set bins in phase such as each bin contains 2000 photons. We recomputed the spectra, for P1 and P2, with a fine binning using more statistics. Two procedures were carried out, (i) using equal bins in phase ($\Delta\phi = 0.01$) within the signal regions and (ii) considering several extensions in phase within the signal regions around the peaks center. For both cases the SED was characterized using a power-law function with a sub-exponential cut-off ($b < 1$). The results of the calculation using equal bins in phase are shown in Table 6.6. The evolution of the b parameter together with the light curve are plotted in Figure 6.4. Smaller bin widths than 0.01 in phase were investigated but the lack of statistics above 10 GeV made the restults irrelevant for this study, as the difference between an exponential and sub-exponential cut-off appears at these energies. The resulting SEDs are shown in Figures 6.6 and 6.7 for P1 and P2, respectively.

To study the SED using several widths within the signal region, I considered bin sizes between 0.01 in phase and the full signal regions.. The results of the computed SEDs are shown in Table 6.7. The evolution of the b-parameter is plotted according

Phase region	N_0	α	E_c [GeV]	b
0.066 - 0.076	$0.6 \pm 0.1 \pm 0.1$	$-1.18 \pm 0.10 \pm 0.05$	$1.1 \pm 0.3 \pm 0.2$	$0.76 \pm 0.08 \pm 0.02$
0.076 - 0.086	$0.6 \pm 0.1 \pm 0.1$	$-1.14 \pm 0.08 \pm 0.05$	$1.2 \pm 0.3 \pm 0.2$	$0.82 \pm 0.08 \pm 0.02$
0.086 - 0.096	$0.5 \pm 0.1 \pm 0.1$	$-1.20 \pm 0.06 \pm 0.05$	$1.6 \pm 0.3 \pm 0.2$	$0.91 \pm 0.08 \pm 0.03$
0.096 - 0.106	$0.7 \pm 0.1 \pm 0.1$	$-1.04 \pm 0.08 \pm 0.04$	$1.0 \pm 0.3 \pm 0.1$	$0.79 \pm 0.08 \pm 0.02$
0.106 - 0.116	$0.4 \pm 0.1 \pm 0.1$	$-1.18 \pm 0.08 \pm 0.05$	$1.5 \pm 0.4 \pm 0.2$	$0.88 \pm 0.10 \pm 0.03$
0.565 - 0.575	$0.9 \pm 0.1 \pm 0.1$	$-0.78 \pm 0.07 \pm 0.03$	$1.2 \pm 0.3 \pm 0.2$	$0.74 \pm 0.06 \pm 0.02$
0.575 - 0.585	$1.3 \pm 0.3 \pm 0.2$	$-0.69 \pm 0.07 \pm 0.03$	$0.8 \pm 0.3 \pm 0.1$	$0.63 \pm 0.05 \pm 0.02$
0.585 - 0.595	$0.8 \pm 0.1 \pm 0.1$	$-0.90 \pm 0.05 \pm 0.04$	$1.7 \pm 0.3 \pm 0.2$	$0.79 \pm 0.05 \pm 0.02$
0.595 - 0.605	$1.0 \pm 0.2 \pm 0.2$	$-0.77 \pm 0.07 \pm 0.03$	$0.9 \pm 0.3 \pm 0.1$	$0.67 \pm 0.05 \pm 0.02$

TABLE 6.6: Parameters obtained with the likelihood method for the sub-exponential cut-off spectral shapes between 100 MeV and 100 GeV using bins of 0.01 in phase, for P1 (top) and P2 (bottom). The normalization factor, N_0, is given in unit of 10^{-10}MeV s^{-1} cm^{-2}. The first error is statistical whereas the second is systematic arising from the uncertainties in the Galactic diffuse model, see Section 6.1.5.

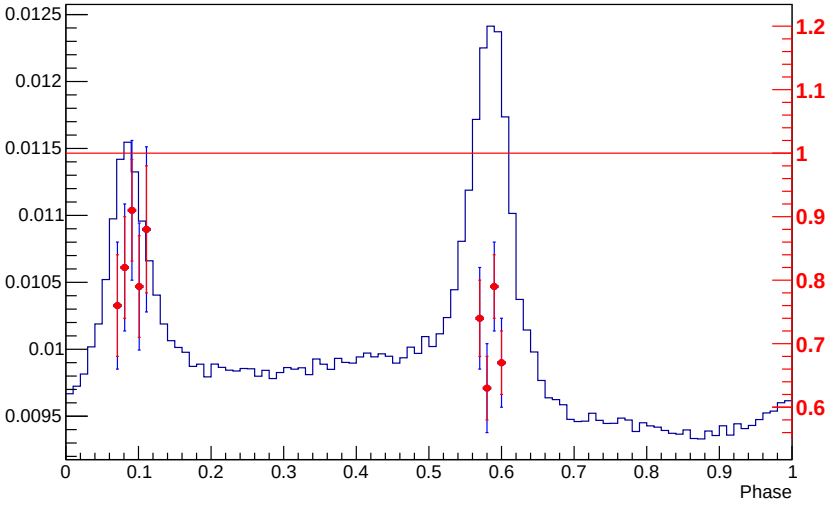

FIGURE 6.4: Evolution of the b-parameters depending on the phase considered. Bins of 0.01 in phase were considered for the calculation. The red bars represent the statistical errors whereas the blue bars represent the sum of statistical and systematic errors.

to the region considered in Figure 6.5. The resulting SEDs are shown on Figures 6.8 and 6.9 for P1 and P2, respectively.

Phase region	$\Delta\phi$	N_0	α	E_c [GeV]	b
0.075 - 0.085	0.010	$0.6 \pm 0.1 \pm 0.1$	$1.13 \pm 0.01 \pm 0.05$	$1.1 \pm 0.3 \pm 0.2$	$0.80 \pm 0.08 \pm 0.02$
0.070 - 0.090	0.020	$1.3 \pm 0.2 \pm 0.2$	$1.13 \pm 0.05 \pm 0.05$	$1.1 \pm 0.2 \pm 0.2$	$0.78 \pm 0.05 \pm 0.02$
0.066 - 0.094	0.028	$1.5 \pm 0.2 \pm 0.3$	$1.12 \pm 0.04 \pm 0.04$	$1.3 \pm 0.2 \pm 0.2$	$0.84 \pm 0.05 \pm 0.03$
0.066 - 0.100	0.034	$1.9 \pm 0.2 \pm 0.3$	$1.16 \pm 0.04 \pm 0.05$	$1.3 \pm 0.2 \pm 0.2$	$0.83 \pm 0.04 \pm 0.02$
0.066 - 0.105	0.039	$2.2 \pm 0.2 \pm 0.4$	$1.15 \pm 0.04 \pm 0.05$	$1.2 \pm 0.2 \pm 0.2$	$0.82 \pm 0.04 \pm 0.02$
0.066 - 0.110	0.044	$2.5 \pm 0.2 \pm 0.4$	$1.13 \pm 0.04 \pm 0.05$	$1.2 \pm 0.1 \pm 0.2$	$0.81 \pm 0.04 \pm 0.02$
0.066 - 0.118	0.052	$3.0 \pm 0.3 \pm 0.3$	$1.12 \pm 0.04 \pm 0.04$	$1.2 \pm 0.1 \pm 0.2$	$0.81 \pm 0.04 \pm 0.2$
0.585 - 0.595	0.010	$0.8 \pm 0.1 \pm 0.1$	$0.90 \pm 0.05 \pm 0.04$	$1.8 \pm 0.3 \pm 0.3$	$0.79 \pm 0.05 \pm 0.02$
0.580 - 0.600	0.020	$2.2 \pm 0.3 \pm 0.3$	$0.77 \pm 0.04 \pm 0.03$	$1.0 \pm 0.2 \pm 0.1$	$0.67 \pm 0.04 \pm 0.02$
0.580 - 0.605	0.025	$2.7 \pm 0.3 \pm 0.4$	$0.78 \pm 0.04 \pm 0.03$	$1.0 \pm 0.2 \pm 0.1$	$0.68 \pm 0.03 \pm 0.02$
0.575 - 0.607	0.032	$3.2 \pm 0.3 \pm 0.5$	$0.80 \pm 0.04 \pm 0.03$	$1.1 \pm 0.2 \pm 0.2$	$0.69 \pm 0.03 \pm 0.02$
0.570 - 0.607	0.037	$3.6 \pm 0.3 \pm 0.5$	$0.80 \pm 0.03 \pm 0.03$	$1.1 \pm 0.1 \pm 0.2$	$0.70 \pm 0.03 \pm 0.02$
0.565 - 0.607	0.042	$4.3 \pm 0.4 \pm 0.4$	$0.78 \pm 0.03 \pm 0.03$	$1.1 \pm 0.1 \pm 0.2$	$0.70 \pm 0.03 \pm 0.2$

TABLE 6.7: Parameters obtained with the likelihood method for the sub-exponential cut-off spectral shapes between 100 MeV and 100 GeV using several phase extensions within the P1 (top) and P2 (bottom) signal regions. The normalization factor, N_0, is given in unit of 10^{-10}MeV s^{-1} cm^{-2}. The first error is statistical whereas the second is systematic arising from the uncertainties on the Galactic modelization, see Section 6.1.5.

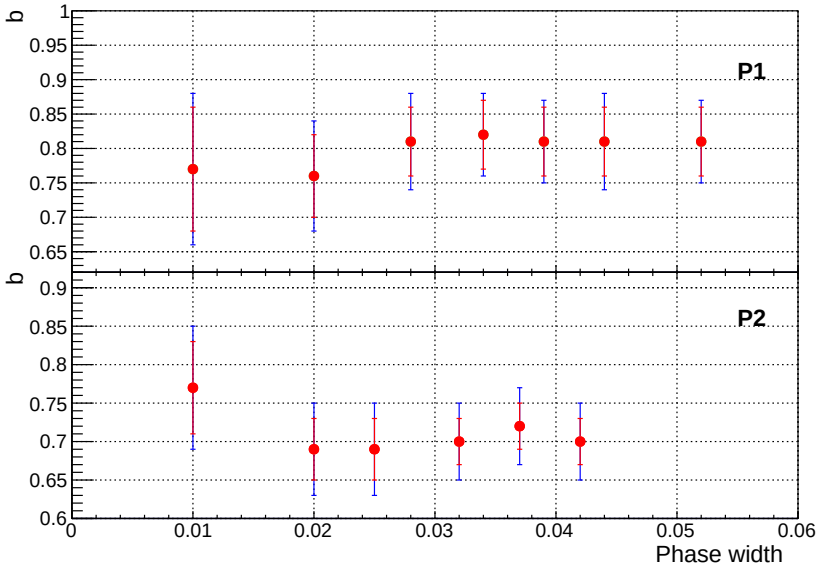

FIGURE 6.5: Evolution of the b parameter depending on the width of the signal region considered. Statistical errors are represented by the red bars, the blue bars represent the sum of systematic and statistical uncertainties.

6.1.5 Study of the systematic errors

The study of the b parameter enables us to determine out whether the SED of the Geminga pulsar is better characterized by a power-law function with an exponential (b=1) or a sub-exponential (b < 1) cut-off. The study of the spectral shape is fundamental to understand the VHE emission mechanisms. The previously computed values tend to disfavor the exponential cut-off with respect to the sub-exponential cut-off. In order to estimate the computed values of the b parameter, the systematic errors were investigated. The systematic errors of the LAT arise from the imperfect knowledge of the IRFs (effective area, energy dispersion, spatial resolution, etc) and of the Galactic diffuse component considered in the source model. The systematic errors are dominated by the uncertainties of the Galactic emission (Abdo et al., 2013). In order to estimate the systematic errors of the computed parameter due to the imperfect knowledge of the Galactic emission, the data were re-analyzed fixing the normalization factor of the Galactic diffuse component to (1 ± 0.06) times the best fit value. This estimation was done considering the phase-averaged emission of the Geminga pulsar in order to gather more statistics. The computed values for the parameters considering the fluctuation of the Galactic component, for a power-law with an exponential and sub-exponential cut-off are shown in Table 6.8.

Source model (Exp)	N_0	α	E_c [GeV]
Galactic +	28.4 ± 0.1	1.23 ± 0.01	2.33 ± 0.01
Galactic -	28.8 ± 0.1	1.22 ± 0.01	2.29 ± 0.01
Relative error	1%	1 %	2 %

Source model (Sub-exp)	N_0	α	E_c [GeV]	b
Galactic +	46.2 ± 1.8	0.97 ± 0.02	0.9 ± 0.1	0.69 ± 0.01
Galactic -	54.1 ± 2.7	0.90 ± 0.02	0.7 ± 0.1	0.65 ± 0.01
Relative error	9%	4 %	14 %	3 %

TABLE 6.8: Calculation of the spectral parameter fitting the SED to a power-law with an exponential (top) and sub-exponential (bottom) cut-off and systematics errors, using biased normalization factor for the Galactic component. The Galactic +/- source models are source models used setting the normalization to the best value (1+/-0.06).

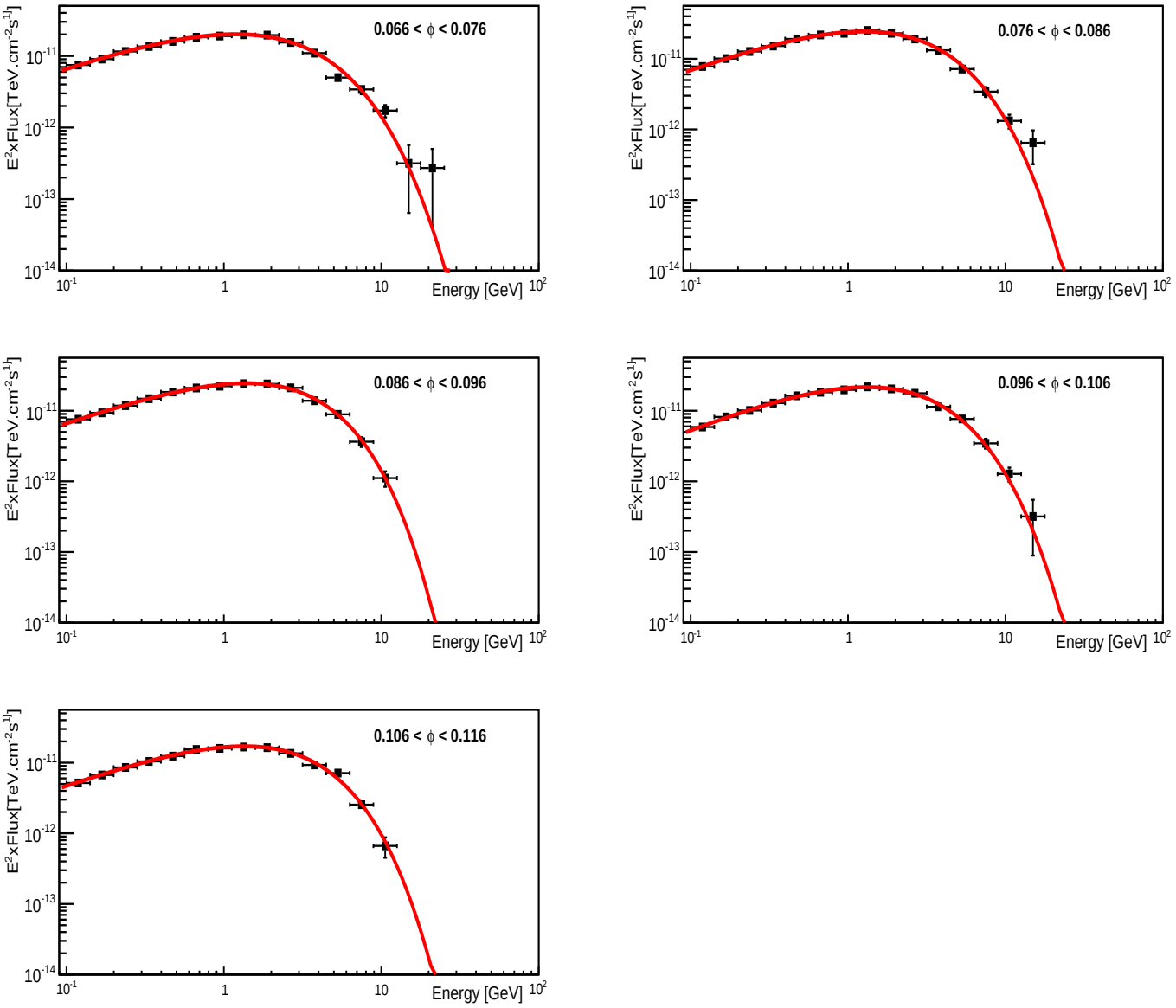

FIGURE 6.6: SED computed using bins of 0.01 in phase within the P1 signal region.

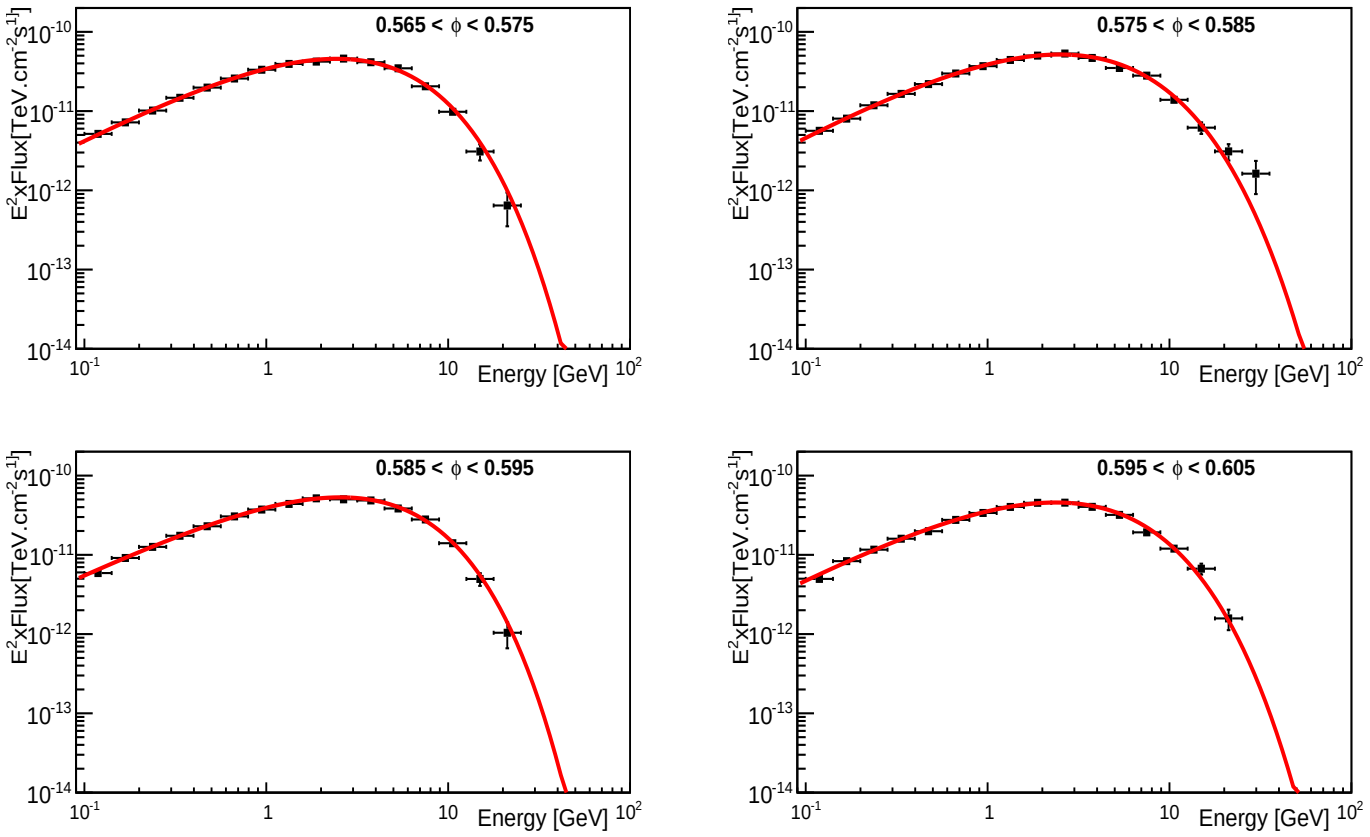

FIGURE 6.7: SED computed using bins of 0.01 in phase within the P2 signal region.

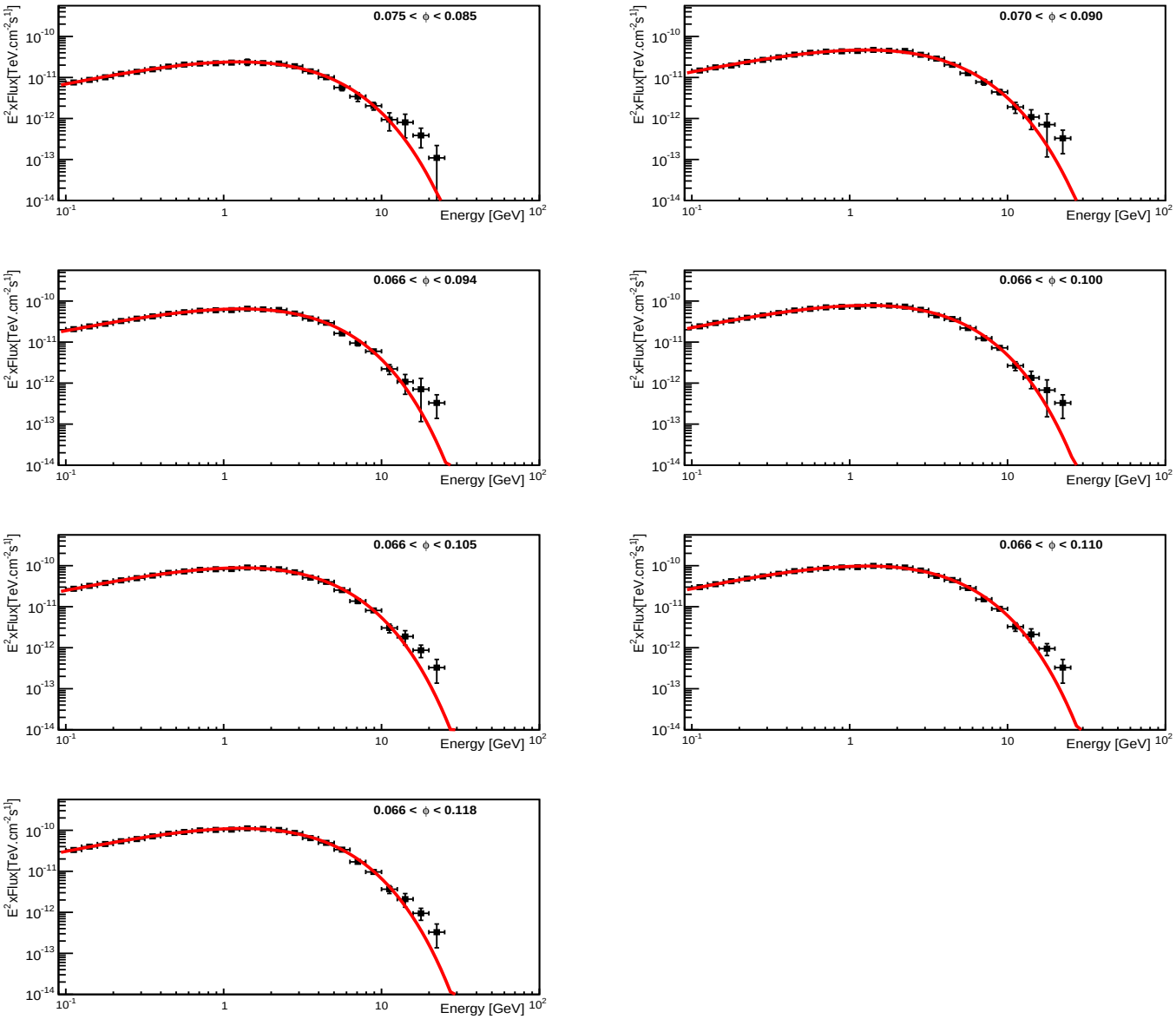

FIGURE 6.8: SED computed using several phase bin sizes within the P1 signal region.

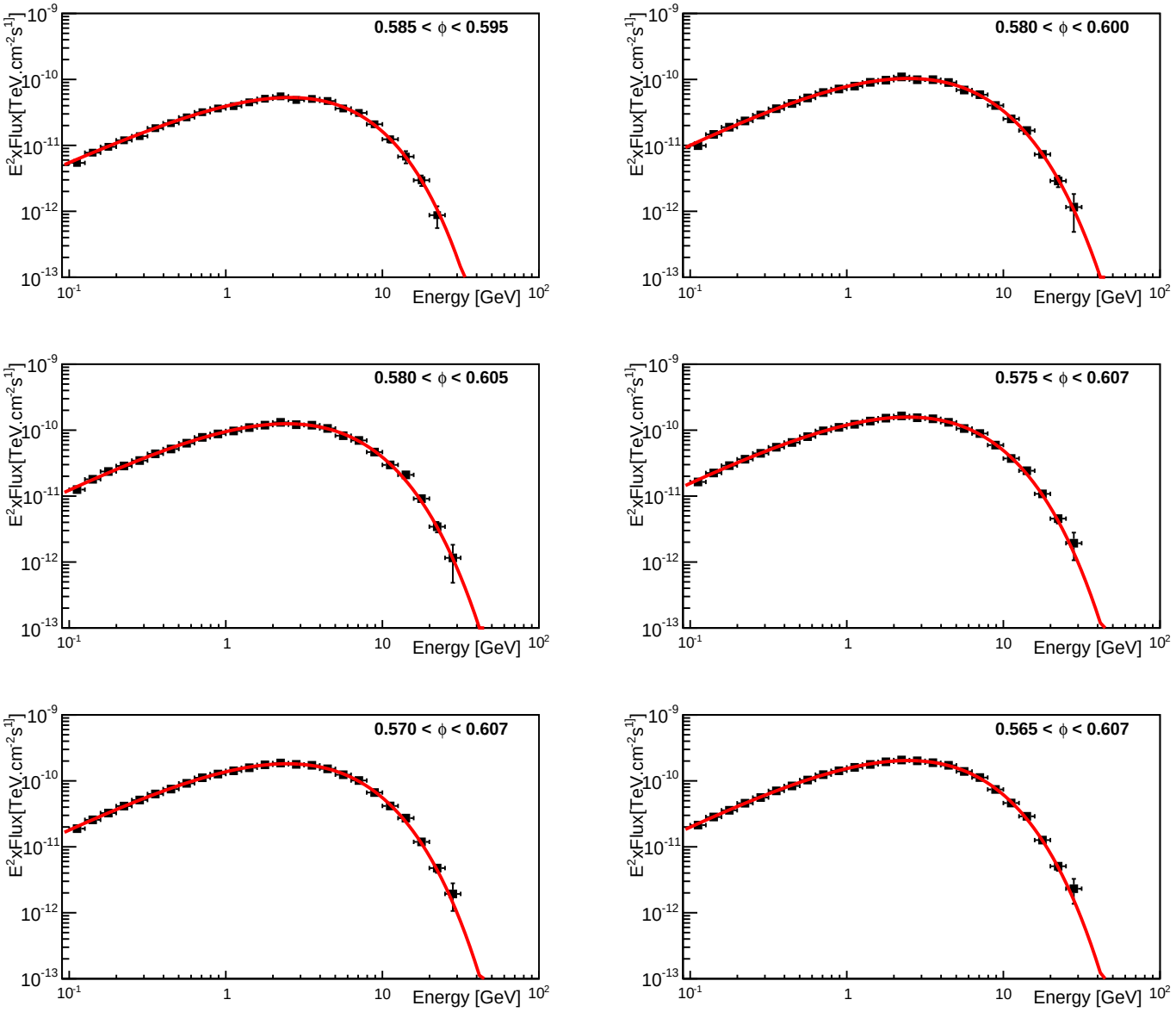

FIGURE 6.9: SED computed using several phase bin sizes within the P2 signal region.

6.2 MAGIC observations and data analysis

So far, only the Crab and Vela pulsars have been detected by IACTs. The detection of the Geminga pulsar by Cherenkov telescopes could shed light on the emission location and mechanisms at work for VHE photons emission in such an aged pulsar. The Geminga pulsar is observable from December to March from the location of the MAGIC telescopes at zenith angles below 35°. The data analysis presented in this thesis was processed using the standard MAGIC analysis chain *MARS* (Zanin et al., 2013). However, for more consistency with the results of the pulsed analysis using *Fermi* LAT data, the phase of the events was computed using the same program, *tempo2* (Hobbs et al., 2006). Besides the search for pulsation, we also investigated the presence of a nebula surrounding the Geminga pulsar.

6.2.1 Data set

Observations of the Geminga pulsar and nebula were performed during the cycle-8, between December 2012 and March 2013, with the upgraded MAGIC telescopes (Aleksic et al., 2014). As previously mentioned for the Crab analysis, this data sample had to be split into two due to the upgrade of the LUTs in January 2013. The analysis of the nebula, however, due to the large extension observed by Milagro and HAWC, was processed using a dedicated diffuse MC. During this period, a total of $\sim$ 75 hours were taken at zenith angles below 35° to ensure the lowest possible energy threshold. The observations were performed in the so-called wobble mode (Fomin et al., 1994), where the source is offset 0.4° from the camera center. The data were taken only during dark time, i.e., no moon or twilight data were taken. The data selection was done checking the event rates. Only subruns with a rate after cleanning higher than 180 Hz were kept for the analysis. All data taken during bad weather or technical problems were discarded, resulting in 63 hours of good data quality. A detailed overview of the effective observation time per night is given in Table 6.9

6.2.2 Search for pulsation

To search for pulsation from the Geminga pulsar, we phased the events using *tempo2* (Hobbs et al., 2006). The *tempo2* software is made compatible with the MAGIC data format by means of a plug-in developed within the MAGIC collaboration. This software was chosen instead of *psearch* (Lopez, 2006) for consistency

Night	Time [hour]
2012-12-10	1.7
2012-12-14	1.9
2012-12-15	3.9
2012-12-16	2.3
2012-12-17	2.3
2012-12-18	4.7
2012-12-19	3.0
2012-12-21	1.2
2012-12-22	0.3
2013-01-05	2.5
2013-01-06	1.9
2013-01-09	2.3
2013-01-10	2.2
2013-01-11	2.2
2013-01-12	2.0
2013-01-13	2.1
2013-01-14	3.7
2013-01-15	2.3
2013-01-16	3.1
2013-01-17	2.6
2013-01-18	1.3
2013-02-06	0.3
2013-02-08	2.0
2013-02-09	2.1
2013-02-10	1.7
2013-02-11	2.0
2013-02-12	4.0
2013-02-13	1.3
2013-03-12	0.6
Total	63

TABLE 6.9: Geminga effective observation time per night for cycle-8 data.

with the *Fermi* analysis. The ephemeris was provided by the *Fermi*-LAT collaboration[2]. For the pulsed analysis, we used the same cuts as those computed for the Crab pulsar analysis, cycle-8, see Section 5.2.2, with two differents cuts for the period ST0301 and ST0302. The light curve was computed in three different energy ranges; above 50 GeV, 100-200 GeV and 50-200 GeV. The signal regions were set according to the values computed from the *Fermi* analysis data, i.e., (phase 0.066 - 0.118) for P1 and (phase 0.565 - 0.607) for P2, see Section 6.1.2. The computed light curve is shown in Figure 6.10. We evaluated the significance of the pulsed signal using the Li & Ma formula 17 (Li and Ma, 1983) and the *H-test* (de Jager

[2]http://www.slac.stanford.edu/~kerrm/fermi_pulsar_timing/J0633+1746/html/J0633+1746_54683_56587_chol.par

et al., 1989), however, the Li & Ma method is more sensitive than other methods, such as the *H-test*, due to the fact that the position of the peaks is known a priori. The background is estimated from the off-pulse region, defined as (0.70 - 0.95) in phase. We computed the significance for P1, P2, and the sum of both peaks. The results of the statistical tests are shown in Table 6.10. No significant pulsation was found in MAGIC data in any of the energy ranges investigated.

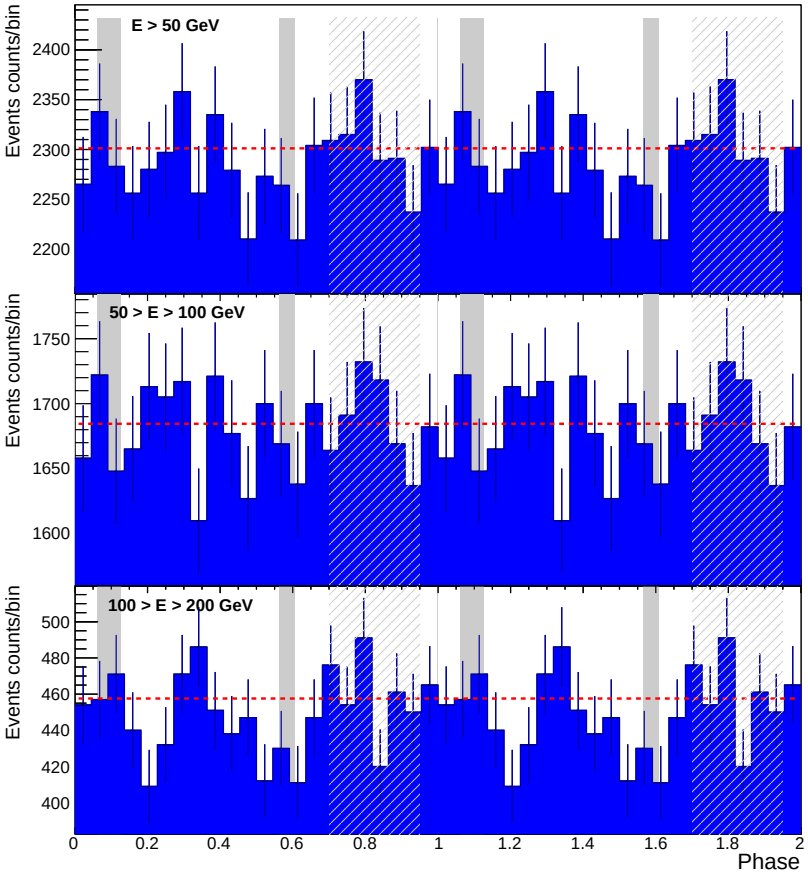

FIGURE 6.10: Light curves of the Geminga pulsar obtained with MAGIC for different energy bins. From top to bottom: above 50 GeV, 50-100GeV and 100-200 GeV. Two cycles are plotted for clarity. The bin width corresponds to $\sim$ 10.8 ms (1/22 of the Geminga rotational period). The shaded areas show the positions of P1 (main pulse) and P2 (interpulse). The white area shows the off-region. The dashed red line represents the averaged number of events in the background region.

Energy range (GeV)	P1	P2	P12	H-test
≥ 50	0.2σ	-0.1σ	0.1σ	0.2σ
50-100	-0.2σ	-0.2σ	0.0σ	0.1σ
100-200	0.7σ	-1.4σ	-0.3σ	1.5σ

TABLE 6.10: Significance computed for P1, P2 and the sum of both peaks. The significances were computed using Li & Ma and the *H-test*.

6.2.3 Search for a surrounding nebula

The search for a steady extended emission was done computing the signal to noise ratio around the Geminga pulsar. Two methods were used, (i) checking at the distribution of the θ^2 parameter and (ii) the calculation of sky maps around the Geminga pulsar. For both methods the cuts were computed using a contemporaneous Crab Nebula sample. Due to the uncertainty regarding the size of the nebula, several extensions around the Geminga pulsar were considered, assuming a value for the signal region of $\theta^2 \lesssim 0.04$, 0.06, 0.08 and 0.1 deg^2. The results of the Li & Ma significance computed for each extension and for different energy ranges are shown in Table 6.11. The results of the θ^2 distribution is shown in Figure 6.11, for the search of signal at low energies, full energy range and high energies.

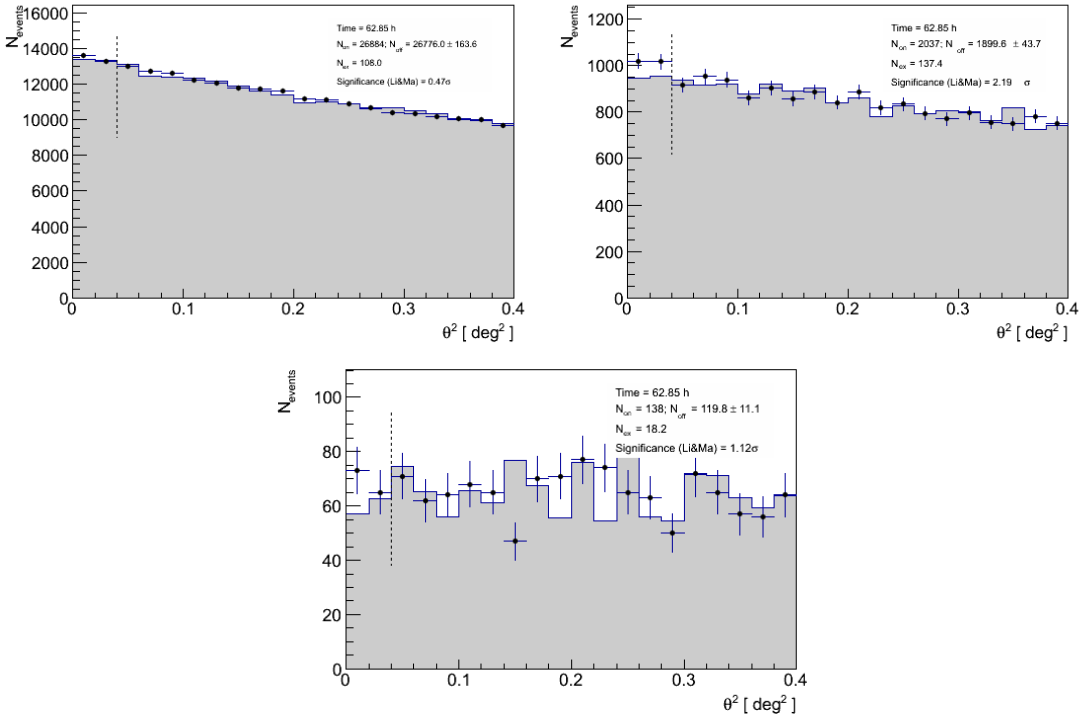

FIGURE 6.11: Distribution of the θ^2 values for several energy ranges: low energies (top left), full range (top right) and high energies (bottom). The signal regions was set to $\theta^2 = 0.04$.

The sky map of the region around the Geminga pulsar was also produced for low energies, full energy range and high energies. The significance in each bin of the sky map (z-axis) was computed using the Li & Ma method applied on a background estimate. Figure 6.12 shows the sky map computed around the Geminga pulsar for the steady emission using MAGIC data. The position of the Geminga pulsar is marked with a cross. The white circle represents the standard deviation of Gaussian function used for the smearing of the sky map.

Signal region [deg^2]	LE	FR	HE
0.04	0.47	2.19	1.12
0.06	0.09	1.80	0.69
0.08	1.00	2.04	0.58
0.1	1.42	2.11	1.19

TABLE 6.11: Results of the Li & Ma statistical test computed for the search of a signal using the θ^2 distribution. The statistical test was computed assuming several extension of the surrounding nebula for the low, full and high energy ranges.

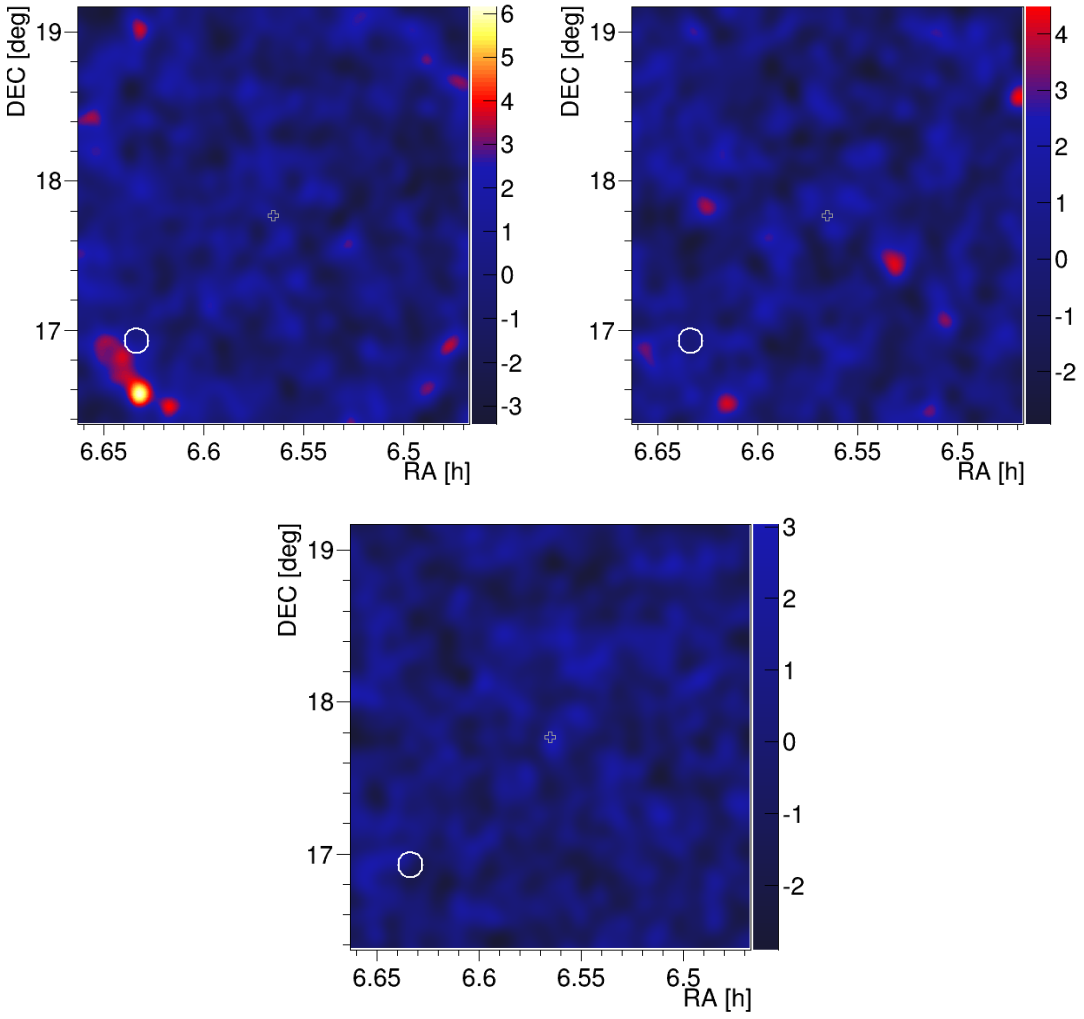

FIGURE 6.12: Full energy range sky map computed around the location of the Geminga pulsar for several energy ranges: Low energy (top left), full range (top right) and high energy (bottom). The cross at the center of the map represents the Geminga pulsar location. The white circle represents the function used for the deconvolution of the sky map.

No significant emission was found from the Geminga nebula above 50 GeV.

6.2.4 Upper limits computation

The search for a signal from the Geminga pulsar and its surrounding nebula resulted in no significant detection. We computed the upper limits on the emission from the pulsar and the nebula using the Rolke method (Rolke and López, 2001) assuming a Poissonian background and requiring a 95% confidence level. For the pulsar upper limits computation, the spectral shape assumed results of the from the extrapolation of P1 and P2 SEDs above 10 GeV with a power-law function, using the *Fermi*-LAT data, see Table 6.5. The differential upper limits computed above 50 GeV for the pulsed emission are shown in Figure 6.13 by the blue arrows. The blue lines on top of the arrows represent the spectral slope assumed for the upper limits computations. The blue dashed line and red dot-dashed line represent the SED fit to a power-law function with a sub-exponential and exponential cut-off, respectively. The dot-dot-dashed blue lines represent the fit of *Fermi*-LAT data above 10 GeV to a power-law function. The statistical error contours for each energy are also plotted for the power law fits at HE, and are computed in the same way as in (Abdo et al., 2010d).

The differential upper limits for the nebula emission above 50 GeV were computed assuming a spectral index of -2.6. In order to estimate the error on the upper limits due to the assumption of such a spectral index value, we also computed the fluctuation of the upper limits by computing them assuming spectral indices of -2.0 and -2.8, which is the typical range of spectral index for PWNe (Kargaltsev et al., 2013). A fluctuation of 13% is observed in the upper limits computation below 120 GeV. For higher energies the fluctuations are below 10%. The computed differential upper limits for the steady emission are represented by the blue arrows in Figure 6.14. The computed phase-averaged SED using 5 years of *Fermi*-LAT data is represented by the black points. The dashed blue line is the result of *Fermi* LAT spectral shape computation for the phase-averaged emission using a power-law with a sub-exponential cut-off, and the red dash-dot line using a power-law with an exponential cut-off. The green point represents the flux level of the Geminga Nebula as reported by MILAGRO (Abdo et al., 2009c).

6.3 Results and discussion

During the Winter 2012/13, the Geminga pulsar and its surrounding nebula were observed for 75 hours by the MAGIC telescopes, to search for emission from the pulsar and its surrounding nebula at VHE. The analysis of 63 hours high quality data resulted in no significant detection. Thus, we computed upper limits above 50 GeV on both pulsed and steady emission. Besides MAGIC data, 5 years of

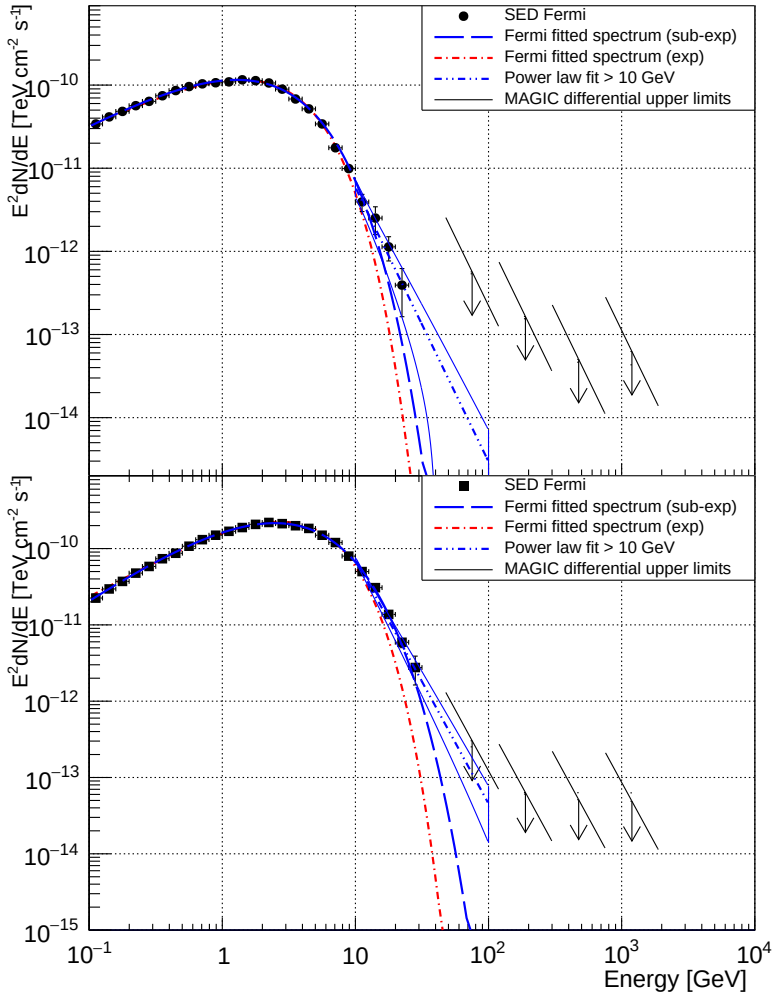

FIGURE 6.13: P1 (top) and P2 (bottom) SED. The differential upper limits are represented by the blue arrows. The blue dashed line represents the SED computed using 5 years of *Fermi*-LAT data using a power-law function with a sub-exponential cut-off and the red dash-dot line using a power-law with an exponential cut-off. The dot-dot-dashed line is the result of the fit of the Fermi data above 10 GeV with a power-law.

Fermi-LAT data were analyzed to derive the pulsed and phase-averaged emission.

The upper limits on the pulsed emission computed using the MAGIC data are at a higher flux level than the power law extension computed above 10 GeV using the *Fermi*-LAT data. The SEDs computed using the *Fermi*-LAT data is represented by a power-law with a sub-exponential cut-off. As reported by (Lyutikov, 2012), a simple power-law could also characterize the emission at high energies, but more statistics would be required to distinguish between both spectral shapes. The upper limits computed using the MAGIC data, being at higher flux level than the

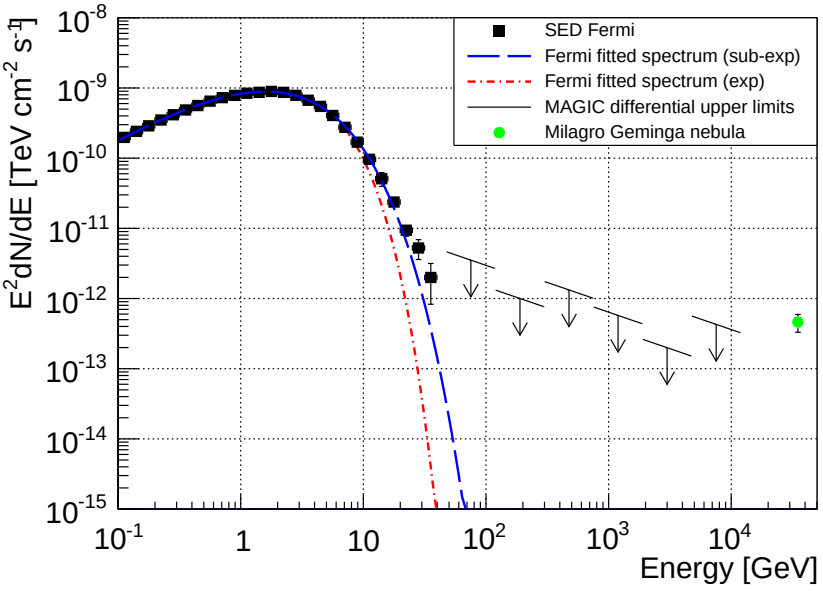

FIGURE 6.14: Phase-averaged spectral energy distribution. The differential upper limits are represented by the blue arrows. The blue dashed lines represent the SED computed using 5 years of *Fermi*-LAT data using a power-law function with a sub-exponential cut-off and the red dash-dot line using a power-law with an exponential cut-off. The green point represents the flux level of the Geminga Nebula as seen by MILAGRO.

Fermi-LAT extrapolation, do not constrain the spectral shape at high-energy. As no clear distinction is made regarding the SED shape, Therefore, the mechanism responsible for the high energy emission from the Geminga pulsar is difficult to establish. At high energy, the emission due to synchro-curvature radiation and inverse Compton scattering are expected to exhibit different spectral shapes. For example, in the framework of the outer-gap model, where the high-energy emission takes place at high altitudes from the neutron star (Cheng et al., 1986b,c), a curvature or synchro-curvature radiation mechanism would exhibit a spectral shape well characterized by an exponential cut-off (Prosekin et al., 2013; Viganò et al., 2015). As the radiation is very sensitive to the pitch angle of the radiating particles, the sum of the emission from particles with the same energy but different angles results in a less abrupt cut-off. Furthermore, calculations of the outer-gap magnetic-field-aligned electric field evolution (Hirotani, 2006b, 2015b) show that the accelerating electric field depends on the height in the gap and reaches a maximum in the center of the gap. Distinct heights with different values of the electric field would accelerate particles at different energies, resulting in a spread of the cut-off energy values. A strong dependency of the cut-off energy on the accelerating electric field is reported by (Viganò et al., 2015). Such a behavior of the cut-off values was reported for the Geminga pulsar (Abdo et al., 2010b). The LAT collaboration studied the phase-resolved evolution of the cut-off energy

for the Geminga pulsar over the whole pulsar rotation. The results show that within the P1 and P2 phase regions, where the computed cut-off values are the highest, these values vary. Considering wider phase ranges, the fluctuations of the cut-off value would result in an a sub-exponential cut-off spectral shape. However, our calculations of the SED using finer bins around the pulses center tend to discard the exponential cut-off as the best fit values computed for the b parameter are significantly smaller than 1. In the case of synchro-curvature radiation, this deviation can arise from the caustic emission (Hirotani, 2006b), i.e, overlapping of photons emitted at different heights and along different magnetic field lines. The caustic effect being more important for P2 than P1, due to the curvature of the magnetic field line, would explain the greater values of b for P1 with respect to P2.

In the case of an inverse Compton (IC) emission or synchroton self-Compton within the outer gap (Hirotani, 2015b), the break in the spectral shape would correspond to a break in the particle distribution function (Lyutikov, 2012) if all the emission comes from this mechanism. If the particles are distributed as a broken power-law, then the IC spectrum would appear as a broken power-law too and a high-energy power-law like tail would be seen as it is the case of the Crab pulsar (Aleksić et al., 2011; **?**) and Vela (Leung et al., 2014). However, in the case of an inverse Compton emission, the power-law tail exhibited by the Geminga pulsar would be much softer than that of the Crab (Aleksić et al., 2014), as can be seen from the spectral fit to a power-law function of the *Fermi*-LAT data above 10 GeV. A hard gamma-ray tail is not expected even if the curvature radiation is produced in a curved magnetic field close to the light cylinder (Bednarek, 2012).

The analysis of the nebula around the Geminga pulsar shows no significant detection at MAGIC energies. The presence of the nebula is unknown at the GeV scale. Indeed, the observations of the Geminga pulsar with the *Fermi*-LAT shows no evidence of a surrounding nebula. The detection of a large nebula similar to the one claimed by the Milagro Collaboration is not straightforward, as its extension is larger than the field of view of the MAGIC telescopes (Aleksić et al., 2016a). Overall, the prospects of detecting the Geminga pulsar with current Cherenkov telescopes are rather low. However, the upcoming Cherenkov Teleskope Array (CTA)(Bernlöhr et al., 2013) could, with a better sensitivity and a lower energy threshold, detect high-energy gamma-ray emission from the Geminga pulsar and thus shed light on the physics of pulsars.

Chapter 7

Evolution of the X-ray and gamma-ray efficiency of young pulsars

Pulsars have been under study for several decades. However, their emission is still poorly understood, as seen in Chapter 2. Several models have been developed in order to explain HE emission from pulsars. Three locations were proposed in the open magnetosphere, namely, the polar cap close to the neutron star surface, located above the magnetic pole, the slot gap, extending up to the null surface, and the outer gap extending from the null surface up to the LC. Several wind models assume that the HE emission arises from acceleration of charged particles beyond the LC. In order to fully understand the underlying physics of pulsars and investigate the consistency of the models describing their emission, multi-wavelengths studies are required. Recently, Vink et al. (Vink et al., 2011) studied the evolution of the X-ray and gamma-ray efficiencies of pulsars according to their age, with the X-ray and gamma-ray efficiencies defined as:

$$\eta_X = \frac{L_X}{L_{sd}}, \qquad \eta_X = \frac{L_\gamma}{L_{sd}}, \tag{7.1}$$

where L_X and L_γ denote the X-ray and gamma-ray luminosity, respectively, and L_{sd} is the spin-down luminosity, see Equation 2.1. They found a trend in the evolution of the efficiency for young pulsars ($\tau_c \leq 1.7 \times 10^4$ yrs, with τ_c the characteristic age of the pulsar, see Equation 2.4) and showed that young pulsars are efficient X-ray emitters and poor gamma-ray emitters, whereas it is the other way around for old pulsars. Furthermore, for older pulsars, both X-ray and gamma-ray efficiency appears to be constant. They also showed that the X-ray luminosity of pulsars and their surrounding PWNe are closely correlated, $L_{X,psr/pwne} \propto \dot{P}^3/P^6$ for young pulsars whereas for older pulsars $L_{X,psr/pwne} \propto \dot{P}/P^{3.5}$, where P and $\dot{P}$ are the pulsar rotation period and first period derivative, respectively. They based

their study on a compilation of X-ray pulsars (Kargaltsev, 2008) from *Chandra* (Weisskopf et al., 2000) observations within the 0.5-8 keV band, and the gamma-ray pulsars detected within the first *Fermi*-LAT catalog of gamma-ray pulsars (Abdo et al., 2010e) within the 100 MeV to 100 GeV band. Such correlation of the X-ray and gamma-ray efficiencies, and the luminosity characterization must be explained by models describing the HE emission from pulsars. Thus, these models must not only attempt to reproduce the HE emission from pulsars, but also correlate it to the X-ray emission, as observed. Such a study would be a powerful way to discriminate between current actual models describing HE emission from pulsars.

In this work, made in collaboration with Prof. Kouichi Hirotani, we analytically compute the efficiency for both X-ray and gamma-ray emission from pulsars in the framework of the outer gap model (Hirotani, 2013), using a one dimensional magnetosphere model. This enhanced model supposes the development of magnetospheric cascades from the accelerated $e^{\pm}$ within the gap. The pulsar magnetosphere is schematically depicted in Figure 7.1. In the gap, the primary $e^{\pm}$ accelerated up to a Lorentz factor $\sim 10^7$ will emit photons via curvature radiation, with energy of a few GeV. These emitted curvature photons will then create pair $e^{\pm}$ by collision with the X-ray photons present in the gap. These secondary $e^{\pm}$ created will emit secondary X-ray photons via synchrotron process, with energy from a few keV up to tens of keV. We assume the X-ray synchrotron photons to be emitted at a distance r_0 from the NS surface within the gap, see Figure 7.1. In order to estimate the efficiency of the X-ray and gamma-ray emission in this scenario, we estimate the evolution of the gap trans-magnetic-field thickness, h_m, according to the pulsar age. This estimation is done within the framework of the minimal cooling scenario (Page et al., 2004), considering both light and heavy element envelopes. We further compute the flux of secondary X-ray photons within the gap. Finally, we estimate the optical thickness due to the emission of these secondary X-ray photons in the gap, and the absorption of the curvature gamma-ray photons.

7.1 The minimal cooling scenario

Due to the extreme conditions in the core of the NS, the equation of state and the composition of the star are very complicated to establish. Some extreme models expect, due to the high matter density, quark deconfinement leading up to "Strange Stars" (Page and Usov, 2002), made entirely of deconfined quark matter. The minimal cooling scenario (Page et al., 2004) is a model of the evolution of the NS temperature, assuming that the star is devoid of any form of matter beyond the standard composition, consisting only of neutrons, protons, electrons and muons to keep the total charge of the star neutral. Furthermore, the minimal

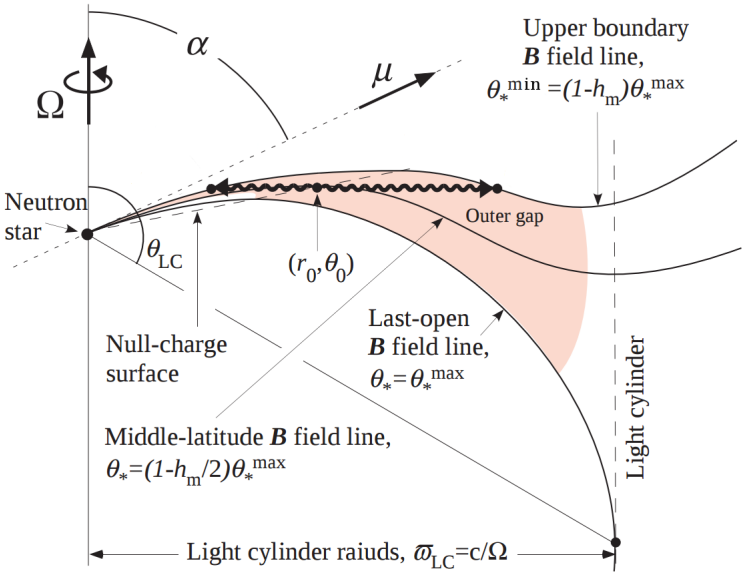

FIGURE 7.1: Side view of the pulsar magnetosphere and the outer gap region. The neutron star (filled circle on the left) rotates around the vertical with a magnetic inclination angle α. The thin solid curves denote the magnetic field lines and the dashed line denotes the null charged surface. The outer-gap region is represented by the pink area. Figure adopted from (Hirotani, 2013)

cooling scenario includes essential ingredients such as the neutron and/or proton superconductivity on the star's specific heat and the neutrino emission. This scenario is based on the APR (Akmal et al., 1998) equation of state. Within this framework, the cooling of the NS is controlled by the emission of electromagnetic radiation, emission of neutrinos and heating processes such as the rotating neutron super-fluid or magnetic field decay. The neutrino emission is strongly dominated by the emission from the core. The significant processes are related to β and inverse β decay of neutrons with protons. The simplest process is the direct Urca (DUrca) process. However, due to the small fraction of protons ($\sim 5\%$) momentum is not conserved during the process. Thus, modified Urca (MUrca) process takes place in the outer core, where a second "spectator" nucleon contributes by absorbing or giving the extra momentum required.

The photon luminosity, on the other hand, is controlled by the NS temperature. The surface or effective temperature of the NS is strongly determined by the chemical composition of its envelope. The envelope is defined as the uppermost layer, extending from the atmosphere down to a boundary where the luminosity in the envelope equals the surface luminosity, and it is several tens of meters thick. A schema of the several layers forming the NS are shown in Figure 7.2. The NS envelope presents a temperature gradient that is strongly dependent on its chemical composition. Even though the magnetic field at the surface, depending on its inclination, can affect the surface temperature, this effect it not as important as the envelope chemical composition. The chemical composition of the envelope

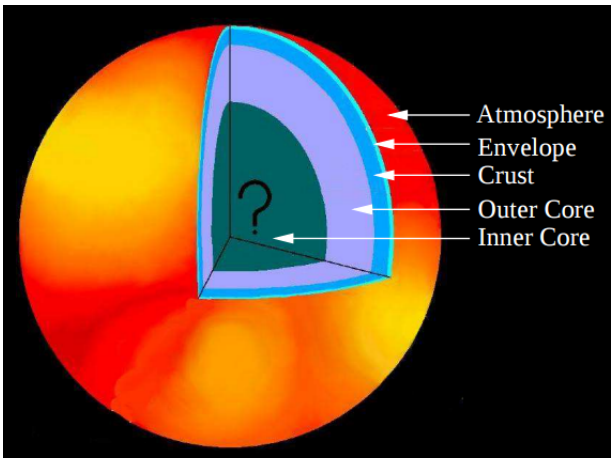

FIGURE 7.2: Schematic view of the several layers forming the neutron star. Extracted from (Page, 2004)

is likely to be determined by processes occurring after the supernova explosion, such as bombardment by HE gamma rays or ejection of nuclei. These mechanisms are totally unrelated to the interior of the NS, and may vary from star to star and evolve with time. For young NS, a light element envelope is hotter than a heavy element one due to a less insulating envelope. For older NS, the surface brightness is much higher for light elements envelope, resulting in a faster cooling than for heavy element envelopes. The evolution of the NS surface temperature according

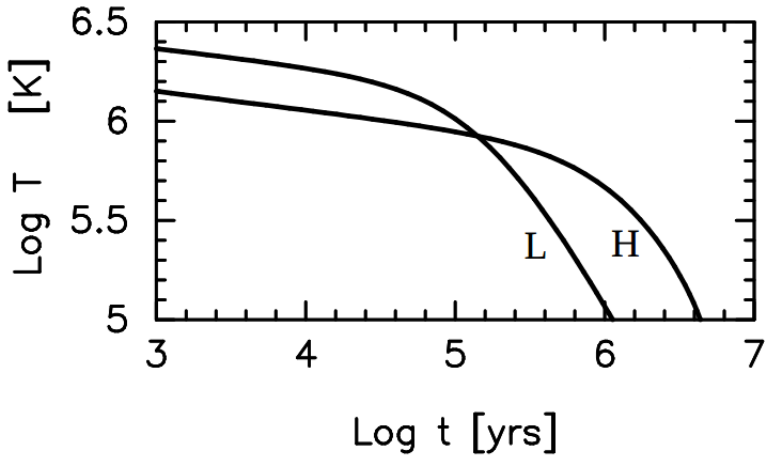

FIGURE 7.3: Evolution of the temperature of the neutron star surface with age, for light (L) and heavy (H) element envelopes. Figure adopted from (Page et al., 2004)

to its age is shown in Figure 7.3 for both light and heavy element envelopes. We consider here the two extreme cases, where the envelope is either made of only light elements or heavy elements.

7.2 Analytical computation of the emission efficiency

In this section, we analytically derive the evolution of the X-ray and gamma-ray efficiency of pulsars depending on the NS age. Within the outer gap, the magnetic-field-aligned electric field that will accelerate charged particles is derived from the inhomogeneous part of the Maxwell equation (Poisson equation for electrostatic potential) (Hirotani, 2008) and is given by:

$$E_{||} \approx \frac{\mu}{2R_{LC}^3} h_m^2, \tag{7.2}$$

where μ is the magnetic moment of the NS, h_m is the gap trans-magnetic-field thickness and R_{LC} the LC radius. The gap trans-magnetic-field-thickness, h_m, is defined such that $\theta_*^{min} = (1 - h_m)\theta_*^{max}$, where θ_*^{min} and θ_*^{max} are the colatitude angles with respect to the rotation axis of the upper and lower boundaries, respectively, of the outer gap, see Figure 7.1. The lower boundary is defined as the last closed field line. We adopt a constant h_m along the gap. The magnetic-field-aligned electric field, $E_{||}$, quadratically depends on h_m due to the fact that the Poisson equation is a second order differential equation. Within the gap, electrons and positron pairs are created via photon-photon pair production. These charged particles are polarized and accelerated by $E_{||}$ until reaching the terminal Lorentz factor

$$\gamma = \left(\frac{3\rho_c^2}{2e} E_{||} \right)^{1/4}, \tag{7.3}$$

where e is the charge on the electron and ρ_c the radius of curvature of the particle's motion in the three dimensional magnetosphere. As we assume in this approach that the inclination angle between the rotation axis and the magnetic axis, $\alpha < 62°$, we consider, as done in (Wang and Hirotani, 2011), that:

$$\rho_c \approx 0.5 R_{LC}. \tag{7.4}$$

The accelerated electrons and positrons will then radiate HE photons by curvature radiation process. The emitted photons will have a characteristic energy

$$h\nu_c = \frac{3}{2} \hbar c \frac{\gamma^3}{\rho_c}, \tag{7.5}$$

where h is the Planck constant and $\hbar = h/2\pi$. The characteristic energy of curvature photons has been estimated to span from ~ 10 GeV for a 1 kyr old pulsar down to ~ 1 GeV for a 100 kyr old pulsar. The resulting gamma-ray luminosity

in the gap due to curvature radiation process is then given by (Hirotani, 2008):

$$L_\gamma \approx 1.23 f_\Omega h_m^3 \frac{\mu^2 \Omega^4}{c^3} \tag{7.6}$$

where f_Ω denotes the flux correction factor (Romani and Watters, 2010), approximated to be unity for an isotropically emitting pulsar and Ω is the pulsar angular velocity.

The evolution of the pulsar period with time is estimated by solving the differential equation

$$-I\Omega\dot{\Omega} = C\frac{\mu^2\Omega^4}{c^3}, \tag{7.7}$$

where $\mathrm{C} = (2/3)\sin^2\alpha$ for a magnetic dipole braking and $1+\sin^2\alpha$ for a force-free braking (Spitkovsky, 2006). Assuming a magnetic dipole braking, we obtain

$$P = 7 \times \mu_{30} \times I_{45}^{-1/2} \left(\frac{t}{10^3 \mathrm{yr}}\right)^{1/2}, \tag{7.8}$$

where the period obtained is given in millisecond, $\mu_{30} \equiv \mu/(10^{30}\mathrm{G\ cm^3})$ and $I^{45} \equiv I/(10^{45}\mathrm{g\ cm^2})$.

The evolution of h_m is controlled by the pair creation within the gap. To solve the evolution of h_m, we consider the cooling emission from the NS and the X-ray emission from the heated polar cap surface. We estimated h_m, using K. Hirotani's numerical simulation (Hirotani, 2013), by expressing it as a function of the NS surface temperature, the pulsar period and the first period derivative which are all time dependent parameters; $h_m = h_m(T, P, (\dot{P}))$. For this calculation, we adopt a magnetic inclination angle, $\alpha = 60°$, a magnetic moment, $\mu = 3.2 \times 10^{30}$, and the NS radius, $r_* = 11.6$ km, as done in (Hirotani, 2013). We determine the evolution of h_m considering both light and heavy element envelopes. Resolving numerically h_m allows us to express it as a simple function of the pulsar age. Hence we get for light element envelope

$$h_m = 0.0025 \left(\frac{t}{\mathrm{yr}}\right)^{0.46} \tag{7.9}$$

and for heavy element envelope

$$h_m = 0.0100 \left(\frac{t}{\mathrm{yr}}\right)^{0.35}. \tag{7.10}$$

The resulting evolution of h_m over time is shown in Figure 7.4 for both light and heavy element envelope.

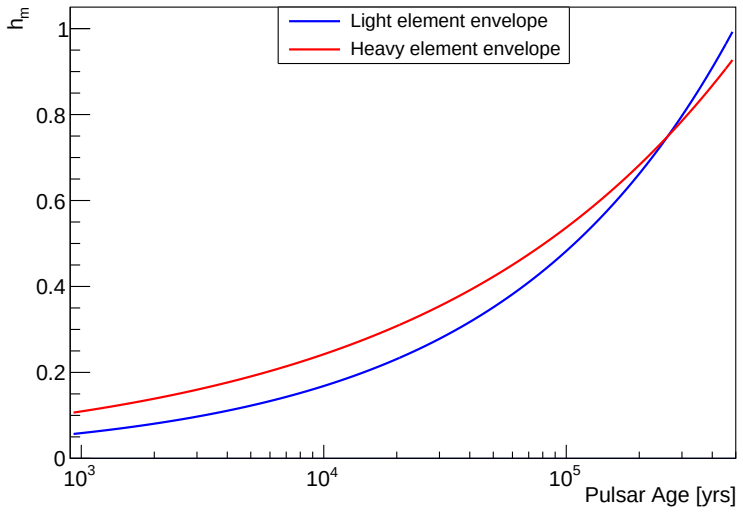

FIGURE 7.4: Evolution of the gap trans-magnetic-field thickness, h_m, depending on the neutron star age. The red curve represents the evolution of h_m considering a light element envelope and the blue curve considering a heavy element envelope

7.2.1 Optical thickness

The curvature gamma-ray photons emitted within the gap will collide with secondary X-rays photons previously emitted, and create $e^{\pm}$ pairs. This reaction is possible if the energy of the colliding X-ray photons is above the given energy threshold:

$$h\nu_{th} = \frac{2(m_e c^2)^2}{(1-\mu_c)h\nu_\gamma}, \tag{7.11}$$

where $h\nu_{th}$ is the threshold energy of the X-ray photon, $h\nu_\gamma$ the energy of the colliding gamma ray, μ_c is defined as $\mu_c = \cos\theta_c$, with θ_c the collision angle between the X-ray and gamma-ray photons. We estimate the energy of each created particle to be half the energy of the colliding curvature photon. The secondary X-ray photons arise from synchrotron emission from these secondary pairs created within the gap and are emitted within the gap, at a distance r_0 from the NS where the null charge surface crosses the middle-latitude field line, see Figure 7.1. The middle-latitude field line is defined by its colatitude, $\theta_* = (1-h_m/2)\theta_*^{max}$. These secondary emitted X-ray photons in the gap are responsible of the gamma-ray absorption.

The optical depth due to the secondary X-ray photons controls both the X-ray and gamma-ray luminosity within the gap. In order to calculate the optical thickness, we first derive the X-ray flux of the second generation of X-ray photons at the emission point. The secondary X-ray photons are considered to be emitted

at a distance r_0 from the NS and is evaluated as follows:

$$F_X(r_0) = \frac{L_X}{E_X \phi(r_0)}, \tag{7.12}$$

where L_X is the X-ray luminosity due to secondary X-ray photons within the gap, E_X the typical energy of secondary X-ray photons and $\phi(r_0)$ is the gap cross-section at the distance where the secondary X-ray photons are emitted. The typical energy of secondary X-ray photons is taken as

$$E_X = \gamma_2^2 \hbar \omega_B \theta_c \tag{7.13}$$

where γ_2 is is the Lorentz factor of the second generation of charged particle emitting secondary X-ray photons via synchrotron mechanism and ω_B is the frequency of gyration of the charged particle along the magnetic field line. The typical energy of X-ray photons has been estimated to span from a few tens keV for a 1 kyr old pulsar down to a few keV for a 100 kyr old pulsar. We assume the gap cross-section at the emission point to be a non-linear combination of the polar cap cross-section and the outer gap cross-section at the LC,

$$\phi(r_0) = \phi_{PC}^{\omega(t)} \phi_{LC}^{(1-\omega(t))}, \tag{7.14}$$

where ϕ_{PC} denotes the polar cap cross-section and ϕ_{LC} the outer gap cross-section at the LC. The parameter ω, lying between 0 and 1, increases with the NS age resulting in an increase of the gap cross-section at the emission point.

As the calculation of the optical thickness requires us to further integrate the secondary X-ray photon flux, we have to take into account its r^{-2} dependency on the flux. The flux of X-ray photons at a distance r from the emission point is given by

$$F(r) = F_0 \left(1 + \frac{r}{f}\right)^{-2}, \tag{7.15}$$

where F_0 is the estimated flux at the emission point, and f is the focal distance of photons measured at the emission point. Near the light cylinder, the magnetic field lines are assumed to be a combination of monopole and dipole magnetic field line. We take into account this effect assuming a focal distance, $f = (5/6)R_{LC}$, which is a trade-off between monopole-like and a dipole-like emitter.

We can then compute the optical thickness, τ, integrating the flux of secondary X-ray emitted within the gap.

$$\tau = (1 - \mu_c)\frac{1}{c}\int_{r_0}^{\infty} \sigma_{pp} F(r) dr \tag{7.16}$$

where σ_{pp} is the pair production cross-section evaluated by $\sigma_{pp} = 0.2 \cdot \sigma_T$, with σ_T the Thomson cross-section, and μ_c is the cosine of the collision angle between the

X-ray and gamma-ray photons. We evaluate the collision angle between the two photons, θ_c by $\theta_c = 0.5 h_m$. Including Eq. 7.15 into Eq. 7.16 we obtain:

$$\tau = (1 - \mu_c)\frac{1}{c}\sigma_{pp} F_0 \frac{f}{1 + \frac{r_0}{f}} \tag{7.17}$$

The optical thickness is estimated to span from unity for a 1 kyr old pulsar down to $\sim 10^{-3}$ for a 10 kyr old pulsar.

7.2.2 Calculation of the X-ray and gamma-ray efficiencies

The X-ray luminosity within the gap is controlled by the optical thickness and the number of seed gamma-ray photons. It is directly related to the gamma-ray luminosity via the optical thickness. The X-ray and gamma-ray luminosity resulting after absorption of the gamma rays are given by:

$$L_X = (1 - e^{-\tau}) L_\gamma, \qquad L_\gamma^2 = e^{-\tau} L_\gamma^1, \tag{7.18}$$

where L_γ^1 denotes the gamma-ray luminosity before absorption and is defined by Eq. 7.6.

For the calculation of the X-ray efficiency, we also take into account the emission from the heated polar cap surface, arising from the bombardment on in-falling positrons on the polar cap surface. The luminosity from the heated polar cap is given by:

$$L_{PC} = \sigma T_{pc}^4 A_{pc} \tag{7.19}$$

where σ denotes the Stefan-Boltzmann constant, T_{pc} the temperature of the polar cap and A_{pc} the polar cap area given by:

$$A_{pc} = \frac{\pi}{2} h_m \left(1 - \frac{h_m}{2}\right) \frac{r_*^3}{\varpi_{LC}} \sin^2(\theta_{LC} - \alpha), \tag{7.20}$$

where θ_{LC} is the angle between the NS rotation axis and the point where the last closed field intersects the light cylinder, see Figure 7.1, and h_m is given by Equations 7.9 and 7.10.

The results of the calculation of the evolution of the X-ray and gamma-ray efficiency are shown on Figure 7.5. The dot-dashed lines represent the efficiency considering a heavy element envelope and the full line the efficiency considering a light element envelope. The empty blue and red squares represent the experimental estimation of the gamma-ray and X-ray efficiency, respectively. The value of w used according to the pulsar age for light and heavy element envelope are displayed in Table 7.1. These values, obtained interpolating the experimental results, are consistent with the obtained values from numerical simulations.

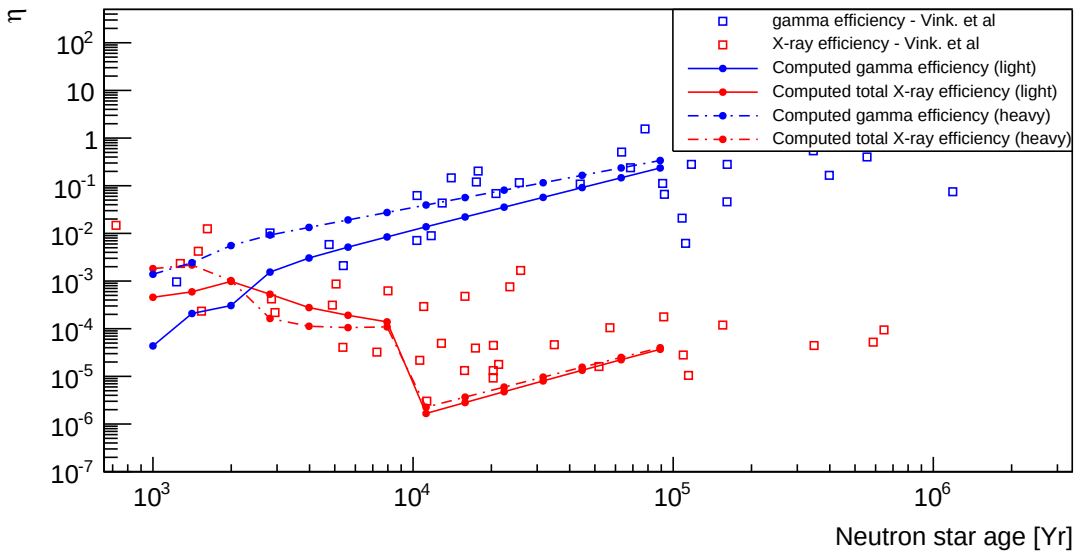

FIGURE 7.5: Evolution of the X-ray and gamma-ray efficiency considering light (full lines) and heavy (dashed lines) element envelopes. The filled circled represents the results from analytic calculation (this work) whereas the empty square arise from observational data.

NS age [kyr]	$w(t)$ (light)	w (heavy)
1.0	0.71	0.64
1.4	0.72	0.68
2.0	0.73	0.69
2.8	0.74	0.74
4.0	0.78	0.80
5.6	0.83	0.87
7.9	0.90	0.94

TABLE 7.1: Evolution of the w parameter determining the cross section of the outer gap at the emission point for light and heavy element envelopes.

7.3 Discussion and conclusion

We analytically derived the efficiencies for X-ray and gamma-ray emission for young pulsars in the framework of magnetospheric cascades within the outer gap, using a one dimensional magnetosphere model. The gap trans-magnetic-field thickness evolution is solved using the minimal cooling scenario for light and heavy element envelopes taking into account the emission from the NS cooling and from the heated polar cap surface. It appears that, for young and middle-age pulsars, the gap is thicker when considering a heavy element envelope. This is expected due to the smaller surface temperature of the NS for heavy element envelopes. We estimated the evolution of the w parameter, controlling the cross section of

the outer gap at the X-ray photons emission point, interpolating the experimental results. It turns out that the resulting efficiencies are extremely sensitive to small variation of w, resulting in an unsmoothed distribution of the efficiencies. We considered the curvature radiation emitted by the accelerated charged particles within the gap, and assumed that the absorption of these gamma rays is only due to the secondary generation of synchrotron X-ray photons. The computed X-ray and gamma-ray emission efficiency appear to be in good agreement with the observational values reported by (Kargaltsev, 2008), for both light and heavy element envelopes. However, the calculation considering a heavy element envelope appear to be more realistic. The light element envelope exhibits an increase of the efficiency for pulsars younger than 2 kyr and slightly underestimate it with respect to the observational results. The gamma-ray efficiency also appears to be underestimated in this case of pulsars younger than 3 kyr. For pulsars younger than 10 kyr, the X-ray efficiency appears to be dominated by the emission of secondary X-rays within the gap, where the optical thickness lies between unity and 10^{-3}. In this case, the absorption of gamma rays is efficient enough to produce secondary X-ray photons within the gap. However, the magnetic-field-aligned electric field strength decreases with the pulsar age. This phenomenon causes a reduction of the optical thickness for pulsars older than 10 kyr, resulting in no production of secondary X-ray within the gap and a drop of the X-ray efficiency. The gamma-ray photons can thus freely escape the gap. The X-ray efficiency of pulsars older than 10 kyr is maintained by the emission from the heated polar cap surface. The emission from the heated polar cap surface is slightly greater for heavy element envelope. This is due to the fact that for heavy element envelope the surface temperature is lower than for light element, which increases the gap trans-magnetic-field thickness. Thus, from Eq. 7.19 and 7.20 we can see that the luminosity from the heated polar cap surface is greater for heavy element envelope.

In our analytical approach, the value of the collision angle between the two photons for pair creation is fixed to $0.5h_m$. However, as the optical thickness depends on the square of the collision angle, a small variation in the estimated value can have a large impact on the computed value of the optical thickness resulting in a strong deviation of the X-ray efficiency. This deviation can have even larger impact for pulsars with ages of the order of $\sim$ 10 kyr, where the optical thickness strongly drops.

In this study we only consider outwardly-emitted gamma-ray curvature photons as the emission from inwardly emitted gamma rays is expected to be much less significant. However, taking into account the inwardly-emitted gamma-ray photons, would increase the secondary X-ray photons flux within the gap, resulting in a higher X-ray efficiency. Numerical simulation solving both the collision angle and the w parameter should lead to a better estimate of the X-ray and gamma-ray emission efficiencies.

Conclusions and outlook

The present work deals with the characterization of the VHE emission from pulsars. This study was done, originally, analyzing data from the MAGIC telescopes. Two pulsars were selected for this analysis, namely, the Crab pulsar, which is a well known gamma-ray emitter with a pulsed emission detected up to the TeV scale, and the Geminga pulsar, the next brightest gamma-ray pulsar in the Northern Hemisphere. In order to discuss the connection with lower energies, *Fermi*-LAT data of these two pulsars were also analyzed. Besides the study from an observational point of view, an analytic approach of the X-ray and gamma-ray emission efficiency has been carried out, following the recent discovery of the correlation between these two quantities.

For the study of the Crab pulsar with MAGIC, a data sample gathering 147 hours of good data quality was collected. The study of the light curve above 50 GeV allowed a significant detection of the signal from the interpeak region, located between P1 and P2, up to 200 GeV. This region, already observed in optical and X-ray, has never been reported at gamma-ray energies before. The SED of the interpeak region is well characterized by a power-law function defined by $\frac{dN}{dE} = f_{100}(\frac{E}{100\mathrm{GeV}})^{-\alpha}$, with $f_{100} = 8.2 \pm 2.4_{stat} \pm 1.48_{sys}$ and $\alpha = 3.8 \pm 0.7_{stat} \pm 0.3_{sys}$, appearing to be slightly softer than the emission from the peaks. The emission from the interpeak region can be explained by several models. Within the LC, this emission can be explained in the framework of the annular gap and the magnetospheric cascades within the outer-gap region. However, due to smaller values of the ratio bridge/P1 with respect to P2/P1, emission from the bridge and the peaks might arise from different location. This is one of the working hypotheses that the annular gap emission model relies on. In the framework of magnetospheric cascades within the outer gap, emission from the peaks and the bridge would arise from the same location. Emission from the interpeak region can also be explain by emission beyond the light cylinder from a cold ultra-relativistic wind. This model, however, requires a special density profile in order to reproduce the narrow peaks observed. Besides the emission from the interpeak region, these three models are also able to explain the emission from the Crab pulsar up to the TeV scale, recently observed by MAGIC.

The observation and data analysis of 63 hours of good data quality from the MAGIC telescopes of the Geminga pulsar and its surrounding nebula resulted in no significant detection so upper limits above 50 GeV were calculated. The resulting upper limits, being at lower energies that those derived by VERITAS, are the most constraining computed so far. In addition to the MAGIC data, 5 years of *Fermi*-LAT data were also analyzed. In order to characterize the SED of the pulsed emission, we compared the power-law function with an exponential and sub-exponential cut-off. We found that the SED is better characterized by a sub-exponential cut-off with b-parameter of $0.81 \pm 0.04 \pm 0.2$, for P1, $0.70 \pm 0.03 \pm 0.2$, for P2 and $0.67 \pm 0.02 \pm 0.2$, for the phase-averaged emission. Within the framework of the outer-gap model, a sub-exponential cut-off is expected if the emission arises from curvature radiation, due to a distribution in energy of the emitting charged particles. We also studied the evolution of the b parameter considering finer phase extensions. It results that the SED always exhibits a cut-off softer than an exponential cut-off. This effect is due to the emission from caustics. In order to characterize a possible VHE emission, the pulsed emission of the Geminga pulsar was fit above 10 GeV to a power-law function. This extension is at lower flux level than the upper limits computed by the MAGIC telescopes, thus cannot be constrained.
No nebula was detected around the Geminga pulsar. However, a TeV nebula was reported by MILAGRO and confirmed recently by HAWC with an extension of $\sim 3°$. Such an extension is bigger than the MAGIC field of view, and could not be detected with the standard wobble observations.

The analytic study of the the X-ray and gamma-ray emissions in the outer gap, led to the calculation of the emission efficiency for young pulsars. This work is based on an extension of the outer-gap model, developed by K. Hirotani, in which magnetospheric cascades appear in the outer gap, due to the acceleration of primary charged particles. The calculations, based on the minimal cooling scenario, were carried out for two cases, namely, light and heavy element envelope. Both cases appear to be in good agreement with the observations reported by the *Chandra* satellite and *Fermi*-LAT. This results confirm the robustness of this extension of the outer-gap model. However, this analytic approach considers fixed trans-magnetic-field thickness along the outer gap and fixed collision angle between the photons during the pair creation process. More robust and precise results would be achieved considering a numerical approach. Furthermore, the trend exhibited in the evolution of the X-ray and gamma-ray efficiency, could help for the detection of new gamma-ray pulsars by constraining their X-ray efficiency.

Several models attempt to describe the emission from gamma-ray pulsars, being within and beyond the LC. The outer gap model and its extension including magnetospheric cascades generating VHE photons, appears to be an elegant description of the gamma-ray emission as it is able to account for the Crab VHE

emission, explain the spectral shape of the Geminga pulsar emission and can reproduce the X-ray and gamma-ray emission efficiency of young pulsars.

The study of pulsar physics requires a low energy threshold, as most pulsars exhibit a cut-off at a few GeV. The Sum-Trigger-II of the MAGIC telescope is expected to provide a better overlap of the SED between the ground-based telescopes and the *Fermi*-LAT. Observations of the Geminga pulsar with the Sum-Trigger-II could allow us to detect a third pulsar using ground-based telescope, and distinguish the spectral shape above 30 GeV. Furthermore, the future Cherenkov Telescopes Array (CTA), expected to have a lower energy threshold and better sensitivity than the current observatories will be a excellent observatory for the study of pulsars.

Appendix A

Starguider and drive bending models of the MAGIC telescopes

A.0.1 Introduction

Due to the size and weight of the MAGIC telescopes, the structures are subject to strong constraints such as gravity, weather conditions, etc, that may affect the accuracy of the pointing. To ensure the proper pointing accuracy of the telescopes, pointing models are regularly built. Their purpose is to correct a potential mispointing. These models are made using the so-called TPoints. A TPoint is the projected image of a bright star onto the camera plane. They are usually taken at the beginning and/or at the end of the night, by pointing the telescopes to bright stars. We can then evaluate the mispointing of the telescopes at given zenith and azimuth angle by comparing the reconstructed and expected position of the star in the camera plane. The mispointing of the telescopes is corrected by applying independent models for each telescope. Two distinct corrections can be applied to correct the mispointing; a first one is applied directly on the drive system of the telescope using Drive bending models, and a second one can be applied during the offline analysis of the recorded events using Starguider bending models.

A.1 Starguider and drive corrections

Two kinds of correction are used in MAGIC. The first one is the drive correction. It is an online correction applied directly on the drive system of the telescopes. This correction is made to compensate at hardware level the constraints applied on the telescope structure due to gravity, weather conditions, or hardware modifications on the telescopes. Once the data are taken with a certain drive correction, we

cannot take the correction back, which means that data taken with a bad pointing model cannot be improved, unless using later good starguider corrections. The models used for the drive correction, so-called Drive bending models are uploaded on the drive computers for MAGIC-1 and MAGIC-2, respectively. The corrections for each telescope are independent. During data taking, the drive system will read the correction models from the corresponding computer and automatically correct the pointing.

The second correction applied is an offline correction using the data provided by the starguider cameras. It is assumed that data are taken with a good drive bending model, but sometimes the drive models may not be optimal. To cross-check the first correction and to correct it if necessary, the starguider is used. The starguider is a high-resolution CCD camera located at the reflector center of each telescope and aligned with the optical axis of the telescope. The purpose of the starguider is to compensate the mispointing of the telescopes at the software level. During data taking, the starguider checks the position of some bright stars in the sky and compares their appearing positions to those from a catalog. An eventual offset between the observed position and the position from the catalog can be observed. This offset, that should be the same as the one between the reconstructed and true position of the observed source, is corrected during the data analysis.

Although these two corrections are complementary, the drive correction is mandatory as it is the first to be applied and the less stable in time. When the drive corrections are good enough, one can choose to run the analysis without the starguider corrections.

A.2 Procedure to take TPoints

TPoints are usually taken during the moon time or twilight, when normal data taking is not possible, or when changing from one source to another. A so-called TPoint lid has to be opened, on which the light of the star focused by the mirrors will be reflected. The procedure to take TPoints is automated. A dedicated program is in charge of pointing the telescopes to a star according to some parameters (zenith angle, star magnitude, etc) defined by the user. This program will also show the stars already pointed to to take TPoints, see Figure A.1. TPoints are then taken as follow: the telescopes are pointed at a bright star. The image of the star is projected onto the TPoints lids, around which dedicated LEDs are located. The position of the star on the TPoint lids is computed thanks to these LEDs. Dedicated software extracts the mispointing comparing the position of the reconstructed image of the star on the TPoints lids and the position of the star in

the sky. The results are stored in a text file. While taking TPoints, no correction is applied to the Drive system. The sample of TPoints used to make new models has to cover the largest portion of the sky possible, in order to obtain a good correction at any azimuth and zenith angle.

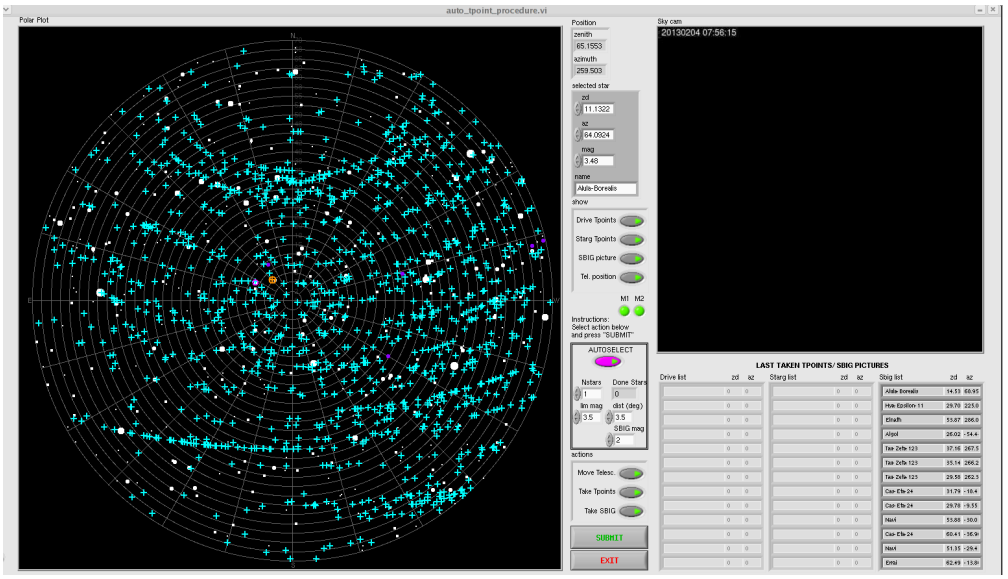

FIGURE A.1: View of the automatic TPoints procedure panel.

A.3 Starguider and drive bending models

The drive and Starguider models used to correct the mispointing are built from the TPoints analysis. Both models require dedicated TPoints. Each TPoint file contains only one line which looks like this:

```
60.39037 47.67021 60.35254 47.62571 15.0325 40.39056 0.01231216 0.0474521
55951.192514 2670 0 158.7 280.9 0 0 5 9 29 20 59.55 3.5 Nekkar
```

Where the columns represent:

- Real Azimuth of the Star
- Real Altitude of the Star
- Azimuth "of System" (that Starguider thinks the star has)
- Altitude "of System" (that Starguider thinks the star has)
- Drive Nominal Right Ascension

- Drive Nominal Declination
- Offset in Altitude
- Offset in Azimuth
- MJD
- Star name

Both Starguider and Drive bending models have the same format. Below is an example of bending model.

```
MAGIC1 24.05.2013 12:57:55.881
S   00   000000   000000  0000000
     IA    0.12745337   0.004940808
     IE    0.23373025   0.0056168211
   FLOP             0             0
     AN -0.0029609959   0.00099251924
     AW -0.00073931756   0.0012897199
   NPAE  0.0058843159   0.006112025
     CA -0.0034474681   0.0073308105
     TF             0             0
     TX             0             0
   ECES  -0.013989572   0.0046299506
   ACES  -0.010099684   0.0026885937
   ECEC -0.0093554549   0.0040188558
   ACEC -0.0025967818   0.0023252158
    NRX             0             0
    NRY             0             0
    CRX  0.0029693895   0.0010441283
    CRY   0.001035968   0.0012193419
 MAGIC1  -0.017872262   0.0011704266
 MAGIC2             0             0
     PX             0             0
     PY             0             0
     DX             0             0
     DY             0             0
END
```

Bending models are multi-parameter functions. The most important parameters are IA and IE which are the offset in azimut and zenith, respectively. AN and AW

are the azimuth and zenith mispointing. *NPAE* is the error of the angle between the azimutal and zenithal axis and *TF* the misalignment between the optical and zenithal axis.

A.4 Application of the model corrections

The corrections of the drive systems are directly applied on the telescopes. The software in charge of the drive of the telescopes will read the models and compute the corrections to apply.

The starguider corrections are optional. The calibration of starguider is made while running *star*, when the Hillas parameters are calculated, but can be modified later. A new starguider model can be applied during the final stages of the analysis, which is convenient when one works with star files from the MAGIC data center at PIC. When running *star*, the analyser does not need the starguider corrections since it is set by default.

A.5 How to check bending models

In order to ensure a good pointing accuracy, the bending models are checked every observation period. The models are checked by means of a dedicated macro that will compute and apply the corrections from a given model to a TPoints sample. The macro returns a set of plots, representing the evolution of the pointing according to the pointing positions of the telescopes, described below.

- The residual 1-D is a one dimension histogram representing the number of recontructed stars at a given distance from the expected position of the star in the camera plane, see Figure A.2. The residuals are fit to a Gaussian function, as this is the shape expected for the PSF. On Figure A.2, the x-axis represents the angular mispointing divided by 0.01, which is the maximum standard deviation required.

- The residual 2-D is a two dimensional plot showing the reconstructed position of the star on the camera plane with respect to its expected position in the camera plane, see Figure A.3.

- Several plots show the correlation of the mispointing according to the azimuth and zenith angles, see Figure A.4.

- Daily plots, showing the evolution of the previously mentioned parameters on daily basis, see Figure A.5.

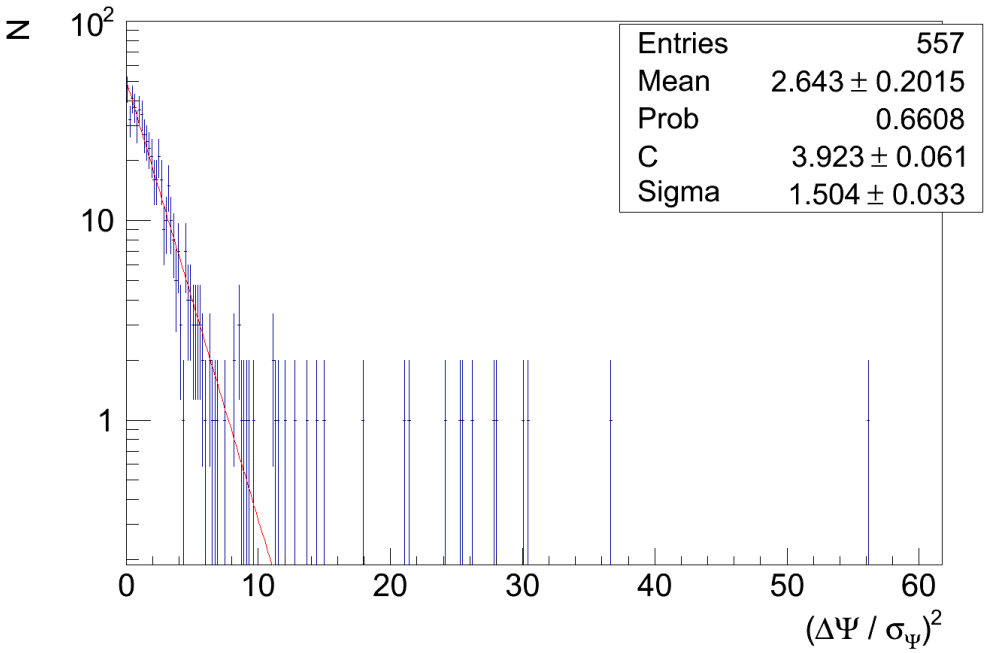

FIGURE A.2: Residuals 1-D. The x-axis represents the deviation (in degrees) of the point divided by the maximum expected deviation: 0.01°. The y-axis represents the counts of stars in a given bin.

A.6 The effects of bending models on the data quality

The accuracy of the bending models may have an impact on the quality of the data reconstruction. For example, as a wrong estimation of the θ^2 parameter might result in a bad fit of the source position while computing the sky maps, etc. In this section we will take a look at the effect of the bending models on the data quality, by comparting two analyses made with good and bad MAGIC-II Starguider models using data from October 2013. The bad model is the one used before the update to the good model. The model of the MAGIC-I telescope did not need to be updated at that period.

A.6.1 Effect on the signal

We may expect that a bad correction of the pointing ruin the signal, as the θ^2 distribution will be biased. Figure A.6 shows a comparison between the θ^2 distribution with the bad and good Starguider models for MAGIC-II. The sensitivities

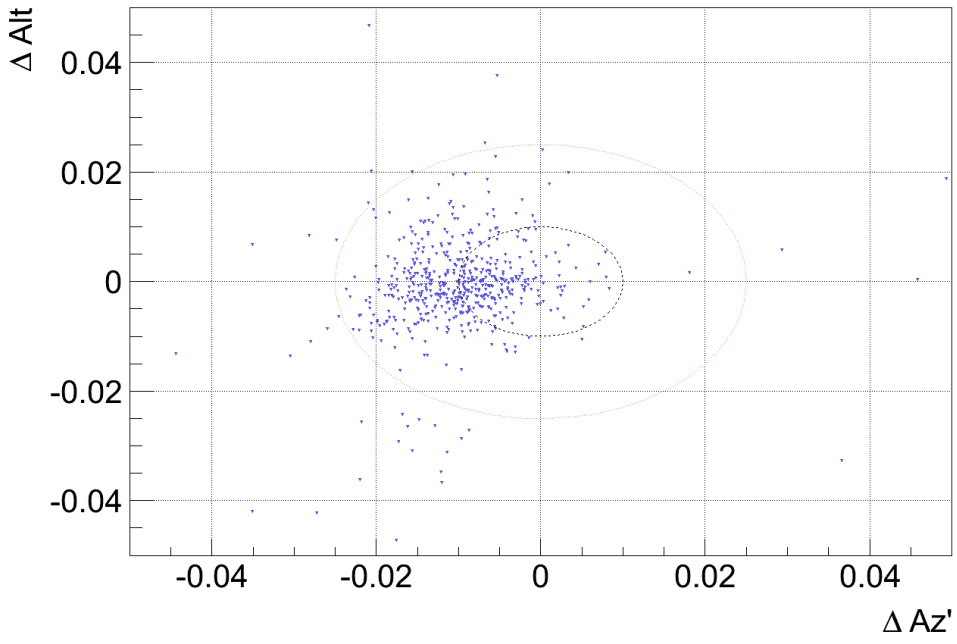

FIGURE A.3: 2-D deviation of reconstructed position of the stars on the camera plane with respect to the expected position, at coordinates (0,0). This map shows two circles; an inner blue one, which represents 1σ of the expected Gaussian distribution (0.01°), and an outer blue one which represents 2σ of the expected gaussian (0.025°).

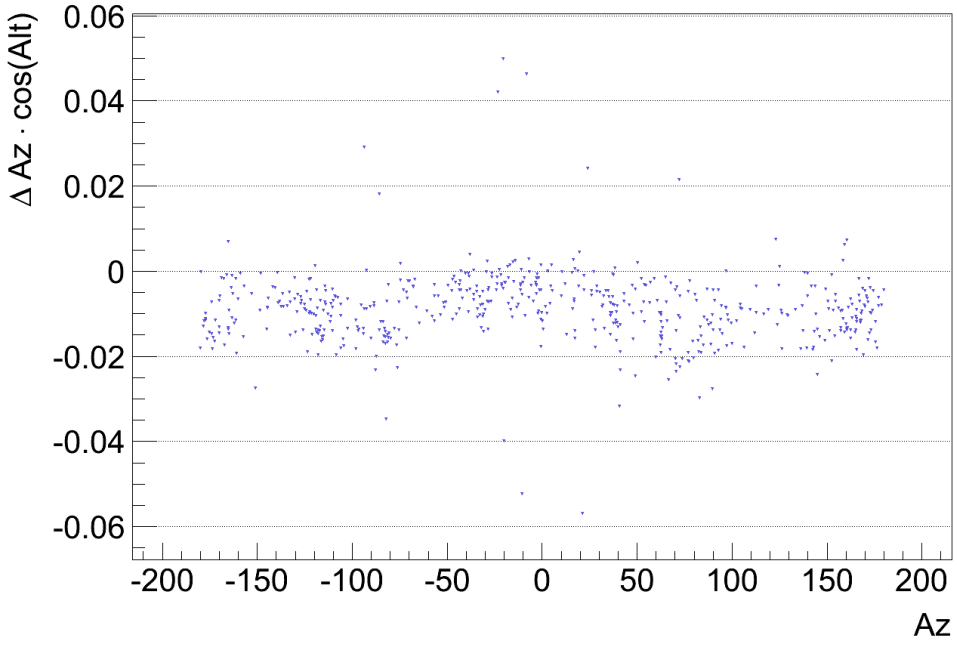

FIGURE A.4: Deviation on the azimuth axis depending on the azimuth of the star.

obtained are 0.52 ± 0.07 % CU considering the bad model and 0.49 ± 0.07 %

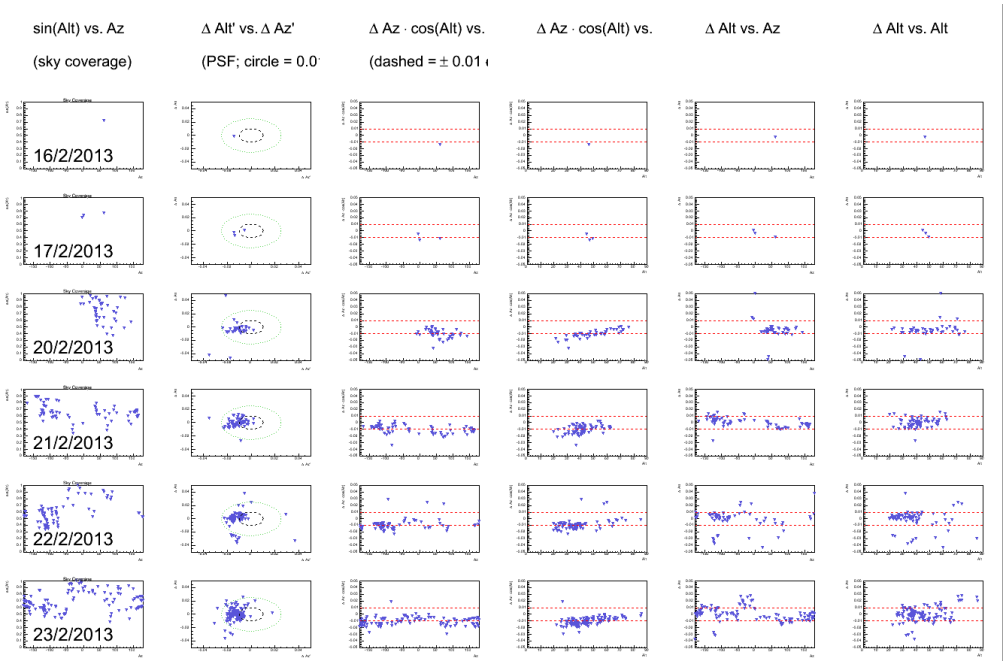

FIGURE A.5: Daily plots, representing the evolution of the pointing according to several parameters.

CU considering the good one, both models being consistent within the statistical errors.

Figure A.7 shows the SEDs of the bad and good models. On these plots, no big improvement can be claimed since both SEDs are compatible within statistical errors. We can observe that the fluctuations increase with energy, which can be due to the fact that the θ^2 is better reconstructed as the energy increases.

A.6.2 Sky map and position reconstruction

The effect of the mispointing can also be checked using sky maps. While computing the sky map, one can compare the reconstructed position of the source with the position given in the data files. Table A.1 gives the angular distances between the reconstructed positions and the position of the source read in the data files, for the two nights analyzed.

In this case we can see that the two models are incompatible with each other,

night	mispointing (bad)	mispointing (good)
October 4th	0.0207 ± 0.0016 deg	0.0162 ± 0.0016 deg
October 5th	0.0116 ± 0.0015 deg	0.0054 ± 0.0015 deg

TABLE A.1: Mispointing computed from the sky map using good and outdated models for the two nights analyzed.

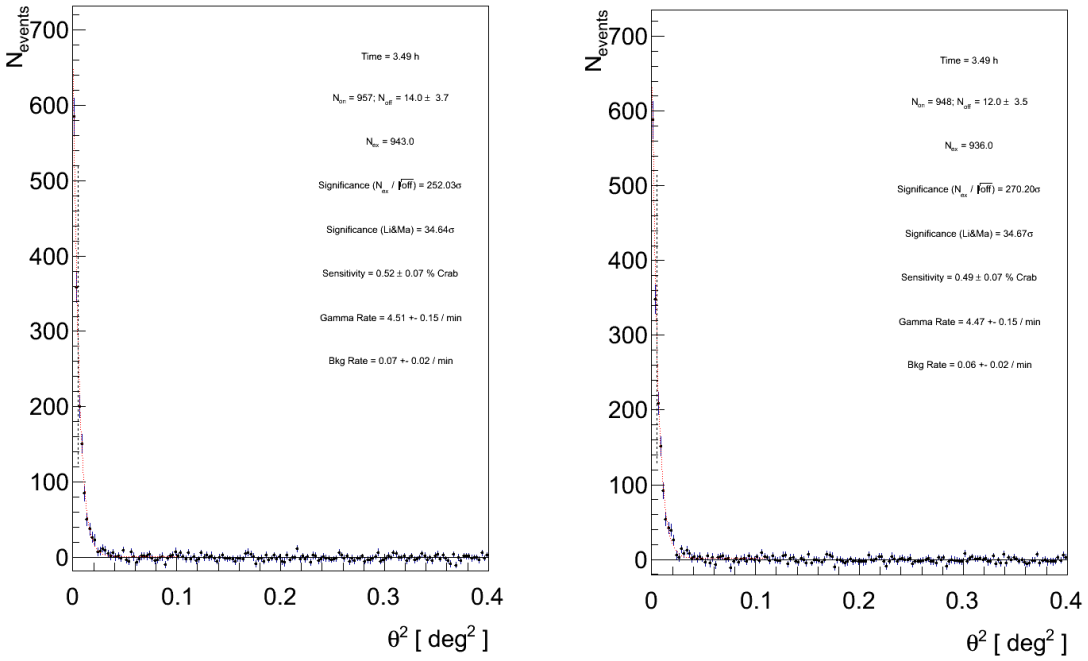

FIGURE A.6: θ^2 distribution the bad and good starguider models for MAGIC2. On the left plot is the old model, on the right the new one.

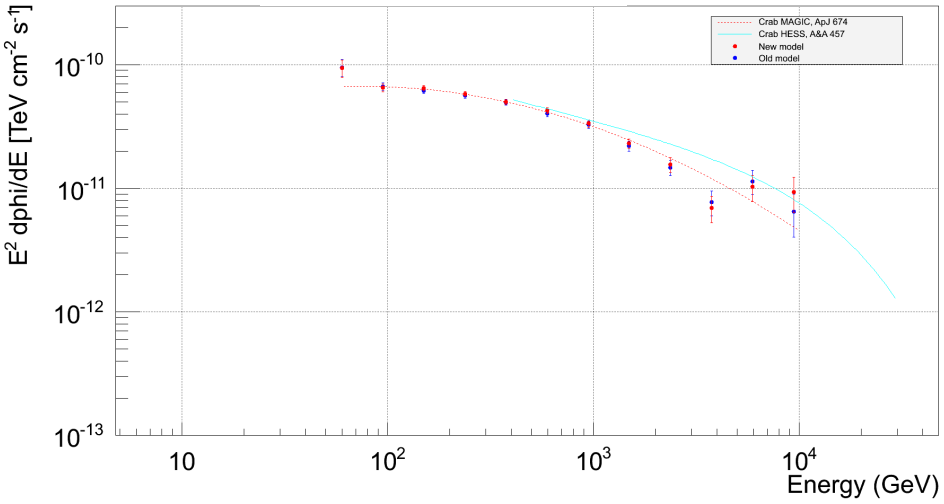

FIGURE A.7: Overlap of Crab Nebula SEDs using good and bad starguider models.

with the good model being more accurate than the outdated one.

A.6.3 Relative mispointing between telescopes

One way to check the relative mispointing between both telescopes is to look at the angular distance between the center of the ellipses and the projected position

of the source on the ellipses axes for each telescopes, called *disp*. A high *disp* difference between both telescopes is due to a dicrepancy between the pointing of both telescopes. Figure A.8 shows the squared differences between the *disp* values of both telescopes, for both models. We chose to plot the squared difference, $(\Delta disp)^2$, to work with positive values. We can see that the distribution for the good model (red one) is more concentrated toward small pointing differences, in the first bins. This means that the pointing difference between both telescopes is smaller in the case of the good model. The good model improves slightly the quality of the data, by reducing the mispointing of the system and the relative mispointing between the telescopes.

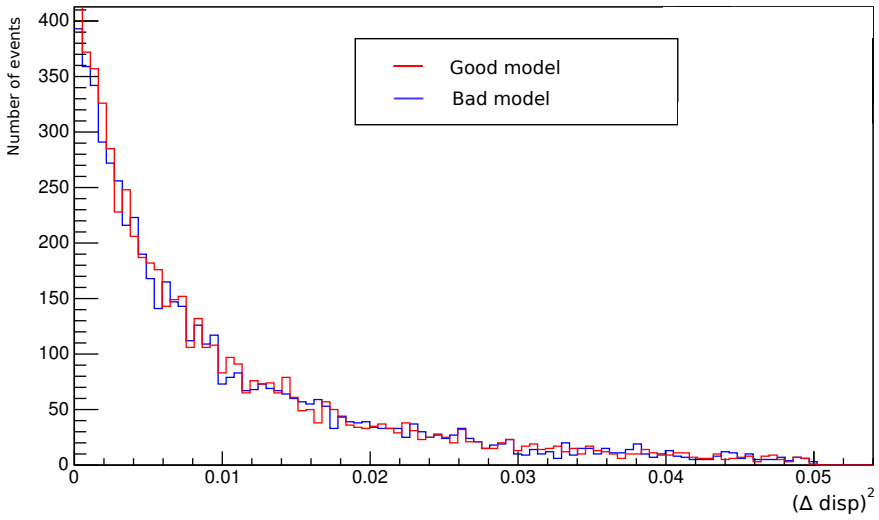

FIGURE A.8: Plot of the squared difference of the *disp* values of both telescopes using good and bad bending model.

Appendix B

Ephemeris

B.0.4 Epheremis used for the analysis of the Crab pulsar

The columns of the ephemeris are sorted as follows:
RA(J2000) DEC(J2000) MJD1 MJD2 t0geo(MJD) f0(s^{-1}) f1($^{-2}$) f2($^{-3}$) RMS O B

where the parameters are defined as:

RA	Right Ascension in J2000 coordinates (hh mm ss.sss)
DEC	Declination in J2000 coordinates (sdd mm ss.ss)
MJD1,2	First and last dates for valid parameters (MJD)
t0geo	Infinite-frequency geocentric UTC arrival time of a pulse (MJD)
	Note: the integer part of t0geo is the barycentric (TDB) epoch of RA, DEC, f0, f1,and f2
f0	Pulsar rotation frequency (s**(-1))
f1	First derivative of pulsar frequency (s**(-2))
f2	Second derivative of pulsar frequency (s**(-3))
RMS	Root-mean-square radio timing residual, in milliperiods
O	Observer code
B	Blank for single pulsars, "*" for binaries.

Table B.1:

05	34	31.972	22	00	52.07	54710	54741	54725.000000182	29.7435534695297	-3.71896D-10	1.88D-20	0.6 J	DE200 0531+21
05	34	31.972	22	00	52.07	54741	54769	54755.000000283	29.7425895603473	-3.71865D-10	9.27D-21	0.3 J	DE200 0531+21
05	34	31.972	22	00	52.07	54771	54801	54786.000000327	29.7415935950438	-3.71846D-10	2.26D-20	0.6 J	DE200 0531+21
05	34	31.972	22	00	52.07	54801	54832	54817.000000193	29.7405977242989	-3.71793D-10	6.40D-21	0.5 J	DE200 0531+21
05	34	31.972	22	00	52.07	54832	54863	54847.000000032	29.7396340427882	-3.71784D-10	1.52D-20	0.7 J	DE200 0531+21
05	34	31.972	22	00	52.07	54863	54891	54877.000000055	29.7386704395432	-3.71736D-10	1.49D-20	0.5 J	DE200 0531+21
05	34	31.972	22	00	52.07	54891	54922	54907.000000168	29.7377069457157	-3.71708D-10	1.28D-20	0.7 J	DE200 0531+21
05	34	31.972	22	00	52.07	54922	54952	54937.000000347	29.7367435247257	-3.71687D-10	1.79D-21	0.5 J	DE200 0531+21
05	34	31.972	22	00	52.07	54952	54983	54968.000000284	29.7357480273088	-3.71653D-10	1.84D-20	0.7 J	DE200 0531+21
05	34	31.972	22	00	52.07	54983	55013	54998.000004202	29.7347847464604	-3.71620D-10	1.71D-20	0.5 J	DE200 0531+21
05	34	31.972	22	00	52.07	55013	55045	55029.000000128	29.7337894619271	-3.71594D-10	5.03D-21	0.5 J	DE200 0531+21
05	34	31.972	22	00	52.07	55044	55074	55059.000000387	29.7328263652358	-3.71552D-10	1.73D-20	0.7 J	DE200 0531+21
05	34	31.972	22	00	52.07	55075	55105	55090.000000120	29.7318311934068	-3.71532D-10	1.28D-20	0.7 J	DE200 0531+21
05	34	31.972	22	00	52.07	55105	55136	55120.000000027	29.7308682287371	-3.71508D-10	1.41D-21	0.6 J	DE200 0531+21
05	34	31.972	22	00	52.07	55137	55167	55152.000000203	29.7298411293166	-3.71467D-10	1.83D-20	1.2 J	DE200 0531+21
05	34	31.972	22	00	52.07	55166	55198	55182.000000148	29.7288783263845	-3.71433D-10	7.74D-21	1.5 J	DE200 0531+21
05	34	31.972	22	00	52.07	55197	55228	55212.000000213	29.7279156072075	-3.71401D-10	1.42D-20	1.0 J	DE200 0531+21
05	34	31.972	22	00	52.07	55229	55255	55242.000000027	29.7269529828518	-3.71372D-10	1.53D-20	0.8 J	DE200 0531+21
05	34	31.972	22	00	52.07	55257	55287	55272.000000251	29.7259904409424	-3.71342D-10	1.21D-20	1.3 J	DE200 0531+21
05	34	31.972	22	00	52.07	55287	55317	55302.000000135	29.7250279952242	-3.71317D-10	-6.06D-20	2.4 J	DE200 0531+21
05	34	31.972	22	00	52.07	55318	55349	55334.000000219	29.7240014045375	-3.71286D-10	9.08D-21	0.9 J	DE200 0531+21
05	34	31.972	22	00	52.07	55348	55379	55364.000000094	29.7230390963695	-3.71243D-10	1.98D-20	0.8 J	DE200 0531+21
05	34	31.972	22	00	52.07	55378	55410	55394.000000202	29.7220768729984	-3.71217D-10	5.59D-21	0.6 J	DE200 0531+21
05	34	31.972	22	00	52.07	55409	55440	55424.000000163	29.7211147042390	-3.71178D-10	2.44D-20	1.2 J	DE200 0531+21
05	34	31.972	22	00	52.07	55440	55471	55455.000000273	29.7201205559067	-3.71169D-10	1.23D-20	0.7 J	DE200 0531+21
05	34	31.972	22	00	52.07	55471	55502	55486.000000008	29.7191264778135	-3.71121D-10	2.65D-20	0.5 J	DE200 0531+21
05	34	31.972	22	00	52.07	55502	55532	55517.000000012	29.7181325014690	-3.71096D-10	5.39D-21	0.9 J	DE200 0531+21
05	34	31.972	22	00	52.07	55531	55561	55546.000000026	29.7172027097242	-3.71059D-10	2.70D-20	0.6 J	DE200 0531+21
05	34	31.972	22	00	52.07	55562	55594	55578.000000214	29.7161768474826	-3.71033D-10	1.51D-20	1.1 J	DE200 0531+21
05	34	31.972	22	00	52.07	55593	55622	55607.000000053	29.7152472306505	-3.71003D-10	-6.21D-22	1.1 J	DE200 0531+21
05	34	31.972	22	00	52.07	55621	55652	55637.000000334	29.7142856236634	-3.70976D-10	3.55D-20	1.0 J	DE200 0531+21
05	34	31.972	22	00	52.07	55653	55682	55668.000000167	29.7132920720754	-3.70929D-10	1.23D-20	0.7 J	DE200 0531+21
05	34	31.972	22	00	52.07	55682	55713	55698.000000203	29.7123306358436	-3.70922D-10	-7.25D-21	0.9 J	DE200 0531+21
05	34	31.972	22	00	52.07	55713	55743	55728.000000142	29.7113692698036	-3.70872D-10	2.12D-22	1.0 J	DE200 0531+21
05	34	31.972	22	00	52.07	55743	55774	55759.000000287	29.7103759618690	-3.70842D-10	9.30D-21	0.6 J	DE200 0531+21
05	34	31.972	22	00	52.07	55774	55805	55789.000000251	29.7094147781873	-3.70814D-10	-1.26D-21	0.7 J	DE200 0531+21
05	34	31.972	22	00	52.07	55805	55824	55814.000000159	29.7086138502273	-3.70784D-10	1.73D-21	0.9 J	DE200 0531+21
05	34	31.972	22	00	52.07	55823	55839	55831.000000157	29.7080692630911	-3.70799D-10	1.16D-19	0.6 J	DE200 0531+21
05	34	31.972	22	00	52.07	55835	55866	55850.000000212	29.7074606092238	-3.70762D-10	5.86D-21	0.6 J	DE200 0531+21
05	34	31.972	22	00	52.07	55865	55876	55870.000000349	29.7068199571155	-3.70738D-10	-1.22D-19	0.4 J	DE200 0531+21
05	34	31.972	22	00	52.07	55876	55883	55879.000000282	29.7065329999919	-3.71298D-10	-2.63D-18	0.6 J	DE200 0531+21
05	34	31.972	22	00	52.07	55883	55896	55889.000000204	29.7062121062649	-3.71205D-10	4.69D-19	0.5 J	DE200 0531+21
05	34	31.972	22	00	52.07	55896	55927	55912.000000254	29.7054749436005	-3.70842D-10	5.35D-20	1.0 J	DE200 0531+21
05	34	31.972	22	00	52.07	55927	55958	55942.000000006	29.7045138528711	-3.70746D-10	2.71D-20	0.4 J	DE200 0531+21
05	34	31.972	22	00	52.07	55958	55987	55972.000000213	29.7035529167260	-3.70725D-10	1.54D-20	0.4 J	DE200 0531+21

TABLE B.2: Ephemeris used for the analysis of the Crab pulsar

05	34	31.972	22	00	52.07	55987	56018	56003.000000285	29.7025600117591	-3.70689D-10	1.95D-20	0.6 J	DE200 0531+21
05	34	31.972	22	00	52.07	56018	56048	56033.000000100	29.7015992238178	-3.70663D-10	3.30D-22	0.5 J	DE200 0531+21
05	34	31.972	22	00	52.07	56048	56079	56064.000000067	29.7006064785813	-3.70632D-10	1.27D-20	0.4 J	DE200 0531+21
05	34	31.972	22	00	52.07	56079	56107	56093.000000353	29.6996778634739	-3.70596D-10	2.40D-20	0.7 J	DE200 0531+21
05	34	31.972	22	00	52.07	56111	56141	56126.000000059	29.6986212852998	-3.70544D-10	-5.78D-21	1.0 j	DE200 0531+21
05	34	31.972	22	00	52.07	56141	56171	56156.000000336	29.6976608297856	-3.70530D-10	1.21D-20	0.9 j	DE200 0531+21
05	34	31.972	22	00	52.07	56171	56201	56186.000000085	29.6967004295785	-3.70523D-10	-1.84D-20	0.6 j	DE200 0531+21
05	34	31.972	22	00	52.07	56201	56232	56216.000000248	29.6957400601021	-3.70494D-10	1.21D-20	0.7 j	DE200 0531+21
05	34	31.972	22	00	52.07	56233	56259	56246.000000149	29.6947797944571	-3.70440D-10	4.28D-20	0.6 j	DE200 0531+21
05	34	31.972	22	00	52.07	56262	56293	56277.000000348	29.6937876209181	-3.70429D-10	1.63D-20	1.2 J	DE200 0531+21
05	34	31.972	22	00	52.07	56293	56324	56309.000000268	29.6927635027479	-3.70402D-10	9.62D-21	0.7 J	DE200 0531+21
05	34	31.972	22	00	52.07	56327	56353	56340.000000366	29.6917714731735	-3.70366D-10	2.34D-20	0.5 J	DE200 0531+21
05	34	31.972	22	00	52.07	56352	56383	56368.000000184	29.6908755256853	-3.70341D-10	1.23D-20	0.6 J	DE200 0531+21
05	34	31.972	22	00	52.07	56383	56413	56398.000000010	29.6899156306415	-3.70313D-10	2.48D-20	0.4 J	DE200 0531+21
05	34	31.972	22	00	52.07	56414	56445	56430.000000372	29.6888918633875	-3.70261D-10	8.51D-21	0.6 J	DE200 0531+21
05	34	31.972	22	00	52.07	56444	56474	56459.000000310	29.6879641525514	-3.70251D-10	1.37D-20	0.4 J	DE200 0531+21
05	34	31.972	22	00	52.07	56474	56505	56489.000000369	29.6870045139419	-3.70215D-10	-1.54D-21	0.5 J	DE200 0531+21
05	34	31.972	22	00	52.07	56505	56537	56521.000000295	29.6859809624148	-3.70186D-10	2.10D-20	0.5 J	DE200 0531+21
05	34	31.972	22	00	52.07	56536	56564	56550.000000352	29.6850534464651	-3.70153D-10	2.65D-20	0.4 J	DE200 0531+21
05	34	31.972	22	00	52.07	56569	56597	56583.000000064	29.6839981009458	-3.70133D-10	-1.02D-20	0.3 J	DE200 0531+21
05	34	31.972	22	00	52.07	56597	56627	56612.000000060	29.6830707527923	-3.70089D-10	6.13D-21	0.5 J	DE200 0531+21
05	34	31.972	22	00	52.07	56628	56658	56643.000000386	29.6820795213856	-3.70066D-10	1.25D-20	0.6 J	DE200 0531+21
05	34	31.972	22	00	52.07	56658	56689	56673.000000049	29.6811203635130	-3.70024D-10	2.27D-20	0.7 J	DE200 0531+21
05	34	31.972	22	00	52.07	56689	56717	56703.000000227	29.6801612883600	-3.70007D-10	-9.25D-21	0.7 J	DE200 0531+21
05	34	31.972	22	00	52.07	56717	56748	56733.000000100	29.6792022849988	-3.69978D-10	1.37D-21	0.3 J	DE200 0531+21
05	34	31.972	22	00	52.07	56748	56778	56763.000000323	29.6782433572042	-3.69940D-10	-9.18D-21	0.6 J	DE200 0531+21
05	34	31.972	22	00	52.07	56778	56809	56794.000000018	29.6772525461978	-3.69912D-10	4.73D-21	1.1 J	DE200 0531+21
05	34	31.972	22	00	52.07	56809	56837	56823.000000170	29.6763257228340	-3.69882D-10	1.96D-20	0.4 J	DE200 0531+21
05	34	31.972	22	00	52.07	56848	56870	56859.000000079	29.6751753074394	-3.69838D-10	-5.20D-21	0.3 J	DE200 0531+21
05	34	31.972	22	00	52.07	56870	56901	56885.000000350	29.6743445108147	-3.69825D-10	1.81D-20	0.5 J	DE200 0531+21
05	34	31.972	22	00	52.07	56901	56931	56916.000000220	29.6733540289012	-3.69770D-10	2.64D-20	0.7 J	DE200 0531+21
05	34	31.972	22	00	52.07	56931	56962	56946.000000251	29.6723955938771	-3.69774D-10	-2.10D-21	0.7 J	DE200 0531+21
05	34	31.972	22	00	52.07	56962	56992	56977.000000041	29.6714052551562	-3.69729D-10	1.16D-20	0.4 J	DE200 0531+21
05	34	31.972	22	00	52.07	56992	57023	57007.000000317	29.6704469490645	-3.69701D-10	1.85D-20	0.5 J	DE200 0531+21
05	34	31.972	22	00	52.07	57023	57054	57039.000000008	29.6694248682130	-3.69664D-10	1.79D-20	0.5 J	DE200 0531+21
05	34	31.972	22	00	52.07	57054	57082	57068.000000022	29.6684986852316	-3.69637D-10	9.70D-21	0.4 J	DE200 0531+21
05	34	31.972	22	00	52.07	57082	57112	57097.000000289	29.6675725758309	-3.69603D-10	2.43D-20	0.4 J	DE200 0531+21

TABLE B.3: Ephemeris used for the analysis of the Crab pulsar

B.0.5 Epheremis used for the analysis of the Geminga pulsar

```
PSRJ              J0633+1746

RAJ               06:33:54.1530            0.0027
DECJ              +17:46:12.909            0.040

PMRA              142.2                    1.1
PMDEC             107.4                    1.2
PX                4.0                      1.3

POSEPOCH          49793.5

F0                4.2175543305799640947     0  2.1039170405856566504e-10
F1                -1.952079842504069107e-13 0  6.3221093259334305307e-18
PEPOCH            55555
DMEPOCH           55225
DM                0
START             54689.6516821
FINISH            56579.6573336
TRACK             -2
TZRMJD            55641.655276521851192
TZRFRQ            0
TZRSITE           coe
TRES              880.219
EPHVER            5
CLK               TT(TAI)
MODE              1
UNITS             TDB
EPHEM             DE405
NITS              1
NTOA              272
CHI2R             -nan                     0
F2                2.710533491413192129e-26  0  0
SIFUNC            2  0
IFUNC1            54633.65528901678771944717 -0.0018974514            0.0
IFUNC2            54640.65528901678771944717 -0.0017220786            0.0
IFUNC3            54647.65528901678771944717 -0.0015407966            0.0
IFUNC4            54654.65528901678771944717 -0.0013544998            0.0
IFUNC5            54661.65528901678771944717 -0.0011641812            0.0
IFUNC6            54668.65528901678771944717 -0.0009709245            0.0
IFUNC7            54675.65528901678771944717 -0.0007758929            0.0
IFUNC8            54682.65528901678771944717 -0.0005803158            0.0
IFUNC9            54689.65528901678771944717 -0.0003854718            0.0
IFUNC10           54696.65528824734792578965 -0.0001926709            0.0
IFUNC11           54703.65528747790085617453 -0.0000032340            0.0
IFUNC12           54710.65528729684592690319 0.0001815283             0.0
IFUNC13           54717.65528711579099763185 0.0003603369             0.0
IFUNC14           54724.65528719165740767494 0.0005319672             0.0
IFUNC15           54731.65528726752381771803 0.0006952695             0.0
IFUNC16           54738.65528721112059429288 0.0008491907             0.0
IFUNC17           54745.65528715471737086773 0.0009927929             0.0
IFUNC18           54752.65528748132055625319 0.0011252718             0.0
IFUNC19           54759.65528780793101759627 0.0012459717             0.0
IFUNC20           54766.65528757935680914670 0.0013543987             0.0
IFUNC21           54773.65528735078260069713 0.0014502318             0.0
IFUNC22           54780.65528738535067532212 0.0015333298             0.0
IFUNC23           54787.65528741991874994710 0.0016037362             0.0
IFUNC24           54794.65528772145626135170 0.0016616807             0.0
IFUNC25           54801.65528802299377275631 0.0017075774             0.0
IFUNC26           54808.65528824018838349730 0.0017420198             0.0
IFUNC27           54815.65528845737571828067 0.0017657728             0.0
```

```
IFUNC28          54822.65528462092333938926 0.0017797620          0.0
IFUNC29          54829.6552807844709604978 6 0.0017850598          0.0
IFUNC30          54836.65527873999963048846 0.0017828693          0.0
IFUNC31          54843.6552766955283004790 5 0.0017745056          0.0
IFUNC32          54850.6552765067899599671 4 0.0017613757          0.0
IFUNC33          54857.6552763180588954128 3 0.0017449561          0.0
IFUNC34          54864.6552760946797206997 9 0.0017267693          0.0
IFUNC35          54871.6552758713005459867 4 0.0017083604          0.0
IFUNC36          54878.6552759476544451899 8 0.0016912715          0.0
IFUNC37          54885.6552760240010684356 1 0.0016770175          0.0
IFUNC38          54892.6552759332480491139 0 0.0016670617          0.0
IFUNC39          54899.6552758425023057498 0 0.0016627920          0.0
IFUNC40          54906.6552759424957912415 3 0.0016654985          0.0
IFUNC41          54913.6552760424892767332 5 0.0016763526          0.0
IFUNC42          54920.6552765472370083443 8 0.0016963877          0.0
IFUNC43          54927.6552770519920159131 3 0.0017264821          0.0
IFUNC44          54934.6552759894257178530 1 0.0017673447          0.0
IFUNC45          54941.6552749268594197928 9 0.0018195030          0.0
IFUNC46          54948.6552761949496925808 5 0.0018832939          0.0
IFUNC47          54955.6552774630399653688 1 0.0019588580          0.0
IFUNC48          54962.6552762446954147890 2 0.0020461360          0.0
IFUNC49          54969.6552750263435882516 2 0.0021448698          0.0
IFUNC50          54976.6552757155222934670 7 0.0022546050          0.0
IFUNC51          54983.6552764046937227249 1 0.0023746980          0.0
IFUNC52          54990.6552762451028684154 2 0.0025043248          0.0
IFUNC53          54997.6552760855120141059 2 0.0026424940          0.0
IFUNC54          55004.6552764312364161014 6 0.0027880610          0.0
IFUNC55          55011.6552767769608180970 0 0.0029397456          0.0
IFUNC56          55018.6552760312115424312 7 0.0030961517          0.0
IFUNC57          55025.6552752854549908079 2 0.0032557879          0.0
IFUNC58          55032.6552762878200155682 9 0.0034170909          0.0
IFUNC59          55039.6552772901850403286 5 0.0035784490          0.0
IFUNC60          55046.6552773623625398613 5 0.0037382266          0.0
IFUNC61          55053.6552774345400393940 5 0.0038947892          0.0
IFUNC62          55060.6552774256269913166 8 0.0040465285          0.0
IFUNC63          55067.6552774167212191969 2 0.0041918866          0.0
IFUNC64          55074.6552770712441997602 6 0.0043293795          0.0
IFUNC65          55081.6552767257744562812 1 0.0044576199          0.0
IFUNC66          55088.6552771249989746138 5 0.0045753377          0.0
IFUNC67          55095.6552775242307689040 9 0.0046813990          0.0
IFUNC68          55102.6552775702220969833 4 0.0047748233          0.0
IFUNC69          55109.6552776162061491049 8 0.0048547972          0.0
IFUNC70          55116.6552767001412576064 5 0.0049206867          0.0
IFUNC71          55123.6552757840763661079 1 0.0049720459          0.0
IFUNC72          55130.6552754886579350568 4 0.0050086224          0.0
IFUNC73          55137.6552751932467799633 7 0.0050303611          0.0
IFUNC74          55144.6552755643642740324 1 0.0050374028          0.0
IFUNC75          55151.6552759354817681014 5 0.0050300817          0.0
IFUNC76          55158.6552758776742848567 7 0.0050089187          0.0
IFUNC77          55165.6552758198668016120 8 0.0049746119          0.0
IFUNC78          55172.6552759318292373791 3 0.0049280249          0.0
IFUNC79          55179.6552760437916731461 9 0.0048701717          0.0
IFUNC80          55186.6552757767058210447 4 0.0048022001          0.0
IFUNC81          55193.6552755096126929856 8 0.0047253725          0.0
IFUNC82          55200.6552766716049518436 2 0.0046410452          0.0
IFUNC83          55207.6552778336044866591 7 0.0045506461          0.0
IFUNC84          55214.6552765766973607242 1 0.0044556516          0.0
IFUNC85          55221.6552753197975107468 7 0.0043575626          0.0
IFUNC86          55228.6552766242166399024 4 0.0042578802          0.0
IFUNC87          55235.6552779286357690580 2 0.0041580818          0.0
IFUNC88          55242.6552772332797758281 2 0.0040595972          0.0
IFUNC89          55249.6552765379237825982 3 0.0039637862          0.0
IFUNC90          55256.6552768838228075765 1 0.0038719164          0.0
IFUNC91          55263.6552772297145565971 7 0.0037851437          0.0
IFUNC92          55270.6552763854851946234 7 0.0037044940          0.0
```

```
IFUNC93          55277.65527554125583264977 0.0036308473          0.0
IFUNC94          55284.65527542493509827182 0.0035649237          0.0
IFUNC95          55291.65527530861436389387 0.0035072732          0.0
IFUNC96          55298.65527633231977233663 0.0034582669          0.0
IFUNC97          55305.65527735602518077940 0.0034180919          0.0
IFUNC98          55312.65527654566540149972 0.0033867495          0.0
IFUNC99          55319.65527573530562222004 0.0033640555          0.0
IFUNC100         55326.65527570293488679454 0.0033496442          0.0
IFUNC101         55333.65527567057142732665 0.0033429755          0.0
IFUNC102         55340.65527650222065858543 0.0033433438          0.0
IFUNC103         55347.65527733386988984421 0.0033498909          0.0
IFUNC104         55354.65527653339086100459 0.0033616206          0.0
IFUNC105         55361.65527573290455620736 0.0033774157          0.0
IFUNC106         55368.65527580909838434309 0.0033960568          0.0
IFUNC107         55375.65527588529221247882 0.0034162432          0.0
IFUNC108         55382.65527663718967232853 0.0034366144          0.0
IFUNC109         55389.65527738909440813586 0.0034557736          0.0
IFUNC110         55396.65527747671876568347 0.0034723107          0.0
IFUNC111         55403.65527756434312323108 0.0034848264          0.0
IFUNC112         55410.65527693404146702960 0.0034919555          0.0
IFUNC113         55417.65527630373253487051 0.0034923899          0.0
IFUNC114         55424.65527599510096479207 0.0034849009          0.0
IFUNC115         55431.65527568646211875603 0.0034683601          0.0
IFUNC116         55438.65527528638631338254 0.0034417585          0.0
IFUNC117         55445.65527488631050800905 0.0034042236          0.0
IFUNC118         55452.65527604561793850735 0.0033550352          0.0
IFUNC119         55459.65527720491809304804 0.0032936376          0.0
IFUNC120         55466.65527740419929614291 0.0032196498          0.0
IFUNC121         55473.65527760348049923778 0.0031328730          0.0
IFUNC122         55480.65527730412577511743 0.0030332948          0.0
IFUNC123         55487.65527700477105099708 0.0029210904          0.0
IFUNC124         55494.65527658398787025362 0.0027966216          0.0
IFUNC125         55501.65527616321196546778 0.0026604314          0.0
IFUNC126         55508.65527596484753303230 0.0025132370          0.0
IFUNC127         55515.65527576647582463920 0.0023559195          0.0
IFUNC128         55522.65527649248542729765 0.0021895104          0.0
IFUNC129         55529.65527721850230591372 0.0020151768          0.0
IFUNC130         55536.65527625718823401257 0.0018342035          0.0
IFUNC131         55543.65527529588143806905 0.0016479736          0.0
IFUNC132         55550.65527543867210624740 0.0014579471          0.0
IFUNC133         55557.65527558147005038336 0.0012656389          0.0
IFUNC134         55564.65527585199743043631 0.0010725953          0.0
IFUNC135         55571.65527612251753453165 0.0008803700          0.0
IFUNC136         55578.65527592551370617002 0.0006905004          0.0
IFUNC137         55585.65527572850987780839 0.0005044832          0.0
IFUNC138         55592.65527603484224528074 0.0003237517          0.0
IFUNC139         55599.65527634117461275309 0.0001496531          0.0
IFUNC140         55606.65527683478285325691 -0.0000165722         0.0
IFUNC141         55613.65527732838381780311 -0.0001738105         0.0
IFUNC142         55620.65527687329449690878 -0.0003210917         0.0
IFUNC143         55627.65527641821245197207 -0.0004576048         0.0
IFUNC144         55634.65527646963164443150 -0.0005827106         0.0
IFUNC145         55641.65527652105811284855 -0.0006959521         0.0
IFUNC146         55648.65527587706310441718 -0.0007970612         0.0
IFUNC147         55655.65527523306082002819 -0.0008859636         0.0
IFUNC148         55662.65527604261296801269 -0.0009627798         0.0
IFUNC149         55669.65527685217239195481 -0.0010278235         0.0
IFUNC150         55676.65527683934487868100 -0.0010815968         0.0
IFUNC151         55683.65527682652464136481 -0.0011247828         0.0
IFUNC152         55690.65527712681068805978 -0.0011582344         0.0
IFUNC153         55697.65527742709673475474 -0.0011829619         0.0
IFUNC154         55704.65527725462743546814 -0.0012001167         0.0
IFUNC155         55711.65527708215813618153 -0.0012109737         0.0
IFUNC156         55718.65527628606650978327 -0.0012169115         0.0
IFUNC157         55725.65527548996760742739 -0.0012193904         0.0
```

IFUNC158	55732.65527563798241317272	-0.0012199300	0.0
IFUNC159	55739.6552757860044948756 7	-0.0012200851	0.0
IFUNC160	55746.6552761262864805758 0	-0.0012214214	0.0
IFUNC161	55753.6552764665684662759 3	-0.0012254903	0.0
IFUNC162	55760.6552760962949832901 4	-0.0012338052	0.0
IFUNC163	55767.6552757260215003043 4	-0.0012478166	0.0
IFUNC164	55774.6552754153453861363 2	-0.0012688891	0.0
IFUNC165	55781.6552751046692719683 1	-0.0012982799	0.0
IFUNC166	55788.6552750400005606934 4	-0.0013371179	0.0
IFUNC167	55795.6552749753245734609 7	-0.0013863854	0.0
IFUNC168	55802.6552757046083570458 0	-0.0014469018	0.0
IFUNC169	55809.6552764338848646730 2	-0.0015193094	0.0
IFUNC170	55816.6552762032879400067 0	-0.0016040624	0.0
IFUNC171	55823.6552759726982912980 0	-0.0017014186	0.0
IFUNC172	55830.6552762274586712010 2	-0.0018114329	0.0
IFUNC173	55837.6552764822263270616 5	-0.0019339558	0.0
IFUNC174	55844.6552759628175408579 4	-0.0020686331	0.0
IFUNC175	55851.6552754434160306118 4	-0.0022149099	0.0
IFUNC176	55858.6552761918283067643 6	-0.0023720368	0.0
IFUNC177	55865.6552769402405829168 9	-0.0025390792	0.0
IFUNC178	55872.6552765600135899148 9	-0.0027149299	0.0
IFUNC179	55879.6552761797865969128 9	-0.0028983232	0.0
IFUNC180	55886.6552762062710826285 2	-0.0030878526	0.0
IFUNC181	55893.6552762327555683441 5	-0.0032819892	0.0
IFUNC182	55900.6552757560493773780 8	-0.0034791032	0.0
IFUNC183	55907.6552752793504623696 2	-0.0036774862	0.0
IFUNC184	55914.6552756477030925452 7	-0.0038753747	0.0
IFUNC185	55921.6552760160629986785 4	-0.0040709744	0.0
IFUNC186	55928.6552766919703572057 2	-0.0042624852	0.0
IFUNC187	55935.6552773678777157329 0	-0.0044481261	0.0
IFUNC188	55942.6552765836531762033 7	-0.0046261599	0.0
IFUNC189	55949.6552757994286366738 4	-0.0047949169	0.0
IFUNC190	55956.6552761494385777041 3	-0.0049528184	0.0
IFUNC191	55963.6552764994412427768 1	-0.0050983978	0.0
IFUNC192	55970.6552764584776014089 6	-0.0052303211	0.0
IFUNC193	55977.6552764175212359987 2	-0.0053474047	0.0
IFUNC194	55984.6552760097620193846 5	-0.0054486314	0.0
IFUNC195	55991.6552756019955268129 7	-0.0055331642	0.0
IFUNC196	55998.6552762096398510038 9	-0.0056003568	0.0
IFUNC197	56005.6552768172841751948 0	-0.0056497622	0.0
IFUNC198	56012.6552764143561944365 5	-0.0056811378	0.0
IFUNC199	56019.6552760114282136783 0	-0.0056944480	0.0
IFUNC200	56026.6552763765939744189 4	-0.0056898637	0.0
IFUNC201	56033.6552767417597351595 8	-0.0056677592	0.0
IFUNC202	56040.6552769303598324768 2	-0.0056287055	0.0
IFUNC203	56047.6552771189599297940 7	-0.0055734619	0.0
IFUNC204	56054.6552763390209292992 9	-0.0055029645	0.0
IFUNC205	56061.6552755590892047621 3	-0.0054183120	0.0
IFUNC206	56068.6552752397765289060 8	-0.0053207501	0.0
IFUNC207	56075.6552749204711290076 4	-0.0052116531	0.0
IFUNC208	56082.6552756695600692182 8	-0.0050925048	0.0
IFUNC209	56089.6552764186417334713 0	-0.0049648771	0.0
IFUNC210	56096.6552734374417923390 9	-0.0048304085	0.0
IFUNC211	56103.6552704562345752492 5	-0.0046907807	0.0
IFUNC212	56110.6552676902138045989 0	-0.0045476959	0.0
IFUNC213	56117.6552649241857579909 3	-0.0044028537	0.0
IFUNC214	56124.6552650701269158162 2	-0.0042579280	0.0
IFUNC215	56131.6552652160680736415 1	-0.0041145449	0.0
IFUNC216	56138.6552657147840363904 8	-0.0039742612	0.0
IFUNC217	56145.6552662134927231818 4	-0.0038385441	0.0
IFUNC218	56152.6552660385059425607 3	-0.0037087530	0.0
IFUNC219	56159.6552658635191619396 2	-0.0035861218	0.0
IFUNC220	56166.6552655902269179932 8	-0.0034717447	0.0
IFUNC221	56173.6552653169419500045 5	-0.0033665625	0.0
IFUNC222	56180.6552647451389930211 0	-0.0032713529	0.0

```
IFUNC223          56187.65526417332876008004 -0.0031867215          0.0
IFUNC224          56194.65526520589628489688 -0.0031130969          0.0
IFUNC225          56201.65526623846380971372 -0.0030507268          0.0
IFUNC226          56208.65526521559513639659 -0.0029996782          0.0
IFUNC227          56215.65526419272646307945 -0.0029598388          0.0
IFUNC228          56222.65526411659811856225 -0.0029309214          0.0
IFUNC229          56229.65526404046977404505 -0.0029124712          0.0
IFUNC230          56236.65526455824146978557 -0.0029038742          0.0
IFUNC231          56243.65526507601316552609 -0.0029043683          0.0
IFUNC232          56250.65526510046038310975 -0.0029130564          0.0
IFUNC233          56257.65526512490760069340 -0.0029289209          0.0
IFUNC234          56264.65526473571662791073 -0.0029508396          0.0
IFUNC235          56271.65526434651837917045 -0.0029776027          0.0
IFUNC236          56278.65526409857557155192 -0.0030079309          0.0
IFUNC237          56285.65526385064003989100 -0.0030404941          0.0
IFUNC238          56292.65526439146196935326 -0.0030739304          0.0
IFUNC239          56299.65526493227662285790 -0.0031068650          0.0
IFUNC240          56306.65526526232861215249 -0.0031379291          0.0
IFUNC241          56313.65526559238060144708 -0.0031657786          0.0
IFUNC242          56320.65526528948976192623 -0.0031891113          0.0
IFUNC243          56327.65526498659164644778 -0.0032066841          0.0
IFUNC244          56334.65526455100189195946 -0.0032173283          0.0
IFUNC245          56341.65526411541941342875 -0.0032199639          0.0
IFUNC246          56348.65526434942876221612 -0.0032136125          0.0
IFUNC247          56355.65526458344538696110 -0.0031974083          0.0
IFUNC248          56362.65526438134111231193 -0.0031706072          0.0
IFUNC249          56369.65526417924411362037 -0.0031325943          0.0
IFUNC250          56376.65526460110413609073 -0.0030828897          0.0
IFUNC251          56383.65526502296415856108 -0.0030211515          0.0
IFUNC252          56390.65526490743650356308 -0.0029471782          0.0
IFUNC253          56397.65526479190157260746 -0.0028609075          0.0
IFUNC254          56404.65526450145989656448 -0.0027624152          0.0
IFUNC255          56411.65526421101094456390 -0.0026519103          0.0
IFUNC256          56418.65526506794412853196 -0.0025297302          0.0
IFUNC257          56425.65526592487731250003 -0.0023963335          0.0
IFUNC258          56432.65526494818914216012 -0.0022522914          0.0
IFUNC259          56439.65526397150097182021 -0.0020982783          0.0
IFUNC260          56446.65526492997742025182 -0.0019350610          0.0
IFUNC261          56453.65526588844659272581 -0.0017634872          0.0
IFUNC262          56460.65526498942199395970 -0.0015844738          0.0
IFUNC263          56467.65526409039739519358 -0.0013989938          0.0
IFUNC264          56474.65526440222311066464 -0.0012080639          0.0
IFUNC265          56481.65526471405610209331 -0.0010127313          0.0
IFUNC266          56488.65526532001968007535 -0.0008140616          0.0
IFUNC267          56495.65526592598325805739 -0.0006131257          0.0
IFUNC268          56502.65526602039608405903 -0.0004109884          0.0
IFUNC269          56509.65526611480163410306 -0.0002086969          0.0
IFUNC270          56516.65526598437281791121 -0.0000072706          0.0
IFUNC271          56523.65526585394400171936 0.0001923090           0.0
IFUNC272          56530.65526476885861484334 0.0003891063           0.0
IFUNC273          56537.65526368377322796732 0.0005822398           0.0
IFUNC274          56544.65526448376476764679 0.0007708877           0.0
IFUNC275          56551.65526528375630732626 0.0009542940           0.0
IFUNC276          56558.65526452329504536465 0.0011317717           0.0
IFUNC277          56565.65526376283378340304 0.0013027065           0.0
IFUNC278          56572.65526405096898088232 0.0014665582           0.0
IFUNC279          56579.65526433909690240398 0.0016228611           0.0
IFUNC280          56586.65526433909690240398 0.0017712241           0.0
IFUNC281          56593.65526433909690240398 0.0019113293           0.0
IFUNC282          56600.65526433909690240398 0.0020429294           0.0
IFUNC283          56607.65526433909690240398 0.0021658453           0.0
IFUNC284          56614.65526433909690240398 0.0022799624           0.0
IFUNC285          56621.65526433909690240398 0.0023852266           0.0
IFUNC286          56628.65526433909690240398 0.0024816396           0.0
IFUNC287          56635.65526433909690240398 0.0025692546           0.0
```

List of Figures

List of Tables

Abbreviations

3FGL	Third Fermi Sources Catalog
ACD	Anti-Coincidence Detector
ADC	Analog to Digital Converter
AEM	ACD Electronics Module
AGILE	Astro-rivelatore Gamma a Immagini LEggero
AGN	Active Galaxy Nuclei
AMC	Active Mirror Control
ASI	Italian Space Agency
a.s.l	Above Sea Level
BH	Black Hole
CCO	Central Compact Object
CFRP	Carbon Fiber Reinforced Plastic
CGRO	Compton Gamma-Ray Observatory
CMB	Cosmic Microwave Background
COMPTEL	Imaging Compton Telescope
CORSIKA	Cosmic-Ray Simulation for Kascade
CR	Cosmic Ray
CRU	Command Response Unit
CTA	Cherenkov Telescope Array
DAMPE	DArk Mater Particule Explorer
DAQ	Data AcQuistion
DM	Dark Matter
DRS	Domino Ring Sample
EAS	Extensive Air Shower
EBM	Event Builder Module
EBL	Extragalactic Background Light
EGRET	Energetic Gamma Ray Experiment Telescopes
EPU	Events Processor Unit
FADC	Flash Analog to Digital Converter
FoV	Field of View
FSSC	Fermi Science Support Center
GASU	Global-trigger/ACD-module/Signal distribution Unit
GBM	Gamma-ray Burst Monitor
GTI	Godd Time Interval
GRB	Gamma-ray Burst
GZK	Greisen-Zatsepin-Kuzmin
HE	High Energy

HAWC	High Altitude Water Cherenkov
HEGRA	High-Energy Gamma-Ray Astronomy
HESS	High Energy Stereoscopic System
IACT	Imaging Atmospheric Cherenkov Telescope
IC	Inverse Compton
IGM	Inter-galatic Magnetic Field
IPRC	Individual Pixel Rate Control
IRFs	Instrument Response Functions
ISM	InterStellar Medium
LAT	Large Area Telescope
LC	Light Cylinder
LIV	Lorentz Invariance Violation
LST	Large Size Telescope
LUT	Look-Up Table
MAGIC	Major Atmospheric Gamma-ray Imaging Cherenkov
MARS	MAGIC Analysis Reconstruction Software
MATELSIM	MAGIC TELescopes SIMultion
MC	Monte Carlo
MET	Mission Elapsed Time
MJD	Modified Julian Date
MOLA	Magic OnLine Analysis
MONSTER	MAGIC Optical NanoSecond Trigger and Event Receiver
MSP	MilliSecond Pulsar
MST	Medium Size Telescope
NS	Neutron Star
NSB	Night-Sky Background
OG	Outer Gap
PC	Polar Cap
PDF	Probability Density Function
PFF	Pair Formation Front
PSF	Point Spread Function
PMT	Photo-Multiplier Tube
PWNe	Pulsar wind Nebulae
PULSAR	PULser And Recorder
QE	Quantum Efficiency
RF	Random Forest
ROI	Region Of Interest
SCLF	Space Charge Limited Flow
SED	Spectral Energy Distribution
SNR	Supernova Remant
SORCERER	Simple, Outright Raw Calibration; Easy, Reliable Extraction Routines
SSC	Synchrotron Self-Compton
SST	Small Size Telescope
STAR	STandard Analysis Reconstruction
TEM	Tower Electronic Module
TKR	Converter TracKeR
TOA	Time Of Arrival

TS	Test Statistic
UTC	Coordinated Universal Time
VCSEL	Vertical Cavity Surface Emitting Laser
VERITAS	Very Energetic Radiation Imaging Telescope Array System
VHE	Very High Energy
VLA	Very Large Array
XMM	X-ray Multi-Mirror

Bibliography

Abdo, A. et al. (2010). Fermi Large Area Telescope Observations of the Crab Pulsar and Nebula. *Astrophys.J.*, 708:1254–1267.

Abdo, A. A., Ackermann, et al. (2009a). Fermi/Large Area Telescope Bright Gamma-Ray Source List. *ApJS*, 183:46–66.

Abdo, A. A. et al. (2009b). Detection of 16 Gamma-Ray Pulsars Through Blind Frequency Searches Using the Fermi LAT. *Science*, 325:840–.

Abdo, A. A. et al. (2009c). Milagro Observations of Multi-TeV Emission from Galactic Sources in the Fermi Bright Source List. *ApJ*, 700:L127–L131.

Abdo, A. A. et al. (2010a). Fermi Large Area Telescope Observations of the Crab Pulsar And Nebula. *ApJ*, 708:1254–1267.

Abdo, A. A. et al. (2010b). Fermi-LAT Observations of the Geminga Pulsar. *ApJ*, 720:272–283.

Abdo, A. A. et al. (2010c). Fermi-LAT Observations of the Geminga Pulsar. *ApJ*, 720:272–283.

Abdo, A. A. et al. (2010d). Fermi Observations of the Very Hard Gamma-ray Blazar PG 1553+113. *ApJ*, 708:1310–1320.

Abdo, A. A. et al. (2010e). The First Fermi Large Area Telescope Catalog of Gamma-ray Pulsars. *ApJS*, 187:460–494.

Abdo, A. A. et al. (2013). The Second Fermi Large Area Telescope Catalog of Gamma-Ray Pulsars. *ApJS*, 208:17.

Acciari, V. A. et al. (2009). A connection between star formation activity and cosmic rays in the starburst galaxy M82. *Nature*, 462:770–772.

Acero, F. et al. (2009). Detection of Gamma Rays from a Starburst Galaxy. *Science*, 326:1080–.

Acero, F. et al. (2013). Constraints on the Galactic Population of TeV Pulsar Wind Nebulae Using Fermi Large Area Telescope Observations. *ApJ*, 773:77.

Acero, F. et al. (2015). Fermi Large Area Telescope Third Source Catalog. *ApJS*, 218:23.

Ackermann, M. et al. (2012a). *Science*, 335:189–.

Ackermann, M. et al. (2012b). The Fermi Large Area Telescope on Orbit: Event Classification, Instrument Response Functions, and Calibration. *ApJS*, 203:4.

Ackermann, M. et al. (2013a). The First Fermi-LAT Catalog of Sources above 10 GeV. *ApJS*, 209:34.

Ackermann, M. et al. (2013b). The First Fermi-LAT Gamma-Ray Burst Catalog. *ApJS*, 209:11.

Ackermann, M. et al. (2014). Fermi-LAT Observations of the Gamma-Ray Burst GRB 130427A. *Science*, 343:42–47.

Aharonian, F. et al. (1999). Phase-resolved TeV gamma-ray characteristics of the Crab and Geminga pulsars. *A&A*, 346:913–921.

Aharonian, F. et al. (2001). Evidence for TeV gamma ray emission from Cassiopeia A. *A&A*, 370:112–120.

Aharonian, F. et al. (2004). Very high energy gamma rays from the direction of Sagittarius A*. *A&A*, 425:L13–L17.

Aharonian, F. et al. (2005a). Discovery of the binary pulsar PSR B1259-63 in very-high-energy gamma rays around periastron with HESS. *A&A*, 442:1–10.

Aharonian, F. et al. (2005b). Discovery of Very High Energy Gamma Rays Associated with an X-ray Binary. *Science*, 309:746–749.

Aharonian, F. et al. (2006a). A detailed spectral and morphological study of the gamma-ray supernova remnant RX J1713.7-3946 with HESS. *A&A*, 449:223–242.

Aharonian, F. et al. (2006b). First detection of a VHE gamma-ray spectral maximum from a cosmic source: HESS discovery of the Vela X nebula. *A&A*, 448:L43–L47.

Aharonian, F. et al. (2006c). Observations of the Crab nebula with HESS. *A&A*, 457:899–915.

Aharonian, F. A. (2004). *Very high energy cosmic gamma ray radiation*. World Scientific Publishing.

Aharonian, F. A., Bogovalov, S. V., and Khangulyan, D. (2012). Abrupt acceleration of a 'cold' ultrarelativistic wind from the Crab pulsar. *Nature*, 482:507–509.

Ahnen, M. L. et al. (2015). Teraelectronvolt pulsed emission from the Crab pulsar detected by MAGIC. *ArXiv e-prints*.

Akerlof, C. W., Breslin, A. C., Cawley, M. F., Chantell, M., Fegan, D. J., Fennell, S., Gaidos, J. A., Hagan, J., Hillas, A. M., Kerrick, A. D., Lamb, R. C., Lawrence, M. A., Lewis, D. A., Meyer, D. I., Mohanty, G., O'Flaherty, K. S., Punch, M., Reynolds, P. T., Rovero, A. C., Schubnell, M. S., Sembrowski, G., Weekes, T. C., West, M., Whitaker, T., and Wilson, C. (1993). Search for Tev Gamma-Rays from Geminga. *A&A*, 274:L17.

Akmal, A., Pandharipande, V. R., and Ravenhall, D. G. (1998). Equation of state of nucleon matter and neutron star structure. *Phys. Rev. C*, 58:1804–1828.

Albats, P., Frye, G. M., and Zych, A. D. (1972). Detection of 10-100 MeV γ-Rays from the Crab Nebula Pulsar NP 0532. *Nature*, 240:221–224.

Albert, J. et al. (2006a). Observation of Gamma Rays from the Galactic Center with the MAGIC Telescope. *ApJ*, 638:L101–L104.

Albert, J. et al. (2006b). Variable Very-High-Energy Gamma-Ray Emission from the Microquasar LS I +61 303. *Science*, 312:1771–1773.

Albert, J. et al. (2007a). Discovery of Very High Energy Gamma Radiation from IC 443 with the MAGIC Telescope. *ApJ*, 664:L87–L90.

Albert, J. et al. (2007b). Unfolding of differential energy spectra in the MAGIC experiment. *Nuclear Instruments and Methods in Physics Research A*, 583:494–506.

Albert, J. et al. (2008a). Implementation of the Random Forest method for the Imaging Atmospheric Cherenkov Telescope MAGIC. *Nuclear Instruments and Methods in Physics Research A*, 588:424–432.

Albert, J. et al. (2008b). VHE γ-Ray Observation of the Crab Nebula and its Pulsar with the MAGIC Telescope. *ApJ*, 674:1037–1055.

Albert, J. et al. (2009). Periodic Very High Energy γ-Ray Emission from LS I +61 303 Observed with the MAGIC Telescope. *ApJ*, 693:303–310.

Aleksić et al. (2012). Phase-resolved energy spectra of the Crab pulsar in the range of 50-400 GeV measured with the MAGIC telescopes. *A&A*, 540:A69.

Aleksić, J. et al. (2011). Observation of the Crab pulsar between 25 and 100 GeV with the MAGIC I telescope. *The Astrophysical Journal*, 742(1):43.

Aleksić, J. et al. (2012). Performance of the MAGIC stereo system obtained with Crab Nebula data. *Astroparticle Physics*, 35:435–448.

Aleksić, J. et al. (2014). Detection of bridge emission above 50 GeV from the Crab pulsar with the MAGIC telescopes. *A&A*, 565:L12.

Aleksic, J. et al. (2014). The major upgrade of the MAGIC telescopes, Part I: The hardware improvements and the commissioning of the system. *ArXiv e-prints*.

Aleksić, J. et al. (2016a). The major upgrade of the MAGIC telescopes, Part II: A performance study using observations of the Crab Nebula. *Astroparticle Physics*, 72:76–94.

Aleksić, J. et al. (2016b). The major upgrade of the MAGIC telescopes, Part II: A performance study using observations of the Crab Nebula. *Astroparticle Physics*, 72:76–94.

Aliu, E. et al. (2008). Observation of Pulsed γ-Rays Above 25 GeV from the Crab Pulsar with MAGIC. *Science*, 322:1221–.

Aliu, E. et al. (2011). Detection of Pulsed Gamma Rays Above 100 GeV from the Crab Pulsar. *Science*, page 6052.

Aliu, E. et al. (2012). Search for a Correlation between Very-high-energy Gamma Rays and Giant Radio Pulses in the Crab Pulsar. *ApJ*, 760:136.

Aliu, E. et al. (2015). A Search for Pulsations from Geminga above 100 GeV with VERITAS. *ApJ*, 800:61.

Archer, A. et al. (2014). Very-high Energy Observations of the Galactic Center Region by VERITAS in 2010-2012. *ApJ*, 790:149.

Arons, J. and Scharlemann, E. T. (1979). Pair formation above pulsar polar caps - Structure of the low altitude acceleration zone. *ApJ*, 231:854–879.

Atwood, W. B., Abdo, A. A., Ackermann, M., Althouse, W., Anderson, B., Axelsson, M., Baldini, L., Ballet, J., Band, D. L., Barbiellini, G., and et al. (2009). The Large Area Telescope on the Fermi Gamma-Ray Space Telescope Mission. *ApJ*, 697:1071–1102.

Atwood, W. B., Ziegler, M., Johnson, R. P., and Baughman, B. M. (2006). A Time-differencing Technique for Detecting Radio-quiet Gamma-Ray Pulsars. *ApJ*, 652:L49–L52.

Auger, P., Ehrenfest, P., Maze, R., Daudin, J., and Fréon, R. A. (1939). Extensive Cosmic-Ray Showers. *Reviews of Modern Physics*, 11:288–291.

Baade, W. and Zwicky, F. (1934a). Cosmic Rays from Super-novae. *Proceedings of the National Academy of Science*, 20:259–263.

Baade, W. and Zwicky, F. (1934b). On Super-novae. *Proceedings of the National Academy of Science*, 20:254–259.

Baring, M. G. (2004). High-energy emission from pulsars: the polar cap scenario. *Advances in Space Research*, 33:552–560.

Baughman, B. M. et al. (2015). TeV Gamma-Ray Emission Observed from Geminga with HAWC. *Proceeding of the 34th ICRC, The Hague, 2015.*

Becker, W. (2009). *Neutron Stars and Pulsars.*

Bednarek, W. (2012). On the origin of sub-TeV gamma-ray pulsed emission from rotating neutron stars. *MNRAS*, 424:2079–2085.

Bennett, K. et al. (1977). COS-B observations of pulsed gamma-ray emission from PSR 0531 plus 21 and PSR 0833-45. *A&A*, 61:279–284.

Bernlöhr, K. (2000). Impact of atmospheric parameters on the atmospheric Cherenkov technique*. *Astroparticle Physics*, 12:255–268.

Bernlöhr, K. et al. (2013). Monte Carlo design studies for the Cherenkov Telescope Array. *Astroparticle Physics*, 43:171–188.

Bertero, M. (1989). Linear inverse and ill-posed problems. *Advances in Electronics and Electron Physics, Academic Press, New York*.

Bertsch, D. L., Brazier, K. T. S., Fichtel, C. E., Hartman, R. C., Hunter, S. D., Kanbach, G., Kniffen, D. A., Kwok, P. W., Lin, Y. C., and Mattox, J. R. (1992). Pulsed high-energy gamma-radiation from Geminga (1E0630 + 178). *Nature*, 357:306.

Bignami, G. F., Boella, G., Burger, J. J., Taylor, B. G., Keirle, P., Paul, J. A., Mayer-Hasselwander, H. A., Pfeffermann, E., Scarsi, L., and Swanenburg, B. N. (1975). The COS-B experiment for gamma-ray astronomy. *Space Science Instrumentation*, 1:245–268.

Bignami, G. F. and Caraveo, P. A. (1992). Geminga: new period, old γ-rays. *Nature*, 357:287.

Bignami, G. F. and Caraveo, P. A. (1996). Geminga: Its Phenomenology, Its Fraternity, and Its Physics. *ARA&A*, 34:331–382.

Bignami, G. F., Caraveo, P. A., and Lamb, R. C. (1983). An identification for 'Geminga' (2CG 195+04) 1E 0630+178 - A unique object in the error box of the high-energy gamma-ray source. *ApJ*, 272:L9–L13.

Bignami, G. F., Caraveo, P. A., Paul, J. A., Salotti, L., and Vigroux, L. (1987). A deep optical study of the field of IE 0630 + 178. *ApJ*, 319:358–361.

Bildsten, L. (1998). Gravitational Radiation and Rotation of Accreting Neutron Stars. *ApJ*, 501:L89–L93.

Bogovalov, S. V. and Aharonian, F. A. (2000). Very-high-energy gamma radiation associated with the unshocked wind of the Crab pulsar. *MNRAS*, 313:504–514.

Bradt, H., Rappaport, S., and Mayer, W. (1969). X-Ray and Optical Observations of the Pulsar NP 0532 in the Crab Nebula. *Nature*, 222:728–730.

Brun, R. Rademakers, F. (1997). ROOT - An object oriented framework. *Nuclear Instruments and Methods in Physics Research Section A: Accelerators, Spectrometers, Detectors and Associated Equipment*, 381(1-2).

Buccheri, R., Bennett, K., Bignami, G. F., Bloemen, J. B. G. M., Boriakoff, V., Caraveo, P. A., Hermsen, W., Kanbach, G., Manchester, R. N., Masnou, J. L., Mayer-Hasselwander, H. A., Ozel, M. E., Paul, J. A., Sacco, B., Scarsi, L., and Strong, A. W. (1983). Search for pulsed gamma-ray emission from radio pulsars in the COS-B data. *A&A*, 128:245–251.

Celik, O. (2008). Observations of the Crab Nebula and Pulsar with VERITAS. *International Cosmic Ray Conference*, 2:847–850.

Chandrasekhar, S. (1931). The Maximum Mass of Ideal White Dwarfs. *ApJ*, 74:81.

Chen, K. and Ruderman, M. (1993). Pulsar death lines and death valley. *ApJ*, 402:264–270.

Cheng, K. S. and Ding, W. K. Y. (1994). Pulsed gamma-ray emission from short-period pulsars. *ApJ*, 431:724–731.

Cheng, K. S., Ho, C., and Ruderman, M. (1986a). Energetic radiation from rapidly spinning pulsars. I - Outer magnetosphere gaps. II - VELA and Crab. *ApJ*, 300:500–539.

Cheng, K. S., Ho, C., and Ruderman, M. (1986b). Energetic radiation from rapidly spinning pulsars. I - Outer magnetosphere gaps. II - VELA and Crab. *ApJ*, 300:500–539.

Cheng, K. S., Ho, C., and Ruderman, M. (1986c). Energetic Radiation from Rapidly Spinning Pulsars. II. VELA and Crab. *ApJ*, 300:522.

Chernoff, H. (1954). On the distributiono of the likelihood ratio. *Ann. Math. Stat.*, 25 :573-578.

Cocke, W. J., Disney, M. J., and Taylor, D. J. (1969). Discovery of Optical Signals from Pulsar NP 0532. *Nature*, 221:525–527.

Collado, T. H. (2015). *Sensitivity studies for the Cherenkov Telescope Array.* PhD thesis, Universidad Complutense de Madrid.

Comella, J. M., Craft, H. D., Lovelace, R. V. E., and Sutton, J. M. (1969). Crab Nebula Pulsar NP 0532. *Nature*, 221:453–454.

de Jager, O. C., Raubenheimer, B. C., and Swanepoel, J. W. H. (1989). A poweful test for weak periodic signals with unknown light curve shape in sparse data. *A&A*, 221:180–190.

de Luca, A., Caraveo, P. A., Mattana, F., Pellizzoni, A., and Bignami, G. F. (2006). On the complex X-ray structure tracing the motion of Geminga. *A&A*, 445:L9–L13.

Du, Y. J., Qiao, G. J., and Wang, W. (2012). Radio-to-TeV Phase-resolved Emission from the Crab Pulsar: The Annular Gap Model. *ApJ*, 748:84.

Duyvendak, J. J. L. (1942). Further Data Bearing on the Identification of the Crab Nebula with the Supernova of 1054 A.D. Part I. The Ancient Oriental Chronicles. *PASP*, 54:91–94.

Dyks, J., Harding, A. K., and Rudak, B. (2004). Relativistic Effects and Polarization in Three High-Energy Pulsar Models. *ApJ*, 606:1125–1142.

Dyks, J. and Rudak, B. (2003). Two-Pole Caustic Model for High-Energy Light Curves of Pulsars. *ApJ*, 598:1201–1206.

Engel, R., Heck, D., and Pierog, T. (2011). Extensive Air Showers and Hadronic Interactions at High Energy. *Annual Review of Nuclear and Particle Science*, 61:467–489.

Fawley, W. M., Arons, J., and Scharlemann, E. T. (1977). Potential drops above pulsar polar caps - Acceleration of non neutral beams from the stellar surface. *ApJ*, 217:227–243.

Fazio, G. G., Helmken, H. F., O'Mongain, E., and Weekes, T. C. (1972). Detection of High-Energy Gamma Rays from the Crab Nebula. *ApJ*, 175:L117.

Fermi, E. (1949). On the Origin of the Cosmic Radiation. *Physical Review*, 75:1169–1174.

Fermi, E. (1954). Galactic Magnetic Fields and the Origin of Cosmic Radiation. *ApJ*, 119:1.

Fichtel, C. E., Hartman, R. C., Kniffen, D. A., Thompson, D. J., Ogelman, H., Ozel, M. E., Tumer, T., and Bignami, G. F. (1975). High-energy gamma-ray results from the second small astronomy satellite. *ApJ*, 198:163–182.

Fierro, J. M., Michelson, P. F., Nolan, P. L., and Thompson, D. J. (1998a). Phase-resolved Studies of the High-Energy Gamma-Ray Emission from the Crab, Geminga, and VELA Pulsars. *ApJ*, 494:734–746.

Fierro, J. M., Michelson, P. F., Nolan, P. L., and Thompson, D. J. (1998b). Phase-resolved Studies of the High-Energy Gamma-Ray Emission from the Crab, Geminga, and VELA Pulsars. *ApJ*, 494:734–746.

Fomin, V. P., Stepanian, A. A., Lamb, R. C., Lewis, D. A., Punch, M., and Weekes, T. C. (1994). New methods of atmospheric Cherenkov imaging for gamma-ray astronomy. I. The false source method. *Astroparticle Physics*, 2:137–150.

Franceschini, A., Rodighiero, G., and Vaccari, M. (2008). Extragalactic optical-infrared background radiation, its time evolution and the cosmic photon-photon opacity. *A&A*, 487:837–852.

Fritz, G., Henry, R. C., Meekins, J. F., Chubb, T. A., and Friedman, H. (1969). X-ray Pulsar in the Crab Nebula. *Science*, 164:709–712.

Giacani, E., Reynoso, E. M., Dubner, G., Goss, W. M., Green, A. J., and Johnston, S. (2005). The neutral gas in the environs of the Geminga gamma-ray pulsar. *Advances in Space Research*, 35:1070–1073.

Giavitto, G. (2013). *Observing the VHE Gamma-Ray Sky with the MAGIC Telescopes: the Blazar B3 2247+381 and the Crab Pulsar*. PhD thesis, Institut de Física d'Altes Energies.

Gini, C. (1921). Measurement of inequality of incomes. *The Economic Journal*, 31:121–124.

Goldreich, P. and Julian, W. H. (1969). Pulsar Electrodynamics. *ApJ*, 157:869.

Greisen, K. (1966). End to the Cosmic-Ray Spectrum? *Physical Review Letters*, 16:748–750.

Grenier, I. A. and Harding, A. K. (2006). Pulsar twinkling and relativity. In Alimi, J.-M. and Füzfa, A., editors, *Albert Einstein Century International Conference*, volume 861 of *American Institute of Physics Conference Series*, pages 630–637.

Halpern, J. P. and Holt, S. S. (1992). Discovery of soft X-ray pulsations from the gamma-ray source Geminga. *Nature*, 357:222–224.

Halpern, J. P. and Ruderman, M. (1993). Soft X-ray properties of the Geminga pulsar. *ApJ*, 415:286–297.

Hanlon, W. F. (2015). "Updated cosmic ray spectrum".

Heck, D., Knapp, J., Capdevielle, J. N., Schatz, G., and Thouw, T. (1998). *CORSIKA: a Monte Carlo code to simulate extensive air showers.*

Heiles, C. and Campbell, D. B. (1970). Pulsar NP 0532: Properties and Systematic Polarization of Individual Strong Pulses at 430 MHz. *Nature*, 226:529–531.

Heitler, W. (1954). The Quantum Theory of Radiation: Third Edition. *Courier Dover Publications*.

Hermsen, W., Swanenburg, B. N., Bignami, G. F., Boella, G., Buccheri, R., Scarsi, L., Kanbach, G., Mayer-Hasselwander, H. A., Masnou, J. L., and Paul, J. A. (1977). New high energy gamma-ray sources observed by COS B. *Nature*, 269:494.

Hess, V. F. (1913a). Über Beobachtungen der durchdringenden Strahlung bei sieben Freiballonfahrten. *Physikalische Zeitschrift*, 13:1084–91.

Hess, V. F. (1913b). Über den ursprung der durchdringenden strahlung. *Physikalische Zeitschrift*, 14:610.

Hewish, A., Bell, S. J., Pilkington, J. D. H., Scott, P. F., and Collins, R. A. (1968). Observation of a Rapidly Pulsating Radio Source. *Nature*, 217:709–713.

Hillas, A. M. (1985). Cerenkov light images of EAS produced by primary gamma. *International Cosmic Ray Conference*, 3:445–448.

Hirotani, K. (2006a). High-Energy Emission from Pulsar Magnetospheres. *Modern Physics Letters A*, 21:1319–1337.

Hirotani, K. (2006b). High-Energy Emission from Pulsar Magnetospheres. *Modern Physics Letters A*, 21:1319–1337.

Hirotani, K. (2008). Outer-Gap versus Slot-Gap Models for Pulsar High-Energy Emissions: The Case of the Crab Pulsar. *ApJ*, 688:L25–L28.

Hirotani, K. (2013). Luminosity Evolution of Gamma-Ray Pulsars. *ApJ*, 766:98.

Hirotani, K. (2015a). Three-dimensional Non-vacuum Pulsar Outer-gap Model: Localized Acceleration Electric Field in the Higher Altitudes. *ApJ*, 798:L40.

Hirotani, K. (2015b). Three-dimensional Non-vacuum Pulsar Outer-gap Model: Localized Acceleration Electric Field in the Higher Altitudes. *ApJ*, 798:L40.

Hobbs, G. B., Edwards, R. T., and Manchester, R. N. (2006). TEMPO2, a new pulsar-timing package - I. An overview. *MNRAS*, 369:655–672.

Hrupec, D. (2008). *Extragalactic sources of rapidly variable high energy gamma radiation*. PhD thesis, University of Zagreb.

Jackson, J. (1999). *Classical Electrodynamics*. John Wiley & Sons Inc, third edition.

Kargaltsev, O. Pavlov, G. (2008). 40 Years of Pulsars: Millisecond Pulsars, Magnetars and More. *AIP. Conf. Proc*, 983.

Kargaltsev, O., Rangelov, B., and Pavlov, G. G. (2013). Gamma-ray and X-ray Properties of Pulsar Wind Nebulae and Unidentified Galactic TeV Sources. *ArXiv e-prints*.

Kennel, C. F. and Coroniti, F. V. (1984). Confinement of the Crab pulsar's wind by its supernova remnant. *ApJ*, 283:694–709.

Kerr, M. (2010). *Likelihood methods for the detection and characterization of gamma-ray pulsars with the Fermi large area telescope*. PhD thesis, University of Washington.

Kirsch, M. G. F., Kendziorra, E., and Staubert, R. (2004). Phase-resolved Spectroscopy of the Crab Pulsar with XMM-Newton. In Camilo, F. and Gaensler, B. M., editors, *Young Neutron Stars and Their Environments*, volume 218 of *IAU Symposium*, page 331.

Kniffen, D. A., Hartman, R. C., Thompson, D. J., and Fichtel, C. E. (1973). SAS-2 Observations of Gamma Rays from the Galactic Plane. *ApJ*, 186:L105.

Knight, H. S., Bailes, M., Manchester, R. N., Ord, S. M., and Jacoby, B. A. (2006). Green Bank Telescope Studies of Giant Pulses from Millisecond Pulsars. *ApJ*, 640:941–949.

Kohnle, A. o. (1996). Stereoscopic imaging of air showers with the first two HEGRA Cherenkov telescopes. *Astroparticle Physics*, 5:119–131.

Kolhorster, V. F. (1913). Messungen der Durchdringenden Strahlung im Freiballon in Grösseren Höhen. *Physikalische Zeitschrift*, 14:1153–1156.

Krennrich, F. et al. (1993). Observation of VHE γ-Emission from the Crab Nebula with the Prototype of the HEGRA Air Cerenkov Telescope Array. *International Cosmic Ray Conference*, 1:251.

Kuiper, L., Hermsen, W., Cusumano, G., Diehl, R., Schönfelder, V., Strong, A., Bennett, K., and McConnell, M. L. (2001). The Crab pulsar in the 0.75-30 MeV range as seen by CGRO COMPTEL. A coherent high-energy picture from soft X-rays up to high-energy gamma-rays. *A&A*, 378:918–935.

Kurfess, J. D. (1971). Observation of Low-Energy Gamma Radiation from NP 0532. *ApJ*, 168:L39.

Laffon, H., Smith, D. A., Guillemot, L., and for the Fermi-LAT Collaboration (2015). New pulsars detected in gamma-rays with the Fermi-LAT. *ArXiv e-prints*.

Langmuir, I. (1913). The Effect of Space Charge and Residual Gases on Thermionic Currents in High Vacuum. *Physical Review*, 2:450–486.

Leung, G. C. K., Takata, J., Ng, C. W., Kong, A. K. H., Tam, P. H. T., Hui, C. Y., and Cheng, K. S. (2014). Fermi-LAT Detection of Pulsed Gamma-Rays above 50 GeV from the Vela Pulsar. *ApJ*, 797:L13.

Li, T.-P. and Ma, Y.-Q. (1983). Analysis methods for results in gamma-ray astronomy. *ApJ*, 272:317–324.

Lombardi, S. (2011). Advanced stereoscopic gamma-ray shower analysis with the MAGIC telescopes. *International Cosmic Ray Conference*, 3:266.

Longair, M. S. (2011). *High Energy Astrophysics*.

Lopez, M. (2006). *Astronomí Gamma con el Telescopio MAGIC: Observaciones de la Nebulosa y Pulsar del Crangrejo*. PhD thesis, Universidad Complutense de Madrid.

López, M. et al. (2013). Simulations of the MAGIC telescopes with matelsim. *Proceeding of the 33rd ICRC, Rio de Janeiro*.

Lundmark, K. (1921). Suspected New Stars Recorded in Old Chronicles and Among Recent Meridian Observations. *PASP*, 33:225.

Lyne, A. G., Pritchard, R. S., and Graham-Smith, F. (1993). Twenty-Three Years of Crab Pulsar Rotational History. *MNRAS*, 265:1003.

Lyubarsky, Y. and Kirk, J. G. (2001). Reconnection in a Striped Pulsar Wind. *ApJ*, 547:437–448.

Lyutikov, M. (2012). The γ-Ray Spectrum of Geminga and the Inverse Compton Model of Pulsar High-energy Emission. *ApJ*, 757:88.

M. S. Blackett, P. (1948). A possible contribution to the night sky from the Cerenkov radiation emitted by cosmic rays. In *The Emission Spectra of the Night Sky and Aurorae*, pages 0–0.

Malofeev, V. M. and Malov, O. I. (1997). Detection of Geminga as a radio pulsar. *Nature*, 389:697–699.

Malov, O. I., Malofeev, V. M., Teplykh, D. A., and Logvinenko, S. V. (2015). The Geminga radio pulsar. New low-frequency results. *Astronomy Reports*, 59:183–190.

Manchester, R. N., Hobbs, G. B., Teoh, A., and Hobbs, M. (2005). The Australia Telescope National Facility Pulsar Catalogue. *AJ*, 129:1993–2006.

Masnou, J. L., Bennett, K., Bignami, G. F., Buccheri, R., Caraveo, P., Damico, N., Hermsen, W., Kanbach, G., Lichti, G. G., and Mayer-Hasselwander, H. A. (1977). Search for gamma-ray time variability of Cygnus X-3 and CG 195+4. In Wills, R. D. and Battrick, B., editors, *Recent Advances in Gamma-Ray Astronomy*, volume 124 of *ESA Special Publication*, pages 33–37.

Mayer, M. et al. (2013). Rapid Gamma-ray flux variability durin the 2013 March Crab Nebula flare. *ArXiv*.

Mayer-Hasselwander, H. A., Bertsch, D. L., Brazier, K. T. S., Chiang, J., Fichtel, C. E., Fierro, J. M., Hartman, R. C., Hunter, S. D., Kanbach, G., Kwok, P. W., Kniffen, D. A., Lin, Y. C., Mattox, J. R., Michelson, P. F., Nolan, P. L., Pinkau, K., Rothermel, H., Schneid, E. J., Sommer, M., Sreekumar, P., Thompson, D. J., and von Montigny, C. (1994). High-energy gamma radiation from Geminga observed by EGRET. *ApJ*, 421:276–283.

Mazin, D. (2007). *A study of very high energy gamma-ray emission from AGNs and constraints on the extragalactic background light.* PhD thesis, Technische Universität München.

Mazin, D. (2009). Constraints on Extragalactic Background Light from Cherenkov telescopes: status and perspectives for the next 5 years. In Bastieri, D. and Rando, R., editors, *American Institute of Physics Conference Series*, volume 1112 of *American Institute of Physics Conference Series*, pages 111–120.

Meegan, C. et al. (2009). The Fermi Gamma-ray Burst Monitor. *ApJ*, 702:791–804.

Meurer, C., Blümer, J., Engel, R., Haungs, A., and Roth, M. (2006). Muon production in extensive air showers and its relation to hadronic interactions. *Czechoslovak Journal of Physics*, 56(27):A211–A219.

Michel, F. C. (1982). Theory of pulsar magnetospheres. *Reviews of Modern Physics*, 54:1–66.

Mochol, I. and Pétri, J. (2015). Very high energy emission as a probe of relativistic magnetic reconnection in pulsar winds. *MNRAS*, 449:L51–L55.

Muslimov, A. G. and Harding, A. K. (2003). Extended Acceleration in Slot Gaps and Pulsar High-Energy Emission. *ApJ*, 588:430–440.

Muslimov, A. G. and Harding, A. K. (2004). High-Altitude Particle Acceleration and Radiation in Pulsar Slot Gaps. *ApJ*, 606:1143–1153.

Muslimov, A. G. and Tsygan, A. I. (1992). General relativistic electric potential drops above pulsar polar caps. *MNRAS*, 255:61–70.

Nepomuk Otte, A., Kondratiev, V., and Lyutikov, M. (2009). Search for emission at 100 GeV from the Crab pulsar in correlation with giant pulses in radio. In *APS April Meeting Abstracts*, page B8004.

Ng, C.-Y. and Romani, R. W. (2004). Fitting Pulsar Wind Tori. *ApJ*, 601:479–484.

Ng, C.-Y. and Romani, R. W. (2008). Fitting Pulsar Wind Tori. II. Error Analysis and Applications. *ApJ*, 673:411–417.

Nieto, D. (2012). *Dark Matter constrains from high energy astrophysical observations*. PhD thesis, Universidad Complutense de Madrid, Departamento de Física Atómica, Molecular y Nuclear.

Nolan, P. L. et al. (1993). Observations of the Crab pulsar and nebula by the EGRET telescope on the Compton Gamma-Ray Observatory. *ApJ*, 409:697–704.

Olive, K. A. and Particle Data Group (2014). Review of Particle Physics. *Chinese Physics C*, 38(9):090001.

Oramas, A. L. (2014). *Multi-year Campaign of the Gamma-Ray Binary LS I +61 303 and Search for VHE Emission from Gamma-Ray Binary Candidates with the MAGIC Telescopes*. PhD thesis, Institut de Física d'Altes Energies.

Pacini, F. (1968). Rotating Neutron Stars, Pulsars and Supernova Remnants. *Nature*, 219:145–146.

Page, D. (2004). The Minimal Cooling of Neutron Stars. *ArXiv Astrophysics e-prints*.

Page, D., Lattimer, J. M., Prakash, M., and Steiner, A. W. (2004). Minimal Cooling of Neutron Stars: A New Paradigm. *ApJS*, 155:623–650.

Page, D. and Usov, V. V. (2002). Thermal Evolution and Light Curves of Young Bare Strange Stars. *Physical Review Letters*, 89(13):131101.

Pavlov, G. G., Bhattacharyya, S., and Zavlin, V. E. (2010). New X-ray Observations of the Geminga Pulsar Wind Nebula. *ApJ*, 715:66–77.

Pellizzoni, A. et al. (2009). High-Resolution Timing Observations of Spin-Powered Pulsars with the AGILE Gamma-Ray Telescope. *ApJ*, 691:1618–1633.

Pétri, J. and Lyubarsky, Y. (2007). Magnetic reconnection at the termination shock in a striped pulsar wind. *A&A*, 473:683–700.

Polikarov, A. (1954). Comptes rendus de l'Académie bulgare des Sciences. 7(2).

Prosekin, A. Y., Kelner, S. R., and Aharonian, F. A. (2013). Synchrotron-to-curvature transition regime of radiation of charged particles in a dipole magnetic field. *ArXiv e-prints*.

Radecke, H. D. and Kanbach, G. (1992). The EGRET high energy gamma ray telescope on GRO: instrument description and scientific mission. In di Gesu, V., Scarsi, L., Buccheri, R., and Crane, P., editors, *Data Analysis in Astronomy*, pages 303–310.

Ransom, S. M., Eikenberry, S. S., and Middleditch, J. (2002). Fourier Techniques for Very Long Astrophysical Time-Series Analysis. *AJ*, 124:1788–1809.

Ritt, S. (2008). Design and performance of the 6 GHz waveform digitizing chip DRS4. *IEEE Nuclear Science Symposium Conference Record*, pages 1512–1515.

Rolke, W. A. and López, A. M. (2001). Confidence intervals and upper bounds for small signals in the presence of background noise. *Nuclear Instruments and Methods in Physics Research A*, 458:745–758.

Romani, R. W. (1996). Gamma-Ray Pulsars: Radiation Processes in the Outer Magnetosphere. *ApJ*, 470:469.

Romani, R. W. and Watters, K. P. (2010). Constraining Pulsar Magnetosphere Geometry with γ-ray Light Curves. *ApJ*, 714:810–824.

Ruderman, M. A. and Sutherland, P. G. (1975). Theory of pulsars - Polar caps, sparks, and coherent microwave radiation. *ApJ*, 196:51–72.

Ryan, J. M. (1989). The scientific objectives of COMPTEL on the Gamma Ray Observatory. *Nuclear Physics B Proceedings Supplements*, 10:121–129.

Rybicki, G. B. and Lightman, A. P. (1991). *Radiative Process in Astrophysics*. Wiley-VCH.

Saito, T. (2010). *Study of the High Energy Gamma-ray Emission from the Crab Pulsar with the MAGIC telescope and Fermi-LAT*. PhD thesis, München.

Schmelling, M. (1994). The method of reduced cross-entropy. A general approach to unfold probability distributions. *Nuclear Instruments and Methods in Physics Research Section A: Accelerators, Spectrometers, Detectors and Associated Equipment*, 340.

Schroedter, M., Kondratiev, V., and Lyutikov, M. (2010). Search for Gamma-ray Emission Coincident with Giant Radio Pulses from the Crab. In *APS April Meeting Abstracts*, page C1018.

Shearer, A. and Golden, A. (2002). Why study pulsars optically? In Becker, W., Lesch, H., and Trümper, J., editors, *Neutron Stars, Pulsars, and Supernova Remnants*, page 44.

Smith, A. J. et al. (2000). *American Institute of Physics Conference Series*, 515.

Spitkovsky, A. (2006). Time-dependent Force-free Pulsar Magnetospheres: Axisymmetric and Oblique Rotators. *ApJ*, 648:L51–L54.

Staelin, D. H. (1970). Observed Shapes of Crab Nebula Radio Pulses. *Nature*, 226:69–70.

Staelin, D. H. and Reifenstein, III, E. C. (1968). Pulsating Radio Sources near the Crab Nebula. *Science*, 162:1481–1483.

Striani, E. et al. (2013). Variable Gamma-Ray Emission from the Crab Nebula: Short Flares and Long "Waves". *Astrophysical journal*, 765:52.

Sturrock, P. A. (1971). A Model of Pulsars. *ApJ*, 164:529.

Swanenburg, B. N., Bennett, K., Bignami, G. F., Buccheri, R., Caraveo, P., Hermsen, W., Kanbach, G., Lichti, G. G., Masnou, J. L., Mayer-Hasselwander, H. A., Paul, J. A., Sacco, B., Scarsi, L., and Wills, R. D. (1981). Second COS B catalog of high-energy gamma-ray sources. *ApJ*, 243:L69–L73.

Tavani, M. et al. (2008). The AGILE space mission. *Nuclear Instruments and Methods in Physics Research A*, 588:52–62.

Tescaro, D. et al. (2013). The MAGIC telescopes DAQ software and the on-the-fly online analysis client. *Proceeding of the 33rd ICRC, Rio de Janeiro, 2013*.

Thompson, D. J. (2004). Gamma Ray Pulsars. In Cheng, K. S. and Romero, G. E., editors, *Cosmic Gamma-Ray Sources*, volume 304 of *Astrophysics and Space Science Library*, page 149.

Thompson, D. J. (2008). Gamma ray astrophysics: the EGRET results. *Reports on Progress in Physics*, 71(11):116901.

Tikhonov, A. and Arsenin, V. (1977). Methods for ill-posed problems. *Scripta Series in Mathematics (Scripta Mathematics, New York, 1977)*.

Topchiev, N. P. o. (2015). GAMMA-400 gamma-ray observatory. *ArXiv e-prints*.

Torres, D. F. and Anchordoqui, L. A. (2004). Astrophysical origins of ultrahigh energy cosmic rays. *Reports on Progress in Physics*, 67:1663–1730.

Usov, V. V. (1975). Wave zone structure of NP 0532 and infrared radiation excess of Crab Nebula. *Ap&SS*, 32:375–377.

Viganò, D., Torres, D. F., and Martín, J. (2015). A systematic synchro-curvature modelling of pulsar γ-ray spectra unveils hidden trends. *MNRAS*, 453:2599–2621.

Vink, J., Bamba, A., and Yamazaki, R. (2011). The Radiative X-ray and Gamma-ray Efficiencies of Rotation-powered Pulsars. *ApJ*, 727:131.

Völk, H. J. and Bernlöhr, K. (2009). Imaging very high energy gamma-ray telescopes. *Experimental Astronomy*, 25:173–191.

W. B. Atwood, et al (2009). The large area telescope on the fermi gamma-ray space telescope mission. *The Astrophysical Journal*, 697(2):1071.

Wagner, R. M. (2006). *Measurement of Very High Energy Gamma-Ray Emission from Four Blazars Using the MAGIC Telescope and a Comparative Blazar Study.* PhD thesis, Max Planck Institu Fur Physik.

Wampler, E. J., Scargle, J. D., and Miller, J. S. (1969). Optical Observations of the Crab Nebula Pulsar. *ApJ*, 157:L1.

Wang, R.-B. and Hirotani, K. (2011). Death Line of Gamma-Ray Pulsars with Outer Gaps. *ApJ*, 736:127.

Weekes, T. C. et al. (1989). Observation of TeV gamma rays from the Crab nebula using the atmospheric Cerenkov imaging technique. *ApJ*, 342:379–395.

Weisskopf, M. C., Tananbaum, H. D., Van Speybroeck, L. P., and O'Dell, S. L. (2000). Chandra X-ray Observatory (CXO): overview. In Truemper, J. E. and Aschenbach, B., editors, *X-Ray Optics, Instruments, and Missions III*, volume 4012 of *Society of Photo-Optical Instrumentation Engineers (SPIE) Conference Series*, pages 2–16.

Wilks, S, S. (1938). The large sample distribution of the likelihood ratio for testing composite hypotheses. *Ann. Math. Stat.*, 9 :60-62.

Woosley, S. and Janka, T. (2005). The physics of core-collapse supernovae. *Nature Physics*, 1:147–154.

Zanin, R. (2011). *Observation of the Crab pulsar wind nebula and microquasar candidates with MAGIC.* PhD thesis, Institut de Física d'Altes Energies.

Zanin, R. et al. (2013). MARS, the MAGIC analysis and reconstruction software. *Proceeding of the 33rd ICRC, Rio de Janeiro, 2013.*

Zatsepin, G. T. and Kuz'min, V. A. (1966). Upper Limit of the Spectrum of Cosmic Rays. *ZhETF Pisma Redaktsiiu*, 4:114.

Zhang, L. and Cheng, K. S. (1997). High-Energy Radiation from Rapidly Spinning Pulsars with Thick Outer Gaps. *ApJ*, 487:370–379.

Zhang, L., Cheng, K. S., Jiang, Z. J., and Leung, P. (2004). Gamma-Ray Luminosity and Death Lines of Pulsars with Outer Gaps. *ApJ*, 604:317–327.